Photoionization-Pumped Short-Wavelength Lasers

by

Henry Cornelius Kapteyn

Abstract

The process of photoionization can create population inversions in highly-excited ions on transitions at short wavelengths. A laser-produced plasma can be used as a bright x-ray source to produce laser action on these transitions. This thesis discusses the first demonstration and the analysis of a new type of photoionization-pumped laser. In addition, future prospects for photoionization-pumped x-ray lasers are discussed.

A review of proposed mechanisms for creating photoionization-pumped lasers is presented along with a review of the physics of x-ray lasers. Following this is a discussion of the first experimental demonstration of two short-wavelength lasers. The population inversions on these transitions, in xenon at 108.9 nm, and in krypton at 90.7 nm, are created by Auger decay following inner-shell photoionization. Gains of exp(7) for the xenon transition and exp(4.5) for the krypton transition were measured. The demonstration of these lasers depended on proper experimental design to limit the deleterious effects of amplified spontaneous emission on the systems. Modeling of the laser dynamics is in good agreement with experiment. Possible superradiance effects in the laser system were also observed.

A novel experimental setup was used to measure the lifetimes of the relevant atomic levels. This setup used a Q-switched and mode-locked laser to create a high repetition rate plasma x-ray source. The technique of time-correlated photon counting was used to

measure the lifetimes of the upper and lower laser levels, with results of 4.75±0.15 and 20.5±2 nsec for xenon, and 2.0±0.1 and 4.5±0.3 nsec for krypton. Neutral-gas collisional quenching coefficients and fluorescence branching ratios were also measured.

Finally, a scheme to create an x-ray laser on the K-α transitions of light atoms and molecules is developed. The population inversion would be created by an ultrafast laser plasma x-ray source. Simulations of this scheme for the case of neon gas with a transition wavelength of 1.46 nm show that a gain of exp(10) could be produced using an excitation pulse of 1-10 Joules in 50 fsec. A laser capable of producing these pulses is technologically feasible using the recently developed technique of chirped pulse amplification in conjunction with new laser materials such as titanium-doped sapphire.

Title page

Photoionization-Pumped Short-Wavelength Lasers

Submitted in partial fulfillment of the degree

Doctor of Philosophy

in Physics

by

Henry Cornelius Kapteyn

Photoionization-Pumped Short-Wavelength Lasers

Henry Cornelius Kapteyn

Dedication

This thesis is dedicated to

my Wife, my Mom, and my Dad,

and my brother Robert, my sister Sanderina, my cats Femto and Miss Kitty, my vacations, my MAC IIx, microsoft word (especially the spelling checker), my new apartment, my VCR, my anticipated greater salary upon filing this theses, and my wife,

and nice sunny beaches, and nice dark laboratories, and nice people, and nice restaurants, and my nice wife,

and...

finishing my thesis.

For number sequence only.

Acknowledgments

Many people were of great help to me in the completion of my thesis work. Foremost among these were my fellow graduate student (and now my wife) Máiréad Murnane, and my thesis advisor Roger Falcone. Máiréad and I worked together on many of the early experiments, and many of the insights gained during the course of this work were the result of discussions with her. Roger was very involved as a thesis advisor, and I gained tremendously from his knowledge and insight. I seriously do not think I could have possibly learned more than I did, during the time I was his student. He's also a nice guy.

Among the other people who have been of assistance are those at the Lawrence Livermore National Laboratory who made many of these experiments possible. Richard W. Lee gave us invaluable support, advice, and encouragement for the experiments done at JANUS. The laser operators, James E. Swain and Paul Solone, did a great job of keeping the sometimes balky laser humming along. M.H. Chen, J.H. Scofield, and M.D. Rosen did various calculations for us as well.

At Berkeley, several other students have played a part in this work. Jon Schachter wrote with me the CCD imaging software discussed in Appendix B. Jing Zhu and Bill Craig did some work with the streak camera as well. Undergraduates Jeff Schuster and Alan Berezin helped with some of the hardware used in the experiments. New graduate students Alan Sullivan and Harald Hamster are keeping the experimental program going. Among the faculty, I would like to thank my qualifying committee, Y.R. Shen, S.P. Davis, and C.K. Birdsall, and thesis committee members Y.R. Shen and C.B. Harris.

Finally, I'd like to thank my mother Maria Kapteyn and my father Robert Kapteyn. They sacrificed far more than most parents, and far more than could be expected of any

parents, to give their children good educations. I wouldn't be writing this today if I had just an average set of parents.

Table of Contents

List of Figures

For number sequence only.

List of Tables

Preface

Although x-ray lasers have been the subject of much speculation for more than twenty years, and relevant experimental work has been going on for almost as long, the entire experimentally successful history of x-ray and XUV lasers has occurred within the last few years during which I have been working on my Ph.D.. The first successful experiments were reported in early 1985, by researchers at the Lawrence Livermore National Laboratory group [1]. These experiments used two beams of the Nova laser to demonstrate laser gain at 20.6 nm in highly ionized selenium. Soon afterwards the group at Princeton Plasma Physics Laboratory [2] demonstrated gain at 18.2 nm in a magnetically confined carbon plasma. Lastly, in late 1986, our group at Berkeley demonstrated gain at 108.9 nm in a partially ionized xenon gas [3]. Since these initial experiments, there have been many other reports of laser gain in similar systems, and the field has advanced technologically to the point where these short-wavelength laser devices are being contemplated for use in real experiments. However, short-wavelength lasers have yet to be used in novel experiments, and the field is still very much in its infancy.

A major difficulty with many of today's x-ray lasers is that they are too expensive. A multimillion dollar laser is used to generate at most several "shots" per day. Science is a trial and error process, and with the cost per shot as much as $100,000, it is very expensive to explore the wonders of nature. The exception to this is the xenon laser which we first demonstrated, and which has been made to operate at 2 pulses per second by the Harris group at Stanford. There are many interesting experiments to do with 108.9 nm light; however, many more experiments, such as x-ray holography, need much shorter wavelengths to be practical. In this thesis I will discuss the details behind our first demonstration of the xenon laser. Then I will move on, to describe how we intend to extend the concepts of the xenon laser to build a small-scale x-ray laser. The goal is discover the

physics necessary to develop an x-ray laser which is as useful and practical as today's table-top visible lasers are, operating regularly at a small cost. Then the real fun will begin!

Introduction

The format of this thesis is as follows: I will begin with an introduction to the basic concepts behind short-wavelength lasers, and the difficulties involved in creating them. I will also briefly discuss the many schemes that have been proposed, stressing those that have been demonstrated experimentally. I will then discuss in detail the history of photoionization-pumped lasers, and how the xenon laser system relates to other work.

In chapter 2, I will discuss the xenon and krypton Auger-decay-pumped systems. I will start by discussing the gain demonstration experiment. I will then discuss the work that evolved into the successful experiment, and the analysis of the experiment that demonstrates the extent of our understanding of these Auger-decay-pumped systems. This includes the computer modeling of the system, the many unsuccessful experiments attempting to demonstrate gain and why they didn't work, and the fluorescence spectroscopy that was used to determine the parameters necessary to successfully model the xenon system.

In chapter 3, I will discuss the future possibilities for extending photoionization-pumped lasers to shorter wavelengths. I have devised new schemes for photoionization-pumped x-ray lasers, and the ultrafast laser technology that has now become available to make these systems a possibility.

There are also two appendices. Appendix A covers the characterization of the microchannel plate streak camera used in the xenon gain experiments. Appendix B explains the operations of the various software programs which have been used in this work.

For number sequence only.

Chapter 1: An Introduction to Short-Wavelength Lasers

Ever since the laser was first invented, people have been trying to develop new lasers at shorter wavelengths. The idea of using stimulated emission to amplify light was first developed (1954) for the microwave region of the spectrum [4,5,6]. This was soon followed by the theoretical(1958) [7] , and experimental(1960) [8] development of lasers at optical wavelengths. Harmonic generation as a means of producing shorter wavelength coherent radiation was demonstrated soon afterwards (1961) [9]. However, since these pioneering years of lasers, progress towards shorter wavelengths has been much slower. Several important milestones are: (1) the demonstration of the argon ion laser [10] in the green (1964), (2) the tunable dye laser [11,12], of which dyes covering the entire visible and into the infrared and ultraviolet regions of the spectrum are now available, (3) rare gas - halogen excimer lasers [13,14], which are efficient laser sources in the 200-300 nm ultraviolet region, and (4) the nitrogen laser at 337 nm [15,16] (1963), and the hydrogen laser at 157 nm [17,18](1970) and 116 nm [19,20](1972). For many years the hydrogen laser was the shortest wavelength laser; however, much progress was made in the production of XUV radiation through harmonic conversion [21].

In contrast to the case of visible wavelength lasers, lasers at very short wavelengths were conceived far in advance of their actual demonstration. The first published work on x-ray lasers, on the subject of photoionization-pumped x-ray lasers, appeared in 1967 [22]. Although many different schemes for making a laser at very short wavelengths were proposed, and many false reports of x-ray "laser" action appeared in print, the first bona-fide x-ray laser was developed in 1984 [1], by a research group at Lawrence Livermore National Laboratory. This nearly two decade gap between conception and experimental demonstration is illustrative of the difficulty of the task. This difficulty is a direct result of the basic physics of the laser.

1.1 The basic physics of stimulated emission

To understand why x-ray lasers are difficult to make, one needs a basic understanding of the physics of laser systems. I will begin with a review of Einstein **A** and **B** coefficients--the interaction of atomic energy levels with a radiation field in thermal equilibrium. I will then discuss basic perturbation theory relating to stimulated emission of atoms, and the fundamental scaling of transition rates and energy requirements as one tries to make lasers at shorter wavelengths. Spontaneous and stimulated emission coefficients can be derived more directly from the quantization of the electromagnetic field [23]; however, the concepts used in the Einstein treatment [24](thermal equilibrium, blackbody radiation) are important to keep in mind. Also, this derivation makes it possible to deal with stimulated emission in a simple semi-classical way, rather than through QED. The primary reason for going through this derivation is to assemble all the relevant relations, derived in a consistent set of units (MKS), in one place. I have yet to find a good single reference for all the relevant equations, while different references use varying definitions and units, making calculations prone to error.

Given a system of two-level atoms assumed to be in thermal equilibrium with a radiation field, one can relate the processes of spontaneous emission and stimulated emission to each other [25]. An atom, left to itself in an excited state, will eventually decay (we will for the moment consider only the case of radiative decay). The rate can be written as the number of atoms in this excited level, times the spontaneous emission rate **A**: $\mathbf{R}_{spont} = \mathbf{N}_2 \mathbf{A}_{21}$ (level 2 is the upper and level 1 the lower level). In addition to spontaneous decay, there is the process of resonant absorption-- the atom in the lower level can absorb a photon, making a transition to the upper level: $\mathbf{R}_{abs} = \mathbf{B}_{12} \rho(\nu_{12}) \mathbf{N}_1$, where $\mathbf{B}_{12}$ is the absorption rate, and $\rho(\nu_{12})$ is the density of photons at the resonant frequency. The inverse process to absorption is stimulated emission, where the atom is de-excited by the interaction with the photon field, emitting another photon : $\mathbf{R}_{stim} = \mathbf{B}_{21} \rho(\nu_{12}) \mathbf{N}_2$. It may not be obvious that

there must be a stimulated emission rate; however, the atom is resonantly excited in stimulated emission in the same way that the atom is resonantly excited in the case of absorption. In thermal equilibrium, the populations in the various states must follow the Boltzmann distribution:

$$\frac{N_1}{N_2} = \frac{g_1}{g_2} e^{h\nu_{12}/kT} , \qquad (1.1)$$

where $\mathbf{h}\nu_{12}$ is the transition energy, and the **g**'s are the degeneracies of the levels. Also, in equilibrium the rate of emission must equal the rate of absorption:

$$N_2 A_{21} + B_{21} \rho(\nu_{12}) N_2 = B_{12} \rho(\nu_{12}) N_1 . \qquad (1.2)$$

Substituting equation 1.1 into equation 1.2 and solving gives:

$$\rho(\nu_{12}) = \frac{A_{21}}{B_{12} \left(g_1/g_2\right) e^{h\nu_{12}/kT} - B_{21}} , \qquad (1.3)$$

which, recalling the derivation of the blackbody radiation field [26], is the thermal radiation distribution

$$\rho(\nu_{12}) = \frac{8\pi h \nu_{12}^3}{c^3} \frac{1}{e^{h\nu_{12}/kT} - 1} \qquad (1.4)$$

if

$$A_{21} = \frac{g_1}{g_2} \frac{8\pi h \nu_{12}^3}{c^3} B_{12} , \qquad (1.5)$$

and

$$B_{21} = g_1/g_2 \; B_{12} . \qquad (1.6)$$

One can now write, using equations 1.2 and 1.6,

$$N_2 A_{21} = N_1 \rho(\nu_{12}) B_{12} \left(1 - \frac{g_1}{g_2} \frac{N_2}{N_1}\right) . \qquad (1.7)$$

Since the left hand side of the equation is the spontaneous decay rate, the right hand side corresponds to the net photon absorption rate, since the two processes must balance in equilibrium. This net absorption rate can be negative, if $\mathbf{g}_1\mathbf{N}_2$ is greater than $\mathbf{g}_2\mathbf{N}_1$. This would not be an equilibrium situation (equation 1.7 would be impossible to satisfy); however, the relations 1.5-1.7 derived for an equilibrium situation are equally valid whether or not the system is in equilibrium. Thus the situation is physically possible, and results in the atomic system adding energy to the electromagnetic field. This is the basis of the laser.

Considering equation 1.5, it is apparent that the ratio of spontaneous to stimulated emission rates increases as $(\mathbf{v}_{12})^3$. Spontaneous emission removes population from the upper level and puts it into the lower level, reducing the population inversion necessary for laser gain. Thus, at shorter wavelengths, spontaneous emission rapidly makes it more difficult to sustain a population inversion.

To obtain an estimate of the stimulated emission rate as a function of wavelength,one can use perturbation theory. The golden rule for transition rates for a harmonic perturbation is [27] :

$$W_{12} = \frac{1}{\hbar^2} \left|H'_{12}\right|^2 \rho_s(\nu_{12}) \quad , \qquad (1.8)$$

where $\mathbf{W}_{12}$ is the transition rate, $\mathbf{H}'_{12}$ is the perturbation matrix element for the transition (where the perturbation is assumed to be $\mathbf{H}'(\vec{r},\vec{t}\,) = \mathbf{H}'(\vec{r}\,)\,(e^{2\pi i\nu t} + e^{-2\pi i\nu t})$) , and ρ_s is the density of final states at the transition. In the semiclassical approximation, one can start by assuming the photon field as a plane wave with the electric field $\vec{\mathbf{E}}\,(\vec{r},t\,) = \vec{\mathbf{E}}\cos(2\pi\nu t)$ perturbing the electron in the atom:

$$2\,H' = -e\vec{E}\cdot\vec{r} = \vec{E}\cdot\vec{D}\,; \quad \left|H'_{12}\right|^2 = \frac{\left|\langle 2|\vec{E}\cdot\vec{D}|1\rangle\right|^2}{4} \quad , \qquad (1.9)$$

where **D** is the dipole moment $\vec{\mathbf{D}} = -e\,\vec{\mathbf{r}}$. Since for unpolarized radiation $\mathbf{E}_x^2 = \mathbf{E}_y^2 = \mathbf{E}_z^2 = \frac{1}{3}\mathbf{E}^2$, and the radiation density $\rho(\mathbf{v}_{12}) = \varepsilon_o \mathsf{E}^2$, the transition rate can be written

$$W_{12} = \frac{\rho(\nu_{12})}{6\,\varepsilon_o\,\hbar^2}\ \rho_s(\nu_{12})\,S_{12} \tag{1.10}$$

where S_{12} is the "line strength"

$$S_{12} = |\langle 2|ex|1\rangle|^2 + |\langle 2|ey|1\rangle|^2 + |\langle 2|ez|1\rangle|^2 . \tag{1.11}$$

Since the transition rate is $\mathbf{B}_{12}\,\rho(\nu_{12})$ for a single atom, this means that

$$B_{12} = \frac{1}{6\,\varepsilon_o\,\hbar^2}\ S_{12}\,\rho_s(\nu_{12}) , \tag{1.12}$$

and consequently from equation 1.5

$$A_{21} = \frac{g_1}{g_2}\frac{8\,\pi^2\,\nu^3}{3\,\varepsilon_o\,\hbar c^3}\,S_{12}\ \rho_s(\nu_{12}) . \tag{1.13}$$

The density of states ρ_s is just the final level degeneracy $\mathbf{g}_2$ times a lineshape function $\mathbf{g}(\nu - \nu_o)$ such that $\int_{-\infty}^{\infty} \mathbf{g}(\nu - \nu_o)\,d\nu = 1$. Additionally, if we define a symmetric line strength function $\mathbf{S} = \sum_{m1}\sum_{m2} \mathbf{S}_{12}$, so that **S** is independent of the direction of the transition, then summing over the final and averaging over the initial states, we get:

$$A_{21} = \frac{1}{g_2}\frac{8\,\pi^2\,\nu^3}{3\,\varepsilon_o\,\hbar c^3}\ S \tag{1.14}$$

$$B_{12} = \frac{1}{g_1}\frac{1}{6\,\varepsilon_o\,\hbar^2}\ S\,g(\nu - \nu_o) \tag{1.15}$$

$$B_{21} = \frac{1}{g_2}\frac{1}{6\,\varepsilon_o\,\hbar^2}\ S\,g(\nu - \nu_o) , \tag{1.16}$$

where for the **A** coefficient is integrated over dν since the total **A** coefficient is what is related to the experimentally observable lifetime.

One can obtain the net absorption per unit length for a collimated beam of light by using equation 1.7. For such a collimated beam, the flux density is related to the radiation density by **I** = ρ c, and thus the absorbed energy (photon energy hν) per unit area for a "slab" of width **dx** is :

$$dI = - I \left(\frac{h\nu}{c} B_{12} \left(N_1 - \frac{g_1}{g_2} N_2 \right) \right) dx \qquad (1.17)$$

This allows us to define an absorption cross section

$$\sigma = \frac{h\nu}{c} B_{12} \qquad (1.18)$$

$$\Delta N = N_1 - \frac{g_1}{g_2} N_2 \qquad (1.19)$$

such that $I = I_o e^{- \Delta N \sigma x}$. Conversely, the gain cross section can be written

$$\sigma_g = \frac{h\nu}{c} B_{21} \qquad (1.20)$$

$$\Delta N = N_2 - \frac{g_2}{g_1} N_1 \qquad (1.21)$$

for $I = I_o e^{\Delta N \sigma_g x}$. It is sometimes useful also to write the gain cross section in terms of the spontaneous emission coefficient:

$$\sigma_g = \frac{\lambda^2}{8\pi} A_{21} g (\nu - \nu_o) \quad . \qquad (1.22)$$

The lineshape function is the only thing left to consider. A transition can be either homogeneously broadened or inhomogeneously broadened, where homogeneously broadened means the linewidth is intrinsic to each individual atom, and inhomogeneously broadened means that each atom has narrow linewidth, but for the ensemble of atoms each line center wavelength varies, resulting in a broad linewidth for the system. For atomic or

ionic laser systems, the common homogeneous broadening mechanism is lifetime broadening, resulting from the uncertainty principle. The lifetime of the upper state is finite, and therefore one will expect that the energy will be uncertain, with a width of about $\Delta E\, \Delta t \approx \hbar$; $\Delta\nu \approx \frac{1}{2\pi\, \Delta t}$. The actual lineshape function for this lifetime broadening (sometimes also called "natural" broadening) is [28] a Lorentzian function, resulting from the fourier transform frequency spectrum of a source of exponentially decaying intensity :

$$g(\nu - \nu_o) = \frac{(\Delta\nu_n / 2\pi)}{(\nu - \nu_o)^2 + (\Delta\nu_n / 2)^2} , \qquad (1.23)$$

where $\Delta\nu_n$ is defined as the *full width at half maximum* of the lineshape:

$$\Delta\nu_n = \frac{1}{2\pi} \sum A , \qquad (1.24)$$

and the sum is over all decays of both the upper and the lower states (The sum of the total decay rates of the upper and lower states). At line center, the lineshape function is

$$g(0) = \frac{2}{\pi} \frac{1}{\Delta\nu_n} = \frac{0.64}{\Delta\nu_n} . \qquad (1.25)$$

With a single dominant rate determining the lifetime of the upper (or lower) state,

$$g(0) = 4\,\tau . \qquad (1.26)$$

The case of inhomogeneous broadening most commonly encountered in short-wavelength lasers is that of Doppler broadening. In a gas, the atoms are moving in random directions with a velocity distribution characteristic of the Boltzmann distribution at the temperature of the gas. The Doppler shift of the emission (or absorption) frequency is $\frac{\Delta\nu}{\nu_o} = \frac{\mathbf{v}_{atom}}{c}$, where ν_o is the center frequency, and $\mathbf{v}_{atom}$ is the velocity of the atom, given approximately by $\frac{1}{2}\, \mathbf{M}_{atom}\, \mathbf{v}_{atom}^2 \approx k\, \mathbf{T}$. Therefore the approximate broadening is

$$\Delta\nu \approx \nu_o \sqrt{\frac{2\,k\,T}{M_{atom}\,c^2}} \quad . \tag{1.27}$$

The lineshape function for Doppler broadening is Gaussian [29] :

$$g(\nu - \nu_o) = \frac{2\sqrt{\ln 2}}{\sqrt{\pi}\,\Delta\nu_d}\, e^{-(4 \ln 2\, (\nu - \nu_o)^2 / \Delta\nu_d^2)} \tag{1.28}$$

where

$$\Delta\nu_d = 2\nu_o \sqrt{\frac{2\,k\,T}{M_{atom}\,c^2} \ln 2} \tag{1.29}$$

is the full width at half-maximum of the lineshape profile. At line center, the lineshape function is

$$g(0) = \frac{2\sqrt{\ln 2}}{\sqrt{\pi}\,\Delta\nu_d} = \frac{0.94}{\Delta\nu_d} \quad . \tag{1.30}$$

The last basic concept I will discuss is that of the oscillator strength. This will provide the basis for obtaining a quantitative estimate of the rates involved. The oscillator strength is related to the line strength, and is defined by [30]

$$f_{if} = \frac{1}{g_i} \frac{4\,\pi\,m\,\nu}{3\,e^2\,\hbar}\, S \quad . \tag{1.31}$$

The reason for this definition is apparent if one calculates an **A** coefficient classically, by calculating the rate of energy loss through radiation of an electron orbiting the atom in the excited state. It has a more fundamental significance, as follows [31]. Taking a sum of the oscillator strengths from an initial state **i** to all final states **f** , and simplifying using the definition of the line strength S, and the fact that $|\langle f|ex|i\rangle|^2 = |\langle f|ey|i\rangle|^2 = |\langle f|ez|i\rangle|^2$ in this isotropic situation, we get:

$$\sum_f f_{if} = \frac{1}{g_i} \sum_f \frac{4\,\pi\,m\,\nu}{\hbar} \sum_{m_i, m_f} \langle i|\,x\,|f\rangle\langle f|\,x\,|i\rangle \quad . \tag{1.32}$$

Now, using the relation

$$\langle 2 | p_x | 1 \rangle = \frac{i}{\hbar} m (E_2 - E_1) \langle 2 | x | 1 \rangle$$
$$= 2\pi i m \nu_{21} \langle 2 | x | 1 \rangle \quad , \qquad (1.33)$$

and the fact that the sum over the final states $\mathbf{f}$, $\mathbf{m_f}$ form a complete set so that we can use the fact that $\sum_2 \langle 3 | A | 2 \rangle \langle 2 | B | 1 \rangle = \langle 3 | AB | 1 \rangle$, we can get the relation

$$\sum_f f_{if} = \frac{i}{\hbar} \frac{1}{g_i} \sum_{m_i} [\langle i | p_x x | i \rangle - \langle i | x p_x | i \rangle]$$
$$= \frac{i}{\hbar} [p_x, x]_{i\,i} \qquad (1.34)$$

since the sum over the initial states cancels the $1/\mathbf{g}_i$. Finally, using the basic commutator $[\mathbf{p}_x, \mathbf{x}]_{i\,j} = -i\hbar\,\delta_{ij}$ for one particle, or for a total position operator consisting of the sum of several electron positions, $[\mathbf{p}_x, \mathbf{x}]_{ii} = -\mathbf{Z}\, i\hbar$, one gets the relation

$$\sum_f f_{if} = Z \quad , \qquad (1.35)$$

where $\mathbf{Z}$ is the number of electrons involved in the initial state. Since there are in general a small number of strong transitions from an initial state, the value of $\mathbf{f}_{fi}$ will be ≈ 1.

In all the preceding discussion, I have assumed electric dipole transitions. Other types of transitions generally have much slower rates and are usually not important in short-wavelength laser atomic physics. In this document, I used **L-S** coupling notation almost exclusively, even though it is not always the most accurate notation for the atom in question. **L-S** coupling means that in combining the angular momentum of all the electrons in a shell, all the electron spins, and all the orbital angular momentums, are combined using the triangle rule. Then the total spin and total orbital momentum are combined to get a total angular momentum. The notation used is the usual $^{(2\mathbf{s}+1)}\mathbf{L_j}$ notation, where the **L** value is

designated **S**,**P**,**D**, etc.... **L-S** coupling is used for light atoms because in this case relativistic spin-orbit coupling is smaller than either spin-spin or orbital coupling. Selection rules for electric dipole transitions in **L-S** coupling are : $\Delta \mathbf{S} = 0$; $\Delta \mathbf{L} = 0, \pm 1$; $\mathbf{L} + \mathbf{L}' \geq 1$ [32]. Often in light atoms, since spin-orbit coupling is small, spin-orbit splitting of states of the same $^{(2\mathbf{s}+1)}\mathbf{L}$ quantum number are not resolvable (especially for K-shell transitions with large intrinsic linewidths), and thus all states can be treated as a single level of the appropriate degeneracy. For heavy atoms, spin-orbit coupling is significant. This means that **L-S** coupling notation is inaccurate; for instance, if an **L-S** coupling basis set is used in a computer code to determine the wave function of the atom, the resulting wave functions will be mixtures of several or many different basis states, of different **L** and **S** but the same **J**. Also, when **L-S** coupling is inaccurate it relaxes the dipole selection rule to $\Delta \mathbf{J} = 0, \pm 1$; $\mathbf{J} + \mathbf{J}' \geq 1$. This means that in heavier atoms, many more transitions are allowed. The other notation I use in the following text is the x-ray shell scheme. in this notation, **K** is used to designate electrons in the 1**s** level, **L** the 2**s** and 2**p** levels, **M** the 3**s**, 3**p**, and 3**d** levels, etc....

1.2 Energy scaling for short-wavelength lasers

Writing the spontaneous emission coefficient in terms of the oscillator strength allows one to obtain a general estimate of its magnitude as a function of transition wavelength. Using equations 1.14 and 1.31 one gets

$$A_{21} = \frac{g_1}{g_2} \frac{2 \pi e^2}{\varepsilon_o m c \lambda^2} f_{12} . \qquad (1.36)$$

Assuming $\mathbf{g}_1 = \mathbf{g}_2 = 1$, $\mathbf{f}_{12} \approx 1/2$, numerically this works out to a lifetime $\tau = 1/\mathbf{A}_{21}$ of $\tau = 3 \times 10^4 \lambda^2$ (MKS units). In the visible @ 500 nm, this corresponds to lifetimes of a few nanoseconds. At soft x-ray wavelengths @ 10 nm, lifetimes are on the order of a few picoseconds. Therefore, to pump an x-ray laser with as little energy as possible, one needs

excitation pulses of about 1 psec or less in length. If longer pulses are used, the upper level is continually re-excited.

At shorter wavelengths, not only do excited state lifetimes get shorter, but also gain cross sections for the transitions get smaller. For a naturally broadened transition, equations 1.22 and 1.26 give us

$$\sigma_g = \frac{\lambda^2}{2\pi} \quad . \qquad (1.37)$$

The important scaling factor to consider is the power requirement to obtain a given gain-length product through the medium. The output intensity of a laser scales as equations 1.20 and 1.21: $I = I_o e^{\Delta N \sigma_g x}$. The total gain-length product for light passing through the medium is thus $\Delta \mathbf{N}\ \sigma_g\ \mathbf{x} = \mathbf{GL}$; this amplification factor determines whether the gain in a laser is sufficient to overcome resonator losses, and is also the observable parameter in a gain measurement experiment. The power per unit volume necessary to sustain a population in the upper level is related to the decay rate and the transition energy: $\Delta \mathbf{N} = \frac{(\mathbf{P/V})}{h\nu} \frac{1}{\mathbf{A}_{21}}$.

Using equations 1.36 and 1.37, the total power necessary to sustain a gain-length **GL** over a cross sectional aperture of area **Area** is :

$$\text{Power} = GL\ (\text{Area})\ (h\nu)\ A_{21} \frac{2\pi}{\lambda^2}$$

$$= GL\ (\text{Area}) \frac{4 \times 10^{-29}}{\lambda^5} \quad , \qquad (1.38)$$

so that the power requirement scales as the inverse fifth power of the wavelength. This means that one would need perhaps 10^9 times the power to make a laser at 10 nm as one would need at visible wavelengths, and 10^{14} times as much at 1 nm. Of course, this equation is valid only for a naturally broadened transition excited with ~100% efficiency, which is in general not the case. If a transition has additional line broadening, the power requirements are correspondingly increased. Also, if the laser transition is excited in an inefficient

manner, more energy is needed for the laser. Laser efficiencies range from ~0.5 for diode lasers, to ~10^{-4} for ion lasers, to <10^{-6} for x-ray lasers. For x-ray lasers, the laser action occurs in a highly ionized plasma and thus there is little control over where the energy goes (one must also expend a lot of energy just to ionize the plasma).

Additionally, a very important fact is that at visible wavelengths, mirrors of reflectance > 99.99% are obtainable. This means that one can construct a resonator, and the total **GL** necessary per pass can be as little as 0.01. In the soft x-ray region, the best mirrorsavailable have a reflectance of ~20-50%. Additionally, the short timescales involved (1 psec at the speed of light is 0.3 mm) make it necessary to use very small resonators, or else the light would not have time to bounce back and forth in the cavity very many times, if at all, during the duration of the laser gain. Thus for x-ray and XUV lasers, resonators are in general impractical. It is then necessary to have enough gain in one pass to amplify randomly occurring spontaneous emission into an intense beam. This requires a **GL** >> 1 (in general, **GL** must be on the order of 10-20). Thus, the total gain per pass necessary is 100-1000 times as much for the x-ray laser as it is for visible wavelength lasers.

There are ways that one can economize on the energy used for an x-ray laser. The first method is that the volume of excited material can be minimized. This can be done by minimizing the aperture area of the laser. The second method is that, since lifetimes are shorter, one can supply the energy in a shorter pulse, reducing the total pulse energy requirements. Since the lifetime varies as λ^2 and the power varies as λ^{-5}, the total energy requirement scales as λ^{-3}. This means that, provided one can continue to compress the pump energy into shorter pulses, the unfavorable scaling of energy requirements with wavelength can be mitigated. The development of laser Q-switching and mode-locking, allowing one to create high energy laser pulses of length <1 nsec, has been instrumental in making x-ray lasers practical. More recently, pulse compression techniques make it possible to generate high-powered laser pulses of <100 fsec duration-- a timescale on order of

transition lifetimes down to 1 nm. Although such short pulses have yet to be used for pumping x-ray lasers, they hold great promise, provided that schemes can be developed where the physical timescales of the excitation processes involved in the laser are also similarly short.

The third way of minimizing the power requirements is to be more modest, and to make lasers at longer wavelengths in the XUV and VUV. This is the approach taken for the xenon laser at 109 nm. Of course, one cannot do the same types of experiments with VUV light that one can do with soft x-rays. However, it is still a significant advancement over visible lasers, and efficient generation of VUV laser light may make harmonic generation of XUV radiation possible. Also, these more modest experiments provide an intermediate step towards developing soft x-ray lasers. Much can be learned from examining these laser systems, as we will see.

Lasers at soft x-ray wavelengths can be constructed even now, however. Considering our scaling arguments, a laser with a wavelength of 100-200 nm would need a minimum of about 10^{12} times the energy of a visible laser. Considering that the smallest visible lasers can run on perhaps 1 milliwatt, this would lead to an estimated power requirement of $\geq 10^{9}$ watts for an x-ray laser. This power level is readily attainable using high powered pulsed lasers. The carbon recombination laser [2] @ 18 nm, developed at the Princeton Plasma Physics Laboratory, uses a peak power of 10^{10} Watts. The Selenium laser @21 nm [1], developed at Lawrence Livermore National Laboratory, uses a peak power of 10^{12} Watts. The most powerful laser now in existence, NOVA at LLNL, has a peak power of about 10^{14} Watts. Thus, lasers at wavelengths much shorter than 10 nm may not seem possible using present equipment. Indeed, for several years now no research effort has demonstrated substantial gain-lengths at wavelengths shorter than ~15 nm, although small gains have been measured at wavelengths as short as 5 nm [33]. However, considering equation 1.38, and using best case but not completely unreasonable parameters (laser aperture of 10 μm^2,

GL=10, and 1% pump energy efficiency), one might need as little as 1 Watt of pump power for a laser at 100 nm, 10^5 W at 10 nm, and 10^{10} W at 1 nm. This makes even a laser at 1 nm sound possible. The problem is finding a suitable physical scheme that can (1) deposit the pump energy in a small volume, and (2) can efficiently use the energy deposited. Although it is unlikely that there exists any x-ray laser mechanism that could be even 1% efficient, it is clear that there is a large gap between presently demonstrated schemes and ideal schemes. Thus there is a potentially large payoff in considering new ways of making short-wavelength lasers.

1.3 A brief survey of short-wavelength laser schemes

This section consists of a brief review of published short-wavelength laser schemes. The emphasis will be on the three basic proven types of schemes: photoionization-pumped schemes, recombination-pumped schemes, and collisionally excited schemes. I will start with photoionization-pumped lasers, since this subject is directly relevant to this thesis. I will also mention briefly ideas that have never been proven, but which appear in the literature. All proven and nearly all proposed XUV and soft x-ray lasers use a high intensity visible laser as an excitation source. The only other power source in existence capable of producing the required energy densities is the pulsed-power discharge-- essentially a large capacitor bank which can be discharged into a small volume on a time scale of ~100 nsec. Primarily due to the less-controlled nature of such discharges, no successful lasers at wavelengths shorter than the 120 nm hydrogen laser [19,20], and the argon excimer laser at 126 nm [34,35], have resulted from such devices.

This section is not intended to be a comprehensive review of short-wavelength lasers. I have yet to find any such review article; however, a number of general review articles have appeared which are helpful if not comprehensive [36,37,38,39,40,41]. Peter Hagelstein's thesis also contains an extensive bibliography of work published prior to 1981 [42].

1.3.1 Photoionization-pumped laser schemes

The concept of exciting XUV lasers using x-ray photoionization was first seriously considered by Duguay and Rentzepis in 1967 [22]. The idea behind x-ray photoionization pumping is to use an x-ray source like a laser-produced plasma, to produce a burst of bright x-rays. These x-rays are then used to excite atoms to high-lying atomic levels, in analogy to the way that visible light flashlamps are used to excite many types of visible and near-infrared lasers. Photoionization is an ideal process to use to produce highly excited states for two reasons. First, x-ray photoionization cross sections are quite broad, so that one can use a broadband x-ray source to produce specific excited states of the atom (any excess energy is taken up by the kinetic energy of the ejected electron). And second, x-rays sufficiently energetic to ionize inner-shell electrons from an atom will preferentially ionize these inner-shell electrons over outer shell electrons, creating a population inversion. Figure 1.1 is a graph of the ionization cross-section of a typical atom as a function of energy. One sees that as the incident photon energy is increased, there is a sudden jump in the ionization cross section. The energy at which this occurs is the binding energy of the inner-shell electron. Below this energy, inner-shell electrons cannot be liberated from the atom due to energy conservation, and thus the only ionization which occurs is due to outer shell ionization. Above the threshold, inner shell ionization is allowed, and this process dominates. Thus, if one illuminates atoms with x-rays of any energy above the ionization threshold, one will create a greater number of highly-excited inner-shell vacancies than of less-excited outer-shell vacancies. These inner-shell ionized atoms can then radiatively decay to the outer-shell ionized state, and since the inner-shell ionized state is more heavily populated, there is a population inversion on the transition.

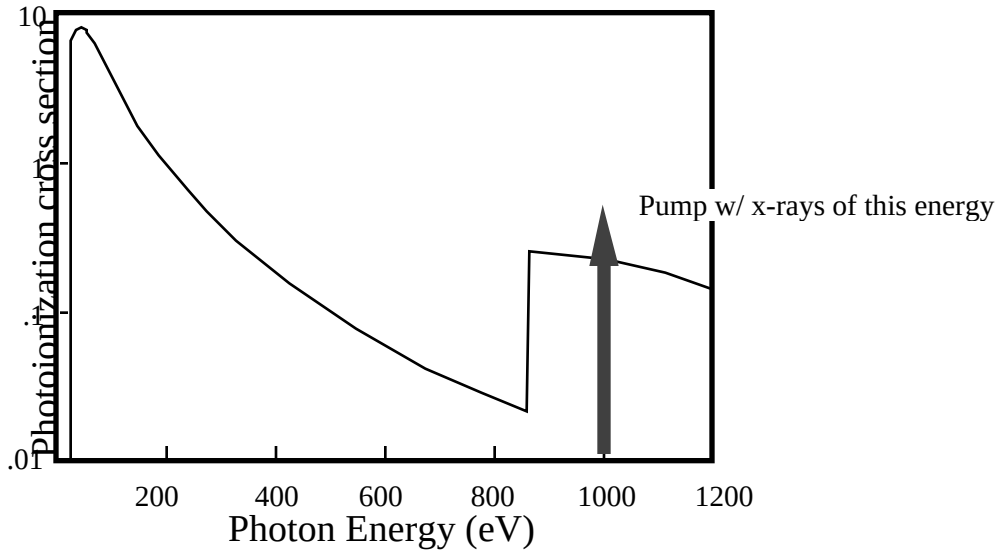

Figure 1.1: Photoionization cross-section of Neon, illustrating the x-ray absorption edge and x-ray photoionization pumping to create a population inversion.

One important factor to note is that this radiative transition has an energy slightly below the absorption edge, since it is a transition from a bound level which is therefore lower in energy than the continuum that the original electron was ejected into. Thus, the laser transition sees a relatively low absorption loss. It is important in short-wavelength lasers to consider loss mechanisms other than absorption on the laser transition, since the net gain, including all loss processes, must be positive. Another important fact is that, in the general case, the inner-shell ionized state has a non-radiative decay mode-- Auger decay. In this process, one outer-shell electron falls into the inner-shell vacancy, while yet another electron is ejected from the atom to carry away the excess energy. Unfortunately, for the longer wavelength inner-shell transitions in light atoms, which one might think are the easiest to invert, Auger decay is by a large factor the dominant decay process. Auger lifetimes are generally on order of a few femtoseconds, compared with a radiative rate 2-3 orders of magnitude slower at wavelengths of ~50 nm. Duguay's solution to this problem was to consider two situations where this Auger decay is relatively unimportant. The first case is

the sodium atom, where there is only one outer shell (3**s**) electron, and thus when the 2**p** electron is ionized, Auger decay is simply not possible. The same situation occurs in all the alkali elements, but at longer wavelengths than the 37.2 nm transition in sodium. The second case is transitions at a short enough wavelength that radiative decay is dominant over Auger decay (the λ^{-2} dependence of the radiative rate is much higher than the weak dependence of Auger rate on transition energy). He considered the Copper K-α transition at 0.154 nm. Duguay and McGuire attempted experiments on the Sodium laser scheme [43]; however these were not successful due to the unfavorable degeneracies of the upper and lower levels, and the fact that electrons produced in the photoionization can easily ionize other sodium atoms, filling the lower laser level. However, this scheme is still potentially viable using shorter excitation pulses, and is still being considered [36]. The Copper scheme remains beyond the current state of technology because of the intense x-ray fluxes needed, and has never been attempted.

Before continuing with the history of photoionization-pumped lasers, I would like to briefly consider why the photoionization cross sections behave as in Figure 1.1. The process of photoionization is basically a radiative absorption transition, as described by equations 1.15 and 1.18, but the final state, instead of being a bound state, is a free electron with a continuum of possible energies. Although the actual calculation of photoionization cross sections is quite involved, even for the case of the hydrogen atom [44], one can gain insight by considering the line strength of the transition. Neglecting degeneracy factors, the line strength is, as in equation 1.11:

$$S_{12} = e^2 \left| \langle 2 | \vec{r} | 1 \rangle \right|^2 = e^2 \int_{r=0}^{\infty} \psi^*_{ql'm'} \, \vec{r} \, \psi_{nlm} \, d\vec{r} \quad , \qquad (1.39)$$

where the bound electron is specified by the usual quantum numbers, and the ejected electron is specified by the wave vector of the electron (a continuous variable), and its angular momentum and spin. Considering the 1**s** radial wave function for a hydrogenic

atom, (ignoring the angular part which merely results in the usual selection rules), its form is:

$$R_{1s}(r) \quad e^{-r/r_o}$$

$$r_o = \frac{a_o}{Z} = \frac{\hbar}{\sqrt{2\, m_e E_b}} \quad , \qquad (1.40)$$

where $\mathbf{E}_b$ is the binding energy of the electron. Now considering the ejected electron as a free electron , its wave function is:

$$\psi_{elec} \quad e^{ikz - i\omega t}$$

$$k = \frac{\sqrt{2\, m_e E_k}}{\hbar} \quad , \qquad (1.41)$$

where $\mathbf{E}_k$ is the kinetic energy of the electron. Near the atomic core, the electron wave function is not that of a free electron. The electron is attracted to the core and the period of the wavefunction decreases somewhat (corresponding to an increased kinetic energy when the electron is near the atom). However, equation 1.41 is sufficient for our purposes. Comparing equation 1.40 with 1.41, one sees that the scale length of the bound electron wave function, $\mathbf{r}_o$, corresponds with the scale length of the free electron, $1/\mathbf{k}$, if $\mathbf{E}_b \approx \mathbf{E}_k$ ($1/\mathbf{k}$ is $1/2\pi$ the period of the plane wave, which corresponds well to the 1/e fall off of the radial wave function in a distance $\mathbf{r}_o$). The wave function overlap, equation 1.39, will thus be large for free electron kinetic energies less than or comparable to the binding energy of the electron (see figure 1.2). Thus, the behavior of the cross section for a particular atomic shell, as the photon energy is increased, is: first, at a photon energy lower than the electron binding energy, ionization is impossible. Above the threshold, the cross section is large, and remains large for photon energies of 2-3 times the threshold energy (corresponding to ejected electron energies similar to the binding energy). Then, at much higher energies, the cross section drops off. For each shell, the behavior is similar; thus the ionization cross section is as shown in figure 1.1.

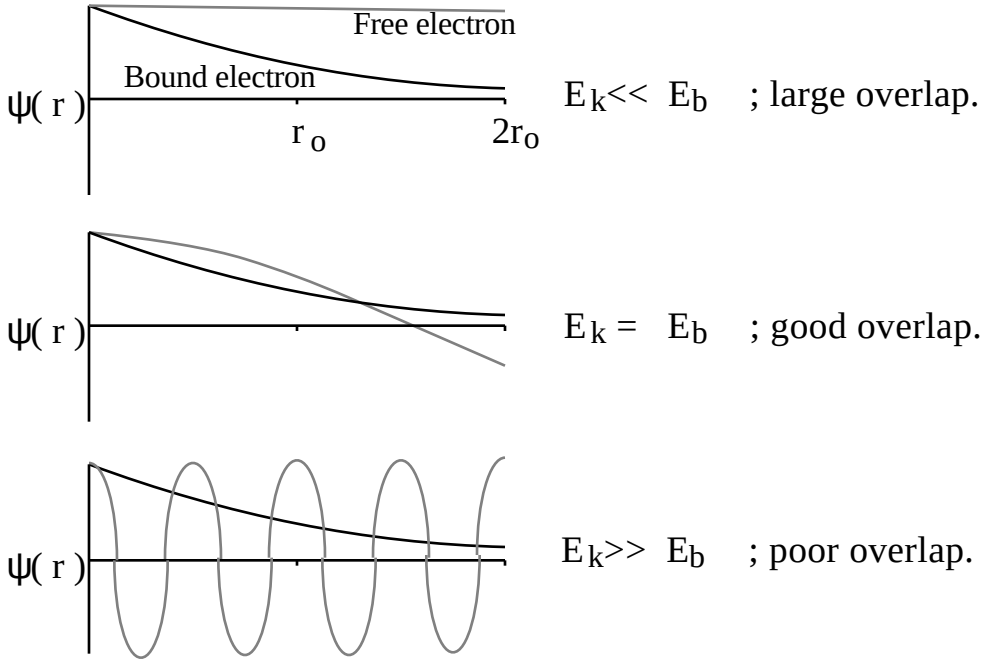

Figure 1.2: Photoionization cross section overlap integral, as in equation 1.39. The cross section is proportional to $\psi_{free} * \psi_{bound}$, which is large for $\mathbf{E}_k \leq \mathbf{E}_b$.

Soon after the original idea of photoionization pumping was introduced by Duguay, variations on the basic scheme began appearing in the literature. The first realization was that, for some atoms, the population inversion created by photoionization need not be self-terminating. In the basic Duguay scheme, the upper level atoms will decay to the lower level, but the lower level atoms do not decay. Population builds up in the lower level,quickly terminating the inversion. However, Stankevich [45] noted that the L-shell hole state produced by the initial K-shell transition may have an Auger rate faster than the rate of the original K-shell transition. With the lower laser level emptying out faster than the upper level fills it, one can have a stationary population inversion. Since the atoms are being rapidly heated, eventually the system will totally ionize and the laser levels will not exist; thus the inversion is only "quasi-stationary", unless the material can be cooled quickly enough.

The original Stankevich paper was found to be based on inaccurate data [46]. However, the idea lived on in the form that one can find atomic systems where the *radiative* K-shell rate is slower than the Auger L-shell rate out of the radiative product state. The additional requirement is that the K-shell Auger decay create a product state sufficiently shifted in energy from the radiative product state, that it does not resonantly absorb at the radiative transition wavelength. The basic level scheme is illustrated in figure 1.3. The requirements for inversion are (1) that the Auger rate from $L \rightarrow MM$ is greater than the radiative rate $K \rightarrow L$; (2) that the transitions $LL \rightarrow KL$ and $LMM \rightarrow KMM$ are sufficiently shifted in wavelength (by the fact that the atoms are more highly charged) that they do not resonantly absorb radiation from the $K \rightarrow L$ transition, and (3) that there is sufficient ionizing flux to produce gain sufficient to overcome the loss. Conditions (1) and (2) are expected to be fulfilled for the K-α transitions for the elements Sulfur (Z=16, λ = 0.54 nm) to Germanium (Z=32, λ = 0.13 nm) [47]. However, more detailed computer simulations [48] show that the primary problem with this type of scheme is that energetic electrons produced in the photoionization process can produce secondary ionizations, leading to rapid stripping of the atoms and destruction of the gain. Axelrod estimated that x-ray pulse risetimes of 5-50 fsec would be necessary in the best case for such a scheme-- this is hardly a "quasi-stationary" inversion.

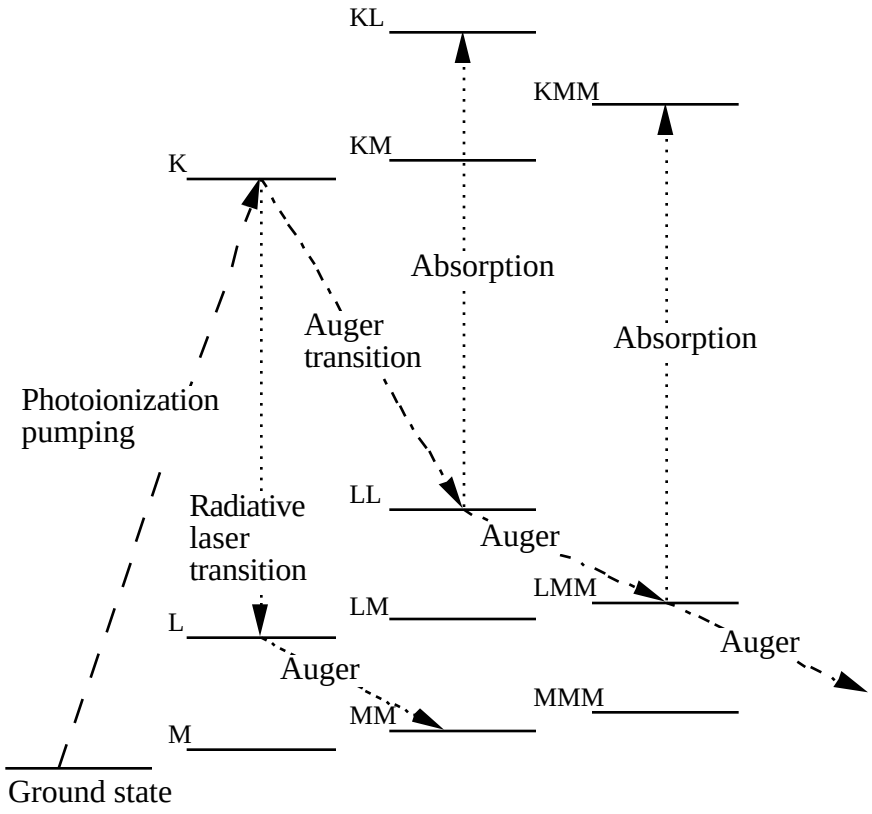

Figure 1.3: Basic level scheme for "quasi-stationary" inversion scheme proposed by Arecchi et al [47]. The letters refer to the shell vacancies of the particular states.

As the basic photoionization-pumped laser schemes seemed less and less practical, more modest photoionization-pumped schemes were introduced. McGuire [49] suggested that, instead of trying to produce a population inversion from a state that is rapidly undergoing Auger decay, one might produce a population inversion from the product state of the Auger decay. The basic scheme is illustrated in figure 1.4. He considered an inversion starting with sodium ions, or the isoelectronic neutral neon; I will refer to the neon case. Auger decay populates a number of levels of the doubly ionized atom. The exact branching ratios to these states must be calculated using computer codes; however, Auger decay to the $\mathbf{1s^2\ 2s^2\ 2p^4\ {}^3P}$ level is not allowed, and thus Auger decay must produce a population inversion between the $\mathbf{1s^2\ 2s\ 2p^5\ {}^3P}$ upper level and this state. That Auger decay to the $\mathbf{1s^2\ 2s^2\ 2p^4\ {}^3P}$ level is

not allowed can be reasoned as follows. The original K-shell hole state is a ^{2}**S** state (**L**=0) with even parity. Therefore combined final state of the atom and the ejected electron after Auger decay must also have even parity and **L**=0 (no external forces are involved in the Auger decay). The final ^{3}**P** state of the atom also has even parity (4 electrons in the **p** shell), and thus the ejected electron must have even parity as well. Therefore it must have **L**=0,2,.... However, there is no way to mix **L**=0,2,... with the **L**=1 ^{3}**P** state, and get **L**=0. Therefore this Auger decay is not allowed in **L-S** coupling, where **L** is a good quantum number. The population inversion is confirmed in experimental Auger spectrum of neon [50].

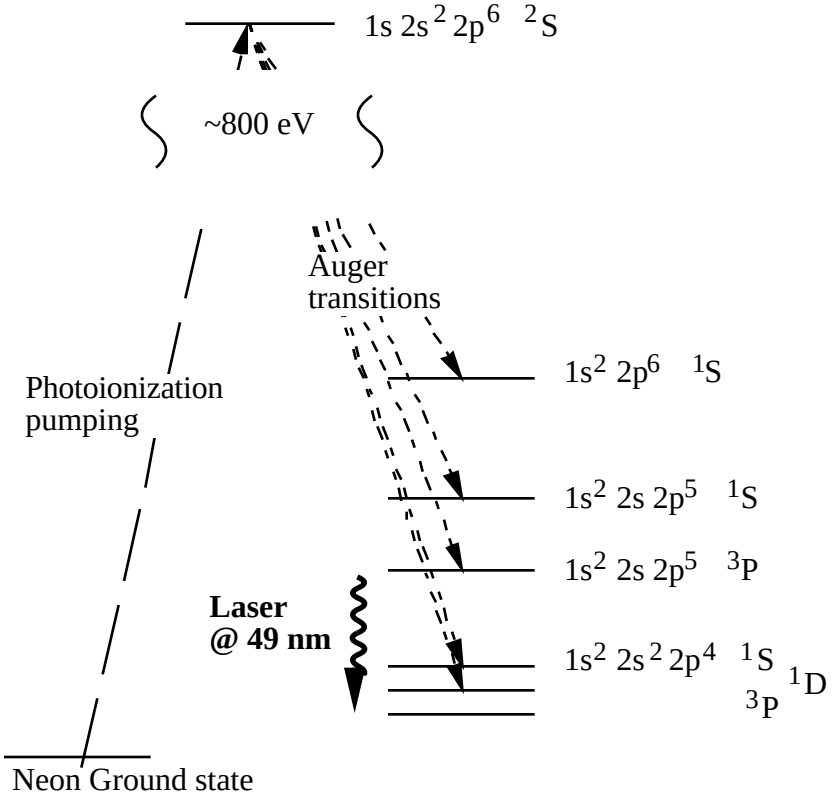

Figure 1.4: Energy level scheme of McGuire Auger-pumped laser in Neon.

McGuire's original scheme has never been tried; the disadvantage of it is that one requires >850 eV photons to ionize a K-shell electron, but the laser photon energy is only 25 eV. Laser intensities of >10^{14} W/cm^2 are needed to make a bright laser plasma source at

keV energies; thus this scheme is inefficient. The large gap in energy between the inner shell and the outer shell is the problem-- most of the energy deposited into the atom is lost in the ejected Auger electron. Heavier atoms have a much smaller energy gap between the outer shell and the next inner shell. For instance in Xenon only 68 eV is required to ionize a 4**d** inner-shell electron-- excited states of outer-shell ionized Xe^{++} lie at energies just a few eV below this. The problem with scaling the McGuire scheme to heavier atoms is that the same selection rule argument McGuire used does not work for the larger atoms, and there is no longer a population inversion between the two ^{3}**P** levels. This is because the inner-shell ionized electron is a **p** or **d** electron in this case, with **L**=1 or **L**=2. In these cases, decay to the ^{3}**P** level is allowed, and an inversion does not exist.

Fortunately (for the completion of my Ph.D.), in heavier atoms other Auger-populated inverting transitions do exist. Figure 1.5 shows the basic energy level diagram of the xenon Auger laser, the demonstration of which constitutes the major part of my thesis. In the xenon laser case, the population inversion is created by Auger decay to the Xe^{++} 4**d**^{10}5**p**^{6} ^{1}**S**$_0$ state, which then can radiatively decay to the 4**d**^{10}5**s**5**p**^{5} ^{1}**P**$_1$ state. The existence of a population inversion on this transition was first noted by Roger Falcone in 1984, based on published Auger spectroscopy data [51]. Although this data had been available since the mid 1970's, misidentification of the ^{1}**S**$_0$ state [52,53] obscured the realization that the Auger decay produced a population inversion. The branching ratio of the Auger decay to the upper and the lower level is about 1:1; however, the higher degeneracy of the lower state (**J**=1, **g**=(2**J**+1)=3) means that a 1:1 branching ratio corresponds to a population inversion. Although I have used **L-S** coupling notation to signify the states involved, these are only an approximation since **L-S** coupling is not a good approximation for the xenon atom. The analogous transition in the krypton atom also demonstrates a population inversion, at a wavelength of 90.7 nm. In the krypton case the Auger decay produces a much less favorable, but still adequate, fractional inversion.

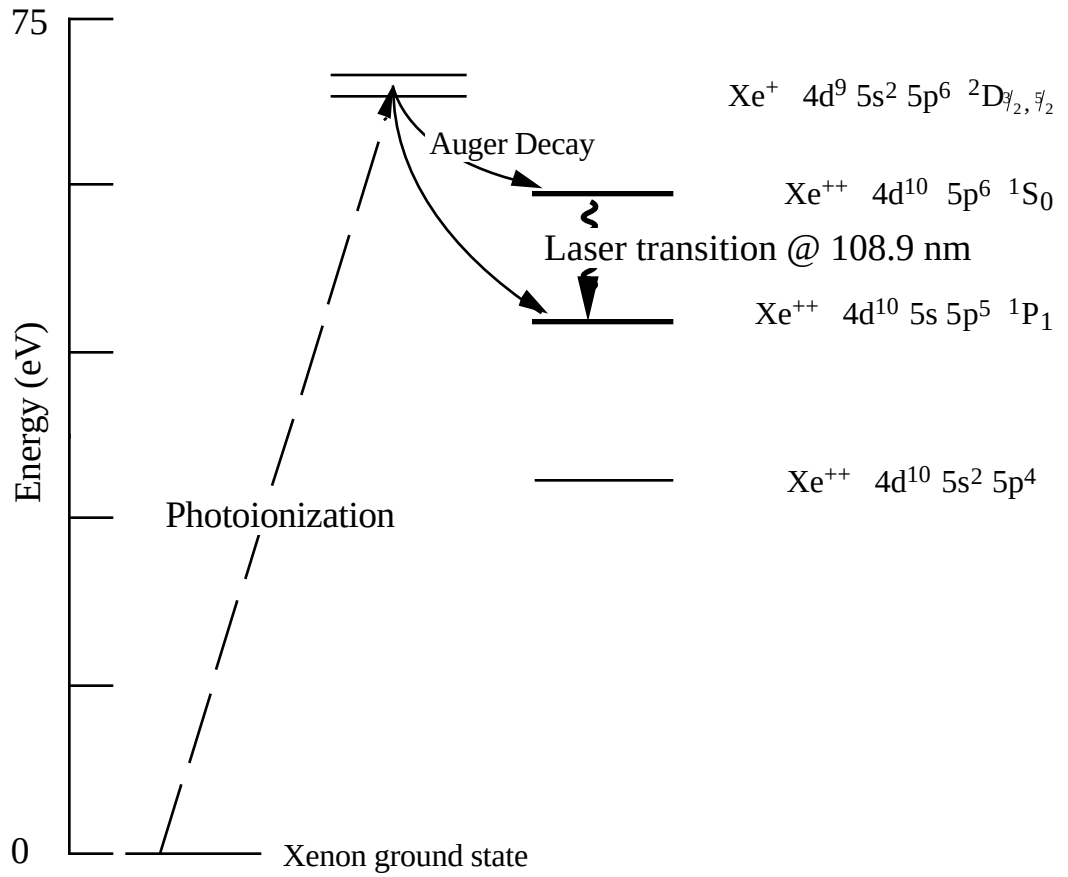

Figure 1.5: Basic xenon laser energy level scheme. Some levels not involved in the laser transition are not included for clarity.

No fundamental selection rules are involved in producing the inversion in the xenon laser, as is the case for the McGuire scheme. The reason a population inversion exists is simply because the energy spacing between successive shells is small. The electron ejected in the creation of the $^1\mathbf{S}_0$ upper laser level has a kinetic energy of only 8 or 10 eV (depending on whether the inner-shell ionized state was a **J**=5/2 or **J**=3/2 state). The electron ejected in the creation of the lower laser level has an energy of 20 or 22 eV-- over twice as high. The process of Auger decay can be described by equation 1.8, using the appropriate perturbation interaction Hamiltonian [54]. Essentially it is a two-electron process, with the perturbation consisting of the coulomb interaction between the two electrons. One

electron falls from the outer shell to the inner shell, while the other one is ejected from the outer shell into the continuum. Since one does not know which of the two electrons does what, one must consider both cases:

$$|\langle f|\, H'\, |i\rangle|^2 = \left|\left\langle i\, c\left|\frac{e^2}{|\mathbf{r}_1 - \mathbf{r}_2|}\right|\, o'\, o''\right\rangle + \left\langle c\, i\left|\frac{e^2}{|\mathbf{r}_1 - \mathbf{r}_2|}\right|\, o'\, o''\right\rangle\right|^2 ,$$

(1.42)

where **i** ,**c**, and **o**' and **o**" stand for the inner-shell, continuum, and the two outer-shell states. Although numerical evaluation of this matrix element is necessary to get a good idea of relative rates, there are several plausible reasons why this interaction might give a population inversion between the $5\mathbf{s}^0 5\mathbf{p}^6$ and the $5\mathbf{s}^1 5\mathbf{p}^5$ states. One is that, for the $5\mathbf{s}^0 5\mathbf{p}^6$ upper laser level, both electrons interacting are identical 5**s** electrons. This means that the two terms in equation 1.42 are identical, and the interference between the two terms is wholly constructive. In the case of the $5\mathbf{s}^1 5\mathbf{p}^5$ state, there can be destructive interference between the two terms, reducing the matrix element. The other reason for the inversion is that the electron ejected in producing the $5\mathbf{s}^0 5\mathbf{p}^6$ state is of very low energy. The less energetic the electron, the longer its period (as in equation 1.41), and the better the overlap with the outer-shell ionized state. This is exactly the same case as photoionization as shown in figure 1.2. Indeed, another way of considering Auger decay is to treat it as the internal photoionization absorption by one electron of the photon emitted when the other electron makes a radiative transition from the outer-shell to the inner-shell. In this case, the ionization of the 5**s** electron producing the $5\mathbf{s}^0 5\mathbf{p}^6$ state is a near-threshold process. Since **s** photoionization cross sections always peak at threshold, the production of the upper level is favored. We see that, although the energy level scheme of the xenon laser is quite different from that first proposed by Duguay in 1967, the basic reasons for population inversion are very similar.

Although the first experimental demonstration of an Auger-pumped laser was the xenon laser (described in detail in the next chapter), a significant body of relevant experimental

work preceded this demonstration. A laser pumped by autoionization was first demonstrated in 1982 by Bokor et al. [55]. Autoionization is the identical process to Auger decay in that the excited state decays through electron ejection, except that the initial excited state has two excited outer-shell electrons, instead of a single excited or ionized inner-shell electron. In Bokor's experiment, an autoionizing state was created through a two photon excitation of barium vapor. The two-photon-excited barium atoms then decayed into excited barium ions. A population inversion at wavelengths of 493 nm and 650 nm was observed. Although this laser was not excited by photoionization, the population inversion was created for essentially the same reasons as in the xenon case.

Population inversions on inner-shell photoionized transitions have also been demonstrated experimentally at visible and ultraviolet wavelengths [36]. The first such scheme was demonstrated by Silfvast et al in 1983, in cadmium vapor [56]. Photoionization was used to remove a 4**d** electron from the $4\mathbf{d}^{10}\ 5\mathbf{s}^2$ neutral ground state of cadmium. Laser transitions from this $4\mathbf{d}^9\ 5\mathbf{s}^2$ level to the $4\mathbf{d}^{10}\ 5\mathbf{p}$ levels, at 325 and 442 nm, were observed.The analogous transition in zinc also shows an inversion between $3\mathbf{d}^9\ 4\mathbf{s}^2$ and $3\mathbf{d}^{10}\ 4\mathbf{p}$ levels at 748 nm [57], as has the transition isoelectronic to cadmium, starting from In^+ produced by laser ablation, at a wavelength of 185 nm [58].

Other photoionization-pumped schemes are based on the process of shake-up during photoionization. Shake-up refers to the possibility that the photoionization process can also excite an outer-shell electron simultaneously with the process of ionizing an inner-shell electron. To preserve parity and angular momentum, the excitation is a "monopole" transition, for instance $1\mathbf{s} \rightarrow 2\mathbf{s}, 3\mathbf{s}$..., or $3\mathbf{p} \rightarrow 4\mathbf{p}, 5\mathbf{p}$.... Actually, shake-up is a result of the "sudden approximation" wave function overlap of the original outer-shell electron with the somewhat contracted outer-shell wave functions of the core-ionized state. Shake-up cross sections can be 10-25% of the primary photoionization cross section [59], and in many cases the product states can radiatively decay into levels that are not shake-up populated, or that

have shorter decay times so that they rapidly deplete. Population inversions through shake-up have been demonstrated by Silfvast et al. in Argon ions at 477 nm [60,61], and in Helium at 164 nm [60]. In the case of helium, the population inversion is between the **n**=3 shake-up state, and the **n**=2 state after the shake-up population into this level has decayed (in the He^+ hydrogenic ion **s** and **p** states are degenerate). Indirect evidence of shake-up population inversion from an autoionizing state of cadmium has also been published [62]. Harris and Caro proposed a shake-up based scheme in Lithium at 113 nm and 165 nm [63].

Since the demonstration of the xenon Auger laser, another Auger-pumped laser has been demonstrated by Walker et al [64]. This scheme starts with zinc vapor, $3\mathbf{p}^6 3\mathbf{d}^{10} 4\mathbf{s}^2$, from which a 3**p** electron is ionized. The inner-shell ionized state then rapidly Auger decays through a super Coster-Kronig process, ending up in a $3\mathbf{p}^6 3\mathbf{d}^8 4\mathbf{s}^2$ level, which inverts with respect to the $3\mathbf{d}^9 4\mathbf{p}$ levels. The transition wavelengths are 131 nm, 127 nm, and 132 nm. Super Coster-Kronig decay refers to the fact that all the electrons involved in the Auger process (3**p**, 3**d**) are in the same shell, and thus have large overlap integrals and high rates. This makes the Auger decay more selective in decaying to the upper level and increases the inversion ratio. However, the trade off is that the 3**p** photoionization cross section is much smaller then the 3**d** cross section, and thus most of the pump x-rays photoionize to states irrelevant to the laser process.

Many proposals for photoionization lasers have yet to be experimentally demonstrated. McGuire proposed another Auger laser scheme, based on Auger decay cascades [65]. He discusses several possible transitions in Al^{3+}, populated by two-step Auger decay initiated by K-shell ionization of the aluminum by >1.5 keV x-rays. The transitions are at about 16 nm. Hagelstein [42] suggested that a direct photoionization population inversion is possible for transitions within a particular shell, as well as the inter-shell transitions of the Duguay scheme. His scheme involved the outer-shell photoionization of neon gas by photons of energy >300 eV. The 2**s** photoionization threshold is 48 eV, while the 2**p**

threshold is 22 eV. Thus, the 2**s** cross section has a slower drop-off with increasing energy, and for sufficiently high incident photon energies will be larger than the 2**p** cross section, resulting in a population inversion between the two states at a wavelength of 46 nm.

Multi-step photoionization schemes have also been proposed. These involve stripping electrons from an atom by successive inner-shell photoionization. Axelrod [66] proposed a scheme for stripping boron to the hydrogen-like state through successive photoionization, in which a population inversion could be created. Multiple stripping, however, requires very high photoionization fluxes. Another recently published work proposes to isoelectronically scale the zinc inner-shell ionization transition into highly-charged ions, using a two-plasma approach. A laser pulse is used to heat a thin foil, and create substantial populations of Zn-like ions, which are then photoionized by the x-rays from another laser-produced plasma [67]. Gain at 2.5 nm is predicted to be feasible. Another work based on multiply-ionized atom photoionization is a combination photoionization-recombination scheme, where upper levels are filled by recombination, and lower levels are depleted by photoionization, creating a steady-state population inversion, provided that cooling of the plasma is sufficient [68,69,70].

Another proposed scheme is the photoionization-transfer laser. In this scheme, photoionization is used to produce an excited state, which is then transferred using an intense laser pulse of visible wavelength into another state, which then is inverted with respect to another state. The intermediate state may or may not be metastable. A metastable level is a level that, due to selection rules, cannot decay through electric dipole or other fast transitions or has a reduced oscillator strength. Thus this intermediate level has a relatively long lifetime, and it can be used as an energy storage level. In general, metastable states are high-spin states, or excited states of neutral atoms, which cannot be accessed through direct photoionization [71]. One exception is the Li^+ 1**s**2**s** state, which can be produced through photoionization of a 1**s** electron from neutral lithium, but cannot decay through Auger or electric dipole processes. This level is isoelectronic to the metastable level used in exciting

the Helium-neon visible laser. Atoms in this level can then be transferred to the 1**s**2**p** state by a modest energy visible laser, and this state can then invert to the helium-like ground state, with a wavelength of 20 nm [72]. The problem with this scheme is the ease with which the lower laser level atoms can be created through outer-shell ionization of lithium by the photoionization electrons. This scheme is still being attempted using synchrotron radiation as the x-ray pump source [73,74,75]. The discussion of other metastable laser schemes is left to the section on collisionally pumped lasers, since many metastable levels are produced through atom-electron collisions.

1.3.2 Other photon-pumped lasers

Another class of x-ray lasers which is related to photoionization lasers is the photoexcitation-pumped laser. In this scheme, photons are used to excite a specific transition in an atom or ion. This excited atom can then invert with respect to another level. Since the resonance absorption to a specific excited state is spectrally narrow, one cannot use a broadband x-ray emitter very efficiently to excite such a laser. Thus, the effort in developing viable systems of this type depends on finding a coincidence between a specific strong emission line in one species, and an absorption resonance in another. A population inversion can be created if the lower laser level is not easily populated by collisions. The photoexcitation scheme was first proposed by Vinogradov et al [76] , and Norton and Peacock [77] in 1975. Most research has focused on a line coincidence between the 1**s**-2**p** resonance transition of He-like sodium @ 1.10027 nm, and the 1**s**-4**p** absorption line of He-like neon @ 1.10003 nm [78,79,80,81], producing possible inversions on 3-2, 4-2, and 4-3 transitions in the neon ion at wavelengths of 5.8 nm, 8.2 nm, and 23 nm. Hagelstein [42] has considered many possible resonances that may be suitable schemes, and a variety of other coincidence schemes appear in the literature [82,83,84]. Recently [85], the first resonantly pumped laser was demonstrated at ultraviolet (217.7 nm and 216.3 nm) wavelengths in a Carbon III plasma pumped by radiation from a Manganese VI plasma. Also, the first experimental

demonstration of resonance-coincidence excitation, but not lasing, in the x-ray region was recently published [86]. Thus resonance pumping remains a viable possibility for soft x-ray lasing.

Resonant photoexcitation of highly excited states can also occur using radiation from a visible-wavelength laser, if one considers multiphoton processes. With a sufficiently intense photon field, a atom can undergo excitation, or ionization, by absorbing two or more photons simultaneously. With the absorption of many photons, one can place atoms in highly excited states, which might then lase at x-ray wavelengths to lower lying levels. A resonant excitation requires that the incident high-intensity photons be an exact fraction of the level excitation energy. Experimental evidence of population inversion in krypton gas using multiphoton excitation was published by Boyer et al [87]; however, no direct measurement of gain coefficients was done. In this system, ultraviolet laser radiation at 193 nm was focused to an intensity of ~10^{14} W/cm^2, exciting neutral krypton atoms into the $4\mathbf{s}4\mathbf{p}^6 4\mathbf{d}$ levels using 4 photons. These levels then invert with respect to the $4\mathbf{s}^2 4\mathbf{p}^5 n\mathbf{l}$ levels. Strong emission in the forward direction was evidence of stimulated emission. Proposals exist for using multiphoton excitation in ionized species to generate inversions at soft x-ray wavelengths [88]. As yet it is unclear whether, for highly excited transitions using many photons to obtain the excitation energy, the multiphoton process can excite an atom without fully ionizing it. The excited level is in general much closer to the ionization continuum than the ground state atom is to the excited state. These highly excited states tend to be heavily perturbed by the high-intensity electric field, making significant population of the excited state difficult [89].

1.3.3 Collisionally excited short-wavelength lasers.

The first x-ray laser to be successfully demonstrated was a collisionally excited laser. The inversion occurred in a highly ionized plasma of Neon-like Selenium at 21 nm, and was demonstrated by a group using the Nova laser at the Lawrence Livermore National Laboratory [1]. The basic idea of this laser scheme is to use electron collisions to produce excited states which can lase to lower-lying levels. The population inversion is to a level which has a short lifetime and is thus continually depleted. The neon-like selenium laser is very similar in principle to the visible argon-ion laser, except that instead of using a gas discharge as the energy source, a high intensity laser was used. The high-intensity pulsed laser heats a small strip of selenium foil to temperatures of several hundred eV, ionizing the atoms enough so that their primary excitations are at x-ray wavelengths, as well as creating electrons of sufficient energy to excite these transitions. The basic energy level scheme is shown in figure 1.6. The reason for a population inversion is that, as is usual with atomic energy levels, the transition down to the ground state has the largest energy gap, and thus by the λ^2 dependence of lifetime (equation 1.36), has the shortest lifetime. Thus, if the rates into the excited levels is comparable, and the $3\mathbf{s} \rightarrow 2\mathbf{p}$ transition radiation is not radiatively trapped, a population inversion will naturally occur.

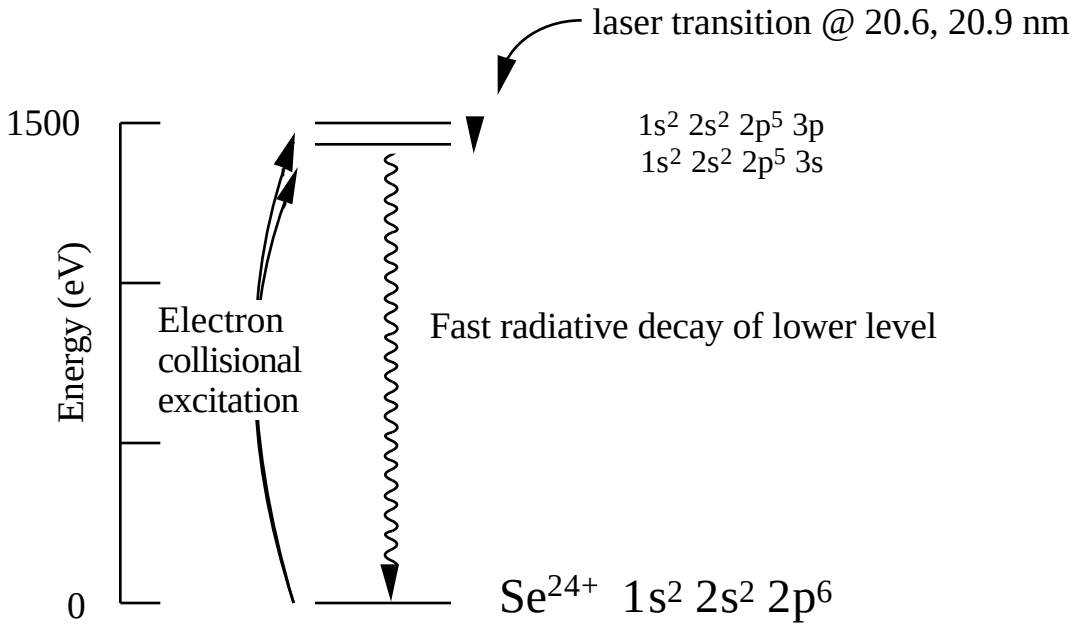

Figure 1.6: Energy level scheme of the Ne-like Selenium soft x-ray laser, developed at the Lawrence Livermore National Laboratory [1]. Population inversion is due to the fast radiative decay of the lower laser level, due to its high transition energy.

The basic $3\mathbf{p} \rightarrow 3\mathbf{s}$ inversion scheme has its roots in the ion laser first demonstrated in 1964 [10]. This first ion transition was on a $4\mathbf{p} \rightarrow 4\mathbf{s}$ transition in argon; subsequently many ion laser transitions on $3\mathbf{p} \rightarrow 3\mathbf{s}$ transitions were found [41,90]. Some of these transitions were in multiply-charged ions on transitions in the ultraviolet; thus, the extension of these schemes to highly-charged ions in the XUV was an obvious idea. It can be traced back at least to Duguay and Savage in 1973 [91], with the first serious published proposal by Elton in 1975 [92]. The other realization critical to the scheme used at LLNL was that neon-like ions are the best candidates in which to produce an inversion, since in plasmas the neon-like ionization stage is heavily populated. This occurs since electron ionization to the fluorine-like state requires removal of an electron from a closed shell, and thus the ionization potential is very large. Inversions in neon-like ions were first discussed by

Zherikhin, Koshelev, and Letokhov in 1976 [93], and subsequent to this a steady stream of theoretical papers, mostly by Soviet physicists, has appeared in print [94,95,96,97].

The experimental demonstration of the neon-like scheme by the LLNL group resulted from the development of the exploding-foil amplifier [98]. In this scheme, the plasma within which the inversion occurs is created from a thin (~100 nm) metal foil, which is completely ionized by the pump laser. In this way, the plasma expands in both directions outward, resulting in a plasma with relatively small electron density gradients compared with a plasma created on a solid target. The low electron density gradient is important in that the index of refraction for the amplifying x-rays depends on the electron density, according to the classical free electron model of the x-ray index of refraction [99]:

$$n = \sqrt{1 - \frac{N e^2}{\varepsilon_\circ m \omega^2}} \quad . \qquad (1.43)$$

Since this index is less than one, and decreasing with increasing electron density, a strong electron density gradient will tend to steer the amplified beam out of the plasma, making long gain-lengths for the light being amplified impossible. However, a recent paper disputes that the index gradient should be a significant effect [100], since the phenomenon of gain-guiding [101] should dominate over the index gradient to keep the amplified beam in the high-gain region of the plasma. Experimental data from experiments at NRL have also shown substantial gain using solid targets [102].

Since the first experimental demonstration in 1985, much subsequent work has been done on these collisional excitation schemes [103]. Some controversy has surrounded the exact mechanisms by which the laser levels are populated; computer codes predicted the highest gain on the J=0 to J=1 transition, contrary to experimental data which showed almost no gain on this line. The present conjecture is that the lines are populated by a number of different processes including collisional excitation, inner-shell ionization of

Na-like ions, and dielectronic and three-body recombination from fluorine-like atoms [104]. The basic neon-like scheme has been extended to shorter wavelengths, as low as Molybdenum @ 10.6 nm - 14 nm [105], and to longer wavelengths by a group at the Naval Research Laboratory [102]. The basic scheme can also be extended to nickel-like atoms. Nickel-like is a bit of a misnomer since the shell structure for these highly ionized atoms is different from that of neutral atoms, and a nickel-like configuration corresponds to the closed shell atom $1\mathbf{s}^2\ 2\mathbf{s}^2\ 2\mathbf{p}^6\ 3\mathbf{s}^2\ 3\mathbf{p}^6\ 3\mathbf{d}^{10}$, with lasing occurring on the $4\mathbf{d} \rightarrow 4\mathbf{p}$ transitions. In larger atoms the inter-shell energy gap is smaller as in the case of the xenon laser, and thus lower plasma temperatures are necessary to excite short-wavelength transitions. Small gains have been observed in nickel-like ions at wavelengths as low as nickel-like ytterbium @ 5.03 nm [33,106]. Schemes in Neodynium-like ions have also been proposed [107].

Quite a different type of collisional excitation laser is collisionally excited transitions in neutral or not highly ionized atoms. In this system, the lasing medium is not a plasma, but excited states are also created through electron collisions. The only method of producing the high electron densities needed for creating population inversions in the XUV using this mechanism, without creating an ionized plasma, is by using the photoelectrons ejected in the x-ray photoionization process. Thus, experimentally these schemes bear more resemblance to photoionization lasers than to the LLNL schemes previously discussed. A laser-produced plasma x-ray source is used to ionize a gas surrounding the plasma, and the electrons ejected though the photoionization process then collide with other atoms, exciting them to high lying states which can then lase. This scheme has been pioneered by Harris's group at Stanford [71,108,109,110,111], and recently a laser pumped in this manner has been demonstrated. For lasers at XUV wavelengths, these highly excited atoms are usually of energy above the ionization continuum; thus, states metastable or quasi-metastable against autoionization are sought. These are usually high-spin states of excited neutral alkalis,

which cannot autoionize due to conservation rules, or have only weak coupling to states that do. Some of these levels can have appreciable radiative rates, and thus make good XUV laser candidates. An energy level diagram of the recently demonstrated Cesium laser [108] is shown in figure 1.7. The upper laser level is populated by electron collisional pumping, while the depopulation mechanism of the lower laser level is unknown. The state which lases normally has a radiative yield of only 0.0014, and thus is not visible in the XUV spectrum unless stimulated emission occurs. This laser is a rare case of an XUV laser which on paper shouldn't work but in fact does, as opposed to the other way around.

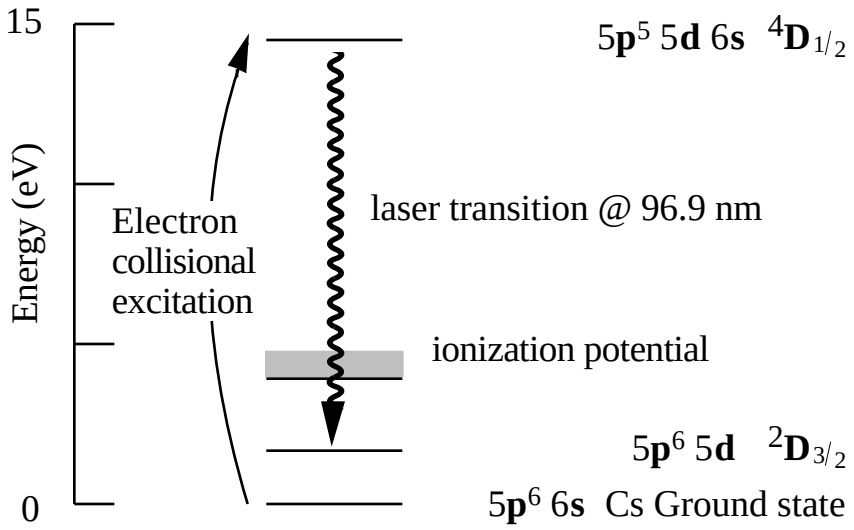

Figure 1.7: Energy level diagram of the neutral cesium XUV laser demonstrated by Barty et. al. [108]. Electrons created by x-ray photoionization excite the laser transition.

Another collisional excitation scheme of a different sort is the charge-exchange scheme [112,113]. In this scheme, collisions between two atoms populate the laser level. The basic idea is that, if one has two different species in a plasma, a collision can transfer an electron in one atom or ion to the other atom, leaving the atom in an excited state, in a process such as $\mathbf{A}^+ + \mathbf{B} \rightarrow \mathbf{A} + (\mathbf{B}^+)^* + \Delta\mathbf{E}$. These charge-transfer collisions have the highest cross section when the energy difference $\Delta\mathbf{E}$ between the initial and final excited ions is positive and not

large-- on order of 0.1-0.5 eV for visible-wavelength transitions [114]. This behavior is due to wavefunction overlap arguments similar to the case of photoionization, this time applied to the atomic translational wavefunctions. Thus, to make the scheme work, one must find two states of similar energy, one in one species which is normally heavily populated (the ground state or an ionic resonance line), and the other in a different species from which laser action can take place. Thus this scheme is quite similar to the resonant photoexcitation schemes in that a near-resonant transition is required.

1.3.4 Recombination-pumped x-ray lasers

Recombination lasers or population inversions on recombination-populated transitions have been demonstrated on soft x-ray transitions at a number of laboratories. The first unambiguous demonstration was by S. Suckewer et al [2,115] at the Princeton Plasma Physics Laboratory. The basic energy level diagram is shown in figure 1.8. The inversion occurs in a highly ionized plasma (the original PPPL scheme used H-like carbon) which is rapidly cooled and is therefore rapidly recombining. Collisional recombination rates are highest into the Rydberg levels of an ion, and these highly-excited atoms then radiatively cascade down to the ground state. A population inversion is thus naturally created in the same way that it is for the LLNL scheme, since the **n**=2 to **n**=1 transition has a much shorter lifetime than the **n**=3 to **n**=2 transition. The only other requirement is that the plasma be cooled on a time scale short compared with the recombination rates, so that the populations do not stay at their equilibrium values. To rapidly cool the ions, three approaches have been demonstrated. The PPPL group used a laser-produced plasma, confined by a magnetic field so that it could expand in only one dimension (a solenoidal field will do this). Since the expansion was restricted, radiative cooling was fast enough that the plasma could be cooled while still at a high enough density for recombination rates to be sufficient to produce substantial gains [116].

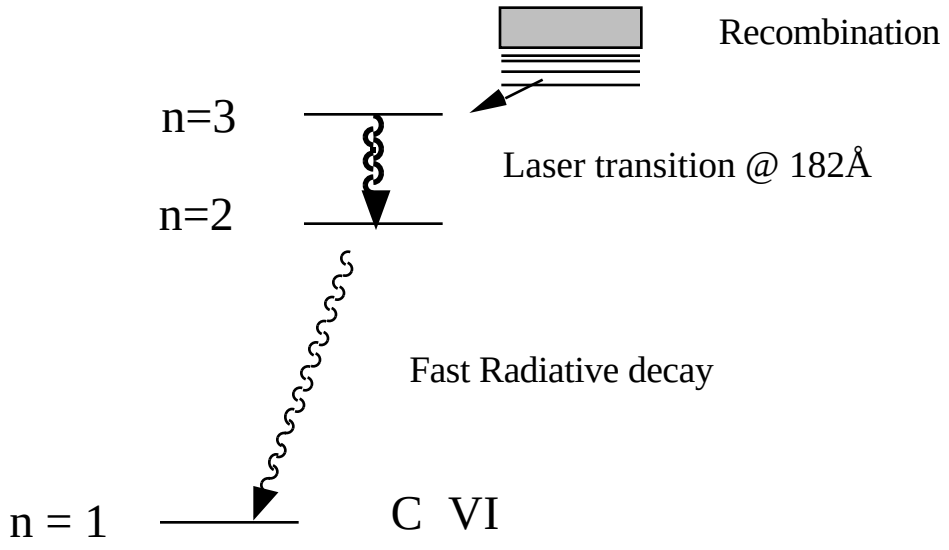

Figure 1.8: Recombination-pumped x-ray laser scheme in carbon, first demonstrated at PPPL [2]. The population inversion is due to rapid cooling and recombination of the ions, and due to the fast decay rate of the lower laser level.

The second approach is to use expansion as the cooling mechanism. In this scheme [117], a thin fiber is ionized, and then allowed to expand. The expansion cools the plasma, resulting in recombination. The fiber must be very small diameter (<10 μm) so that the density of atoms is still high enough to produce substantial gain, when the fiber has expanded sufficiently to cool.

The third approach is to used a cold surface against which the ionized plasma can be conduction cooled. One successful approach is to use a blade protruding into the plasma region [118] (which also provides additional radiation cooling through radiative cooling from high-Z impurities). Another approach is to use a thick fiber as the plasma target [115]. In this case, ionization of the fiber is incomplete and conduction cooling to the unheated core of the fiber is important.

The basic concept of the recombination laser dates back at least to Gudzenko and Shelepin in 1965 [119]. Numerous theoretical investigations have been published [68,116,120,121,122]; however, the first demonstration of a recombination laser was not until 1979, by Silfvast et al. [123]. He demonstrated gain on transitions in the infrared, and later in the visible [124,125], in singly, doubly, and triply ionized atoms. Previous papers have inferred the existence of a population inversion on recombination-populated transitions, but had not demonstrated gain [126,127].

Since the initial soft x-ray results in carbon, smaller gains have been demonstrated in shorter wavelength soft x-ray lines, in both H-like and in Li-like ions. There have been reports of marginal inversions on transitions with wavelengths as low as 4.2 nm [128]. Gain results for transitions in Li-like Aluminum (12.9 nm) and Silicon (15.4 nm) have been recently published [118].

Other related proposals for recombination lasers include the photoionization-recombination lasers mentioned previously [69,70]. Here, a population inversion can be sustained in a quasi-static situation by depopulating the ground state of the ion by photoionization; provided the plasma is kept cool, recombination will continue to take place, creating a population inversion in the usual manner. Thus, the electrons "circulate" in the atom, recombining, decaying to the ground state, and then getting photoionized to start the process again. The difficulty with this scheme is to keep the plasma cool; however this may be possible in some cases.

Lastly, a recent proposal suggests that a population inversion can be created on radiative recombination transitions [129]. The idea here is that if one ionic level is underpopulated with respect to thermodynamic equilibrium, a population inversion exists between the continuum and this level, and gain will result. The gain has a very broad bandwidth, giving the

advantage of tunability, and the disadvantage of low gain cross sections (comparable to the cross sections of the inverse process of photoionization).

1.3.5 Miscellaneous other x-ray laser proposals

Numerous other x-ray laser schemes have appeared in print. I will not attempt to review all of them; however, a brief (uncritical) mention is in order.

One popular scheme is x-ray lasing among the transverse eigenstates of a relativistic electron beam channeled in a crystal [130,131,132,133]. If a beam is incident nearly along an axis of a crystal, the electron is in a one-dimensional potential well in the transverse direction due to the crystal field, and the electron will have a discrete set of transverse energy eigenstates. Radiative transitions can occur between these levels, and the radiation is then Doppler shifted into the x-ray or gamma-ray region of the spectrum. Stimulated emission can also occur; however, the high beam currents necessary make this scheme difficult (both in terms of accelerator technology and for crystal survivability). Spontaneous channelling radiation has been observed [134]. Another related scheme, in that it uses Doppler shifts, is to have laser action in a relativistic atomic beam, with the output shifted into the x-ray region (and the pump laser shifted to longer wavelengths into the visible or IR) [135].

Another scheme proposes that a population inversion may be formed by velocity selection in the plume of an expanding laser-produced plasma [136].

Free electron lasers are also a potential x-ray laser source [137,138]. However, the scaling laws for free electron lasers, as in the case of atomic lasers, are quite severe, and great difficulty is expected in demonstrating an FEL at wavelengths below 100 nm. Harmonic generation [139,140] of soft x-rays in FEL's is also a possibility which may be more practical.

1.3.6 Conclusion

As one can see, there have been many proposed x-ray laser schemes, and a number of demonstrated methods for obtaining XUV and soft x-ray lasers. The field has expanded rapidly in the past few years, and probably will continue to do so. A lot of work remains to be done to develop a truly practical scientific tool, and to demonstrate its usefulness.

Chapter 2: Auger-Decay-Pumped Short-Wavelength Lasers

In this chapter I will discuss my work in demonstrating and understanding the Auger-decay-pumped short-wavelength lasers in xenon at 108.9 nm and in krypton at 90.7 nm [3,141]. The demonstration of these schemes was the culmination of a long process of experimental investigation and trail-and-error experimentation-- at least five different unsuccessful types of experiments were tried at the JANUS laser at the Lawrence Livermore National Laboratory before the gain experiment finally worked. Prior to these experiments, experiments done here at Berkeley gave some evidence of population inversion, and parameters necessary for the successful modeling and planning of the LLNL experiments were measured. After the successful demonstration, follow-up work was done to test the extent of our knowledge of the dynamics of the laser system. In addition, a substantial amount of instrumentation development was crucial to the success of these experiments.

The organization of this chapter is as follows: first I will give a short re-introduction to the laser scheme, and to the experimental work of others that led to the realization that a population inversion might exist on this transition. I will then discuss the successful gain demonstration experiment. Then I will discuss the planning of this experiment and the modeling done to determine its feasibility. I will also discuss the unsuccessful experiments-- deliberation over why they didn't work not only led to the design of the successful experiment, but also to a greater understanding of photoionization-pumped lasers in general, and to the development of a computer model which could successfully predict much of the experimental data. I shall then discuss these models.

Next I will discuss the experiments done at Berkeley. The major experiment done at UCB was the measurement of the lifetimes of the levels involved in the laser transition, using the technique of time-correlated photon counting. These experiments were set up, for the most part, before the successful gain demonstration experiment was performed, although

many of the final results were obtained later on in follow-up work. I will also discuss other experiments done at Berkeley, including fluorescence measurements, and also some very early data taken at Berkeley which suggested that the transition did invert, and which "kept me going," despite the fact that the initial LLNL experiments were unsuccessful. The success of this work depended on the scientific process, learning more with every experiment whether it worked or not, and continuing persistently despite setbacks.

2.1 Background

The basic energy level scheme has already been introduced in figure 1.5. X-rays from a laser-produced plasma inner-shell ionize 4**d**-shell electrons from xenon (or 3**d** for krypton), and these ionized atoms subsequently undergo Auger decay. The Auger decay branching ratios create a population inversion between the Xe^{++} $4\mathbf{d}^{10}5\mathbf{p}^{6}\ {}^{1}\mathbf{S}_{0}$ state and the $4\mathbf{d}^{10}5\mathbf{s}5\mathbf{p}^{5}\ {}^{1}\mathbf{P}_{1}$ state (the designations are only approximate since **L-S** coupling is not valid). For krypton the inversion is between the Kr^{++} $3\mathbf{d}^{10}4\mathbf{p}^{6}\ {}^{1}\mathbf{S}_{0}$ state and the $3\mathbf{d}^{10}4\mathbf{s}4\mathbf{p}^{5}\ {}^{1}\mathbf{P}_{1}$ state. The fact that there is a population inversion between the two levels can be determined through Auger-electron spectroscopy. In Auger electron spectroscopy, the electrons ejected by the Auger decay process are energy analyzed. Since the Auger decay process ejects an electron of definite energy, each peak in the spectrum corresponds to decay between two particular states. Provided the efficiency of the electron spectrometer is calibrated, the amplitudes of the peaks yield relative Auger rates into the states. Thus, provided the peaks are correctly identified, one can determine whether population inversions exist. Figure 2.1 shows the data of Aksela et al [51] for the xenon Auger spectrum.

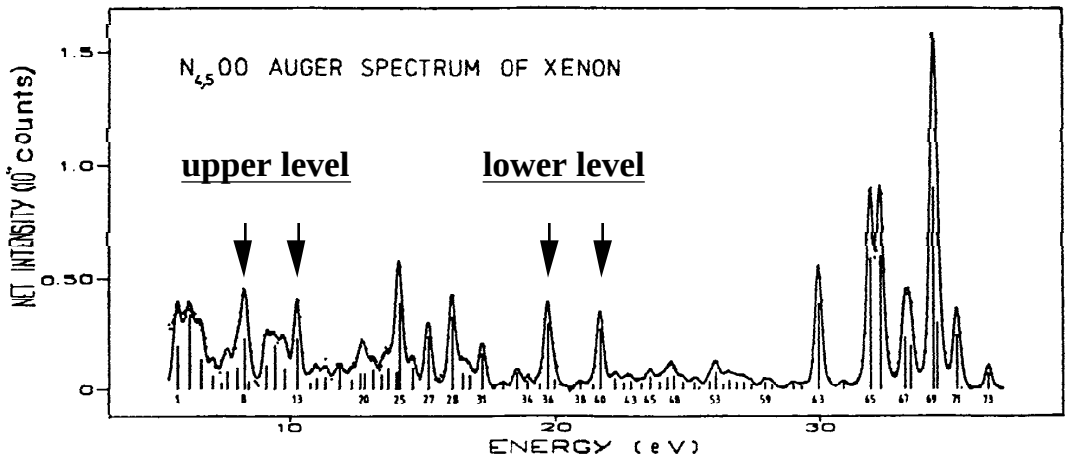

Figure 2.1: Auger electron spectrum of Xenon [51], showing the population inversion on the Xe^{++} $4\mathbf{d}^{10}\ 5\mathbf{p}^{6}\ {}^{1}\mathbf{S}_0 \rightarrow 4\mathbf{d}^{10}\ 5\mathbf{s}\ 5\mathbf{p}^{5}\ {}^{1}\mathbf{P}_1$ transition. Lines 8 and 13 correspond to decay to the upper level, and 36 and 40 to the lower level.

In figure 2.1, the peaks corresponding to decay to the upper and the lower levels are highlighted. The rates into each level are about the same, but the degeneracies of the states result in an inversion. There are two transitions to each level since the **d**-ionized state is ${}^{2}\mathbf{D}_{3/2}$ and ${}^{2}\mathbf{D}_{5/2}$. High-resolution Auger data for xenon has been available since 1972; however, the first published data had the upper laser level misidentified [52]. Thus, this inversion remained undiscovered. The reason for this misidentification was that the radiative transition at 108.8951 nm [142] was originally misidentified as a Xenon I line. This identification was corrected by Hertz in 1975 [53]. He observed that the emission intensity for this line as a function of incident electron energy had a threshold at the 4**d** ionization potential, thus identifying the line as an Auger product state. The correct optical identification of the line led to the correct Auger line identification in Southworth et al. [143]. The Auger electron spectrum of krypton shows a much smaller inversion on the 90.7117 nm [142] transition, with decay to the lower level roughly twice the magnitude as to the lower level [144]. With the correct identification, population inversion is apparent if one is

looking for inversions. In a way, it is surprising that several years passed before someone (RWF) recognized it. In fact, in the case of krypton, McGuire [145] correctly re-assigned the upper laser level in the Auger spectrum, in a paper published the same year as his original Auger laser proposal. Apparently he missed the inversion on this transition.

A recent comprehensive work on the spectrum of xenon III [146] shows the upper $5\mathbf{p}^6\ {}^1\mathbf{S}_0$ level to be a mixture of 56% $5\mathbf{p}^6\ {}^1\mathbf{S}_0$ + 39% $5\mathbf{s}5\mathbf{p}^4(^1\mathbf{D})5\mathbf{d}\ {}^1\mathbf{S}_0$, at an energy of 210857 cm^{-1}. The lower $5\mathbf{s}5\mathbf{p}^5\ {}^1\mathbf{P}_1$ level is identified as 44% $5\mathbf{s}^2 5\mathbf{p}^3(^2\mathbf{D})5\mathbf{d}\ {}^1\mathbf{P}$ + 28% $5\mathbf{s}5\mathbf{p}^5\ {}^1\mathbf{P}$ + 7% $5\mathbf{s}^2 5\mathbf{p}^3(^2\mathbf{P})5\mathbf{d}\ {}^1\mathbf{P}$ + 7% $5\mathbf{s}5\mathbf{p}^5\ {}^3\mathbf{P}$ + 6% $5\mathbf{s}^2 5\mathbf{p}^3(^4\mathbf{S})5\mathbf{d}\ {}^3\mathbf{D}$ at an energy of 119026 cm^{-1}. Thus, the lower laser level is identified as a $5\mathbf{s}^2 5\mathbf{p}^3 5\mathbf{d}$ level, illustrating the heavy interconfiguration mixing of states in this heavy atom. Indeed, the laser transition could equally as validly be called a $5\mathbf{s}5\mathbf{p}^4 5\mathbf{d} \rightarrow 5\mathbf{s}^2 5\mathbf{p}^3 5\mathbf{d}$ transition. Also, this work lists decay wavelengths (intensities) from the upper laser level at 353.182 (7), 194.2913 (12) , 168.4194 (2), 158.5770 (12), 142.5999 (10), 137.5295 (8), 117.3146 (9), 112.4428 (7), 108.8954 (20), and 101.6188 (2) nm. If the intensity figures are correct, the 108.9 nm line is only 22% of the total decay of the upper level. This is inconsistent with the data presented in this thesis as will be discussed, but these line intensities are only visual estimates.

2.2 The gain demonstration experiment

The measurement of gain on the xenon and krypton transitions was done using the JANUS (now called Phoenix) laser system at the Lawrence Livermore National Laboratory. This laser is capable of producing 1.06 μm laser pulses of duration 100 psec to 1 nsec, with energy as high at 150 Joules (at 1 shot/ 40 min). This facility was run by J. Swain and P. Solone of LLNL, and a laser beam was provided to us for doing experiments.

A diagram of the basic xenon laser configuration is shown in Fig. 2.2 . The idea behind demonstrating gain in this experiment is to form a long thin excited region, and look

down the length of the region with a detector. One can then vary the excited length, and if a transition is inverted, the intensity of the transition should increase faster than linearly with length. In the geometry of this experiment, a Nd:YAG laser pulse with an energy of ~55 Joules and a pulse width of 1 nsec was directed into a target cell containing 1 torr of xenon gas. The laser was focused to a 50 μm x 9 cm line focus onto a solid tantalum target. The power density on target is on the order of 10^{12} W/cm^2, sufficient to heat the target to a temperature of 10-30 eV. The target then emits broadband soft x-rays which radiate into a large solid angle. A 3 mm x 3 mm x 9 cm long channel faces the plasma and is 2 cm away from it and parallel to it. This channel defines the long and narrow region which is excited by the x-rays, and viewed by the detection system. The channel was also usually covered with a filter of 150 nm thick parylene.

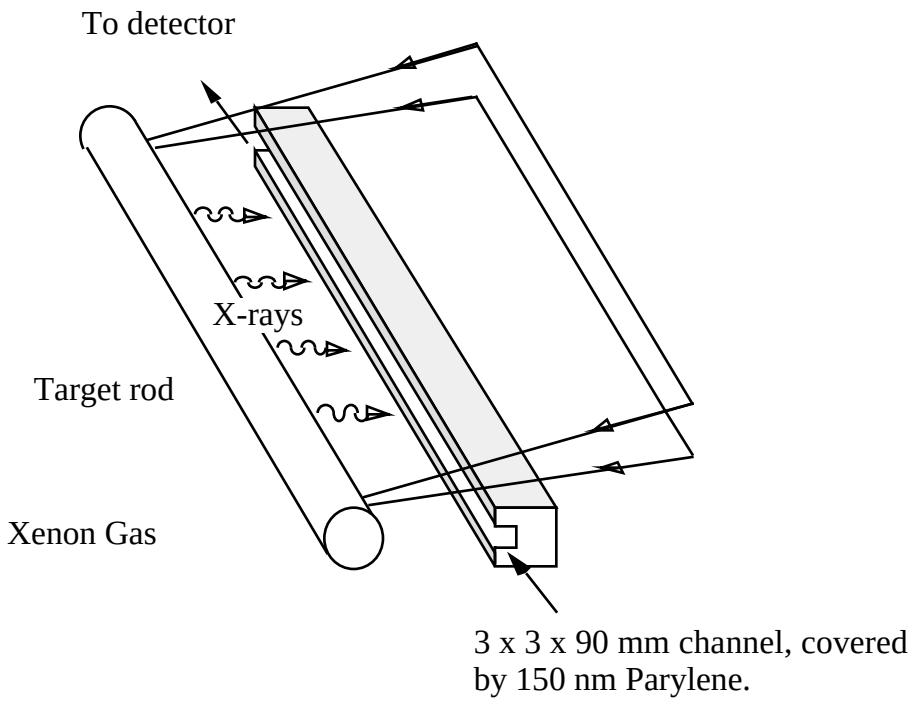

Figure 2.2: Basic xenon laser configuration.

The effect of the parylene (pure **CH** polymer) is to allow the x-rays to enter the channel but to prevent light at 108.9 nm from entering [147]; a graph of the transmission of the filter vs photon energy is shown in figure 2.3. The channel is thus isolated from the plasma except that the x-rays from the plasma uniformly excite it. The parylene filter was replaced after every shot since it was destroyed by the shock wave from the plasma. The 150 nm parylene was obtained (Nova Tran Corp, Clear Lake, WI) deposited on glass plates with a release agent between the parylene and the glass. The filter holder assemblies were glued to the plates with 5 minute epoxy, and then the plastic was steamed off while simultaneously gently prying the filter assemblies from the glass. Adequate time for the epoxy to dry (preferably overnight) was necessary to prevent excessive deposition of glue residue onto the filter, although the discoloration caused by this residue seemed to have a negligible effect on filter performance.

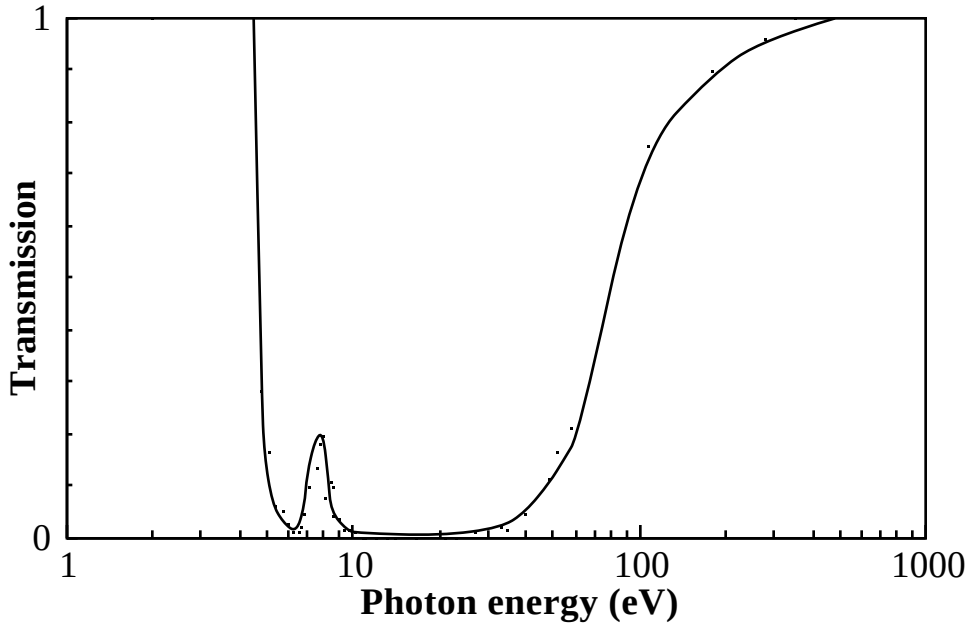

Figure 2.3: Transmission of 150 nm thick parylene filter as a function of photon energy. Transmission of the soft x-ray pump flux through the parylene is ~70%, while the transmission for 108.9 nm light is <2% [147].

The basic experimental configuration is shown in figure 2.4. The xenon-filled target chamber is connected to a 0.5 m Seya mount vacuum spectrometer, and is isolated from it by a 1 mm thick lithium fluoride window. Fluorescence from the ionized xenon is dispersed by the spectrometer and detected using an x-ray streak camera, which records the emission intensity as a function of time and wavelength for each laser shot. The slit of the streak camera is placed along the dispersion axis of the spectrometer. In our experiments data was taken with a wavelength resolution of 1.5 nm and a time resolution of 200 psec. The streak camera was modified for high sensitivity in the vacuum ultraviolet by replacing the normal photocathode with a microchannel plate with adjustable gain, as discussed in Appendix A. The streak camera was triggered by a photodiode placed at the beginning of the JANUS amplifier chain, using the appropriate length of delay cable to time the trigger properly. The output of the streak camera was recorded on calibrated film and digitized by the staff at LLNL using an optical scanner, giving us a record of intensity vs. time of the emission line. The calibration on the film consisted of a "wedge" on the side of each film, which was exposed to a known light flux, continuously varied along one axis. The optical density of the experimental data was then compared with this wedge.

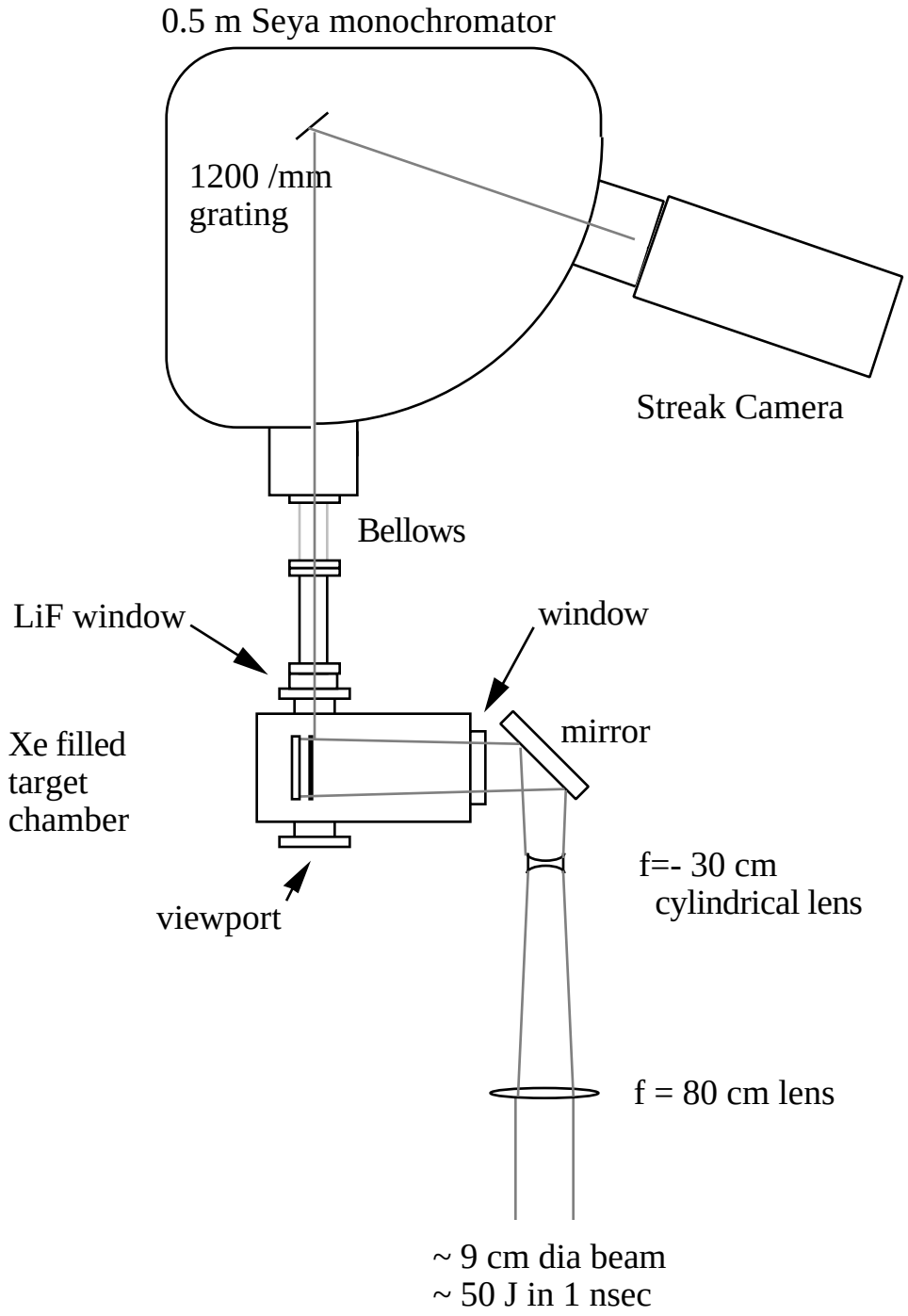

Figure 2.4: Basic experimental setup for the xenon gain demonstration experiment.

The experiment is performed by observing the fluorescence intensity of the xenon transition as a function of illuminated length of the channel. This length is varied by

shadowing portions of the channel from the x-ray source, using sheet metal cutouts placed between the x-ray source and the channel. This technique maintains constant plasma light source characteristics and constant electron and ion densities along the length of the channel, except at the very ends. Apertures limit the collection solid angle of the detector so that the field of view is confined to inside the channel. The detection efficiency is approximately constant along the length of the channel, since the channel-slit distance is considerably longer than the channel length. This was verified by the observation of approximately equal signal intensity when only either half -length of the channel was illuminated. Most data were taken with the illuminated lengths centered along the slot to minimize end effects.

Experimental results for the xenon case are shown in figure 2.5. As is apparent, when the illuminated length is increased, the output intensity increases exponentially. This experiment was done using 84% isotopically enriched ^{136}Xe at a pressure of 1 torr. This expensive ($8000 /liter STP) isotope was used since the hyperfine separation for the 108.9 nm line is comparable to the Doppler width of the line, and thus a mix including odd isotopes would yield a smeared-out line and lower gain (isotope splitting is not expected to be significant for this transition [148]). Even-even isotopes have **I**=0, and thus no hyperfine splitting. The spectrometer was set to 1 mm slits, yielding a spectral resolution of 1.5 nm. The useful length of the streak camera slit was ~20 mm (the rest of the ~25 mm long slit was shadowed by parts of the spectrometer), yielding a spectral range of ~30 nm. The accuracy of the absolute wavelength determination from the data was about ±3 nm; in the experiments, the only spectral line visible in the entire region was the 108.9 nm line. This in itself is significant evidence of stimulated emission, since in our UCB experiments at low excitation levels, the 108.9 nm line was not at all dominant.

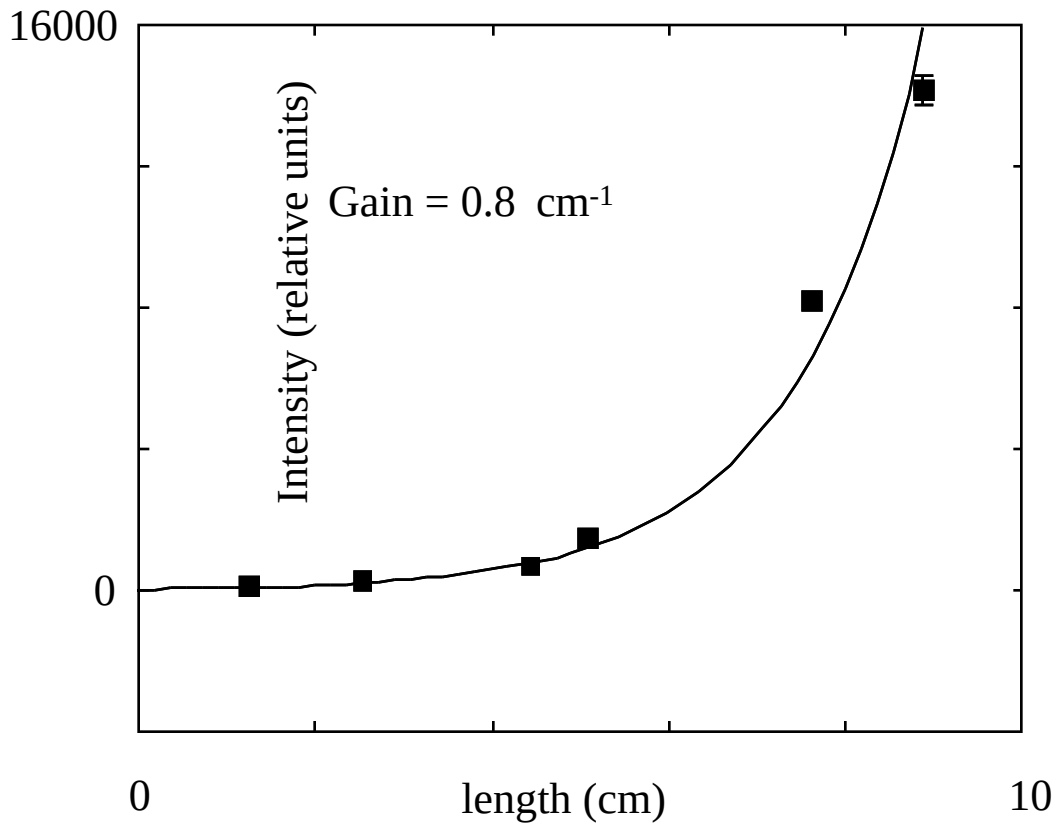

Figure 2.5: Intensity as a function of illuminated length for the xenon gain experiment [3]. Experimental parameters are : incident energy 55 Joules± 10% (net, after reflection losses) in 1 nsec, at a pressure of 1 torr ^{136} Xe, and a target-channel distance of 2 cm.

A sample data set is shown in figure 2.6. This includes the raw streak camera data, and the calibrated lineout of the xenon line. The sweep speed of the streak camera is approximately 80 psec / mm; thus, the pulse width in this case is ~600 psec. The experimental data in Figure 2.4 was fit to an exponential gain function to determine the gain per centimeter at line center. This gain function is not simply an exponential, but is generated as follows. First, the spontaneous emission source which is being amplified is not at the far end of the amplification medium, but is distributed along the length of the excited region. Assuming uniform excitation, this corresponds to:

$$I_{out} = \int_{x=0}^{L} i_o \, dx \, e^{\gamma x} = \frac{i_o}{\gamma}\left[e^{\gamma L} - 1\right] , \qquad (2.1)$$

where γ is the gain per cm, **L** is the total length of the excited region, and $\mathbf{i}_o$ corresponds to the brightness of the spontaneous emission (an adjustable parameter for fitting purposes). This expression is not yet complete, however. One must also take into account the linewidth of the transition. Assuming gaussian line broadening (valid for the xenon case), equation 1.28 is applicable:

$$i = i_o \, d\nu \, \frac{2\sqrt{\ln 2}}{\sqrt{\pi}\,\Delta\nu_d} e^{-(4 \ln 2 \, (\nu - \nu_o)^2 / \Delta\nu_d^2)}$$

$$\gamma' = \gamma_o e^{-(4 \ln 2 \, (\nu - \nu_o)^2 / \Delta\nu_d^2)} , \qquad (2.2)$$

where γ_o is the gain at line-center. These functions must be plugged into equation 2.1, and integrated over the linewidth. The integral must be done numerically, and is independent of the actual Doppler width:

$$I_{out} = \int_{\nu=-\infty}^{\infty} \frac{i}{\gamma'}\left[e^{\gamma L} - 1\right]$$

$$\int_{\Delta\nu=-\infty}^{\infty} \left[e^{\left(\gamma_o L e^{-4 \ln 2 \, (\Delta\nu/\Delta\nu_d)^2}\right)} - 1\right] . \qquad (2.3)$$

This numerically generated function was then fit to the data, varying γ_o and the constant multiplier. It was found that integrating from $\Delta\nu/\Delta\nu_d$ = -3 to 3 in steps of 0.1 was sufficient to give an accuracy in the function of < 1%. One can also use an analytical approximation to equation 2.3, to fit to reasonably large (γ**L** > 3) gain-lengths [149,150].

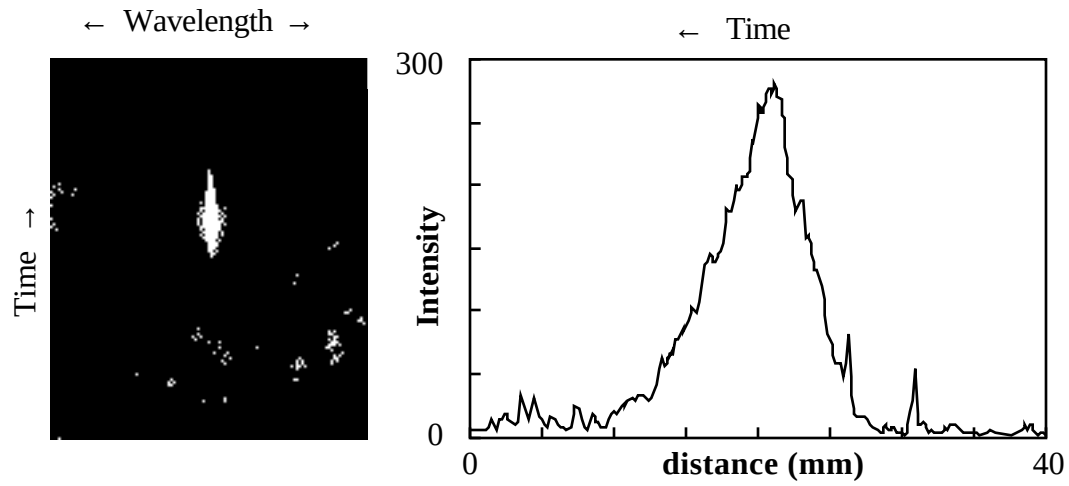

Figure 2.6: Sample xenon laser data "shot"; shown is a reproduction of the photographic data, and the quantitative lineout corresponding to the 108.9 nm intensity. The distance to time conversion is ~80 psec / mm, yielding a pulse FWHM of ~600 psec.

Data was also taken using the naturally occurring xenon isotopic mixture, with and without the parylene filter separating the lasing region from the plasma region. The isotopic mixture of xenon is ^{151}: 124, 0.1%; 128, 1.9%; 129, 26.4%; 130, 4.1%; 131, 21.2%; 132, 26.9%; 134, 10.4%; 136, 8.9%. In both cases, the peak intensity achievable was much less with the natural isotopic mix. Figure 2.7 shows the gain curve for the case of no parylene and the normal isotopic mixture. The gain coefficient is about $^1/_2$ the case of figure 2.5, and the peak intensity is about $^1/_{50}$ of this case. In the case of normal xenon but with the parylene filter, the peak intensity observed was 450, about 50% greater than without the filter. In the case of ^{136}Xe without the parylene filter, the maximum intensity observed was 475. Thus, the effect of using the isotope and of using the parylene filter is moderate,except in the case where both are used together. In this case, the output intensity is dramatically higher.

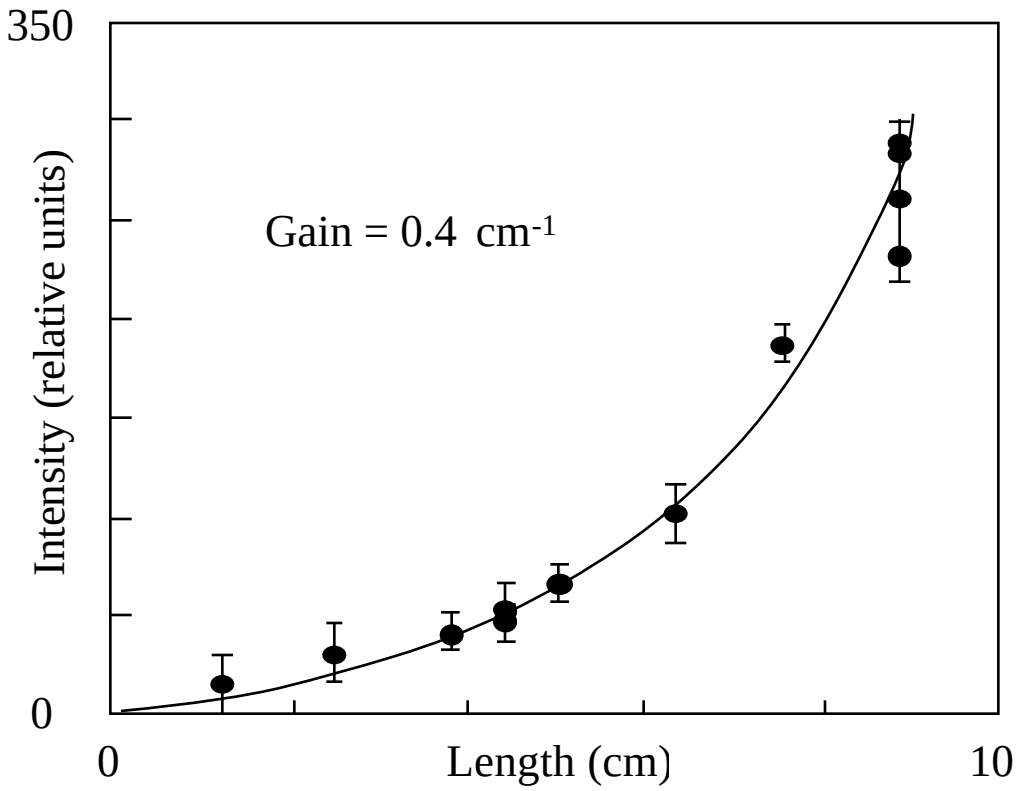

Figure 2.7: Gain curve for xenon, using 1 torr natural xenon, and no parylene filter isolating the gain region [3].

The effect of the isotopically enriched gas is quite straightforward: the only possible effect it can have is to result in a narrower linewidth than in the case of natural xenon, increasing the gain coefficient, and thus increasing the output intensity. The effect of the parylene filter is less apparent, though. The filter affects the excited region in two ways. First, it reduces the x-ray flux to the excited region. This would reduce the output intensity, except that the filter has the beneficial effect of filtering out mostly the low energy x-rays which are not capable of ionizing 4**d** electrons. These x-rays will only ionize the outer-shell 5**s** and 5**p** electrons, increasing the density of free electrons. Since a high electron density might Stark broaden the transition, or directly quench the upper level, one could plausibly argue that enhanced emission might result from the parylene due to this filtering effect. However, this effect would be the same for either the isotopic or the natural xenon; what is

observed is that the parylene has a dramatic effect in the case of the isotopic xenon, but a small effect in the case of the natural xenon. Although gain coefficients were not measured for every case due to beam-time constraints at JANUS, one can estimate them using equation 2.3, the measured gain and output intensity of the data from figure 2.7, and assuming a 0.7 attenuation in the total excitation (corresponding to $\mathbf{i}_o$ in equation 2.1) when the parylene decreases the x-ray flux. Estimated gain for the case of natural xenon with parylene is 0.51 cm^{-1}, an enhancement of ~27% over the case without the parylene. For the case of isotopic xenon with no parylene, the estimated gain is 0.47 cm^{-1} -- this corresponds to an enhancement of ~70% in the gain when parylene is present. Thus, the gain enhancement depends of the isotope used, which is not consistent with the Stark broadening or electron quenching arguments.

The second effect of the parylene is to isolate the excited region from 108.9 nm light originating closer to the plasma. This light can induce stimulated emission of laser radiation in directions other than along the axis where it is observed by the detector, resulting in a depletion of the gain as population is quenched due to this amplified spontaneous emission. This ASE quenching would be expected to depend on the gain per unit length, as observed in the experiments. Thus, ASE will act to "clamp" the gain at a value depending upon the geometry of the experiment. This explanation of the data is consistent with the fact that some previous gain-measurement experiments did not succeed, as will be discussed later.

The time structure of the emission from xenon shows interesting behavior as a function of increasing output intensity. Using the 1 nsec pump laser pulse and at low output intensity, the emission pulse width varies from 600 to 1200 psec. As the intensity increases (with increasing pumped length) a double peak structure appears, as shown in figure 2.8. The second peak is delayed by about 800 psec and has an intensity 1/2 to 1/3 of the first peak. As the pumped length is increased further, the two peaks reduce in separation until at the highest intensities a single peak of about 450 psec FWHM is observed. This effect may

be due to superradiance ringing in the xenon system, as will be discussed later [152]. It may also be due to gain-dynamics of the system-- M. Sher at Stanford has observed using a streak camera that the shape of the output beam varies as a function of time in their xenon laser experiment [153]. The beam starts out round, and becomes annular at later times, presumably because of gain depletion and termination of the inversion in the region near the plasma with high initial gain. One could conceive that a double-pulse structure might be the result of such a "moving" beam, or some similar spatial effect.

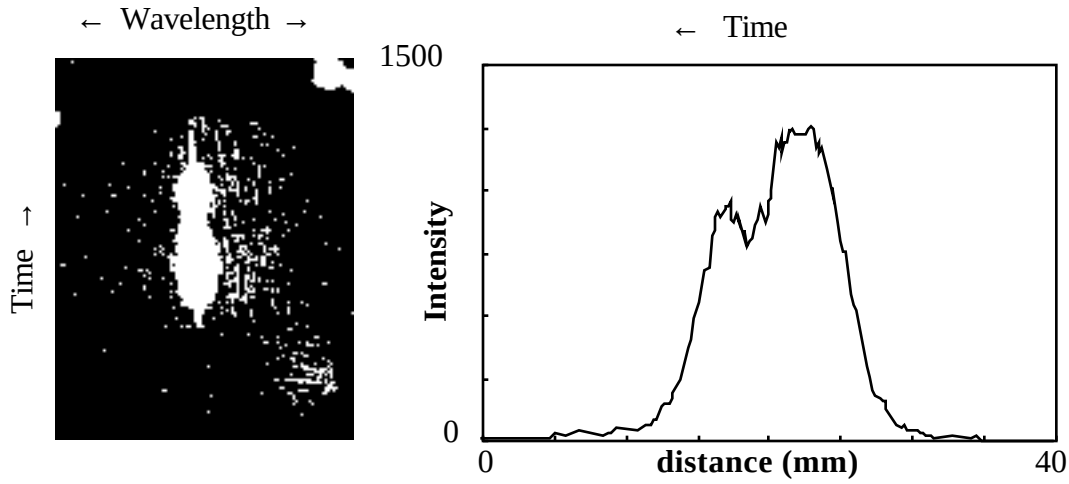

Figure 2.8: Streak camera trace of the double-pulse structure often observed.

For the case of gain on the analogous krypton transition, the experimental arrangement of figure 2.4 was slightly modified. At a wavelength of 90.7 nm, lithium fluoride is opaque [154]; thus, instead a capillary array window was used in a differential pumping geometry [155]. A capillary array window is a window consisting of a large number of long, thin tubes (50μ diameter, 2 mm thick, mfr. Galileo Electro-optics) fused together to create a window with high impedance to gas flow, but with 50% clear aperture to radiation directed along the axis of the tubes. The capillary array separates the gas filled target cell from an intermediate chamber connected to the slit and pumped on by a sorption pump. The spectrometer slit assembly was sealed to gas flow through all but the

500 μm x 5 mm slit by an O-ring, and the spectrometer was pumped by a turbomolecular pump. With this arrangement, pressure of several torr can be maintained in the target cell, with a pressure of ~10^{-2} torr in the intermediate chamber, while maintaining a pressure in the vacuum spectrometer and at the streak camera of less than 5 x 10^{-5} torr. The capillary array was placed within 5 mm of the excited gas region so that photons with energy above the gas ionization potential could also be detected without too much absorption in passing through a long length of absorbing gas. Although this arrangement is not necessary for the krypton transition @ 13.67 eV (the ionization potential of krypton is 14.0 eV), we did not want to miss any other possible laser transitions (none were found). The capillary array window has only a small acceptance angle for light to pass through, since the tubes are very long and thin. However, the length/diameter ratio of ~40 was sufficiently large that careful machining was sufficient to obtain alignment of the array without any further adjustment. Gas was fed into the target chamber on a continual basis using a needle valve adjusted for the proper flow rate. The natural isotopic concentration of krypton was used for these experiments since it consists of 88% even-even isotopes with no hyperfine splitting [156]. This experimental arrangement otherwise was similar to figure 2.4, except that the channel-to-plasma distance was decreased to ~1 cm to provide increased excitation. The only complications in doing the experiment were (1) adjusting the needle valve to maintain the correct pressure, and (2) dust created by vaporizing the tantalum target tended to clog the capillary array, and thus gas was forced backward through the capillary array between each shot while venting the chamber.

The experimental data for the case of the krypton is shown in figure 2.9. In anticipation that the excited state lifetimes would be shorter for these shorter wavelength transitions, 500 psec excitation pulses, instead of 1 nsec, were used. From the data that was taken, two sets with pump laser energy equivalent to within 10% were located. Although few data points were taken, the measured gains are substantial. Also, the fact

that the 90.7 nm line was by far the brightest line visible (the only other lines in the krypton spectrum were two at 55-60 nm, much dimmer than the 90.7 nm line), and that the time duration of the output was ~300 psec (much shorter than the measured lifetime of 2.0 nsec) are also indications of stimulated emission. Also, the output is comparably bright to the xenon laser output at its brightest.

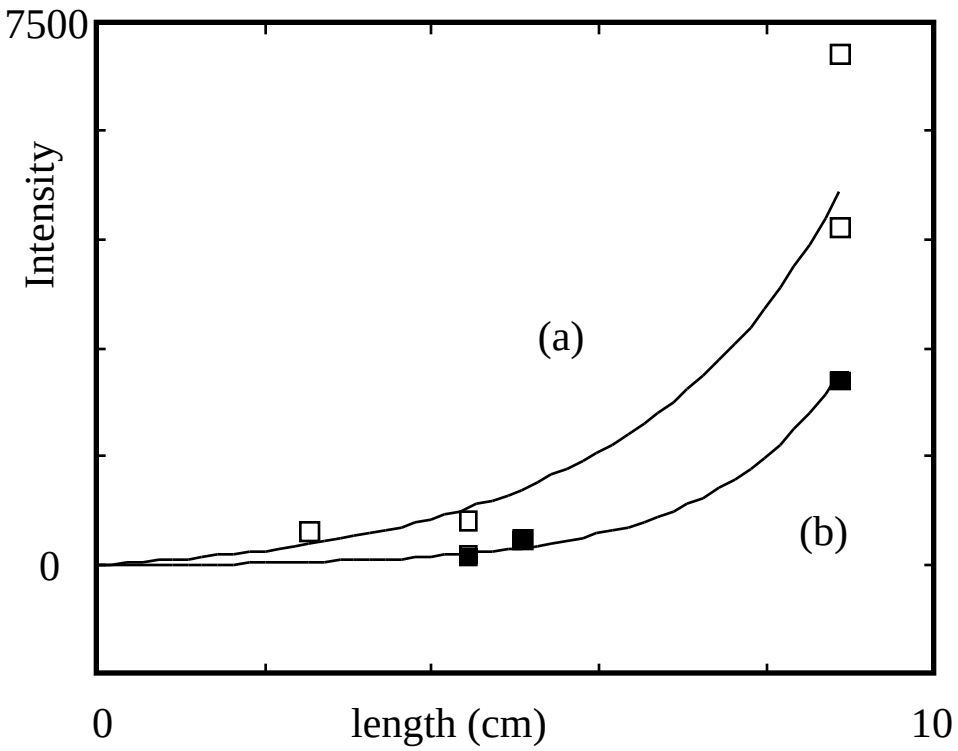

Figure 2.9: Intensity as a function of length for krypton emission at 90.7 nm [141]. Curve (a) indicates a fit to data taken with a pump energy of 50 J yielding a gain coefficient of 0.5 cm^{-1}. Curve (b) indicates a fit to data taken at a pump energy of 38 J yielding a gain of 0.7 cm^{-1}.

Another set of experiments done at LLNL was to use a mirror at one end of the excited length, to try to observe multipass gain and enhanced output. For this set of experiments, a different target configuration was used, as illustrated in figure 2.10. The same chamber and capillary array window were used. However, in order to observe gain with less pump laser

energy (at ~4 Joules/ shot, the repetition rate of JANUS is ~5 min/ shot vs ~40 min/shot @ 70J), the region observed was from adjacent to the target to ~3 mm away from it. The target was placed at the end of a long thin slot to limit the gain transverse to the viewing axis in vertical direction; in the horizontal transverse dimension, geometrical divergence and absorption of the x-rays limits the gain. A 1 mm thick lithium fluoride window, with a surface reflection of ~10% [154] at 108.9 nm, was used as a back reflector. The ~4J used to pump the laser is sufficient to produce an x-ray emitting plasma and bright output at 108.9 nm even though the power density on target is only about 5×10^{10} W/cm^2 (below an energy of ~3 Joules, the signal dropped dramatically). The xenon pressure was optimized for maximum output intensity-- data was taken at 5 torr pressure. The gain curve for the case of non-isotopic xenon with and without the LiF mirror is shown in figure 2.11. The mirror enhances the output intensity by a factor of 4, much greater than the 10% mirror reflection. Multi-pass amplification is thus possible. However, the 9 cm length of the excited region corresponds to 300 psec propagation time, and the duration of the output pulse is ~600 psec, so that in the present configuration a resonator with two mirrors would not function very effectively. Thus a resonator configuration was not attempted.

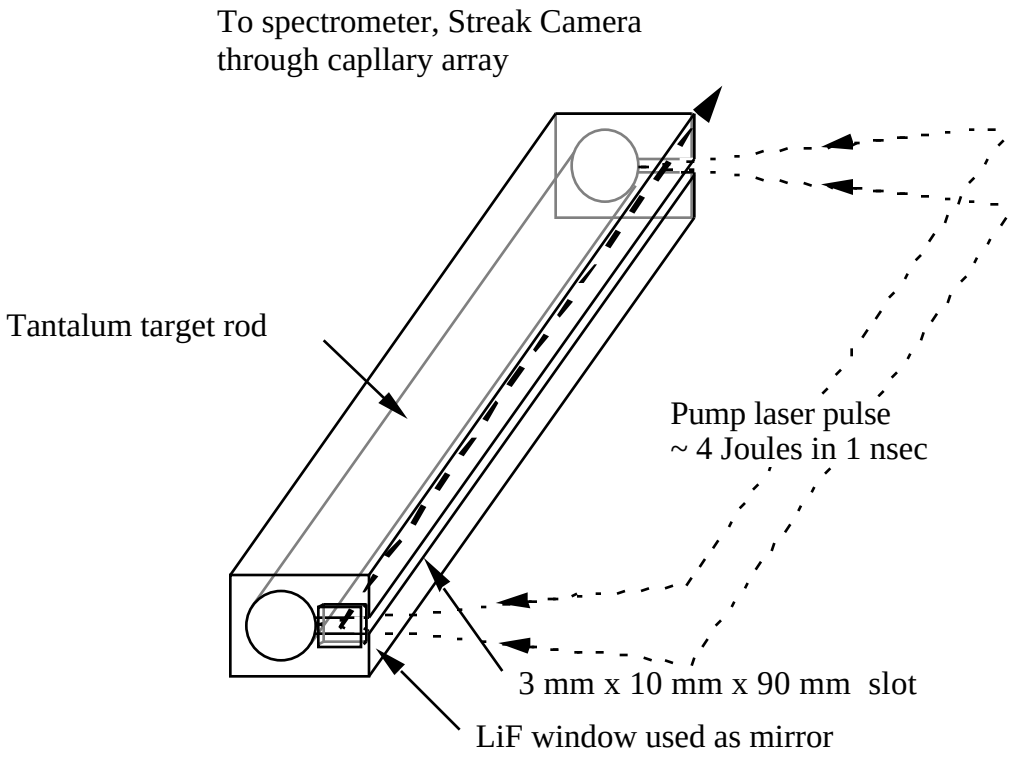

Figure 2.10: Setup used at LLNL to demonstrate multi-pass gain on the xenon laser. Amplification occurs in the region near the plasma target, and a LiF window with ~10% surface reflection at 108.9 nm is used as an end mirror.

The measured gain coefficient both with and without the LiF mirror was about 1.1 cm^{-1}. The factor of four enhancement is also less than one might expect given a single pass gain of $\sim \mathbf{e}^{10} > 10^4$. This is a reflection of the fact that the laser system is saturated, and that amplified spontaneous emission is limiting the observable gain.

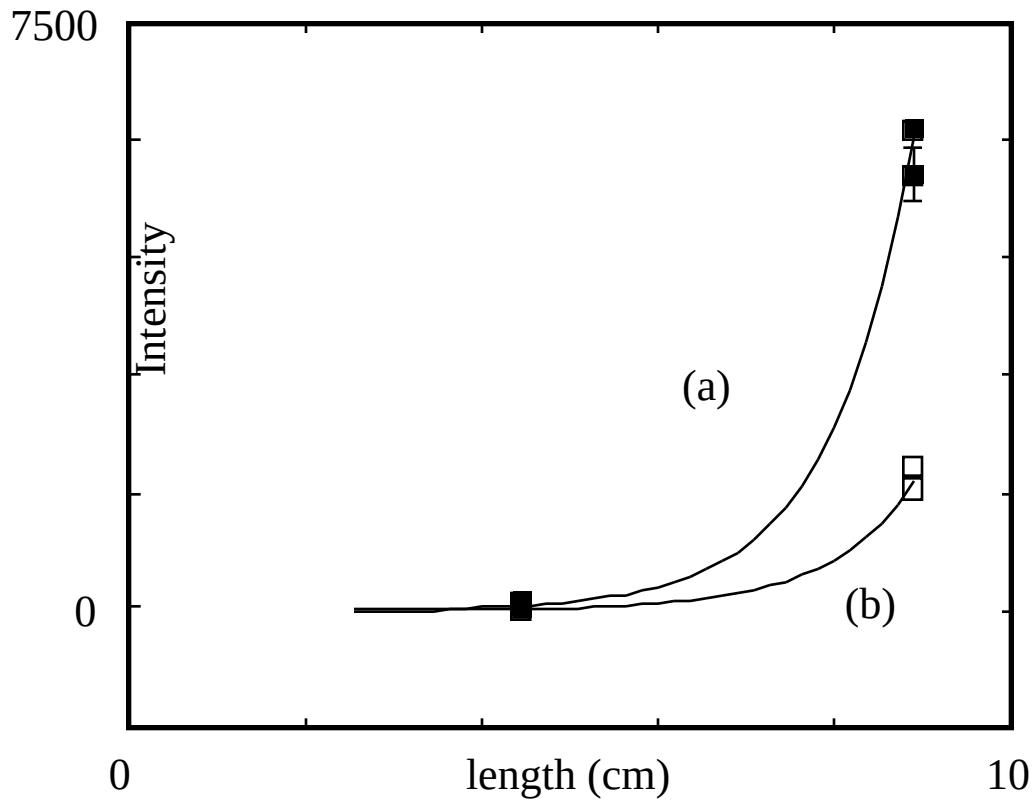

Figure 2.11: Intensity as a function of length for xenon 108.9 nm emission [141]. Curve (a) indicates a fit to data taken with a lithium fluoride reflector yielding a gain coefficient of 1.12 cm^{-1}. Curve (b) indicates a fit to data taken without the reflector and yields a gain of 1.09 cm^{-1}.

The last set of experiments done at JANUS was to survey the rare gases xenon, krypton, and argon in the spectral range of 50-120 nm to search for any other laser lines. Both the configuration of figure 2.2 and of 2.9 was used, with varying pressures and pump pulse energy and time duration. This survey was not exhaustively systematic due to the limited beam time. For the most part the data were taken using the configuration of figure 2.9, and 100 psec pump pulses. Data was taken using Polaroid film and was only qualitatively examined. No other laser lines were apparent. In fact, the only other lines consistently observed were a pair of lines each, at 65.5 and 69.5 ± 2 nm for xenon, and at 54 and 57 nm in krypton. They were dim but visible on shots covering the appropriate wavelengths, and

apparently had very short lifetimes (≤ 100 psec excitation pulse length). However, they were not nearly as bright as the laser lines, and did not exhibit any non-linear growth, as far as I could tell. They are most likely transitions from the mixed $5\mathbf{s}5\mathbf{p}^5\ {}^1\mathbf{P}_1$ levels identified as (25 and 28) and (27 and 31) of figure 2.1 down to the ground state configuration, probably the ${}^3\mathbf{P}_{0,1,2}$ levels which are very closely spaced and not resolvable with the streak-camera spectrograph. The line pair in krypton is assumed to be the analogous transitions.

2.3 Supporting work to the LLNL experiments

2.3.1 Simple gain calculation code

Prior to the successful demonstration of the xenon laser, a computer code (GAIN4) was developed help design the experiment and predict approximately how much gain one might be able to measure in a particular experimental configuration. This code went through an evolutionary process along with the design of the experiment itself; I shall discuss the final version of the code used to design the successful experiment discussed in the previous section. This discussion will be a conceptual discussion of the code; details are given in Appendix B.

The code uses published experimental data, including ionization cross sections, branching ratios, and basic experimental properties of laser-produced plasmas to predict excited state densities in the xenon gas illuminated by the laser-plasma produced x-ray source. The laser-produced plasma is not modeled in itself, but is assumed to be a uniformly emitting source of blackbody x-ray emission. The absorption of the parylene filter is then taken into account, and the resulting flux is used to calculate ionization of the xenon $4\mathbf{d}$ and outer-shell electrons. The Auger branching ratios are then used to predict populations in the upper and the lower laser levels, and the gain coefficient. The code is time independent, and calculates only cumulative populations (the populations one would get

immediately after a δ-function x-ray excitation pulse was used). A more detailed description of the modeling follows.

The x-ray source was assumed to be a blackbody radiator with a temperature of 30 eV [26]. Physically, the laser pulse is heating the material of the plasma, and provided the plasma is optically dense, it will radiate as a blackbody. The blackbody assumption is not completely accurate, but it has been found experimentally that plasmas consisting of high-Z elements (tantalum is Z=73) do have approximately blackbody radiation distributions since they have a very dense, quasi-continuous, line spectrum. The blackbody relation is a radiation flux per unit area, so that one must know the surface area of the plasma emitting the radiation. One could assume that the area is the area of the laser spot; however, this is not necessarily accurate since a plasma formed by a >100 psec pulse is actually formed in a low density region away from the target. Substantial heat conduction can occur, so that instead of a flat radiating blackbody source, one can have a roughly hemispherical radiating region (hemicylindrical for a line focus plasma). In practice, a better way of estimating the radiation is to assume a blackbody frequency spectrum, and to set the total intensity to correspond to a specific conversion efficiency of laser energy in to x-ray energy out. This circumvents the area question, and total conversion efficiency is a consistent number that varies only slowly with the actual spot size in the intensity range in question. A total efficiency of 7% is assumed in the calculations done. This is an estimate based on published data [157] for plasmas produced by 1.06 μm light, and is probably accurate to within a factor of 2.

A flat blackbody emitter has a Lambertian distribution $\mathbf{I} = \mathbf{I}_o \cos(\theta)$, where θ is the angle between the radiation direction and the normal of the surface [158]. However, the source is not necessarily flat. In the case of a spherical radiator, the distribution will of course be uniform, and thus the actual radiator will have a distribution function somewhere in between. A

uniform distribution was used in the simulation since it is the most conservative assumption given that the slot is directly opposite the line focus radiator.

The source in the model is assumed to be a line broken into 200 uniformly distributed segments for numerical integration purposes. The x-rays are attenuated by the parylene filter function (figure 2.3), and by absorption in the xenon. The cross sections of the xenon 4**d**, and the 5**s**,**p** levels are used by the model. These are taken from Berkowitz [159]; he deduces partial photoionization cross sections for the subshells from various experimental data. The data is shown in figure 2.12. The ionization is calculated first for a point plasma, with resulting excited state densities as a function of distance from the x-ray source. This function is then integrated over the length of the plasma, and over the length of the channel, resulting in excited state densities, electron densities, and gain along the length of the channel. The gain-length is calculated for along the length of the channel, and transverse to it at the center of the channel. The gain along the length of the channel is shown in figure 2.13, as a function of plasma-channel separation. The gain is calculated from the excited state density of 4**d** ionized atoms, assuming a gain cross section of 3.2×10^{-13} cm^2, and branching ratios of the Auger decay to the upper and lower levels of 0.0435 and 0.0514; the relation is $\textbf{Gain}\ (cm^{-1}) = \mathbf{N}_{4d}\,\sigma_g\left(0.0435 - \frac{1}{3}\,0.0514\right)$. The gain cross section of 3.22×10^{-13} cm^2 was obtained from equations 1.22 and 1.30 using the measured 4.75 nsec lifetime of the upper laser level (as will be discussed later), assuming that the 108.9 nm decay is the only strong decay from this level, and that the transition is Doppler broadened. Lifetime broadening of this transition is an order of magnitude smaller than the Doppler broadening. Hyperfine splitting was not taken into account; therefore the results are valid only for the case of the isotopically enriched xenon. The Auger branching ratios were estimated from the Aksela data of figure 2.1 to be 0.045 and 0.055 for the upper and lower levels, and were then adjusted for the fact that Auger decay to triply ionized atoms also occurs with a branching ratio of ~21%.

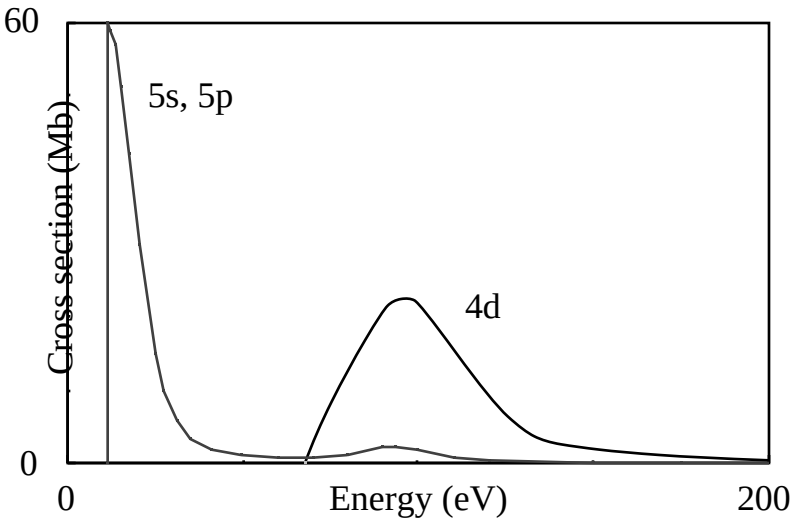

Figure 2.12: The photoionization cross sections for the xenon 4**d** and 5**s**,**p** electrons as a function of x-ray photon energy. Data from Berkowitz [159].

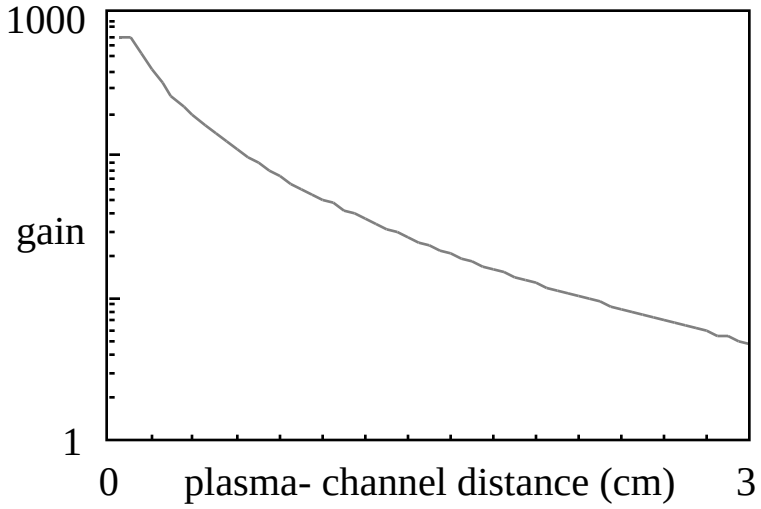

Figure 2.13: Total gain along the length of a 9 cm long channel, illuminated by the x-rays from an 8 cm long , 55 Joule plasma using a total conversion efficiency to x-rays of 7%. The xenon pressure is 1 torr. The gain is a function of channel-plasma separation.

The electron density was also calculated in the simulation. Electron quenching of the level might be expected to become important at electron densities of $>10^{16}$ /cm^3, given

typical electron collisional cross sections of ~10^{-16} cm^2 [160]. One problem of calculating the electron density is the fact that secondary electrons are being created through ionization. This was taken into account by calculating a maximum secondary electron density , simply estimated by the ejected electron energy divided by the ionization potential of xenon. Given the typical ionization cross section of ~10^{-16} cm^2, collisional ionization will occur at a rate of (~100 psec- 1 nsec)$^{-1}$. Thus the process of secondary ionization will be significant. The electron density will be between the values given by the primary and the total of the primary and the secondary electron densities.

At the channel-plasma distance of 2 cm, the total gain along the length of the channel is estimated to be $\mathbf{e}^{13}$, which would be easily measurable in the experiment. The maximum gain across the 3 mm transverse width of the channel is calculated to be $\mathbf{e}^{0.5}$ = 1.7 giving an aspect ratio of longitudinal/ transverse gain of 25; thus, output along the length of the channel should be dominant in this experiment. The primary and total (primary+secondary) electron densities at the center of the channel are calculated to be 4 x 10^{14} /cm^3 and 1.2 x 10^{15} /cm^3-- low enough that electron quenching would not be expected to be important. The excited state density along the channel as a function of position along the 9 cm channel is shown in figure 2.14. The excited state density is reasonably constant along the slot, and thus varying the excited length by shadowing the plasma should give a linear increase in gain-length with illuminated length, for all but the longest excited lengths. Thus the simulation predicts that the gain measurement experiment should work (as it did).

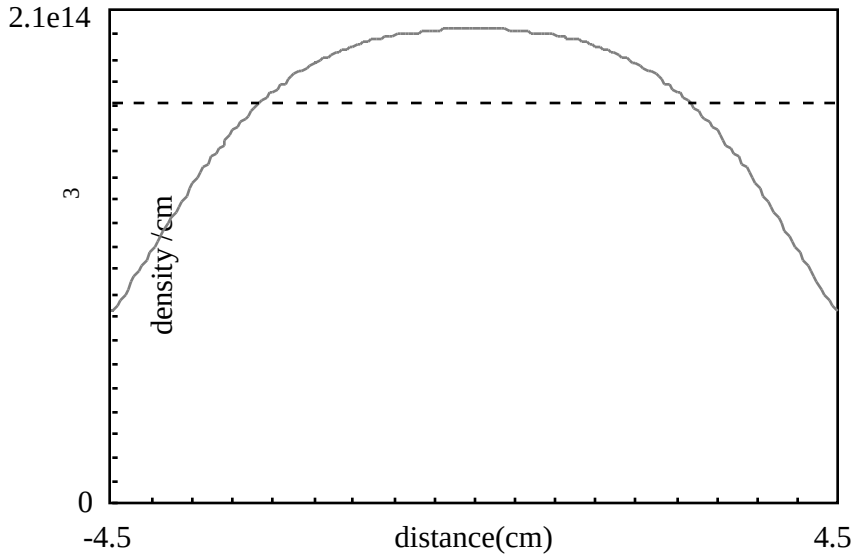

Figure 2.14: Excited state density along the 9 cm slot, for a plasma-channel separation of 2 cm and a xenon pressure of 1 torr. The density is constant to within ±20% of the average value of 1.7 x 10^{14} /cm^3 (shown) for 80% of the total length.

The effect of the filter on the electron and excited state densities can be calculated by removing the filter from the calculation. In this case, the longitudinal gain increases by 50% from $\mathbf{e}^{13}$ to $\mathbf{e}^{20}$, while the electron density increases from 4 x 10^{14} cm^{-3} to 8 x 10^{14} cm^{-3} (primary) and from 1.2 x 10^{15} cm^{-3} to 2.1 x 10^{15} cm^{-3} (total). Thus, the filter reduces the electron density by a greater factor than it reduces the gain.

2.3.2 Other attempted experiments : a discussion of ASE effects

Prior to the successful experiment, a number of different experimental geometries were attempted. In all cases, the computer models predicted that substantial gain should be measurable, nevertheless the experiments failed. Figure 2.15 illustrates some of the experiments attempted.

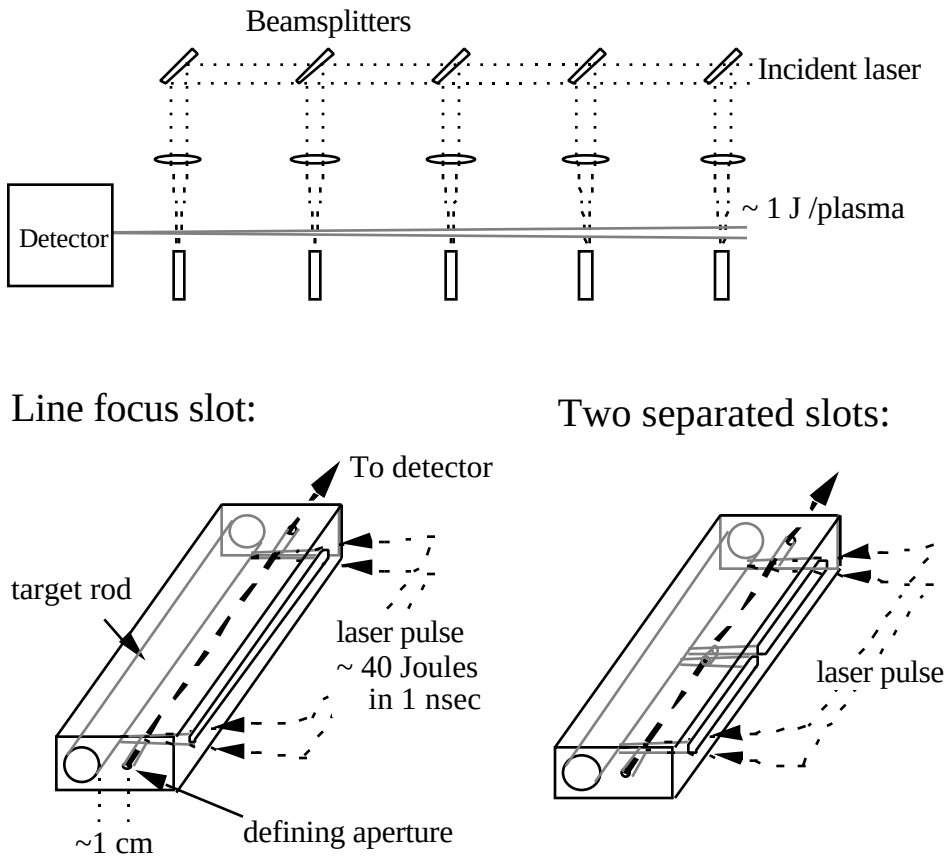

Figure 2.15: Various unsuccessful experimental geometries.

All of these experiments were designed to look for gain along a specific path, about 1 cm away from the exciting plasma. The rational for this was that electron quenching or

broadening might destroy any population inversion, and thus looking farther away, where the electron density was less but the gain should still be substantial, seemed reasonable. The problem with this rationale was that it did not consider the limiting effects of amplified spontaneous emission on the observable gain. To get a sense of why ASE is important, consider the simplest case of a population inversion: an atom at the center of a uniformly excited sphere. Figure 2.16 illustrates the case. Suppose this atom undergoes spontaneous emission. The photon then travels through the excited region, undergoing stimulated emission, and exits. Given a total gain-length of **gl** from the center, an average of $e^{\mathbf{gl}}$ photons will exit the region. This results in a decreased effective spontaneous emission lifetime $\tau' = \tau / e^{\mathbf{gl}}$. Thus, the upper laser level will be depleted more rapidly than in the case of an isolated atom, and the gain will be correspondingly decreased. In the case of a self-terminating inversion where the lower level fills, the gain will terminate much more quickly than for a low gain situation. Thus the geometrical shape of the excited region can have a dramatic effect on the measurable gain. Though this fact is obvious when explained in a simple fashion, most lasers naturally are long and thin, and also have low single pass gain. ASE effects in high-gain dye-amplifiers are observed; however, in this case the dye medium has an easily controllable geometry and ASE effects can easily be avoided. In the case of x-ray pumping, optics is difficult and one is more or less stuck with the geometry of a highly diverging pump source. Thus, previous measurements of gain produced by laser-plasma pumping only observed small gains [56,123] on transitions that were not self-terminating, and ASE effects were never seriously considered.

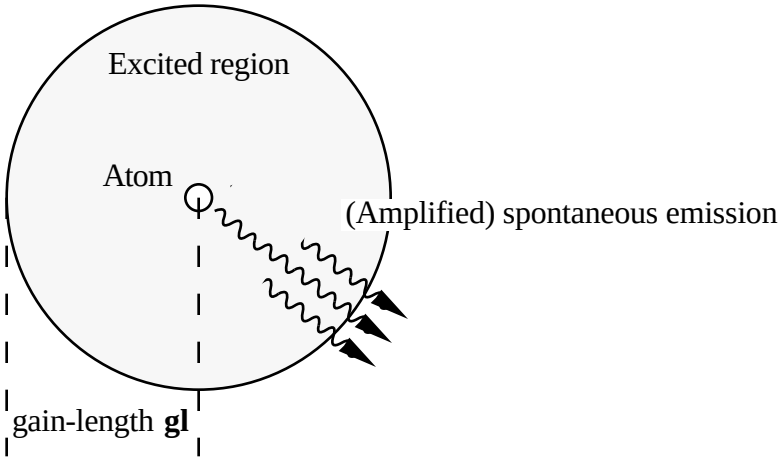

Figure 2.16: Hypothetical case of spontaneous emission of an atom in a region of population inversion.

The effect of ASE quenching is to clamp the maximum gain per unit length attainable. One might expect the approximate clamping value to be when the effective lifetime of the state is equivalent to the excitation pulse length, $\tau' \approx \tau_{pulse}$, where τ' is determined by the average gain-length traversed by a spontaneous emission photon. Considering the case of the line focus plasma arrangement used in the successful experiment, a calculation of the gain-lengths in various directions can be instructive to consider, since it will give an indication of the flux intensities in various directions. The GAIN4 program was modified (GAIN5) to calculate the gain-length for a line-focus source in the longitudinal, transverse, and radial directions, as defined in figure 2.17. The radial gain-length is defined as the gain-length radially outward from the plasma to a distance **r**. Radiation coming from the other direction, radially inward, would not be expected to be important because of the diverging nature of the x-ray source. This radial gain-length is difficult to define since the gain very close to the plasma, at very high densities, is unknown because electron quenching or broadening may reduce the gain. In this model only depletion of the xenon through ionization, and ionization out of the excited level, is taken into account. This is done by taking the actual excited state density as:

$$N^{*}_{4d} = N_{4d}\, e^{-\left(N_{total}/N_{xenon}\right)} \quad , \qquad (2.4)$$

where $\mathbf{N}^{*}_{4d}$ is the actual 4**d** ionization density, $\mathbf{N}_{4d}$ is the ionization calculated from the cross section and photon intensity, and $\mathbf{N}_{xenon}$ is the xenon density. The gain-length in the radial direction is also adjusted for the geometrical divergence of the x-rays:

$$GL(r + dr) = \left(\frac{r}{r + dr}\right)\left(\frac{r + l}{r + l + dr}\right) GL(r) + \gamma(r)\, dr \quad , \qquad (2.5)$$

where **GL** is the gain-length, **l** is the length of the plasma, and γ is the gain per unit length. The geometrical factor was chosen to reflect the 1/**r** divergence close to the plasma where the source looks like a line, and 1/$\mathbf{r}^2$ divergence far from the plasma where the source looks like a point.

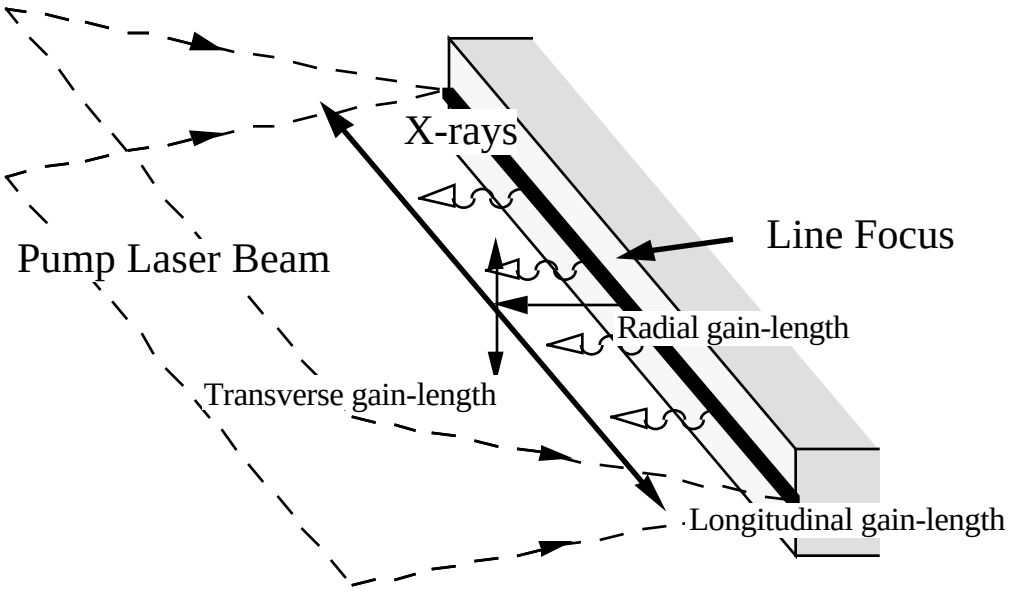

Figure 2.17: Longitudinal, transverse, and radial gain-lengths defined for a line focus plasma, at a given distance **r** from the plasma.

Given an atom at a distance **r** from the plasma, the flux impinging upon it will come from any of the three (longitudinal, transverse, or radial) directions, and this flux will cause stimulated emission. The solid angle for the longitudinal flux is smallest, so that the lifetime

will first be limited by the gain-length in the transverse or radial directions. Figure 2.18 shows the simulation results for the conditions of the laser experiment. We see that the longitudinal gain-length peaks at a distance from the plasma of ~2 mm. At this distance, the electron density is between 3 and 7 x 10^{16} cm^{-3}. Since, in experiments using similar pressures and looking at a distance of 0-3 mm from the target, bright laser emission was observed, it is possible that electron quenching is not important for this laser geometry. At the distance of 2 cm, where the slot was located, the longitudinal gain is $\mathbf{e}^{23}$, while the transverse and radial gains are $\mathbf{e}^{12}$ and $\mathbf{e}^{9}$. If the gain clamps when $\tau' \approx \tau_{pulse}$ with $\tau' = \tau / \mathbf{e}^{\mathbf{gl}}$, then given the aspect ratios from this data, one might expect ASE clamping to occur at a longitudinal gain-length of:

$$\frac{4.75 \text{ nsec}}{e^{(gl)_{t,r}}} \approx 1 \text{ nsec} \qquad (gl)_{t,r} \approx 1.6$$
$$(gl)_l \approx \frac{23}{10} (gl)_{t,r} = 3.6$$
$$\approx 0.4 \text{ cm}^{-1} \text{ for a 9 cm length}, \qquad (2.6)$$

where I have taken to be $\mathbf{e}^{10}$ the average of the transverse and longitudinal gain-length. Although this estimation of the point at which ASE saturation becomes important is crude, the agreement with experiment where clamping of the gain at ~0.5 cm^{-1} was observed, is remarkable.

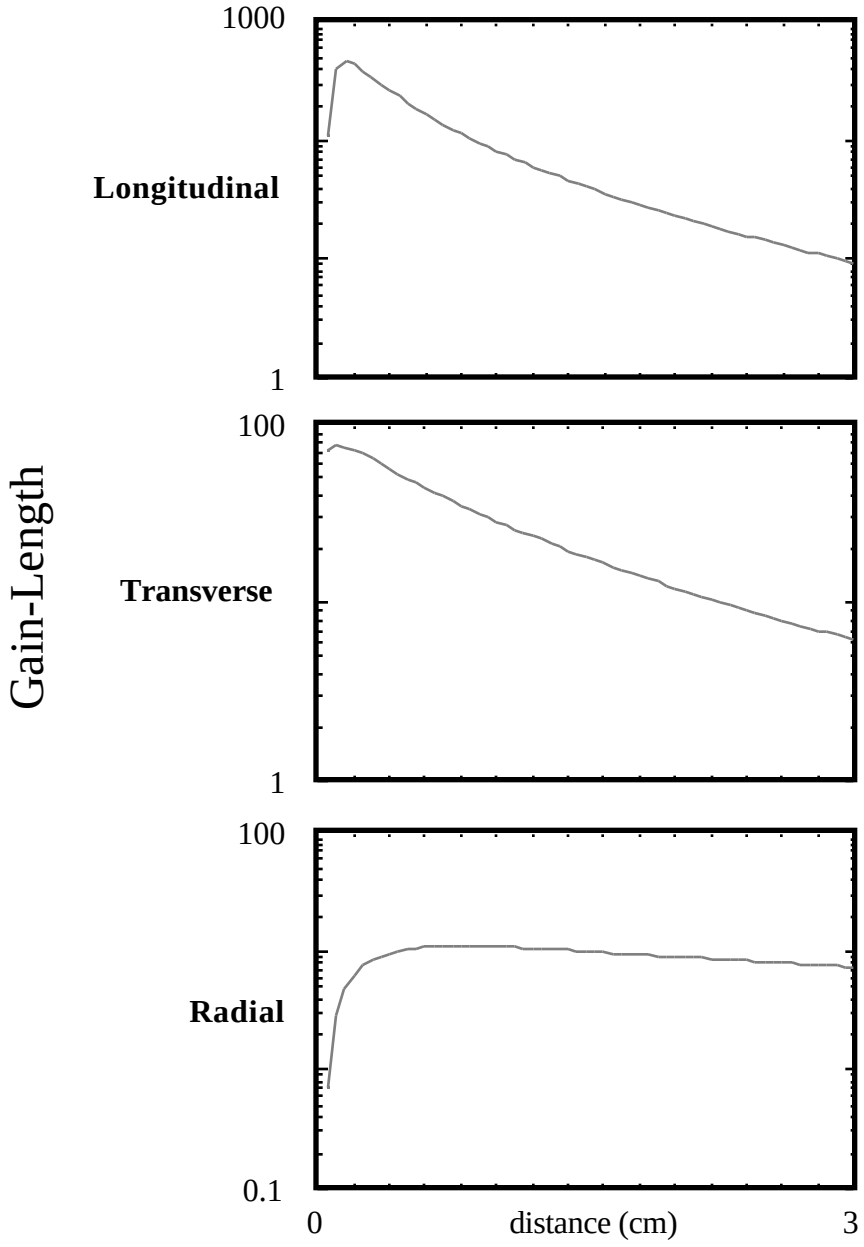

Figure 2.18: Gain-length products for the longitudinal, transverse, and radial directions for a 8 cm long line-focus plasma with 55 J total laser energy (7% x-ray conversion efficiency) and 1 torr xenon pressure.

The explanation as to why the other experiments failed is rooted in the ASE saturation problem. If one looks at the aspect ratio of the longitudinal to the transverse and the radial gain-length product, as shown in figure 2.19, this ratio is most favorable very near the

plasma, but not so near that the xenon is depleted. Thus, the best place to look for gain is as near the line focus as one can get without depletion or quenching destroying the gain. As the distance from the line focus increases, the aspect ratio decreases, asymptoting to 1 for the case of the longitudinal/transverse ratio (when the line focus looks like a point focus), and to zero for the longitudinal/radial ratio. The radial ratio crosses below 1 at **r** = 3.5 cm. Thus, far from the plasma, one would expect that most of the 108.9 nm flux is moving radially outward from the plasma, and that the measurable gain in the longitudinal direction would be small. So to see gain, one must look at the correct distance away from the plasma, and the previous experiments failed because they were looking at a region too far from the plasma, out of fear that electron quenching might destroy the gain. In fact ASE quenching, which is important far from the focus, was limiting the gain. Although given the data of figure 2.19, one might expect to see some gain at **r** = 1 cm, quenching in the radial direction might be enhanced by the fact that the plasma itself as a blackbody will radiate intense 108.9 nm light, enhancing the flux in the radial direction. Also, these experiments were generally done using a higher xenon pressure than assumed in the simulation-- the simulation shows that the radial ratio crossing point moves inward (2.8 cm @ 2 torr, 2 cm @ 5 torr) with higher pressure, although the peak longitudinal/radial aspect ratio (close to the focus) is higher. Also, it must be noted that in the two-slot line focus configuration of figure 2.15, small but inconclusive gain was measured. The slot configuration used in many of the experiments was an attempt to control ASE quenching in the transverse direction; however, it was apparently not sufficient.

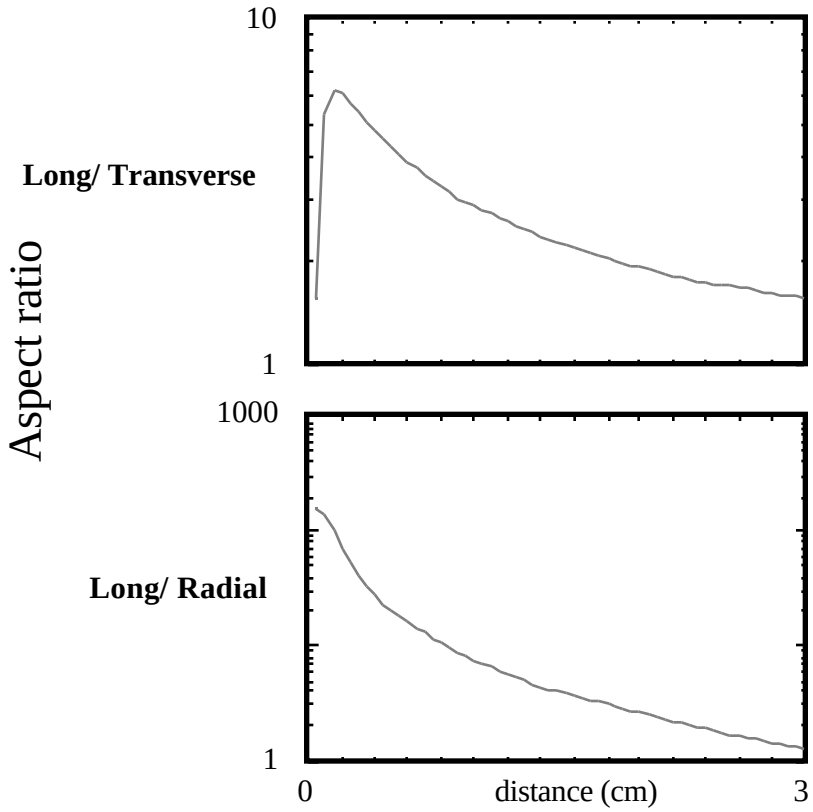

Figure 2.19: Aspect ratios for the simulation of figure 2.18.

For the case of a point focus plasma as in one of the experiments of figure 2.15, the situation is even worse. The transverse gain is the same in all directions, and thus is clamped at a small gain. Figure 2.20 shows the transverse gain and the transverse/radial aspect ratio for a 1 Joule point focus, as a function of distance from focus. Farther than 1.4 cm from the plasma, the gain-length in the radial direction dominates, and the flux primarily travels radially outward. But for the most part, the gain in all directions is similar and thus ASE will severely limit observable gain. One recent paper by Silfvast and Wood [161] proposes to take advantage of the radially out-going energy by using a focusing mirror to collimate it. In the situation described below, one would not expect the output to be very collimated, as the effective source region is the region $\mathbf{r} < 1.4$ cm where the gain is similarly high, and thus clamped, in all directions. Given different conditions, this crossing point can much closer to

the plasma. However, the Silfvast paper fails to take into account ASE depletion of the gain, and the quality of the output beam and efficiency of energy extraction are probably much less favorable than stated in the paper.

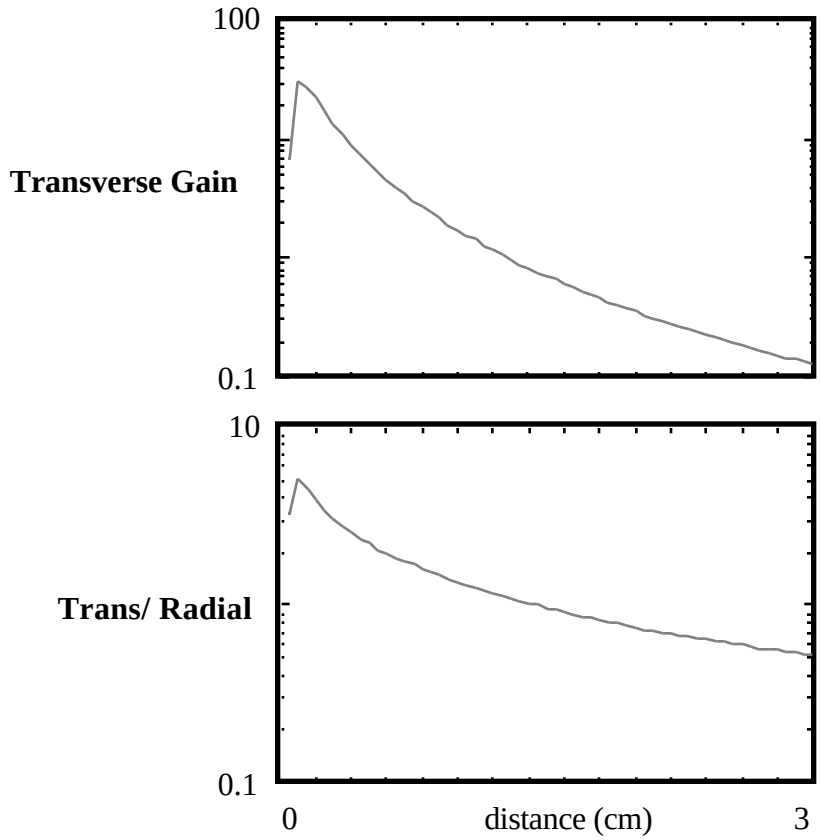

Figure 2.20: Transverse gain and transverse/radial ratio for a point focus plasma of 1 Joule laser energy, using 2 torr xenon pressure.

The hypothetical case of varying the length of the line focus, while maintaining the total pulse energy as constant, is shown in figure 2.21. As the line focus gets longer, the gain in the longitudinal direction increases, since the lower energy density allows gain closer to the plasma without ionization depletion of the xenon. In contrast, the transverse and radial gains decrease, because of the lower energy per unit length. Thus the aspect ratio increases considerably more rapidly with length than one might first expect. Also, the distance at which the radial gain overtakes the longitudinal gain moves outward, allowing one to extract

energy into the output laser beam more efficiently. This model assumes a constant conversion efficiency of pump laser energy into x-ray energy; in reality, as one makes the plasma longer, the power per unit area incident on the target decreases, and the plasma therefore becomes cooler and less efficient at converting laser energy to x-rays.

One observation from the research of the Harris group at Stanford, and of our research, is that x-ray emitting plasmas can be produced with power levels as low as 5 x 10^{10} W/cm^2 [150]. This allows the use of an energy per unit length as low as 0.2 Joules cm^{-1}. However, the ingenious method of using a grooved target with a grazing incidence pump beam, first demonstrated by Sher et al. [162] (illustrated in figure 2.22) allows the plasma to be broken into many small sections in a straightforward manner, increasing dramatically the possible excitation length for a given pump laser energy. It also quite naturally produces a traveling-wave excitation due to the grazing incidence pump beam, eliminating propagation time effects since the x-ray excitation pulse moves along with the 108.9 nm light being amplified. The traveling-wave velocity can also be adjusted, by using a grating pair, to more precisely match the propagation velocity of the light [108]. The good aspect ratio allows a very long gain-length ($\mathbf{e}^{40}$), and thus saturation of the laser transition resulting in efficient extraction of laser energy from the excited gas.

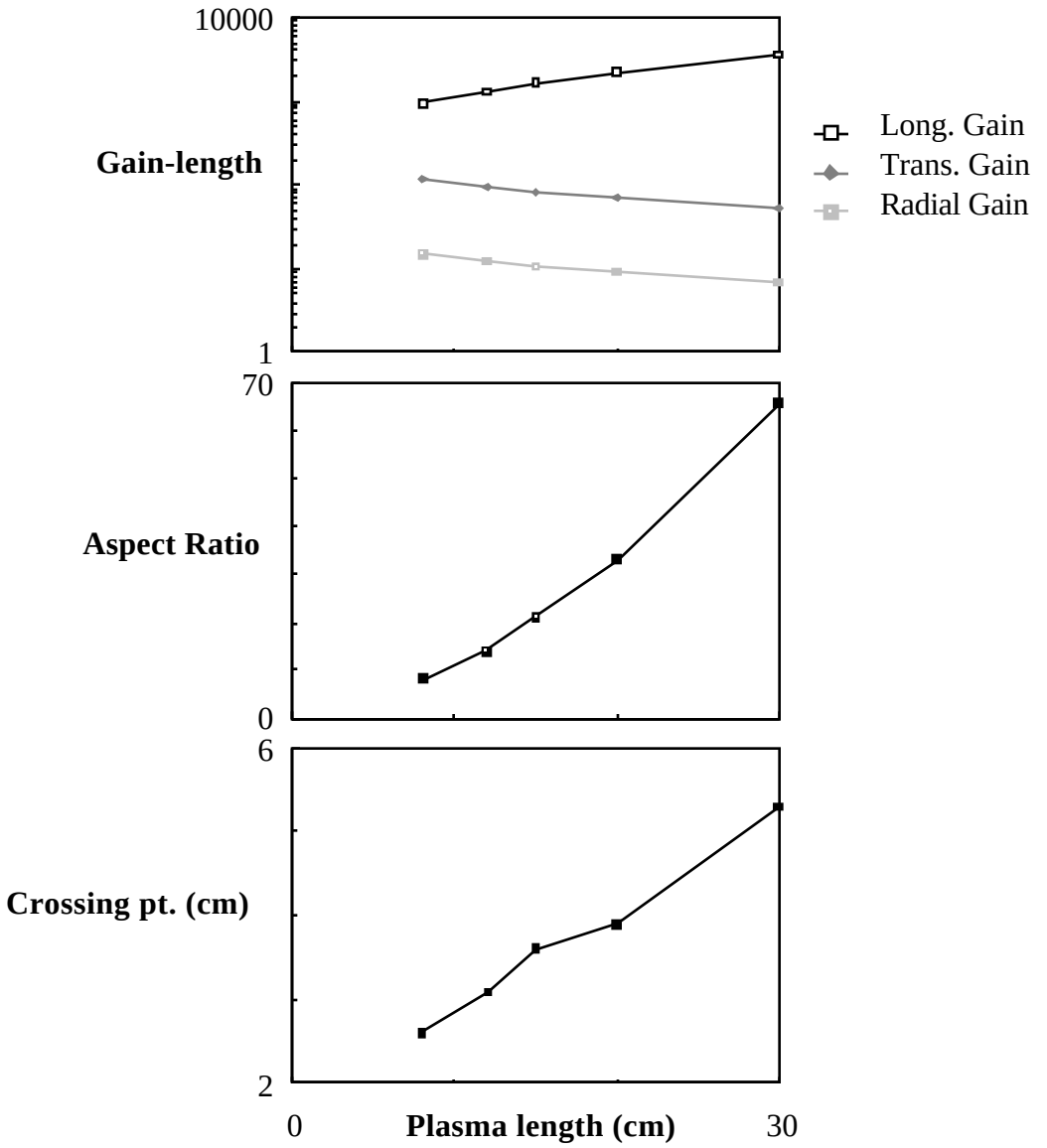

Figure 2.21: The peak gain in the longitudinal, transverse, and radial directions, the peak longitudinal/transverse aspect ratio, and the distance at which the radial gain exceeds the longitudinal gain for a 55 Joule line focus plasma of varying length. The xenon pressure in this case is 2 torr.

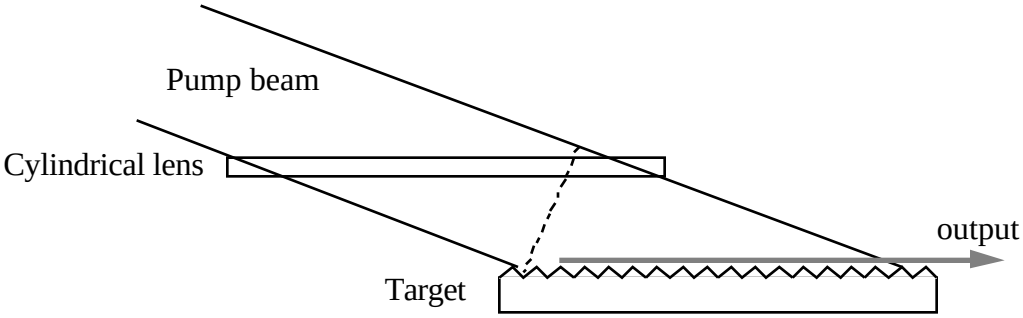

Figure 2.22: The traveling-wave geometry used by Sher et al. with the xenon Auger laser [162]. The grazing incidence pump beam allows traveling-wave excitation, and the grooved target allows the plasma to be broken up into a large number of small plasmas, each with a higher peak intensity than would be possible with a flat target.

2.3.3 Time dependent ASE model of the LLNL experiment

Using the concept of ASE quenching it is possible to construct a time dependent model of the gain dynamics of the xenon laser experiment. One advantage of the experiment we did at LLNL is that, when the parylene filter is used to isolate the long, narrow channel (see figure 2.2), the resulting system of which the output is observed has a simple geometry. The region inside the channel is more or less uniformly pumped by the x-ray source (see figure 2.14), and has a very well defined geometry. Evidence indicates that electron quenching effects aren't important, so that it is fruitful to try to model the dynamics of what goes on in this system. Since the streak camera spectrograph records a time history of the laser output, it would be illuminating to model this output on the computer, using the concepts developed in the last section.

The computer program MONTE CARLO (see Appendix B for details) does just that. As one might guess, Monte Carlo computational methods are used to develop a model for the gain dynamics of the system. To understand the model, lets us consider the simplified picture of the experiment, as shown in figure 2.23. The model assumes a uniformly excited

channel of length/width ratio of 30, as in the experiment. To estimate the effects of ASE quenching, a Monte Carlo calculation is done. Spontaneous emission is assumed to originate starting from anywhere in the channel, in any direction, with uniform probability. So a starting point and random direction is randomly picked, and the distance the photon travels before exiting the channel is calculated. This procedure is repeated $>10^7$ times, building up a distribution function as shown in figure 2.24.

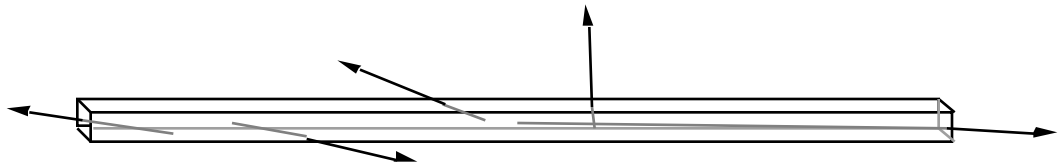

Figure 2.23: Schematic diagram of the simplified experiment simulated in the code MONTE CARLO. A uniformly excited channel of Length/Width = 30 is assumed, and ASE is calculated using a Monte Carlo model.

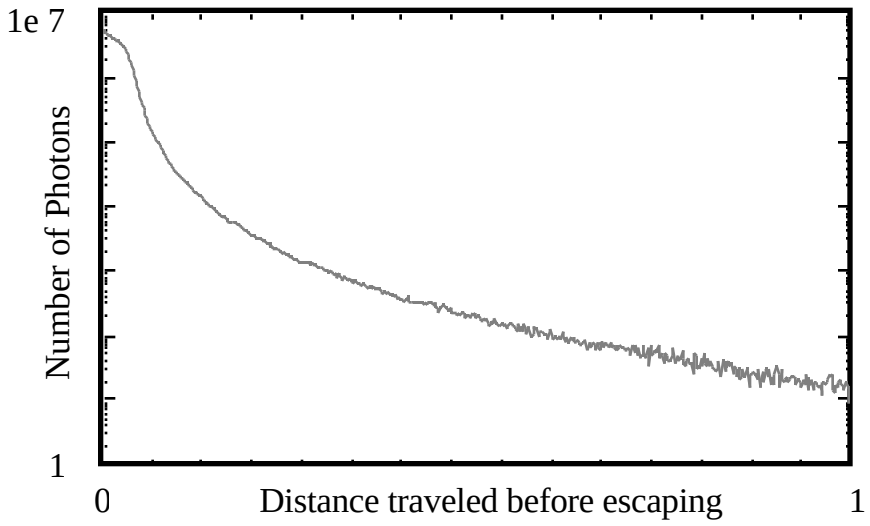

Figure 2.24: Monte Carlo generated distribution function of the probability of a photon traveling a specified distance before escaping the geometry of figure 2.23. The length is in units of the total channel length. The total number of iterations was 10^8 and the data is divided into 600 bins; thus, uniform probability would be 1.66×10^5 photons/bin.

This distribution function can then be used to calculate an ASE quenched effective lifetime:

$$\tau' = \tau \Big/ \sum_{l=0}^{1} f(l) \int_{\Delta\nu=-\infty}^{\infty} \left[\frac{1}{\sqrt{\pi}} e^{-(\Delta\nu)^2} e^{\left((GL)_o \, l \, e^{-(\Delta\nu)^2} \right)} \right] \quad ,(2.7)$$

where $(\mathbf{GL})_o$ is the gain-length at line center for the entire channel length and **f(l)** is the normalized distribution function of figure 2.24. The integral corresponds to the average number of photons exiting the region given the original photon traveled a distance in the excited region corresponding to the gain-length $(\mathbf{GL})_o$. It must be averaged over the Doppler linewidth, as in equation 2.2. This function is then convolved with **f(l)** to obtain an average number of photons escaping the region for each spontaneous emission photon, given a specific total gain-length $(\mathbf{GL})_o$ in the channel. The effective lifetime can then be calculated for any given gain-length along the region to obtain the distribution function shown in figure 2.25.

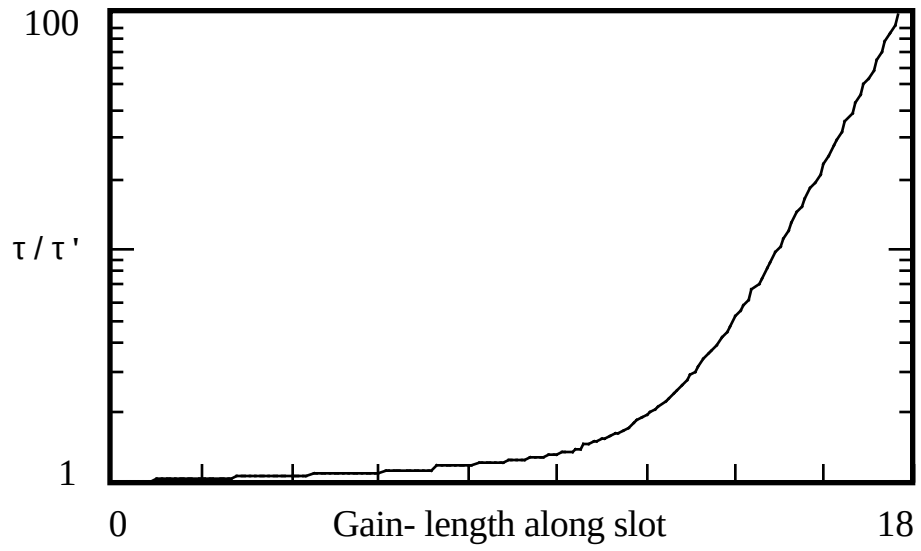

Figure 2.25: ASE lifetime shortening as a function of total gain-length along the slot, for a slot with aspect ratio 30.

A rate equation model can then be constructed for the laser system. The model assumes that the region is not only uniformly pumped, but is also uniformly depleted. It also ignores propagation time effects. Thus, the excitation of the laser is determined only by an upper and a lower level population, and one can use a simple rate equation as illustrated in figure 2.26. Auger decay populates the upper and the lower levels according to the measured branching ratios, and the upper level is transferred to the lower level according to the effective lifetime, which depends on the total gain (which depends on the upper and lower level populations). The lower level also decays with a 20.5 nsec lifetime, measured as discussed later. Neutral gas collisional quenching of the laser transition, also measured as discussed later, is not important at the xenon pressure of 1 torr, and is ignored.

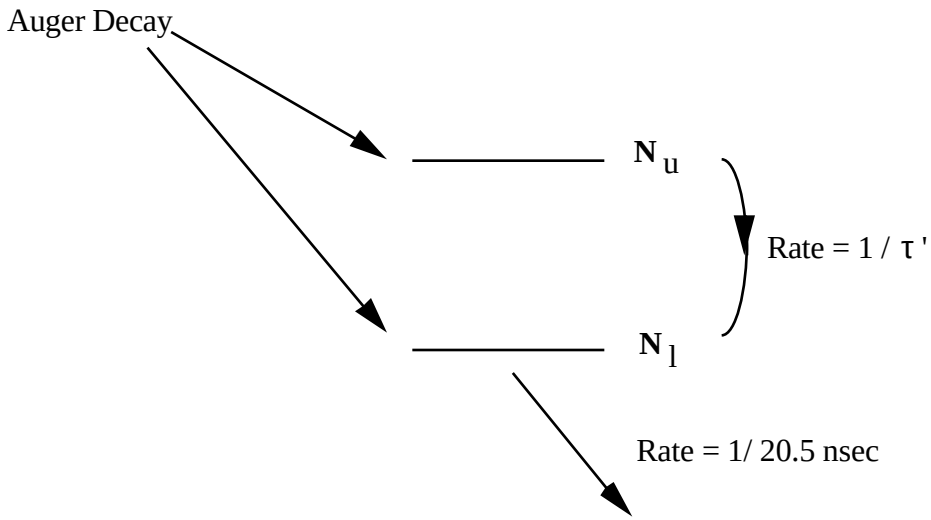

Figure 2.26: Rate equation model of the xenon laser experiment.

In this way, the population dynamics of the system can be modeled. However, the output intensity is the experimentally observable quantity. The output intensity is estimated by generating another distribution function (simultaneously with the one of figure 2.24), which is the number of photons that exit the channel in a direction within 1/60 radian (in both transverse directions) of the longitudinal direction. This is the direction observed by the

detector. From this distribution function, in conjunction with the distribution function of figure 2.24, one can calculate the fraction of the total photon emission which is in this "beam" direction. This function is shown in figure 2.27. This parameter can then be used in conjunction with the model, to determine the output beam intensity.

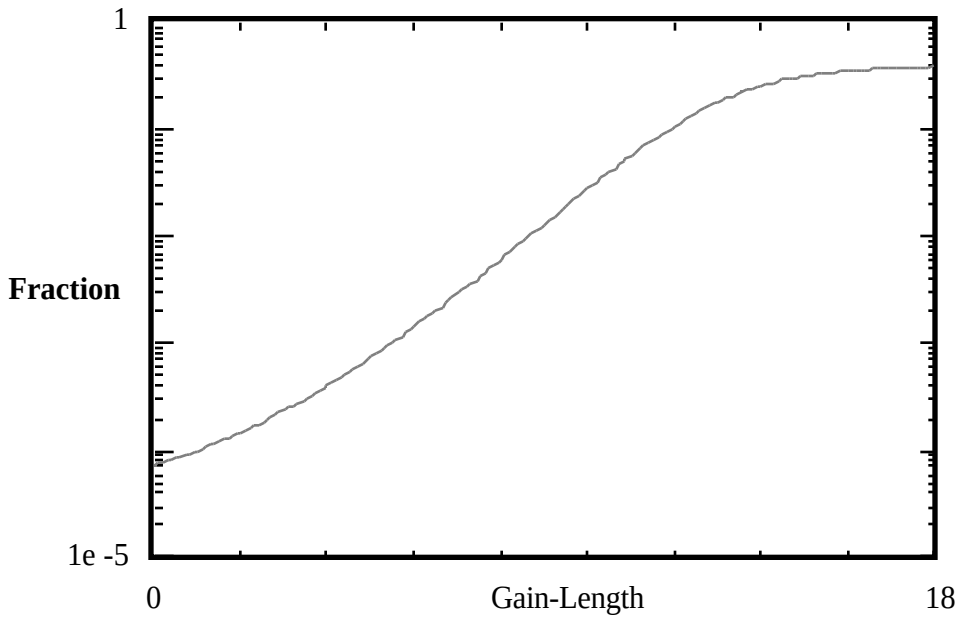

Figure 2.27: Fraction of photons exiting the excited region in the output beam, as a function of total gain-length of the slot. At low gain, the curve asymptotes to the solid angle of the output beam (within 1/60 radian of the axis). At high gain, the fraction nears 0.5, all out one or the other end.

Figure 2.28 shows the results of a simulation assuming $\mathbf{e}^{13}$ total gain in the case of impulse excitation, as predicted by the time-independent model GAIN4. Shown are the output profiles as a function of time, and the resulting peak intensities fitted to the same gain curve (equation 2.3) as the experimental data. The simulation output fits this gain-curve well at low excitation intensities, as would be expected. The fitted gain is 0.87 cm^{-1}-- remarkably close to the experimentally observed value of 0.8 cm^{-1}.

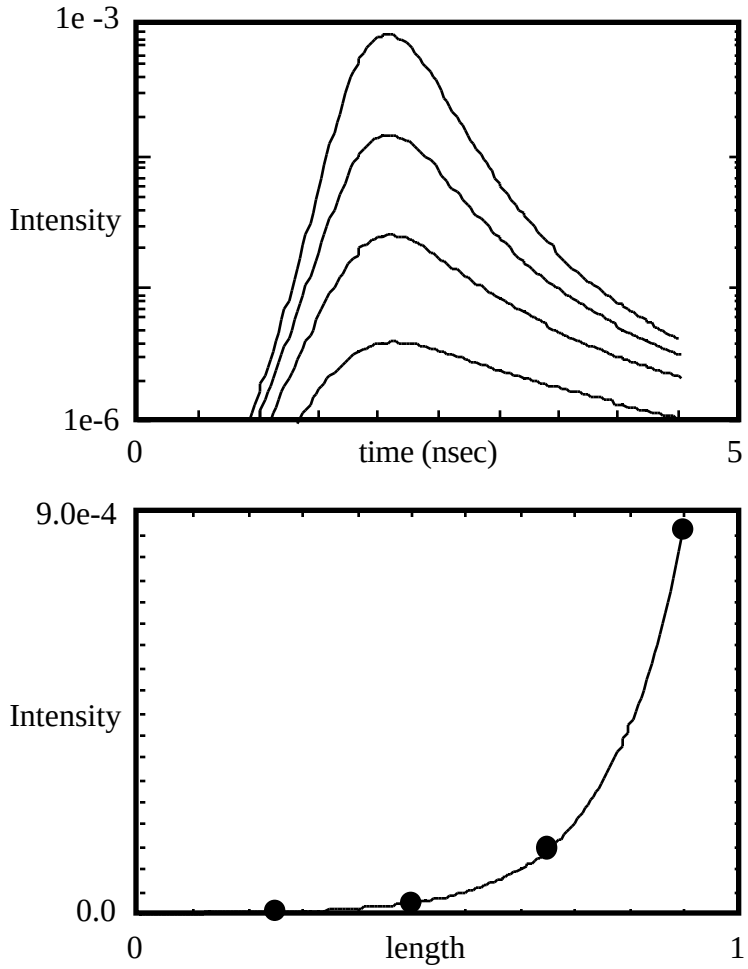

Figure 2.28: Time dependent simulation prediction of output intensity as the illuminated length changes (for 1/4, 2/4, 3/4, and full lengths). The first graph is intensity vs time, and the second graph is peak intensity vs length. The peak intensity data is fitted to a gain curve for 0.87 cm^{-1} gain at line center.

The code also predicts that the laser is near saturation. This is manifested by the fact that as the excitation is increased, the fitted gain coefficient does not increase proportionately, but levels off at a value of ~1.27 cm^{-1}. The fit function also becomes inaccurate as the output intensity as a function of length becomes linear instead of exponential at the longer lengths.

The program also predicts the output efficiency of the system. In the case of a full illuminated length, the efficiency, in terms of fraction of 108.9 nm photons emitted into the output beam, is predicted to be 0.0012. This corresponds to a total beam energy of 13 nJ, taking into account the branching ratios and the photon energy. One can compare this number (approximately) as follows: First, the beam passes through the LiF window, with a transmission of ~40%-- the value from published data [154], and also as measured by me. The "beam" is then is clipped by the 1mm slit after traveling ~40 cm, so that the initial 3 mm diameter beam is now ~7 mm diameter, and ~7% of the beam passes through the slit. Then the beam reflects off the grating, with efficiency of ~10% (an educated guess). Then the beam is clipped again by the 1 mm streak camera slit, with the 1 cm high entrance slit imaged at the exit. This is another 10% factor. Then, the microchannel plate efficiency is ~2% at 108.9 nm [163]. In total, on would expect to see $0.4*0.07*0.1*0.1*0.02*13x10^{-9}$ = 7.3×10^{-14} J = 4×10^4 photons. Experimentally, we can estimate the number of photons observed by comparing with noise traces, which can be assumed to be single photons. The single photon signal (Appendix A, equation A.1) works out to be ~12 counts-mm^2, in the intensity units used. Given a peak signal (figure 2.5) of 14,000 counts in a 8 mm x 1 mm streak trace for the brightest streak trace, this intensity corresponds to ~10^4 photons. This is in good agreement with the predicted value, considering the uncertainties in this estimate.

The pulse length predictions of the model are compared with experiment in figure 2.29. The plot is of pulse width vs. peak intensity, and the experimental data is for all laser shots that did not malfunction. This analysis lumps in isotope, non-isotope, parylene, and non-parylene data; this was done to obtain reasonable statistics. The justification for doing this is that the data still fall along a single curve, taking into account the large statistical scatter. The simulation output also fits the same intensity-pulse length curve for reasonably large fluctuations in parameters. Data for the parylene and non-parylene cases are shown differently.

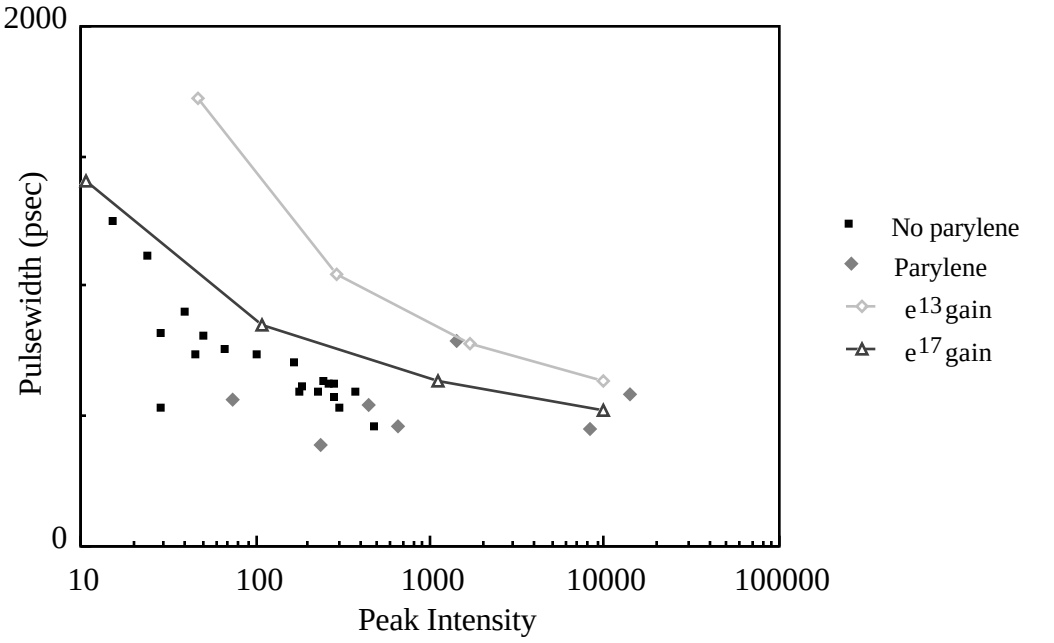

Figure 2.29: Pulse width dependence on peak intensity for all JANUS xenon laser shots with total energy of 55J ± 10%, compared with simulation data for total excitation of $\mathbf{e}^{13}$ and $\mathbf{e}^{17}$. The model predicts pulse length dependence reasonably well assuming the higher excitation level.

The solid curves are predictions of the computer code. The intensity scaling is chosen so the peak intensity is equivalent in both cases. The upper curve is the pulse width predictions of the model using the same parameters assumed previously. As one can see, the predictions significantly overestimate the pulse width, although the general trend of pulse width vs. intensity appears accurate, and the pulse width at the highest intensities is reasonable. The other curve is an adjusted model where the total impulse excitation gain-length is increased from $\mathbf{e}^{13}$ to $\mathbf{e}^{17}$, increasing the ASE quenching of the transition. In this case, the pulse length agreement between experiment and theory is much better. However, this comes at the expense of agreement of the gain coefficient-- in the case of $\mathbf{e}^{17}$ excitation, the measurable gain is predicted to be 1.1 cm^{-1} (compared to the experimental 0.8 cm^{-1}).

There are several possible explanations for the discrepancy between experiment and simulation. The data shots without the parylene filter would be expected to be shorter in pulse width than the predictions due to increased ASE quenching; however, even the parylene shots seem to fall well below the unadjusted curve. The model does assume uniform excitation and depletion of the region, which is not the case in reality. The ends of the channel will be depleted more quickly than the center, since at the ends the depleting beam in the longitudinal direction will be more intense (it will have passed through a longer gain-length). Since gain is a non-linear process, it would be expected that any non-uniformities would increase gain quenching and shorten the pulse width. The channel is also not uniformly excited (see figure 2.14); this will lead to increased ASE quenching due to the increased transverse gain-length product in the center of the channel. However, simulations done assuming a 50% larger transverse gain-length have little effect on the pulse width; thus this effect is probably minor. Electron quenching of the transition may also lead to a shorter pulse length even if it doesn't have a major effect on the measured gain (quenching may become important only after the peak of the gain has passed in the system).

Propagation time effects are also not taken into account in the model. The time of propagation along the 9 cm channel is 300 psec, comparable to the 1 nsec excitation pulse. In actuality the situation is even more complex than this in that the propagation speed of the light being amplified is modified by the presence of laser gain. This occurs since the laser wavelength is near an atomic resonance (the laser transition), and thus the index of refraction for that wavelength will be modified [164,165]. The group velocity of the light at line center in a high-gain medium is:

$$v_g = \frac{c}{(1+\beta)} \qquad (2.8)$$

where

$$\beta = \frac{c\,G\sqrt{\ln 2}}{\pi^{3/2}\,\Delta\nu_D} \qquad (2.9)$$

for Doppler broadening, or

$$\beta = \frac{c\,G}{2\pi\,\Delta\nu_n}\ , \qquad (2.10)$$

for natural broadening, where **G** is the gain per unit length in the medium. For the Doppler broadened xenon system, with a gain of 0.8 cm^{-1}, β=1.2. Thus, the propagation speed of the xenon light would be expected to be slightly less than 1/2 the speed of light, and it will vary in time as the gain varies. Thus one would have to do a very complex simulation of the laser geometry to determine the effect of propagation delay on the pulse width. However, this effect may be a possible cause of the anomalously short pulse width.

Finally, one likely possible explanation has to do with the double pulse structure sometimes observed (figure 2.8). The most likely explanation for this behavior is that it is superradiant ringing. Superradiance is an effect where an ensemble of excited atoms can radiate in stimulated emission coherently, so that the electromagnetic fields add directly and the intensity of the photon field can increase as the square of the number of radiating atoms. This results in much more rapid stimulated emission than is the case when the emission photons add incoherently to the field, and thus superradiance results in much more rapid depletion of the gain. Essentially, all of the dipoles associated with the atoms become phase coherent, and radiate coherently. This coherent output completely depopulates the upper level, transferring it to the lower level. Ringing can then result when photons become re-absorbed in the medium, repopulating the upper level and resulting in another, lower intensity superradiance pulse. This is in contrast to the ASE model, where amplified spontaneous emission will transfer population into the lower level at an accelerated rate only until the upper and lower level become statistically populated and the gain becomes zero.

Superradiant ringing has been observed in a number of systems, mostly in the infra-red [152,166]. It was first discussed by Dicke in 1954 [167].

The reason that superradiance effects might be expected in the xenon laser system is that the coherence lifetime of the laser level is quite long. Intuitively, one might expect superradiant behavior when the dephasing time of the transition is comparable to the time it takes light to travel a gain-length of $\mathbf{e}^1$. For an atomic system such as the xenon laser, the dephasing time of the transition is equal to the lifetime of 4.75 nsec, while the transit time is only ~1 cm/**c** = 30 psec. Thus superradiant behavior might be expected. This is in contrast to most solid state or molecular lasers where the homogeneous linewidth of the transition (= (dephasing time)$^{-1}$) is much broader than the natural linewidth, and thus the dephasing time is very short.

In a more detailed analysis [168,169,170], one must consider the inhomogeneous broadening of the system, and the solid angle for which the superradiant pulse is emitted. In this case, the superradiant lifetime is defined as:

$$T_R = \tau_{spont} \frac{8\pi}{n \lambda^2 L} = \frac{g_D(0)}{GL} \quad , \qquad (2.11)$$

where **n** is the density of inverted states, and **L** is the excited length of the region (**GL** is the gain-length). The center expression is valid in general for a system of large fresnel number [171] (as is the xenon laser : $\mathbf{N} = \mathbf{a} / \pi\lambda\mathbf{L} \approx 300$). The last expression is valid only for Doppler broadened systems, where $\mathbf{g}_D(0)$ is defined in equations 1.29 and 1.30. For a gain-length of $\mathbf{e}^{13}$ in the xenon laser, $\mathbf{T}_R$ = 25 psec. Since the superradiant lifetime is much shorter than the spontaneous lifetime, one would expect to see superradiant behavior in the xenon system, with the consequences of shorter output pulse duration, and superradiant ringing. Unfortunately, time-dependent simulation of superradiance has only been attempted for systems of low fresnel number [152,166] with very well controlled initial parameters. A

superradiance simulation of the xenon laser system would be at best a situation to be left to a full-time theorist, and at worst completely impractical.

2.3.4 Conclusion

In conclusion, the xenon laser system is quite well understood. Simple numerical simulations do quite well at predicting the behavior of the experiment, and where the models fail, a reasonable qualitative explanation exists for the discrepancy. The xenon laser is actually one of the simpler laser system demonstrated to date-- a population inversion is created in an atomic system as the result of a simple decay process, and the upper laser level then simply decays to the lower.

2.4 Fluorescence spectroscopy experiments

Successful demonstration of the gain experiment depended on accurate modeling of the laser system. The accuracy of the model predictions depend on the accuracy of the data used in the model. An especially critical parameter which had not previously been measured was the lifetime of the laser levels. Not only does the gain coefficient depend on the spontaneous emission rate (equation 1.22), but also the time dependence of the gain depends on the lifetime of the state; this is especially critical in the case of a self-terminating laser. The lifetime of the lower laser level is important in determining whether the laser is indeed self-terminating. Atomic physics codes can be used to calculate these lifetimes. However, for large atoms such as xenon the results can be regarded as approximate at best--initial code estimates of the lifetime varied from 50 psec to 4.4 nsec. Thus, we undertook to measure the lifetimes of the levels ourselves, using the novel experimental apparatus which I shall describe below.

Also important in determining the feasibility of the laser is the branching ratio of Auger decay into the relevant states, and branching ratios of the radiative decays out of the states. The Auger branching ratio can be derived from previously measured data (figure 2.1). The radiative branching ratios were examined by observing the fluorescence intensities of the states in a separate experiment. These experiments provided more confirmation that the transition should invert (and provided critical encouragement to continue experimentation when things were not going well).

Lastly, I will discuss two experiments that we did here at Berkeley that showed evidence of population inversion. Although these experiments were not published since there may have been other possible explanations for the observed data, in retrospect the experiments demonstrated population inversion using very modest table-top laser sources.

2.4.1 Lifetime measurements using time-correlated photon counting

The apparatus used to measure the lifetimes of the relevant states is shown in figure 2.30. Much of the early development of this apparatus was done in conjunction with Máiréad Murnane. The technique used for these measurements was that of time-correlated photon counting (TCPC). TCPC has been extensively used to measure excited states lifetimes of atoms and molecules excited by visible laser light and by synchrotron radiation; however, this apparatus was the first to use the technique in conjunction with a plasma x-ray excitation source. Referring to figure 2.30, the idea behind TCPC is to use an impulse excitation source to excite atoms, and then to detect single fluorescence photons from the desired transition. The lifetime of the state is determined by repetitively measuring the delay between the time of impulse excitation and the time that a photon arrives at the detector. Statistically, the probability of detecting a photon at time **t** past the arrival of a δ function excitation is just $P \quad e^{-\mathbf{t}/\tau_{spont}}$; thus if a histogram of photon arrival times is constructed from the data using a multichannel analyzer, this histogram will decay with the lifetime of the excited level.

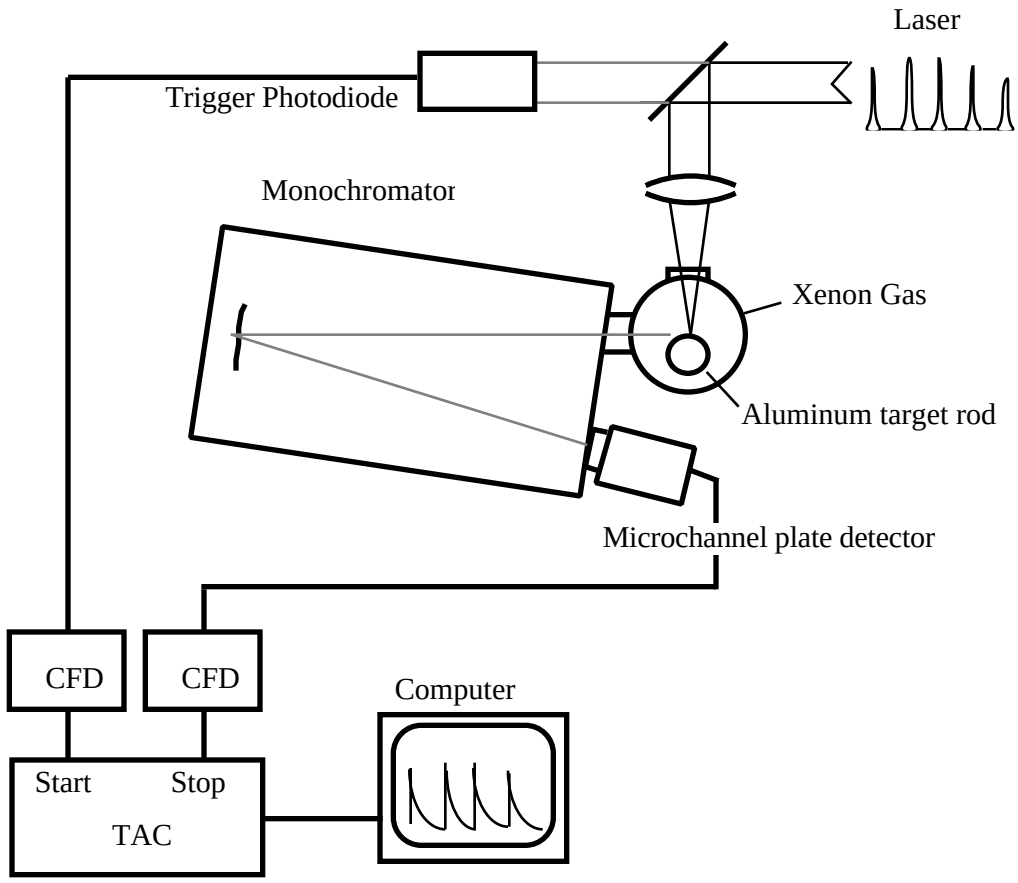

Figure 2.30: Basic time-correlated photon counting apparatus.

The output of a mode-locked and Q-switched Nd:YAG laser (Quantronix model 416) is focused onto a rotating aluminum rod in a target cell, to form a laser plasma x-ray source. The output of this laser is a burst of 90 psec long pulses at 10 nsec intervals, with a total of ~20 pulses per burst. Since the laser can be Q-switched at a rate up to 500 hz, the effective repetition rate of excitation pulses on target is up to 10^4 sec^{-1}. The maximum single pulse energy is 70 μJ, and the beam is focused by a 10 cm focal length lens to an approximately 10 μm diameter spot (near diffraction limited), resulting in a power density on target of 5 x 10^{11} W/cm^2. Xenon gas at a pressure ranging from 0.1 to 10 torr surrounds the target and is ionized by the broadband soft x-rays emitted from the laser-produced plasma. A monochromator with a fast, windowless microchannel plate detector is

used to observe the short-wavelength xenon fluorescence. Single photon pulses from this detector are amplified and sent to a constant fraction discriminator and then to a time-to-amplitude converter, which measures the time interval between an initial signal from a reference photodiode illuminated by the laser pulse, and the detected single photon. Data from the TAC is then sent to an IBM PC computer, which constructs a histogram of photon arrival times. Since the output of the laser is a repetitive burst of pulses, the display is a series of identical decay curves, which are separated by 10 nsec and later added together by the computer software (program MCA). The spacing between the decay curves is determined by the optical round trip time in the laser cavity and serves as an accurate time scale calibration.

The spectrum of the laser-produced plasma radiation is shown in Figure 2.31. This spectrum was taken with an Acton grazing-incidence monochromator (model 551, 300 g/mm grating) looking directly at the plasma emission, using an aluminum target rod. The fall-off in plasma emission above ~150 eV is real, although the fall-off at low energies is due in part to reduced grating efficiency. In any case, there is sufficient radiation in the 67-130 eV range necessary to excite the laser transition through Auger decay. The temperature of the plasma source, estimated by the peak of the emission curve, is in the range of 20-30 eV.

The target rod is moved continuously by a clock motor, to give the plasma a new section of target with each shot. 1/2" diameter aluminum rod was used; a rotation rate of 1 rpm was used for the rod when operating the laser at 50 hz, and 7 rpm when operating the laser at 500 hz. This results in a motion of 13 μm (9.3 μm) between successive laser bursts. The rod was also fed in the vertical direction using an 80 thread / inch threaded rod to pull it upwards as it rotated. The usable length of the 3 ft long rod (given that used target rod could not pass through the o-ring vacuum seal used in the target arrangement) was about 4 inches, giving a continuous run-time of >4 hrs at 50 hz, and ~45 min at 500 hz.

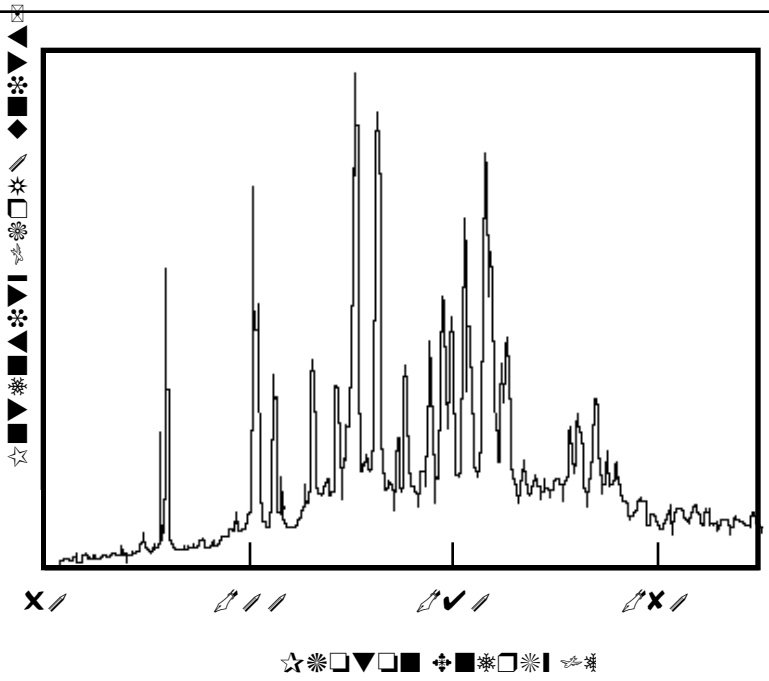

Figure 2.31: Spectrum of laser-produced plasma radiation created by a Q-switched, mode-locked Quantronix 416 laser, focussed onto an Aluminum target rod with a 10 cm fl lens.

Since the microchannel plate must operate at pressures of $<10^{-5}$ torr, which is much lower than the desired xenon pressure, a window was used to separate the target chamber from the monochromator. For measuring the lifetime of the 108.9 nm transition, a lithium fluoride window mounted near the monochromator slit was used. For the other transitions, a capillary array window (2mm thick, 50 μm pores, Galileo Electro-optics) arrangement, similar to that used in some of the gain experiments, was used. A diagram of this arrangement is shown in figure 2.32. An intermediate chamber is sealed off by an O-ring to the spectrometer slit on one side, and by the capillary window on the other, and is pumped on by a sorption pump to maintain a pressure of $\leq 10^{-2}$ torr. The capillary array window is placed within a few mm of the excited gas to limit the effects of self-absorption on the signal level (the mean free path for 90 nm light @ 1 torr xenon pressure is 5 mm). The pressure in the chamber is kept constant using a capacitive manometer pressure transducer

(Vacuum General model CML-10) and a electrically actuated valve (Vacuum General CV2-41) together with a simple Op-Amp feedback circuit (UCB manufacture 86-49).

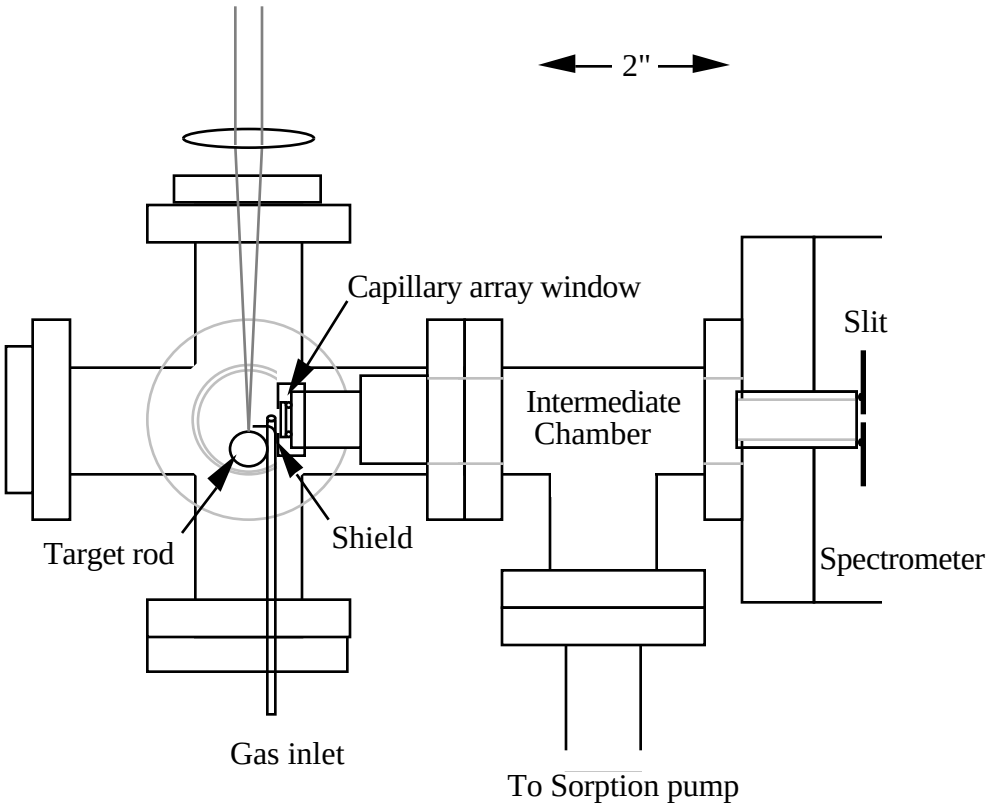

Figure 2.32: TCPC Chamber setup using a capillary array window.

One of the major difficulties with this experiment is that the laser plasma produces debris as well as x-rays, and this debris can block the optical path for the VUV fluorescence. In experiments using the LiF window, a simple metal shield (mounted on a feed-through rod, so that it could be adjusted from outside the chamber) was placed between the plasma and the window to block the direct line of sight. Visible fluorescence from the plasma could then be used to properly adjust the position of the shield, so that the spectrometer grating could see the fluorescence from the gas, but not get coated by direct plasma blow-off. In the case of the capillary array window, not only must the window be very close to the plasma, but also gas is continually being sucked into it. Even without a line

of sight between the plasma and the window, the array rapidly became clogged with aluminum dust. Different target materials (tantalum, titanium) resulted in marginal improvement; however, the problem was finally solved by feeding the input xenon gas through a small tube so that it blew the gas directly onto the capillary array. In this way, primarily clean xenon was sucked through the array. A small shield was used to block the direct line of sight, and also xenon was pumped directly out of the target chamber into the vacuum pump so that the net gas flow in the target chamber was directed away from the capillary array. With these precautions, the systems could be run for ~1 hour at 50 hz repetition rate, before it was necessary to back-flow some air through the capillary to blow out the accumulated dust. At 500 hz, the capillary still became clogged in < 2 min run time.

The monochromator (MacPherson model 225, 600 g/mm grating) was set to a slit width of 50-150 μm, depending on the particular level being measured. The fluorescence of the desired wavelength is detected by the microchannel plate (MCP) photomultiplier(Galileo Electro-optics model FTD 2003); an MCP was used in this experiment since MCP's have a much faster timing response than conventional photomultiplier tubes. The output of the FTD 2003 is a pulse of <500 psec FWHM, with a jitter between the photon arrival time and the time of the peak of the output pulse of ~50 psec [172,173,174]. In contrast, the best photomultiplier tubes typically have jitter of ~0.5 nsec [175]. The microchannel plate detector used was uncoated, with a quantum efficiency at 90-110 nm ranging from 1 to 5% [163].

The typical single-electron signal has a peak amplitude varying from 10-50 mV, using a voltage of 2400 V on the MCP. The signal is then amplified using a fast **x10** 1 nsec DC amplifier (Lawrence Berkeley Lab Manufacture, 18X 1281P-2), to obtain a signal of maximum amplitude ~500 mV. Another 200 Mhz amplifier (Avantek GPD 202 microwave amplifier chip in a impedance-matched box) together with appropriate 50 Ω impedance attenuators (Mini-circuits, Inc.) was also sometimes used and works equivalently well. Faster amplifiers (Avantek GPD 401,2,3 chain) were found to give somewhat degraded time

resolution-- the resulting pulses were apparently too short for the constant fraction discriminator.

The constant fraction discriminator (CFD) used was an ORTEC model 934 Quad CFD. A CFD is used to obtain precise timing information from pulses of varying amplitude; the basic principle of operation is illustrated in figure 2.33. The input pulse from the MCP is split into two signals. One of the signals is inverted in amplitude, and the other is delayed by a time on order of the pulse width. The two pulses are then summed, giving a waveform as shown, with a zero-crossing point that corresponds to the time of the peak of the input pulse, independent of the amplitude of the pulse. A zero-crossing detector can then produce a constant amplitude output signal precisely timed to the input pulse. CFD's typically have a time walk of ~30 psec over an amplitude range of a factor of 5, with specifications of <150 psec walk-off. The time resolution of the setup was not found to vary greatly with the setting of the zero-crossing detector on the CFD; the best setting was -1.5 mV. The threshold setting was varied somewhat to vary to count rate, but generally was set to ~0.5 V (corresponding to a threshold of 50 mV).

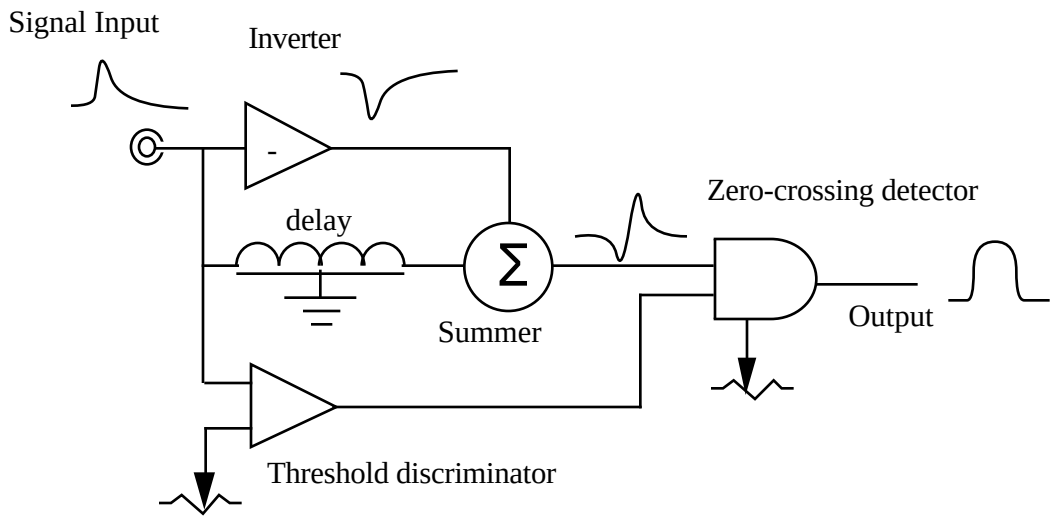

Figure 2.33: Basic CFD configuration.

The output of the CFD is then fed into the stop input of an ORTEC model 467 time to amplitude converter (TAC). A TAC is merely a fast voltage ramp, started by a start pulse, and stopped by a stop pulse input. The output voltage is then proportional to the time delay between the two signals. The start pulse signal is derived from a photodiode (Hewlett Packard 2-4220 8342) with output FWHM ~500 psec. The signal is adjusted to ~1 V peak, and then is mixed with a TTL signal delayed from the Quantronix Q-switch timing box. The TTL signal is attenuated by 10 dB, and is then put into the **RF** input of a Mini-Circuits ZAD-3 mixer. The photodiode is put into the **I** input of the mixer, and the mixer output is then put into another channel of the CFD. The CFD output is then used to start the TAC. The mixer was used so that the CFD would trigger consistently on a specific pulse in the Q-switch burst of the Quantronix laser. If the mixer were not used, the CFD would always trigger on the pulse in the burst with amplitude just above the CFD trigger level; this situation was found to degrade somewhat the time resolution of the system. The output pulse width of the trigger CFD was set to be > 10 nsec, so that only one trigger pulse is generated for each Q-switch burst. This is necessary since the TAC is not capable of being recycled at 10 nsec intervals.

The TAC was generally used on the shortest full-scale time of 50 nsec, or on the 100 nsec scale. The 0-10 V output of the TAC is read by a Stanford Research Systems model SR245 computer interface module into an IBM PC. The 12 bit resolution of the SR245 A/D results in a time resolution of about 12.5 psec. The data was taken using the program MCA (see Appendix B), which constructs a histogram of voltages corresponding to photon arrival times. Figure 2.34 shows the response of the photon counting apparatus when the grazing-incidence Acton spectrometer was set to directly view 100 eV soft x-rays from the plasma at reduced intensity. The 10 nsec separation between successive peaks can be used for accurate time-scale calibration. The width of the resulting peaks is less than 300 psec (FWHM). Although individual contributions to this width from timing jitter in the

microchannel plate and from the finite duration of the plasma cannot be determined from this data, subsequent measurements using the same apparatus with a plasma produced by 100 fsec pulses yielded a FWHM of ~60 psec [176]. Thus, the 300 psec FWHM is probably a measure of the duration of x-ray emission from the plasma. The electronics have a jitter of 40-50 psec; this was determined by feeding the same signal into both the start and stop channels of the CFD and TAC. This resolution, convolved with the MCP resolution of ~50 psec yields an impulse response of ~60 psec, as observed.

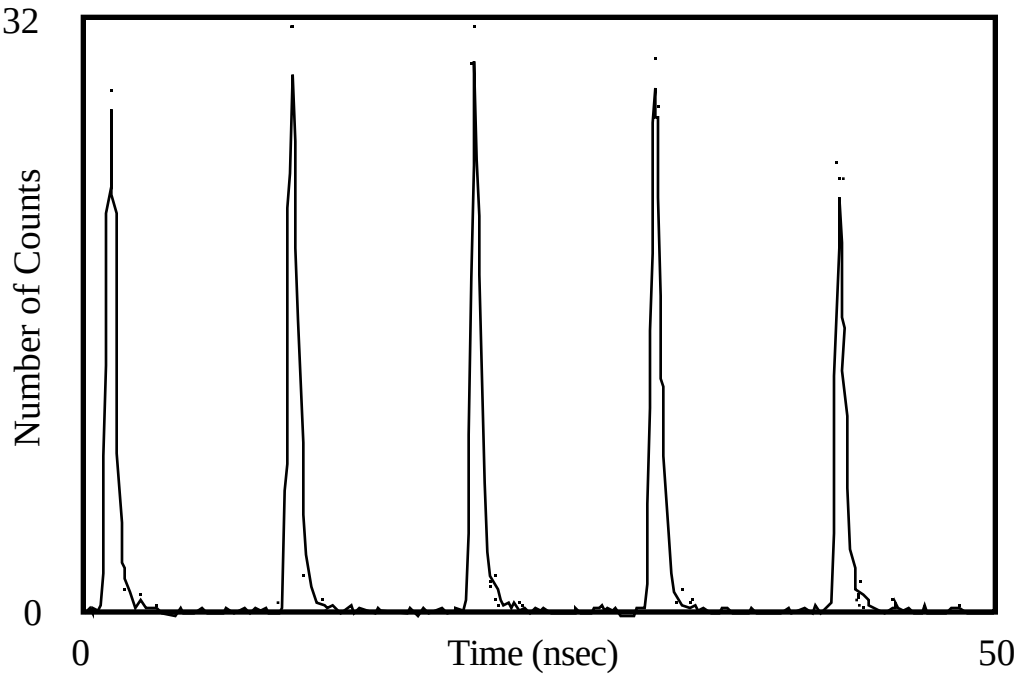

Figure 2.34: Short pulse response of the TCPC apparatus. The data was obtained by observing 100 eV photons emitted from a plasma produced by 100 psec mode-locked, Q-switched pulses. Shown are the data points and an averaged line.

Figure 2.35 shows a typical decay time measurement on the krypton 90.7 nm transition, which is the shortest lifetime transition I measured. The single decay curve is the result of software summation over four separate decay curves as in figure 2.34. Several thousand points are required for a reasonable fit, and even at the 50 hz repetition rate of the laser this

curve can be acquired in less than 10 minutes. Although at 50 hz, using the 50 nsec timescale, the effective repetition rate is 50 hz * 4 (or 9) pulses/burst * 60 sec = 12,000 (or 27,000) pulses per minute, one must limit the photon detection rate to << 1 photons/pulse. The reason for this is that the TAC can only catch one photon per trigger. Thus, if the probability of catching one photon per pulse is ~1, the probability of a second photon arriving at the detector will be ~1 as well. Since this photon will be ignored by the TAC, such a situation will result in a distortion of the data. This is called "pile-up" error. In general, the repetition rate for triggering the TAC was limited to below 0.1 triggers per Q-switch burst. It is important to note that the relevant probability in this situation is the number of triggers per laser pulse, not per Q-switch burst since distortion of the data will result only from differing detection probabilities between different parts of a single decay curve. A lower overall probability of detecting a photon on the second or third or fourth decay curve as opposed to the first will not affect the lifetime measurement. Thus, if the trigger rate is limited to 0.1 per burst, this corresponds to 0.02 per pulse, and the probability of the occurrence of a second undetected photon will be 0.02*0.02 = 0.0004, which corresponds to only a few missed photons for every decay curve.

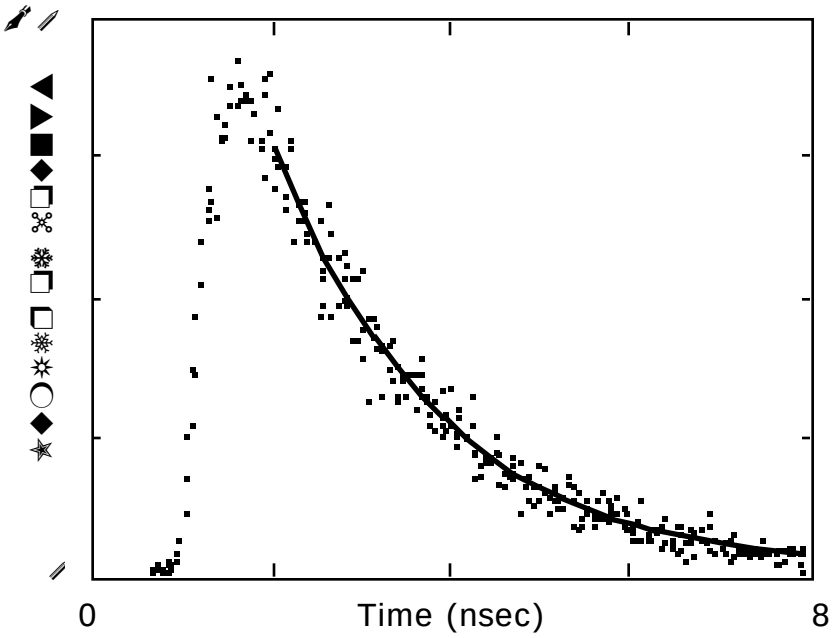

Figure 2.35: Lifetime measurement of the krypton 90.7 nm transition at a krypton pressure of 1 torr. The decay is fitted to a lifetime of 1.84 nsec.

The data is fit by the software to an exponential decay curve. This fit is simply a linear least-squares fit to the log of the number of counts in each bin [177], with a statistical weight for each bin simply proportional to the total number of counts in the bin. The slope of the line corresponds to the lifetime of the state, and the statistical error can also be determined. The data is fit for the interval after the complete excitation pulse has arrived, out to a time when the total count number in each bin is still well above the background level. Background counts are the result of either of two effects. The first is that another transition may be nearby in wavelength. For instance, a very strong Xenon II line is at 110.5 nm, near the 108.9 nm line; however, the signal level for the 108.9 nm line was sufficient that the slits could be closed to <50 μm, it which point interference was negligible. In general this type interference can easily be estimated by moving the spectrometer wavelength, and making sure that the count rate drops to near zero on both sides of the line of interest. One must also be reasonably certain from spectroscopy tables that no other lines lie at the same

wavelength [178]. The other background source was fluorescence from plasma debris. Debris from the plasma, if it is stopped in field of view of the monochromator, can cause spurious counts. This problem is severe at very low pressures (<0.1 torr); at higher pressures the debris is stopped very near the target (<1 mm) and does not effect the measurement. A debris signal is easily differentiated from an x-ray signal by its time structure.

The decay time of the transitions was found to vary with pressure in a consistent way. Figure 2.36 shows linear fits of transition **A** coefficients as a function of gas pressure, for the xenon and krypton transitions. Table 2.1 gives the zero-pressure extrapolated lifetime and collisional quenching coefficients for the transitions. As will be discussed later, there is more than one strong transition for the xenon lower level; the 90.2 nm line is the best transition on which to do a lifetime measurement as it is bright and spectrally well separated from other lines. For the other levels, the line listed is the brightest decay. The error values quoted in the table are somewhat larger than the errors in figure 2.36 because they take into account non-statistical errors that appear in the data, manifested by a somewhat larger than standard deviation variation in the lifetime with repeated measurements. This error is probably due to electrical noise pick-up on the detector input to the constant fraction discriminator. Noise on this input will vary the effective threshold level for the photons, and noise with period ≤ the lifetime being measured will result in some distortion of the decay curve since the photon detection probability will vary.

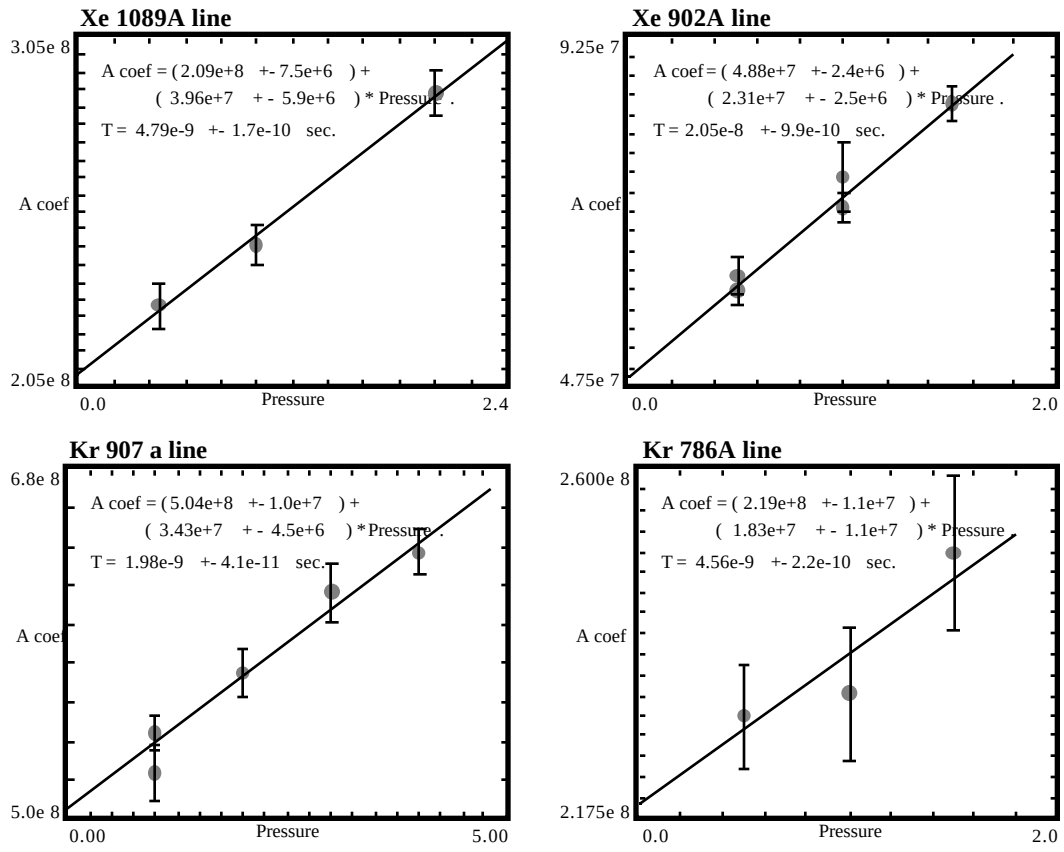

Figure 2.36: Variation of transition **A** coefficient with gas pressure, for the transitions observed.

Level	τ (nsec)	**C**(torr-sec)$^{-1}$	Trans. λ(nm)	Trans. Lower level
Xenon upper laser level:				
$5s^0 5p^6\ ^1S_0$	4.75 ± 0.15	2.8 ± 0.2 x 10^7	**108.8954**	$5s^1 5p^5\ ^1P_1$
Xenon lower laser level:				
$5s^1 5p^5\ ^1P_1$	20.5 ± 2.0	2.3 ± 0.5 x 10^7	**90.1745**	$5s^2 5p^4\ ^3P_0$
Krypton upper laser level:				
$4s^0 4p^6\ ^1S_0$	2.0 ± 0.1	3.4 ± 0.6 x 10^7	**90.7117**	$4s^1 4p^5\ ^1P_1$
Krypton lower laser level:				
$4s^1 4p^5\ ^1P_1$	4.5 ± 0.3	1.8 ± 1.1 x 10^7	**78.5968**	$4s^2 4p^4\ ^1D_2$

Table 2.1: Measured lifetimes and collisional quenching coefficients for the xenon and krypton upper and lower levels. The wavelengths for the Xenon transitions are from Persson et al. [146]. The krypton upper level wavelength is from Agentoft et al. [142], while for the lower level the wavelengths are from Striganov and Sventitskii [178].

The collisional quenching coefficient is stated in terms of (torr-sec)$^{-1}$. This quenching coefficient was found not to vary with excitation intensity (corresponding to the photon counting rate); thus the quenching must be due to collisions with neutral atoms. A collisional cross-section can be estimated using the mean velocity of the atoms:

$$\frac{3}{2} k T = \frac{1}{2} M \mathbf{V}^2 \qquad \mathbf{V} = \sqrt{\frac{3 k T}{M}}$$

$$\sigma_{coll} = \frac{\mathbf{C}}{\left(3.3 \times 10^{16} \ {}^{atoms}/_{cm^3\ torr}\right) \mathbf{V}}$$

$$\approx 3.6 \times 10^{-14}\ cm^2 \ \text{ for Xenon 108.9 nm} \ . \qquad (2.12)$$

This is a very large cross section, corresponding to a collisional radius of ~1 nm, many times the size of the actual atom. This can be understood qualitatively as follows. Consider the case of the 108.9 nm transition, where the transition energy is 11.385 eV, or 91,832 cm^{-1}. The ionization potential of neutral xenon is 12.13 eV, or 97,834 cm^{-1}; thus the xenon laser transition is of an energy just below the ionization potential for neutral xenon. Considering figure 2.37, the process of energy exchange, where the xenon laser level is de-

excited and a ground-state xenon atom is excited, can be accomplished with very little atomic kinetic energy exchange, since many rydberg levels of the neutral atom exist at an excitation energy of ~11.38 eV. Moore [179] lists 6 rydberg levels within 2k**T** ~400 cm^{-1} of 91,832 cm^{-1}. Thus, many states are easily energetically accessible, and the cross section can be high. The energy exchange process consists of polarization of the neutral xenon atom by the Xe III ion, and transfer of the excitation through a quasi-molecular level crossing. For the other laser levels, the situation is similar; since several rydberg levels typically contribute in each case, one would expect the quenching cross sections to be similar for all the levels. For the higher energy transitions, ionization of the neutral xenon is possible. Again one would expect cross sections of similar magnitude since the averaged oscillator strength is continuous above and below the ionization threshold.

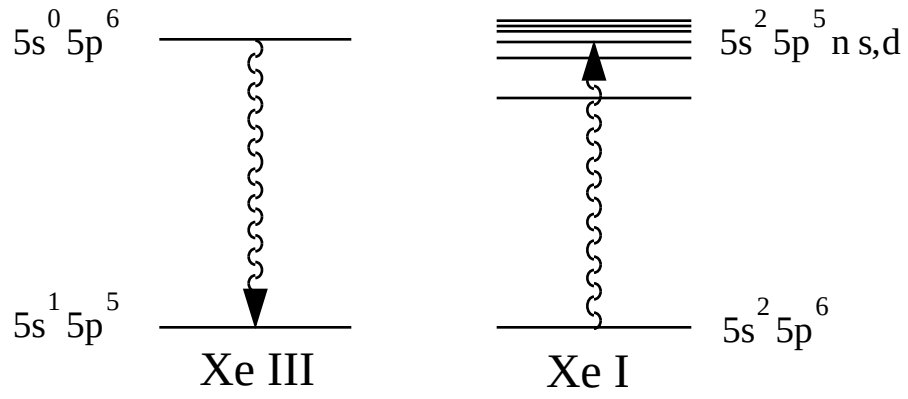

Figure 2.37: Illustration of neutral-gas collisional quenching process.

At higher excitation flux, the observed decay time of the upper laser level becomes longer with increasing laser energy, as shown in figure 2.38. This result is caused by radiative trapping of the 108.9 nm emission. Although the transition is initiallyinverted, repetitive excitation pulses cause a build up of lower level population to a steady state level which destroys the population inversion. The data indicates a maximum opacity of about $\mathbf{e}^{0.15}$. Although it is difficult to compare this value with theoretical estimates due to the non-

local nature of the trapping and the complex geometry of the excited region, the result does indicate that there is significant pumping of the Xe III states, even for plasmas of total energy <1 mJ. This trapping can effect the lifetime measurement; data was always taken at two excitation levels (generally full power and 35% power, attenuated by a colored glass filter), and compared. In general, trapping doesn't affect the data too much-- trapping is smaller at low pressure, and thus the **A** coefficient graph will tend to intercept at the same zero-pressure rate.

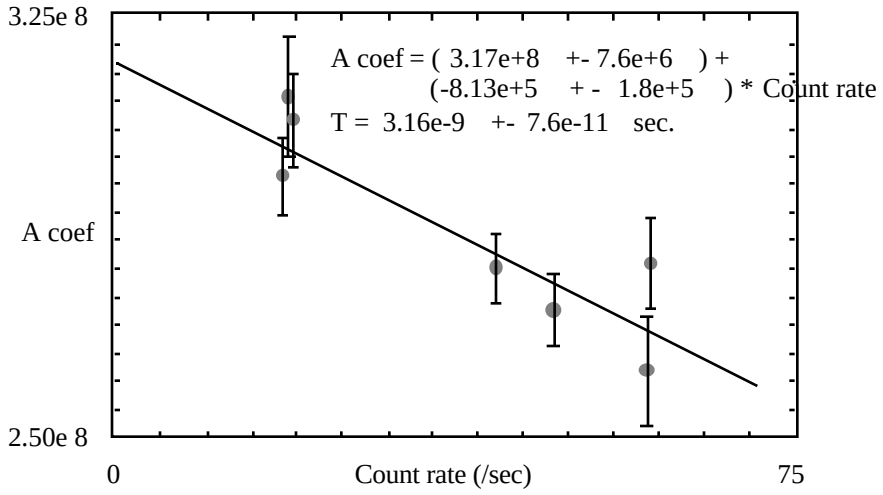

Figure 2.38: Variation of Xenon 108.9 nm transition **A** coefficient with counting rate, corresponding to excitation intensity. The xenon pressure was 3 torr. The reduced **A** coefficient at high excitation is the result of radiative trapping.

Referring to table 2.1, the lifetime of the xenon lower laser level is 20.5 nsec, much longer than the 10 nsec separation between successive excitation pulses. Although there is no fundamental reason why the lifetime of this state is not measurable using the apparatus of figure 2.30, it was found that the statistical error in this measurement was very high. This is because the signal level does not decay very much over the 5-10 nsec interval over which the lifetime can be fit. Thus, the experimental arrangement was modified. A Pockels cell pulse selector and crossed polarizers was used to select a single pulse of the Q-switch burst,

rejecting the others by a factor of ~200. This dramatically reduces the effective pulse repetition rate; thus the laser Q-switch rate was raised to 500 hz. The Pockels cell driver (Bournlea Instruments, Ltd. model 3150) is not capable of running at 500 hz, so a divide by two circuit was added to the Pockels cell variable delay, and the resulting pulse repetition rate was 250 hz. Data was then taken in the usual way by using program MCA (the mixer was not necessary in the trigger channel CFD input). This allowed us to follow the entire decay of the 90.2 nm line for several lifetimes.

To compensate for the somewhat lower count rate, the apparatus was run at a higher proportion of (photons detected / laser pulses). It is necessary in this case to correct the data to compensate for pile-up error. For this correction, one must know the total number of laser pulses used to obtain a given set of data. Consider, for example, that 10,000 pulses were used for a particular data set. Say channel 1 contains 100 counts and channel 2 contains 96 counts. From the data one knows that the chance a photon was detected before channel 2, precluding the possibility of detecting a photon on channel 2, is 100/10,000= 1%. Thus, to compensate for this, one can adjust the channel 2 count to 10,000/(10,000-100)*96 = 96.96 counts. In this way, the data can be adjusted [180,181] such that

$$(N_j)_{adjusted} = (N_j) * \left(\frac{N_{total}}{N_{total} - \sum_{i=1}^{j-1} N_i} \right) . \qquad (2.13)$$

Of course, the statistical weight for each channel is still equal to the original number of counts in that channel, and thus use of this adjustment has its limit. Also, very importantly, one is assuming that the probability distribution for detecting photons, that is determined by the complete data set, is representative of each particular shot; i.e., that all shots in the data set are identical. Pulse-to-pulse energy fluctuations in the laser will cause pile-up error to be more severe for a high-energy pulse than for a low energy pulse, distorting the data in a way that can not be compensated for by equation 2.13 [182,183]. This is why pile-up corrections

were not used for the Q-switch burst data-- the individual pulses are of varying amplitude. However, modest pile-up correction was helpful for the pulse-selected experiment. The only other change made in the equipment was to trigger the SR245 computer interface with every laser pulse, instead of only when a photon was detected. This way the computer can keep track of the total number of laser pulses.

The major problem with the TCPC setup using the Pockels cell is that the Pockels cell is activated by a 8,000 Volt pulse, approximately 5 nsec in duration. This pulse creates severe electrical noise pickup problems, and as mentioned before electrical noise can alter the photon detection threshold of the CFD, causing fluctuations in the data. Electrical noise from the Pockels cell is very severe (typically any BNC cable will pick up 10-100 mV p-p noise pulses from it)-- the problem is made even worse since the MCP output is amplified. Extreme care was taken to avoid ground loops, and to shield all components, placing the GPD 202 amplifier as close to the MCP detector as possible. It was also found necessary to shield the MCP voltage divider box with aluminum foil. Even with these precautions, the data show fluctuations of ~5% in photon count rate. Fortunately the period of these fluctuations is only a few nsec, which is several times shorter than the lifetime being measured. Thus, the fluctuations tended to average out. The error value for the 90.2 nm lifetime reflects the increased uncertainty in the measurement. When measuring shorter lifetimes, the non-pulse-selected setup is superior. Possible improvements to reduce the noise are (1) moving the TCPC setup into a different room from the laser and pulse selector, or (2) to improve the single photon amplitude distribution of the photon detector. Microchannel plates tend to give a wide single photon pulse height distribution that peaks at low amplitude. This means that there are a substantial number of photon pulses of amplitude near the discriminator threshold, and noise can significantly effect the count rate. In contrast, if a photomultiplier tube with a narrow single-photon pulse height distribution, or a specially selected MCP detector with a narrow pulse height distribution, is used, the

threshold can be set so that the count rate is insensitive to noise. The noise will then only effect the zero-crossing trigger timing, slightly degrading the resolution but otherwise not affecting the system.

In conclusion, the technique of time-correlated photon counting has proven to be very useful for measuring the lifetimes of the laser levels. The data obtained was instrumental in determining the feasibility of the xenon laser system. Although I have only used the system to measure lifetimes of interest to me, the system is of great general applicability. The system is relatively simple and inexpensive, consisting of a commercial laser, a spectrometer, and miscellaneous vacuum and electronic equipment. Previous measurements of VUV lifetimes [184,185] used synchrotron radiation sources of limited availability. The measured lifetime data is of use not only for short-wavelength laser studies, but also for comparison with theoretical calculations, and for the identification of transitions. All transitions starting from the same upper level will have the same measured lifetime.

2.4.2 Fluorescence intensity measurements

Another set of experiments I performed at Berkeley was to look at the spectrum of x-ray excited xenon. The reason for doing this was to verify that a population inversion exists in the xenon system. Although the Auger spectroscopy data (figure 2.1) indicates an inversion on the transition, to verify this I measured the fluorescence intensity of the decays of both the upper and the lower laser levels. Figure 2.39 shows the basic scheme. The upper level decays to the lower through the laser transition, and the lower level decays through 5 transitions, all in the VUV, to the ground state configuration of Xenon III. The aggregate intensity of the lower level decays will also reflect the population put into it by decay of the upper level.

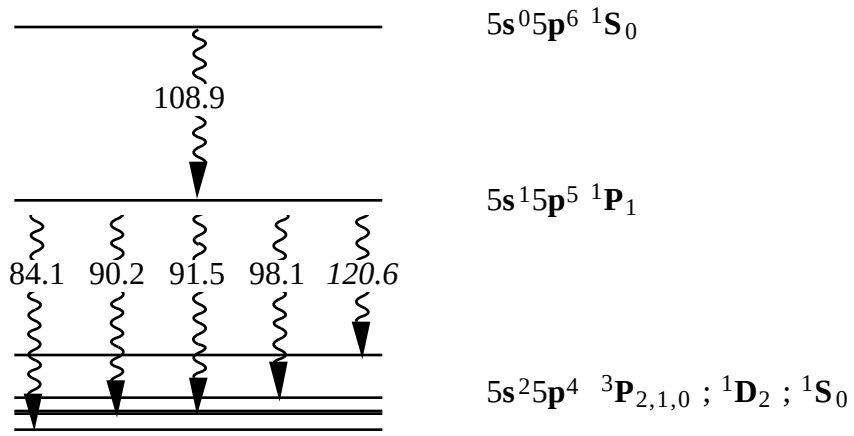

Figure 2.39: Fluorescence decay of the xenon Auger laser levels. Decay wavelengths, in nm, for the major decay routes of the upper and the lower levels are shown. The 120.6 nm transition was not definitively observed in these measurements.

The ionization threshold of xenon corresponds to 101.85 nm, so that four of the decay wavelengths are strongly absorbed by neutral xenon atoms, as well as being below the LiF wavelength cutoff. Since we wish to obtain the absolute intensities of these fluorescence lines, the arrangement used previously for the TCPC is unsuitable. At a pressure of ~1 torr, the absorption length of 90 nm light is ~5 mm. But the observed x-ray pumped region extends from adjacent to the capillary array, to a distance of ~1-2 cm away from it, making it impossible to accurately correct for the self-absorption. Thus, one must use a lower gas pressure to avoid self-absorption. It was found that lowering the gas pressure to a fraction of a torr resulted in signal levels too small to accurately be measured when using the Quantronix 416 laser for the x-ray source. Instead, a Quanta-Ray DCR 2A was used to produce the x-ray plasma. This laser puts out ~500 mJ in a 10 nsec pulse at 10 hz-- an average power of ~5 watts, compared to 50-100 mW for the Quantronix. With this higher power level, it was necessary to move the capillary array window farther from the plasma to avoid debris problems. Also, at the ~0.05 torr pressure used in the target chamber, an intermediate pumping chamber was not required to maintain the pressure at the MCP to

$< 5 \times 10^{-5}$ torr. Thus, the capillary array window was moved closer to the spectrometer slit, ~6.35 cm away from the plasma. Although about half the VUV fluorescence is absorbed after passing through 6.35 cm, the excited region is at a sufficiently well-defined distance to correct for the absorption. An end-view of the target geometry is shown in figure 2.40. At these pressures the debris fluorescence problem is quite severe; thus the plasma was positioned considerably above the viewing aperture position, as shown. The data was taken using the same MacPherson 225 monochromator and FTD 2003 microchannel plate detector as previously, and the amplitude output of the MCP was sampled using a Stanford Research systems model SR250 boxcar integrator, set to a 60 nsec gate so as to catch >90% of the fluorescence from all the lines while avoiding the detection of debris fluorescence.

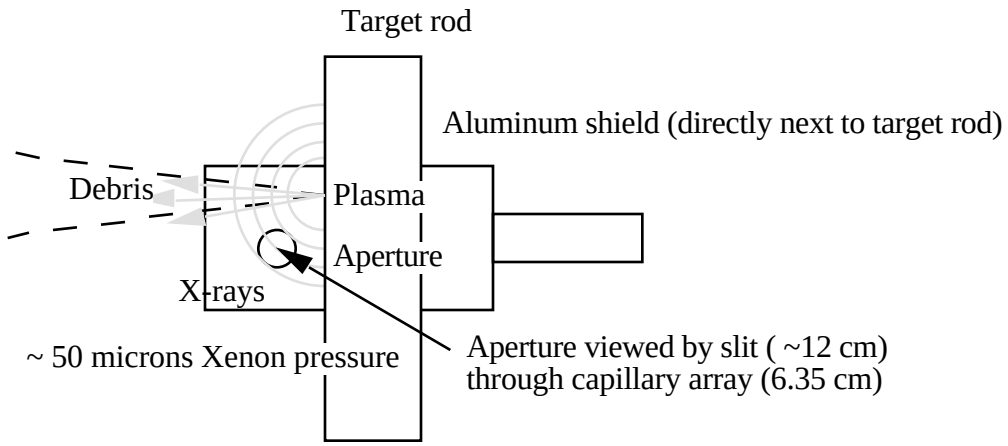

Figure 2.40: End view of target geometry for fluorescence intensity measurement.

Spectral scans were taken in the regions where the fluorescence lines were expected, and the peak intensity of each of the lines was determined. All lines except the 120.6 nm line were clearly visible and spectrally resolved at the 0.15 nm resolution of the monochromator using 50 μm slits. The 120.6 nm line may have been partially obscured by a transition at 120.65 nm, which was itself very dim. The resulting intensity data is shown in table 2.2, along with adjustments for self-absorption and for microchannel plate quantum efficiency.

Transition λ	Intensity	Gas trans.	MCP eff.	Adj. Intensity.
Xenon upper laser level:				
108.8954	1.63±0.23	100%	3.2%	1±0.15
	1.57 ± 0.1			0.96±0.07
				_____
			Average:	1 ± 0.1
Xenon lower laser level:				
84.0151	1.6 ± 0.23	52%	7.1%	0.85±0.1
90.1745	1.45±0.1	50%	6.6%	0.86±0.06
91.5487	0.50±0.07	50%	6.4%	0.307±0.04
98.1097	0.51±0.08	59%	5.4%	0.314±0.04
120.5929	0.1±0.08	100%	1.4%	0.14±0.11
				_____
			Total:	2.5± 0.2

Table 2.2: Fluorescence intensity measurements for the xenon laser transitions. Xenon gas absorption coefficients are from Samson [186], and microchannel plate efficiency is from Martin [163]. The monochromator efficiency is assumed to be constant over the 80-120 nm interval. The adjusted intensity is normalized to the 108.9 nm intensity.

Taking into account the fluorescence cascade, the data indicate a initial population ratio of the upper to the lower level of 1 : 1.5± 0.3, or an inversion ratio (taking into account degeneracies) of 1: 0.5±0.1. Thus, the measurements again indicate that there should indeed be a population inversion. The error value in this measurement does not, however, take into account uncertainties in the MCP quantum efficiency, or variations in monochromator grating efficiency. The MCP error is hard to estimate since there is some variation in efficiency between individual MCP's, and the characteristics of the particular MCP used have not been measured. However, the efficiency curve used is relatively pessimistic for this measurement [187], as the most likely deviation is that the quantum efficiency could have a faster drop-off at long wavelengths. The data does agree quite well with the Auger spectroscopy data, and thus provides further confirmation of a population inversion. As mentioned at the beginning of this chapter, recent work on the spectrum of xenon III has

been published. This work claims that the upper laser level has a total of 10 different decays, due to the fact that the state is heavily mixed. Moreover, the intensity values stated in the table are such that the laser transition is only 22% of the total decay amplitude. If this were the case, my measured decay ratios would indicate that the branching ratio of Auger decay into the laser level would have to be much greater than is consistent with the data of figure 2.1. Also, if the laser transition has such an unfavorable branching ratio, the resulting gain cross- section would be only 22% as large as I used in my calculations. This would mean that, since the gain simulations are reasonably accurate, the x-ray flux assumed in the calculations must be a factor of five too small, which is unlikely. Although many of the transitions (listed in table 2.3) are not in the VUV, I looked in previous spectral data taken using laser-produced plasma excitation. Unfortunately, the system used for the fluorescence intensity measurements can not be run for long periods due to debris clogging, so the only broad spectra I have were taken using the LiF window. Thus, the only two lines the I might possibly see are the 112.4 and 117.3 nm lines. There is no sign of the 112.4 line in any spectra, and although there is a weak line at 118.0 nm, the wavelength does not appear to be correct. There are also other identified Xe III lines at 117.38 and 117.42 nm. Had this tabulation been published while I was running the experiment, it would have been possible to look for some of these lines, and possibly to measure their lifetimes, confirming (or otherwise) their origin. It is most likely the intensity estimates given are not accurate; according to the text, the intensity estimates are "visual estimates of photographic density, and are on a uniform scale only within limited wavelength ranges". Also, a Hartree-Fock code run done for us by the Harris group at Stanford [188] gives a branching ratio of 95% to the laser transition, and one done by M. Chen at LLNL [189] gives a branching ratio of 85%. Although these codes may not include sufficient configuration mixing(the Stanford run says that most of the lower level decay is to the $^1\mathbf{D}_2$ level), the preponderance of evidence is that probably the intensity of the longer wavelength decays is very low, and that most if not

nearly all of the decay is through the laser transition. Table 2.3 is a summary of the known and measured parameters of the laser transitions.

Level	τ (nsec)	**C**(torr-sec)$^{-1}$	λ(nm)	Lower level	B.R.
Xenon upper laser level:					
$5s^0 5p^6\ ^1S_0$	4.75 ± 0.15	2.8 ± 0.2 x 10^7	**108.8954**	$5s^1 5p^5\ ^1P_1$	~1
			353.182	$5s^2 5p^3(^4S)6d\ ^5D_1$	<<1
			194.2913	$5s^2 5p^3(^2P)6s\ ^1P_1$	<<1
			168.4194	$5s^2 5p^3(^2P)6s\ ^3P_1$	<<1
			158.5770	$5s^2 5p^3(^2D)5d\ ^3S_1$	<<1
			142.5999	$5s^2 5p^3(^2P)5d\ ^3P_1$	<<1
			137.5295	$5s^2 5p^3(^2D)6s\ ^3D_1$	<<1
			117.3146	$5s^2 5p^3(^4S)6s\ ^3S_1$	<<1
			112.4428	$5s^2 5p^3(^4S)5d\ ^3D_1$	<<1
			101.6188	$5s^2 5p^3(^4S)5d\ ^5D_1$	<<1
Xenon lower laser level:					
$5s^1 5p^5\ ^1P_1$	20.5 ± 2.0	2.3 ± 0.5 x 10^7	**90.1745**	$5s^2 5p^4\ ^3P_0$	0.34
			84.0151	$5s^2 5p^4\ ^3P_2$	0.34
			91.5487	$5s^2 5p^4\ ^3P_1$	0.12
			98.1097	$5s^2 5p^4\ ^1D_2$	0.13
			120.5929	$5s^2 5p^4\ ^1S_0$	<0.05
Krypton upper laser level:					
$4s^0 4p^6\ ^1S_0$	2.0 ± 0.1	3.4 ± 0.6 x 10^7	**90.7117**	$4s^1 4p^5\ ^1P_1$	~1
Krypton lower laser level:					
$4s^1 4p^5\ ^1P_1$	4.5 ± 0.3	1.8 ± 1.1 x 10^7	**78.5968**	$4s^2 4p^4\ ^1D_2$	~1
			70.4838	$4s^2 4p^4\ ^3P_2$	<1
			73.2259	$4s^2 4p^4\ ^3P_0$	<1
			91.9143	$4s^2 4p^4\ ^1S_0$	<1

Table 2.3: Measured lifetimes, collisional quenching coefficients , and branching ratios for the xenon and krypton upper and lower levels. The wavelengths for the Xenon transitions are from Persson et al. [146]. The krypton upper level wavelength is from Agentoft et al. [142], while for the krypton lower level the wavelengths are from Striganov and Sventitskii [178]. The branching ratios are estimates only, good to within a factor of 2.

2.4.3 Gain measurements with low-energy lasers

Two experiments I did with Máiréad Murnane at UC Berkeley showed evidence of population inversion in the xenon system using much lower energy lasers than the energy of the JANUS laser at LLNL. Although the evidence of gain in these experiments was not as unambiguous as in the LLNL experiment, and in one case was indirect, they do shown that gain can be measured in these VUV transitions using very low energy pump lasers.

The first experiment involved the time-correlated photon counting setup. At one point during the attempt to get the apparatus working well with low background, the laser system was modified to produce 1 mJ pulses in 100 psec. This was done by using the Quantronix 416 laser with the Pockels cell pulse selector to produce 100 psec pulses at 10 hz. This pulse was then passed through a 1/4" diameter Nd:YAG head to amplify the single pulses to ~1-5 mJ. This pulse was then focused onto the target in the usual way, and the usual TCPC setup was used to measure the lifetime. The resulting decay curve is shown in figure 2.41. At the time it was distressing that the lifetime of the transition varies depending on the time interval to which the curve is fit. Just after the excitation pulse, the decay time is very fast, fitting to a decay constant of about 1 nsec. At later times, however, the decay has a much longer time constant of ~5.8 nsec. This 5.8 nsec decay is considerably longer than the natural lifetime of the state, 4.75 nsec. Thus there is radiative trapping of the transition, and the short lifetime at early times is consistent with ASE lifetime shortening of the transition. The gain (or absorption) length necessary for the observed behavior is ~$\mathbf{e}^{1}$, which is reasonable agreement with the gain-length of $\mathbf{e}^{0.5}$ predicted by the program GAIN6 for a 1 mJ point-focus plasma. Thus, looking at the excitation-intensity dependence of transition lifetimes is a possible method for indirectly identifying inverting transitions.

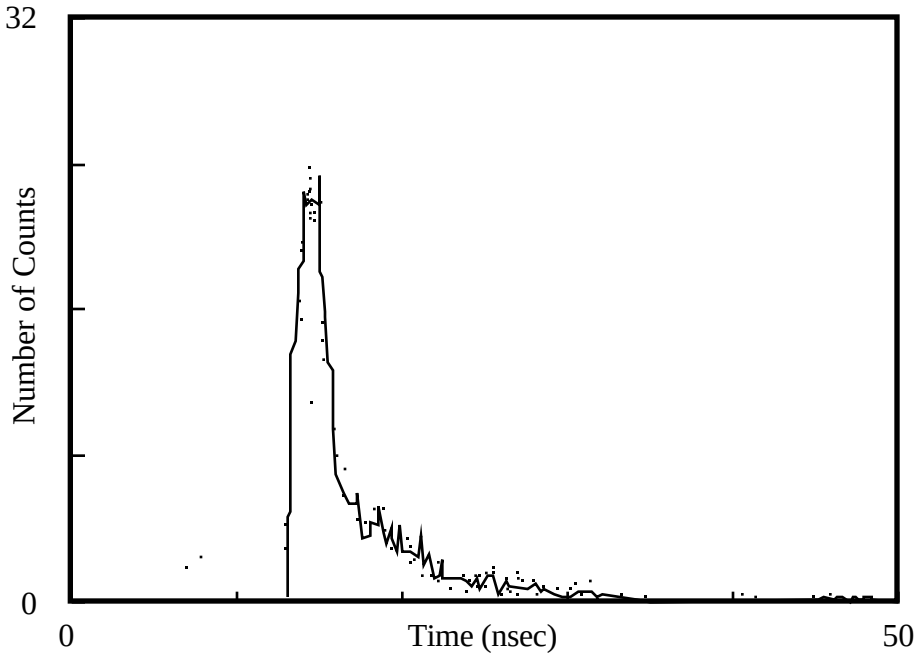

Figure 2.41: TCPC lifetime measurement of the 108.9 nm decay using a single 1 nJ excitation pulse. The xenon pressure was 3 torr. The decay curve fits to a lifetime of 1 nsec at early time, and of 5.8 nsec at later times.

The other experiment showing evidence of gain used the Quanta-ray DCR-2A laser, and two point focuses of ~150 mJ each. The basic setup is shown in figure 2.42. Two beams are incident on either side of the target rod. A chopper wheel was used to, alternately with every shot, fire both, or either one, or neither of the laser beams. The plasma farther from the slit was used as the light source, and preceded by 1.3 nsec the other plasma, which was used as the amplifying medium. In this way the light source would be bright even during the leading edge of the amplifying pulse, in case gain was only present for a short time. The emission was detected by the Acton 551 spectrometer and MCP detector arrangement, but the data was sampled with a SR250 boxcar integrator set to a 2 nsec gate, and the gate time was scanned over the time of the laser pulses to obtain time-resolved data. The Stanford Research Systems SR265 Software was used for data acquisition, and a short external program was used to sort the data into separate graphs for both beams present, the amplifier

only and the light source only. Figure 2.43 shows the resulting data; the first graph is the pulse intensity profiles for each situation, and the second graph is ((Both plasmas) - (light source)) / (amplifier). If gain is present, this parameter will be greater than one, as indeed it is for some period of time. Thus, the experiments indicate gain at early times and absorption at later times, as expected. However, the gain is very small (40%), and thus thus the results are not very conclusive. Plasma light-focusing effects have been known to create spurious gain measurements [190] in these two-plasma measurements. Also, at the time we expected to measure larger gains than those observed. In retrospect, ASE clamping was limiting the measurable gain, as one would expect.

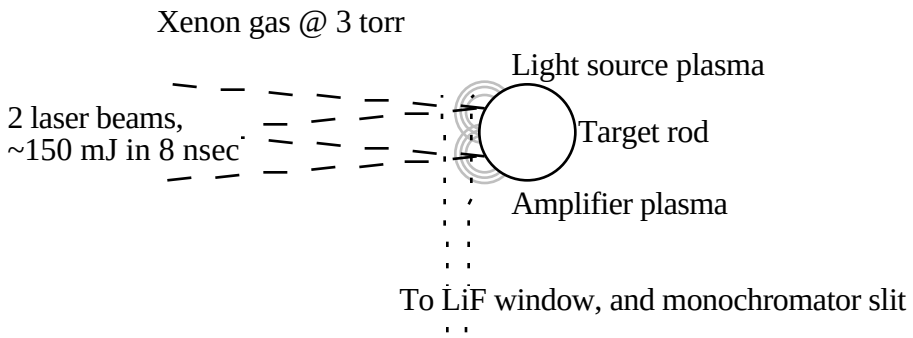

Figure 2.42: Basic two-plasma gain measurement setup.

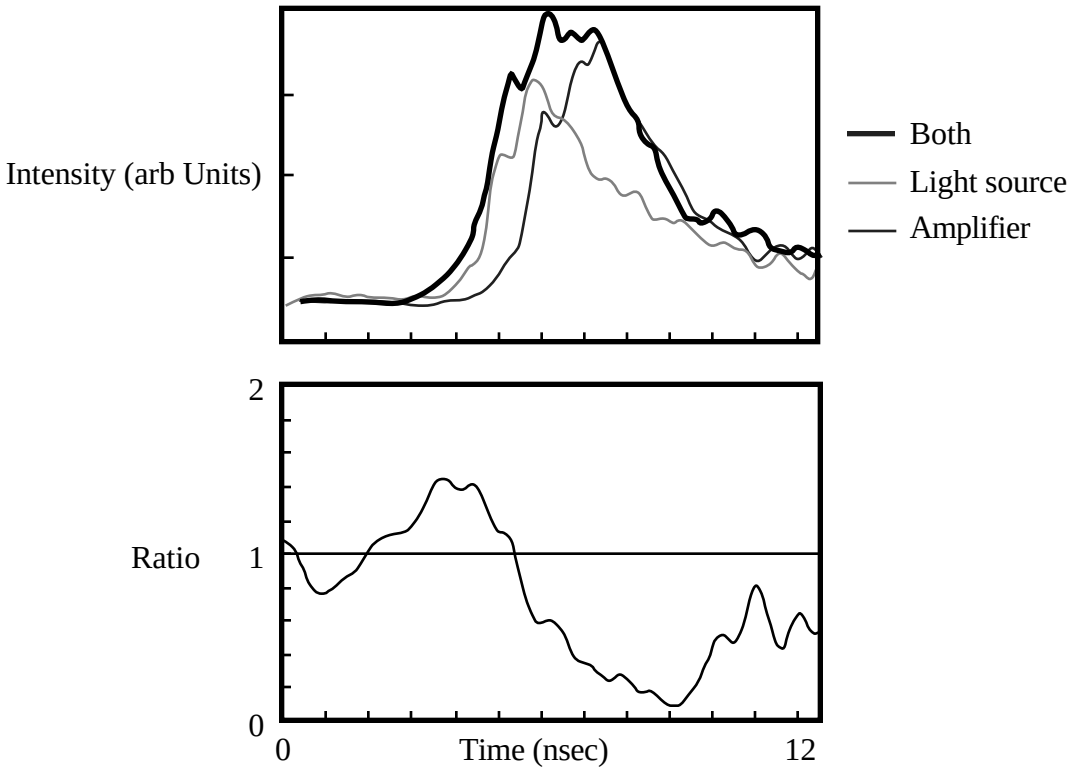

Figure 2.43: Data from two-plasma gain experiment. The top graph is the light intensity for each of the two plasmas, and both plasmas. The bottom curve is ((Both plasmas) - (light source)) / (amplifier), a measure of the gain in the transition, as a function of time (>1 means gain, <1 means absorption).

2.4.4 Conclusion

Small-scale experiments have great utility in short-wavelength laser research. The success of the TCPC experiment illustrates that table-top laser systems can be used to create laser-produced plasmas that are useful in the study of highly excited atoms (or molecules, for that matter) previously only accessible through the use of synchrotron radiation sources. Also, currently available synchrotron sources have pulse-widths much longer than the pulse width of currently available laser plasma sources, making it potentially possible to measure shorter lifetimes with the laser plasma apparatus. Although I have only looked at transitions

of direct relevance to my research, there are many systems for which excited states lifetimes could be measured using this apparatus. This data would be of tremendous use in sorting out complex spectra, and in providing transition probability data for applied physics uses. It would also serve to test atomic physics codes. Also, optical trapping and gain measurements indicate that very modest laser systems are potentially capable of pumping these short-wavelength lasers.

Chapter 3: Photoionization-Pumped X-Ray Lasers

Our successful demonstration of the xenon and krypton lasers has shown that photoionization pumping is a viable method of producing short-wavelength lasers. This fact leads one to consider what to do next. First I will briefly consider future development of the xenon and krypton lasers. Although interesting possibilities exist for making the xenon laser a useful device, even more interesting is the possibility of extending the mechanism of photoionization pumping to shorter wavelengths. The bulk of this chapter is a specific scheme which I have developed.

3.1 Future development of the xenon and krypton lasers

The xenon laser may itself have uses, as a bright source of VUV light for research, and for such applications as the lithographic production of integrated circuits. These applications require the further development of the xenon system, to make it more efficient, and to increase the output intensity. The Harris group at Stanford has done much of this type of work, as was mentioned previously, using traveling-wave excitation. Another possibility is to construction a laser resonator for the xenon laser, to obtain a higher quality output beam. The construction of a resonator is not an easy task, though. The limited gain lifetime makes a very short resonator necessary. Moreover, the relatively low reflectivities (30%-70%, LiF coated Aluminum) for mirrors at 108.9 nm mean that the single pass gain in a resonator must be high to overcome losses. High gain will further reducing the gain lifetime through ASE quenching. Also, the diverging nature of the x-ray source means that, if the gain is high in the region where the resonator extracts energy, the gain will be even higher very near the plasma where it would be difficult for a resonator to efficiently extract the deposited energy. This will result in even shorter ASE reduced gain lifetimes. However, with careful design a resonator may be possible, and since the single-pass gain necessary in

this case would be low compared to that necessary for a traveling-wave excitation, a resonator may make much smaller-scale xenon lasers possible (see figure 3.1). An alternative to very short resonators might be a synchronously-pumped long resonator. In this scheme, most suitable for the krypton laser with its short lower level lifetime, repetitive pulses from an amplified Q-switched, mode-locked laser could be used to repetitively excite the gas with every pass through the resonator (figure 3.2)

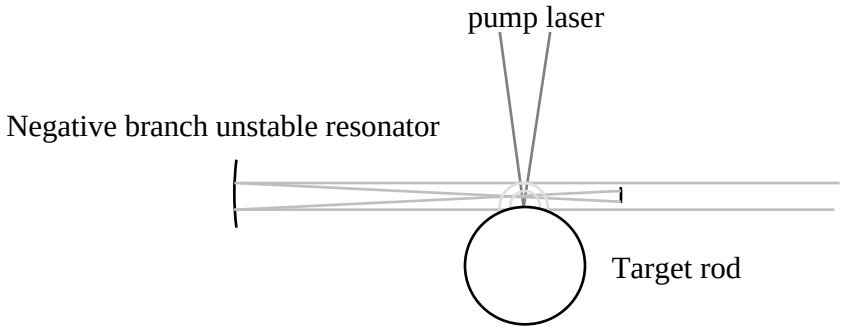

Figure 3.1: Possible conceptual diagram of a xenon laser resonator, using a negative branch unstable resonator [191] to provide efficient output coupling of the light, and mode coupling into the high-gain region very near the plasma.

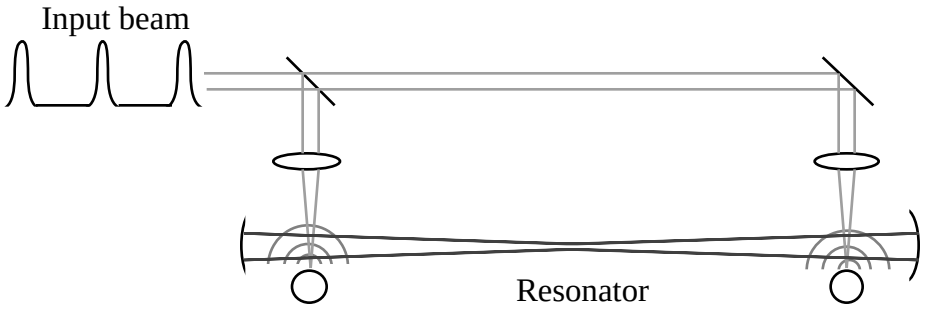

Figure 3.2: Conceptual design of a synchronously-pumped krypton laser resonator design.

3.2 Photoionization-pumped lasers at shorter wavelengths

Extending the scheme of photoionization pumping to make lasers at XUV or soft x-ray wavelengths would be of great interest. There are a number of possible avenues to consider that might be successful.

3.2.1 Other Auger lasers

First, one might consider extending the xenon Auger laser scheme to shorter wavelengths. This was the basis for the krypton scheme. However, the scheme that works in the xenon and krypton cases will not work for argon. The argon atom has an electronic structure of $1\mathbf{s}^2 2\mathbf{s}^2 2\mathbf{p}^6 3\mathbf{s}^2 3\mathbf{p}^6$; thus it has no **d** shell electrons, and is fundamentally different from xenon and krypton. Indeed, examination of the Argon Auger spectrum [192,193] shows no apparent population inversion in this transition, which is actually at a longer wavelength (107.1 nm) than in Krypton. In neon, no population inversion exists on this transition either [50,193]; however, there does exist the inversion between the $\mathbf{1s}^2\ \mathbf{2s}^2\ \mathbf{2p}^4\ {}^3\mathbf{P}$ level and the $\mathbf{1s}^2\ \mathbf{2s}\ \mathbf{2p}^5\ {}^3\mathbf{P}$, as discussed in chapter 1. This scheme remains a viable one that quite probably will work. The problem with it is that keV photons are necessary to inner-shell ionize the neon, and laser-produced plasmas of the type created by small-scale lasers as used for the xenon laser have essentially no emission at ~1 keV (the blackbody temperature is ~10-50 eV). Shorter laser pulses would be able to produce the desired plasma temperature. However, the laser system would then be much more complex than in the case of the xenon laser, and would result in a laser of transition wavelength of 48.8 nm, significantly but not spectacularly shorter in wavelength than in the case of the xenon and krypton transitions.

Another possibility is to isoelectronically scale the Auger scheme to higher ionization stages. For instance, the transition in cesium IV analogous to the xenon III 108.9 nm might invert, at a shorter wavelength due to the increased ionic charge. One could populate the

transition by pre-ionizing the cesium with an excimer laser (the ionization potential of cesium is at 318 nm), and then using a laser-produced plasma x-ray source to create the population inversion. If 248 nm light is used to fully ionize cesium vapor @ 10^{17} cm^{-3}, the recombination time would be ~15 nsec, and an excimer pulse of ~1 Joule could be used to ionize a ~2mm x 2mm cross sectional area (the photoionization cross section @ 248 nm is 6×10^{-20} cm^2 [194]) which could then be photoionized with plasma x-rays. Another possibility is that shake-off processes will create a substantial population inversion in Cs IV through ionization of neutral cesium. In xenon, shake-off happens ~21% of the time as a result of inner-shell ionization [195]. However, probably the shake-off will only populate the less-excited levels of cesium IV since the upper levels won't be energetically accessible. One problem with developing this idea of Auger schemes in ions is the lack not only of Auger spectra but even of energy level positions for these ionic levels. Extrapolating from ionization potentials and known energy levels, one can estimate that the equivalent Auger transition in cesium IV would be in the wavelength region of 60-80 nm. One potential problem with the system might be electron quenching since the electron density would be the similar to the atom density. However, the xenon laser seems reasonably robust against electron collisional effects, and quenching may not be a problem.

It may even be possible to extend the scheme to even shorter wavelengths using highly ionized atoms in a laser-produced plasma. In this case, it is possible that the same plasma might produce the ions and the pump x-rays. Extrapolation of other proven photoionization-pumped schemes to shorter wavelengths has been considered theoretically [67], and should be considered for these Auger lasers. The other possibility for creating more highly ionized atoms is to used cascaded Auger decay [65].

3.2.2 Direct photoionization-pumped schemes

One disadvantage of the Auger-decay-pumped schemes is that the radiative transition is a $\Delta n = 0$ transition, i.e. 5**s**-5**p** or 4**s**-4**p**, etc. If one considers smaller atoms such as neon with generally larger energy spacing between the levels, the energy gap between shells becomes wider much more quickly than the transition energies of the intra-shell transitions. Thus the scheme does not scale favorably to very short wavelengths. This fact leads one to consider schemes where the laser transition is an inter-shell transition. The sodium scheme proposed by Duguay (discussed in chapter 1) is an obvious case to consider. The problem with this scheme is electron collisional population of the lower laser level, which could be ameliorated by using very short (psec) excitation pulses to produce a population inversion in a time short compared to the electron collisional excitation time. Advances in modern ultra-short pulse laser technology may finally make the sodium scheme practical. The major disadvantage of this scheme is that is is not scaleable to shorter wavelengths. It will not work in highly ionized plasmas since the electron density is very high and the ionization stage populations will be dominated by closed shell ion stages (as in the case of the neon-like selenium x-ray laser). Creating a plasma with more ions in the sodium-like rather than in the neon-like ion stage would appear to be impossible, and since the neon-like ground state configuration is the lower laser level in the Duguay scheme, a population inversion on this transition in highly ionized species would be difficult.

Next, one might consider the more general case of inner-shell ionization lasers. The "quasi-stationary" population inversion schemes discussed in chapter 1 (figure 1.3) have not been seriously considered since the work of Axelrod [48]. He showed that even under quasi-stationary conditions, the population inversion would last at most 50 fsec, due to depletion of the atoms being ionized. In 1976 when this work was published, the development of ultrashort pulse lasers was in its infancy, and pump lasers of pulse duration ≤100 fsec were considered fantasy. Now, Máiréad Murnane in our group has built a laser

system capable of generating 2.5 mJ in 100 fsec, or a peak power of ~25 GW [196], and Maine et al. [197] have developed lasers of pulse length of ~1 psec with peak powers of ~1 TW. In the near future, relatively modest laser systems will be developed which are expected to provide more than 10 TW peak power in pulses <100 fsec. Moreover, Máiréad Murnane has shown that these ultrashort laser pulses can be used to produce very short x-ray pulses [198]. Thus, the new generation of laser systems now being developed may be capable of producing population inversions in some of these inner-shell pumped laser systems.

When one considers the pump laser requirements of these quasi-stationary laser schemes, one finds that even lasers of 10 TW would probably be inadequate to produce a laser. The sulfur scheme considered by Axelrod had a transition wavelength of 0.54 nm. This is a very short wavelength, and thus one would expect it to have very high power requirements by equation 1.38. The logical next step is to consider similar systems with a longer transition wavelength, and thus more modest power requirements. The problem with this approach is that the "quasi-stationary" inversion scheme requires electrons in the **n**=3 shell to have an Auger cascade, and thus this scheme is not applicable for atoms much lighter than sulfur. However, even the quasi-stationary schemes do not allow for population inversions for times of >50 fsec, and thus it makes sense to consider self-terminating inversions in the lighter atoms. A search of the literature revealed no published analysis of such systems, but my analysis shows that such systems may indeed be a feasible way of implementing a photoionization-pumped x-ray laser.

3.3 X-ray lasers on K-α transitions

In this section I will discuss the possibility of creating a population inversion on the K-α transitions of the light elements. Although I will also discuss L-shell transitions, the reason that I am concentrating on K-shell transitions is that they have the best fluorescence

yields at a given wavelength [199], and this translates into the highest gain cross-section at a given wavelength.

3.3.1 General introduction

The basic energy level diagram for such a K-α laser system is shown in figure 3.3. X-rays incident onto atoms can ionize a 1**s** electron from the atom, provided the x-rays are sufficiently energetic to do so. Given the ionization cross section behavior as in figure 1.1, a population inversion will result between the $(1\mathbf{s})^{-1}$ level and the $(2\mathbf{p})^{-1}$ level, and laser action can occur.

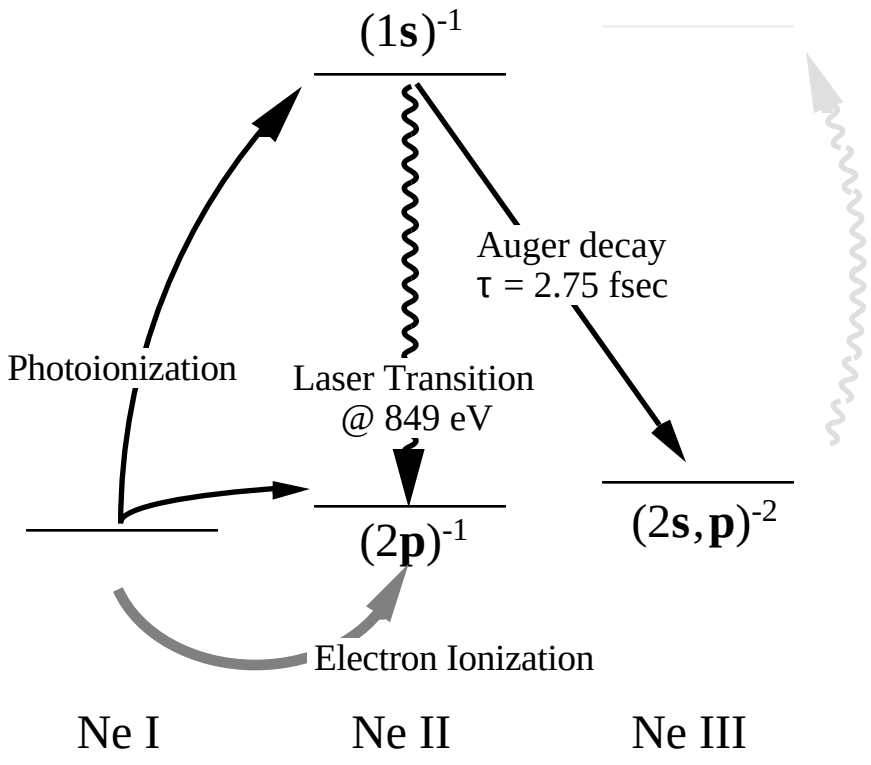

Figure 3.3: Basic energy level diagram of lasers on K-α transitions-- the case of neon is shown here. X-rays ionize 1**s** electrons from a neutral atom, and the laser transition is $(1\mathbf{s})^{-1} \rightarrow (2\mathbf{p})^{-1}$. Auger decay provides rapid depletion of the upper level, while electron ionization provides rapid filling of the lower level.

For all but the alkali atoms, upper laser level can usually decay much more quickly through Auger decay than through the radiative transition. The Auger decay is a very rapid depletion of the upper laser level, populating various states of the doubly-ionized species. The lower laser level is the ground state of the ion, which does not decay any further. The inversion is thus self-terminating, unless recombination of the ions is very fast. One crucial question is whether the Auger decay fills any levels that have a resonance transition at the same wavelength as the laser transition. If this were the case, then the Auger decay would effectively fill the lower laser level, terminating the inversion on a time scale comparable to the Auger decay lifetime. If this is not the case, the transition would terminate on the time scale of the radiative lifetime (where the radiative lifetime is defined by $\tau_{RAD} = 1/A_{21}$, but is not directly measurable). The answer to this question is that for light atoms, the extra atomic charge in the Auger product states shifts the $(1\mathbf{s})^{-1} \rightarrow (2\mathbf{p})^{-1}$ transition in these atoms sufficiently that these transitions are not in resonance with the laser transition [200]. The transition linewidth for an atomic transition is naturally broadened, with a linewidth given by equation 1.24. For example, the neon K-α transition has a linewidth of 0.24 eV [201,202], corresponding to an Auger rate of 2.75 fsec. The transition is at an energy of 848.6 eV, while the transitions of the Auger product states are at energies [200,203] of 854.1 ($^3\mathbf{P}$-$^3\mathbf{P}$), 854.8 ($^1\mathbf{P}$-$^1\mathbf{D}$) and 849.8 ($^1\mathbf{P}$-$^1\mathbf{S}$) eV for the Neon III $(2\mathbf{p})^{-2}$ configuration, and at even higher energies for Auger product states missing one or two 2**s** electrons. All these transitions are separated by several linewidths from the laser transition.

Given that the Auger decay is solely a depletion of the upper level and does not fill the lower level, we can define a self-terminating inversion time of:

$$\tau_{ST} = \tau_{RAD} \ln\left(\frac{g_{lower}}{g_{upper}} + 1\right) , \qquad (3.1)$$

where the self-terminating lifetime is determined by the radiative lifetime and the upper and the lower level degeneracies. This expression is the time required for the population

inversion of a transition to fall below zero given an initial population solely in the upper state.

Since the upper level is rapidly depleted, it must be pumped by a very intense flux of x-rays. When pumping the laser with x-rays above the ionization threshold of the K shell, most of the x-rays ionize the K-shell electrons populating the upper level. However, the ionization cross section for outer-shell electrons is not zero at these x-ray energies; it is generally 1-2 orders of magnitude smaller than the inner-shell cross section. However,since the lower laser level does not decay, intense pumping of the laser with x-rays will eventually fill the lower level. If we define $\mathbf{R}_{th}$ as the ratio of the inner-shell to the outer-shell cross section above the inner-shell ionization threshold, we can then define another timescale for the termination of the inversion:

$$\tau_F = \tau_{AUGER} R_{th} \left(\frac{g_{lower}}{g_{upper}} \right) , \qquad (3.2)$$

which is the time necessary for the inversion to go to zero assuming x-ray pumping at constant intensity starting at t=0, and neglecting radiative decay.

Table 3.1 gives the relevant parameters for the atoms from boron to neon. The situation is complicated somewhat by the fact that some inner-shell photoionization-pumped levels have no allowed radiative decay, and thus only decay through Auger processes (a few are even metastable). The radiative lifetime shown is that of the levels which do decay, and the degeneracies must be taken into account when calculating the radiative rate from the fluorescence yield [204] and the Auger linewidth [201,202], as was done here. The only transition in the table for which the Auger linewidth has been measured is neon. The others are calculated Auger rates, but for neon agreement between calculation and experiment is excellent. The degeneracy factors must also be taken into account for the photoionization cross section ratio $\mathbf{R}_{th}$. The lower level photoionization cross section only considers the 2**p**

subshell cross section; in the x-ray energy range of interest, the 2**s** subshell cross section is generally larger, but this level does not correspond to the lower laser level.

Element	hν (eV)	τ_{AUGER}	τ_{RAD}	$\mathbf{g}_{PI}$	$\mathbf{g}_{upper}$	$\mathbf{g}_{lower}$	$\mathbf{R}_{th}$	τ_{ST}	τ_{F}
B	183	10.2	1500	12	3	1	99	430	340
C	277	10.3	1230	18	6	6	47	850	480
N	392	7.03	510	8	3	9	32	710	670
O	525	4.57	550	18	18	20	62	410	310
F	677	3.32	255	12	12	15	50	210	210
Ne	849	2.75	152	2	2	6	37	210	310

Table 3.1: Comparison of K-α laser parameters for the light elements. All times are in fsec. The columns are : (1) Transition energy in eV [199], (2) Auger lifetime = $1/\mathbf{A}_{AUGER}$ [201,202], (3) Radiative lifetime = $1/\mathbf{A}_{RAD}$ [204], (4) The total degeneracy of photoionization-populated levels [179], (5) Degeneracy of PI populated levels which have allowed radiative transitions (the upper laser level), (6) Degeneracy of lower laser levels, (7) Ratio of photoionization cross sections for the upper and the lower laser levels [205], (8) Self-terminating inversion lifetime, and (9) Lower level filling inversion lifetime.

On examining the data, the most favorable atom for sustaining an inversion seems to be nitrogen. However, the most striking aspect of these numbers is the lack of variation. There is a factor of 4 variation in transition energy, and a factor of 10 variation of the radiative rates; however, the time for which an inversion could be sustained (the lesser of τ_{ST} and τ_{F}) varies only by a factor of 3. In all cases, excitation pulses on order of 100 fsec should be capable of producing a population inversion.

There are of course other factors which determine the relative feasibility of the various systems. The gain cross section for the transition, assuming atomic linewidths, is given by equations 1.22 and 1.26, and is simply

$$\sigma_g = \frac{\lambda^2}{2\pi}\frac{\tau_{total}}{\tau_{RAD}} = \frac{\lambda^2}{2\pi}\omega_f \quad , \tag{3.3}$$

where ω_f is the fluorescence yield. The gain cross section will vary considerably among the elements, determining the peak power necessary for a population inversion. Another consideration is that computer models indicate that the primary inversion-limiting process is actually electron ionization, and not any of the processes tabulated in table 3.1. The photoionization and Auger decay processes both liberate energetic free electrons. The electrons can collide with neutral atoms, ionizing them and, more often than not, creating an ion in the lower laser level. Thus, the magnitude of the electron ionization cross section is important; this will tend to favor the more closed-shell atoms such as neon, which have a high outer-shell ionization potential [160].

Another very important consideration is the actual level linewidth. The parameters of table 3.1 are for free atoms. The only species which actually normally exists as a free atom is neon; boron and carbon are solids, while Nitrogen, Oxygen, and Fluorine are diatomic molecules. Since the x-ray transition is an outer-shell to inner-shell transition, when the outer-shell electron characteristics change, as they to for a solid or molecular species, the x-ray transition line shape changes. As a rule, free atoms have the narrowest linewidth, limited only by the natural lifetime broadening. Since the gain cross section varies inversely with linewidth (equations 1.25, 1.30), the wider the linewidth, the lower the gain cross section, and the more difficult it will be to make a laser. It may be possible to obtain free atoms by vaporizing a solid or dissociating a molecular gas just before x-ray laser pumping occurs. However, this technique would add a tremendous technical complication to the experiment, as well as requiring substantial experimental development.

Solids typically have large x-ray linewidths on order of the valence band widths (~10 eV [206,207]), compared with natural linewidths of ~0.1 eV (from table 3.1 and equation 1.24). Thus the gain cross section is much reduced. Also, at solid densities, the ejected photoelectrons and Auger electrons lose their energy through collisions on a time scale of a few fsec. The net result of the two effects is that in solids, very high peak intensities with

risetimes on the order of the Auger lifetime would be necessary to produce a population inversion. This is not yet technologically feasible.

Molecules have an x-ray emission structure that reflects the molecule's band structure. Although molecular bands are composed of discrete vibrational levels, the x-ray transition is split into many subcomponents, and thus is much wider than in the atomic case. Also, the atomic 2**p** orbital character that results in the x-ray emission is usually split into several molecular orbitals, further spreading out the x-ray emission. Rotational splitting is much smaller than the natural linewidth, and is thus not important. The complexity of the emission spectrum increases rapidly with complexity of the molecule; for complex molecules the emission spectrum is usually of a width comparable to solid-state x-ray emission [208]. For simple molecules with high symmetry, the broadening can be moderate. Thus certain molecules (CO_2, CH_4, N_2, O_2, F_2) are possible candidates for these schemes. However, I shall first consider the case of atomic neon gas, since it would have the narrowest linewidth.

3.3.2 Simulation of a laser on the neon K-α transition

As was mentioned in the previous section, the determining process limiting the time duration of the population inversion is the process of electron collisional ionization. If the density of neon gas is kept sufficiently low, electron ionization rates can be kept slow enough to ameliorate the ionization problem, and the inversion would terminate on the τ_{ST} and τ_F time scales of table 3.1. However, the power requirements for making a laser scale inversely with the density of the neon. Ignoring the subtleties of the laser system and the fact that the inversion is self-terminating, one can write the gain per unit length as:

$$\gamma = \sigma_{1s} \left(\frac{I_{x\text{-}ray}}{h\nu_{pump}} \right) N_{neon}\, \tau_{upper}\, \sigma_{gain} \quad , \qquad (3.4)$$

while the absorption due to outer-shell ionization at the laser wavelength is $N_{neon}\ \sigma_{abs}$, giving a net gain of

$$\gamma_{net} = N_{neon}\ \sigma_{abs}\left(\frac{I}{I_{th}} - 1\right)\ , \text{where}$$

$$I_{th} = \frac{\sigma_{abs}}{\sigma_{1s}}\frac{h\nu_{pump}}{\tau_{upper}}\frac{1}{\sigma_{gain}}\ , \qquad (3.5)$$

where $\mathbf{I}_{th}$ is the threshold pump intensity required to show net gain, which is a function of the absorption cross section at the laser wavelength, the 1**s** electron photoionization cross section, the pump photon energy, the lifetime of the upper laser level, and the gain cross section. The threshold intensity is independent of the density of neon gas that is being illuminated; for neon it is about 10^{13} W/cm^2 [209]. The absolute gain, however, is proportional to the density of neon, and thus at lower density a longer length, with the same minimum flux intensity, is needed to obtain a given gain-length. Thus, total power requirements rapidly increase with decreasing density of neon. So a maximum initial density of neon is imperative to make this laser scheme practical. What happens to this energy is that the x-rays penetrate a farther distance into the neon, and thus the cross sectional area of the gain region becomes larger.

One way of using a high density of neon while ameliorating the electron ionization problem might be to "dilute" the neon gas in hydrogen, imbedding the atoms in a matrix of frozen molecular hydrogen. The reason behind this is that at the ~1 keV photon energies of the pump and laser wavelengths, hydrogen is practically transparent to x-rays. At the neon inner-shell threshold, the ionization cross section of molecular hydrogen is 4 x 10^{-23} cm^2, while the neon ionization cross section is 3 x 10^{-19} cm^2. Even below the neon threshold at the laser transition energy, the absorption cross section for neon is 2.4 x 10^{-20} cm^2. This means that neon can be diluted in hydrogen to densities of well under 1% and still the hydrogen will have insignificant absorption at both the x-ray pump wavelength and at the laser wavelength. The advantage of doing this is that the electron ionization cross sections do not have the same behavior as the photoionization cross sections; the electron ionization cross sections for hydrogen and neon are roughly of similar magnitude(~10^{-16} cm^2 at peak

~100 eV). Thus, using dilution, one can create a situation where most of the x-ray energy is absorbed by the neon, and most of the electron kinetic energy is absorbed by the hydrogen. As the electrons lose energy, new electrons are ionized from the hydrogen at near-threshold kinetic energies (~10 eV); however, most of these new electrons have insufficient energy to ionize neon (the ionization potential for hydrogen is 15.4 eV, while that of neon is 21.6 eV).

The disadvantage of this dilution scheme is that cryogenic techniques are needed to construct a solid hydrogen-neon target. However, both solid hydrogen and solid neon targets have in the past been used for laser-produced plasma and inertial confinement fusion experiments [81,210]. The boiling points of neon and of hydrogen are very similar (Ne 27 K, H_2 20 K); thus, it should be possible to construct a suitable target by freezing the appropriate neon-hydrogen gas mixture onto a cooled substrate. The frozen layer need only be 10-100 μm thick, since geometrical divergence of the x-ray flux away from the ~10 μm wide pump plasma will mean that the population inversion will occur only very close to the target.

Since the electron impact ionization is impossible to predict accurately in an analytical model, I developed a computer model (XRAYLASER) of this system to prove the feasibility of the scheme. The model is based on the level diagram of 3.3. Five atomic "levels" are used in the scheme: the ground state neon, the upper $(1\mathbf{s})^{-1}$ and lower $(2\mathbf{p})^{-1}$ laser levels, the neon $(2\mathbf{s})^{-1}$ level, and another level representing all Auger product states. The $(2\mathbf{p})^{-1}$ level actually consists of two fine-structure components-- the $^2\mathbf{P}_{1/2}$ and $^2\mathbf{P}_{3/2}$ levels. However, the two levels are separated by 0.097 eV [179], which is considerably smaller than the transition linewidth of 0.24 eV, and thus these two components can be considered as one combined level. Photoionization pumps the upper and lower laser levels and the $(2\mathbf{s})^{-1}$ level according to numerically input cross sections. Photoionization of the hydrogen buffer is also taken into account. The molecular nature of the hydrogen is approximately taken into account by

depleting the ground state hydrogen at half the rate of ionization, corresponding to ionization of one of the two hydrogen atoms in the molecule.

The basic experimental geometry considered in the model is illustrated in figure 3.4. The x-ray source is modeled as a blackbody emitter of time-varying temperature, in close proximity to the pumped region with a thin filter of 3 μm beryllium separating the two regions. The blackbody emitter corresponds to the laser heated region, which is a thin (~200-500 Å, the absorption depth for the visible laser light) layer deposited onto the beryllium, with the neon-hydrogen mixture frozen onto the other side. The x-ray emitter would be a high-Z material chosen to have an emission spectrum appropriate to pumping the neon inner-shell transition. For incident laser pulses of <100 fsec, the x-ray emitter will stay intact and at solid density; the expansion velocity of the heated plasma layer would be ~1Å/fsec and thus there is insufficient time for expansion to significantly effect the plasma [211]. The beryllium acts to absorb low energy x-rays which are capable only of producing outer-shell ionization, and thus are detrimental to the creation of a population inversion. The beryllium also separates the hot x-ray region from the laser region, so that thermal ionization of the neon does not take place. Electrons would have to have an energy of $>10^4$ eV to transverse 3 μm in the ~50 fsec timescale of the population inversion, but the plasma temperature is < 1 keV.

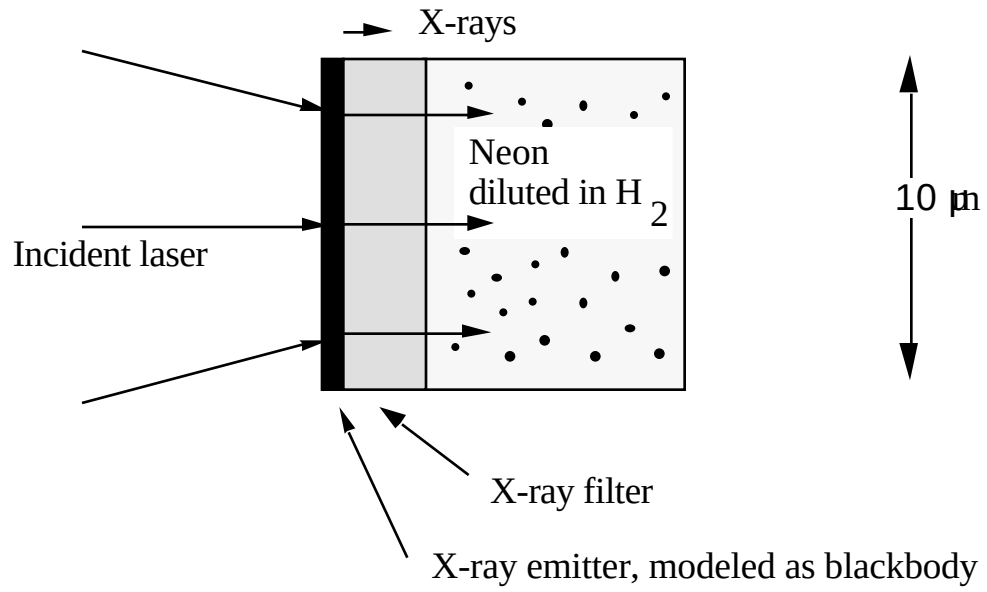

Figure 3.4: Basic experimental geometry of the neon K-α laser.

The temperature function T(t) for the plasma that is used in the simulation is:

$$T(t) = C\left(\int_{t'=-\infty}^{t} \mathrm{sech}^2(1.76\, t'/\tau)\, dt'\right)^{4/9}, \qquad (3.6)$$

where **t** is the FWHM of the heating pulse, assumed to be the **sech**^{2} pulse shape typically generated by ultrashort pulse lasers. The temperature varies as the integrated energy to the $^4/_9$ power, the exponent obtained from an analytical model of the laser heating of solids [212]. The $^4/_9$ exponent also agrees with the numerical simulations of Máiréad Murnane [211], and her model also shows that during the time of the incident laser pulse the plasma temperature continues to rise with the cumulative flux on target. Thus equation 3.6 should be a good model of the plasma temperature, and the x-ray flux as a function of time is then calculated using the usual blackbody formula [26].

Electron ionization in the neon-hydrogen mix is modeled using numerical electron distribution array. Photoionization and Auger decay place electrons into the appropriate

energy bins in the array. Electron collisional ionization is taken into account using numerically input electron ionization cross sections. The electron collisional cross sections to the neon $(2\mathbf{s})^{-1}$ and $(2\mathbf{p})^{-1}$ levels and for hydrogen are used to calculate collisional ionization rates as a function of electron energy. The secondary electron distribution for each ionization process is assumed to have the same energy distribution as the corresponding photoionization cross section; this assumption is justified in the dipole electron ionization approximation for electrons of energy high compared to the ionization potential, and is assumed true for all electrons in this model. From the secondary electron distribution one can also estimate the average energy loss per collision, and thus obtain a cooling rate, in eV/fsec, as a function of electron energy for the electrons. Each bin in the electron distribution is cooled to lower energies, and the appropriate number of secondary electrons, based on the total energy lost in the electron cooling, is added according to the assumed secondary electron distribution. This procedure is done for the neon $(2\mathbf{s})^{-1}$ and $(2\mathbf{p})^{-1}$ levels, and for the hydrogen.

The Spitzer electron self-collision time (corresponding to the thermalization time due to electron-electron collisions) is [213] $t_c = 11.4 \sqrt{A\,T^3}/nZ^4 \ln\Lambda$ sec. This corresponds to a time of 30 fsec for a typical electron density of 10^{20} cm^{-3} and temperature 10 eV for the completely cooled electrons. Thus some thermalization takes place for these low-energy electrons. However, for the ejected electrons of energy ~500 eV, the thermalization time is several picoseconds. This compares with the electron energy loss rate in hydrogen of ~35 eV/fsec, so that inelastic collisions in the hydrogen cool the electrons to low temperature in 10 - 30 fsec. Thus, electron thermalization is only important when the electrons are insufficiently energetic to cause any secondary ionization, and is therefore neglected in the model.

The atomic parameters necessary for the model were obtained from compilations of published experimental and theoretical data. The measured spectral linewidth (0.24 eV) of

the neon K-α transition yields an Auger rate of $(2.7\ \text{fsec})^{-1} \pm 5\%$ [202]. The experimental radiative yield (0.018) determines the radiative rate to be $(150\ \text{fsec})^{-1} \pm 10\%$ [204]. The subshell photoionization cross sections are derived from Yeh and Lindau [205], normalized to the experimental data from Henke et al. [209] and Berkowitz [214]. They are shown in figure 3.5. The electron ionization cross sections are taken from Tawara and Kato [160], with subshell ionization according to the Lotz formula [215]. The cross sections are accurate to ~5-10%. The x-ray transition energy is 848.6 eV [216]. Theoretical calculations for the transition energies of the Ne^{++} Auger product states [200,217] confirm that this resonant absorption is many linewidths removed from the laser transition. Since only one average Auger product state was considered in the model, an average Auger electron ejection energy was used in the simulation, determined to be 790 eV using Auger branching ratios and energies from Bhalla et. al. [217].

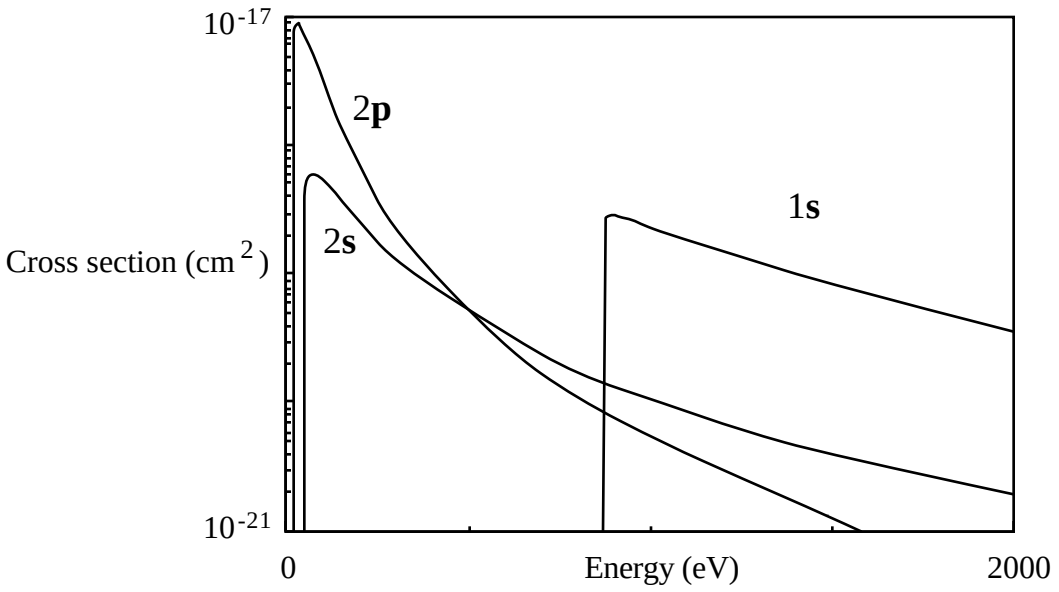

Figure 3.5: Neon 1**s**, 2**s**, and 2**p** subshell photoionization cross sections [205,209].

The model is thus a rate equation model where photoionization populates the Neon $(1\mathbf{s})^{-1}$, $(2\mathbf{s})^{-1}$, and $(2\mathbf{p})^{-1}$ levels, and the ionized hydrogen level, while depleting the neutral

species and ionizing electrons. Electron ionization populates the Neon $(2\mathbf{s})^{-1}$ and $(2\mathbf{p})^{-1}$ levels, and the ionized hydrogen level, also depleting the neutral species and ionizing more electrons. Auger decay depletes the Neon $(1\mathbf{s})^{-1}$ level, populating the Auger level and creating electrons. And finally radiative decay transfers population from the $(1\mathbf{s})^{-1}$ to the $(2\mathbf{p})^{-1}$ level. The results of a simulation are shown in figure 3.6. Shown are the blackbody temperature, the gain at line center, and the $(1\mathbf{s})^{-1}$, $(2\mathbf{s})^{-1}$, and $(2\mathbf{p})^{-1}$, and Auger level densities, all as a function of time, assuming a 50 fsec FWHM pump pulse centered at time t=0, with a peak blackbody temperature of 600 eV. The neon density was 10^{20} cm^{-3}, diluted in solid H_2 at a density of 2.1 x 10^{22} cm^{-3}. With these parameters, a peak gain of 10 cm^{-1} can be obtained, with a total time duration of the gain of ~50 fsec. The pumping flux is ~4 times that necessary to exceed the gain threshold. The peak of laser gain occurs just after the peak of the pump pulse, at t= 11 fsec. At this time, the plasma temperature is 500 eV, and the ratio of electron ionization to photoionization to radiative decay rates into the lower $(2\mathbf{p})^{-1}$ level is approximately 9 : 3 : 1. Thus, electron ionization is the dominant process limiting the time duration of the population inversion. The blackbody radiation intensity is 6.7 x 10^{15} W/cm^2, and the intensity within the range of 870-1350 eV, where the neon inner-shell cross section is highest, is 1.6 x 10^{15} W/cm^2. Thus, 20-25% of the radiation from the blackbody emitter is useful for producing the population inversion-- figure 3.7 illustrates the good overlap between the x-ray emission and the absorption. The total electron density is 7.5 x 10^{19} cm^{-3}, with a mean temperature of 22 eV. The neon is about 3.5% ionized, and the hydrogen is about 0.2% ionized. The beryllium filter at this point has absorbed an average of ~8 eV per atom in the region near the x-ray emitter, and ~2 eV per atom in the region near the neon. Thus, although the filter is partially ionized, the energy deposition falls far short of the 27.5 eV per atom necessary to strip both outer shell electrons from beryllium, and the beryllium will still function to filter the x-ray emission. Thermal conduction of heat from the beryllium will also cause negligible ionization of the neon.

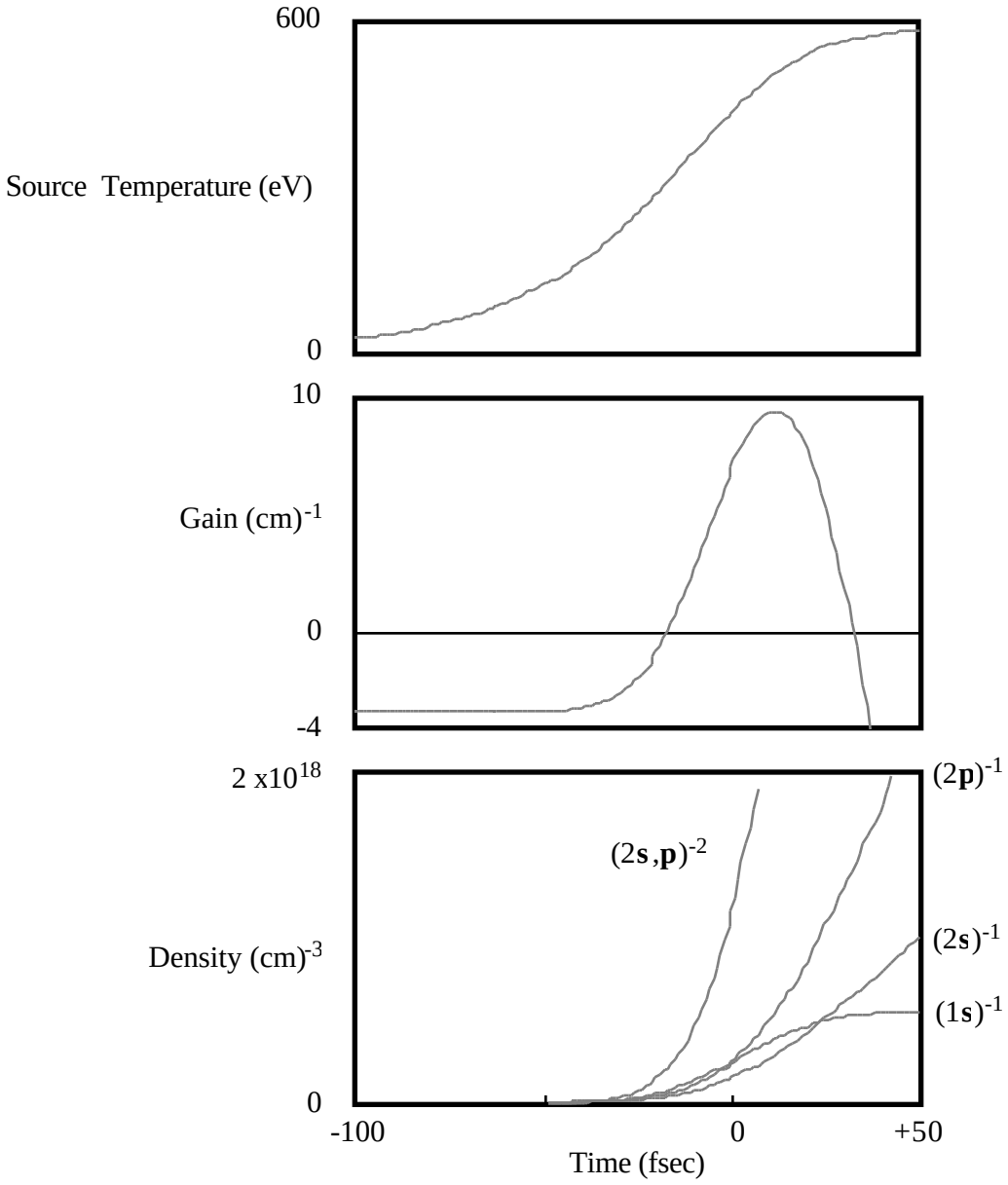

Figure 3.6: Simulation results for the neon system, using a density of 10^{20} cm^{-3} of neon in solid hydrogen, a 600 eV peak blackbody temperature, and a 3 μm thick beryllium filter.

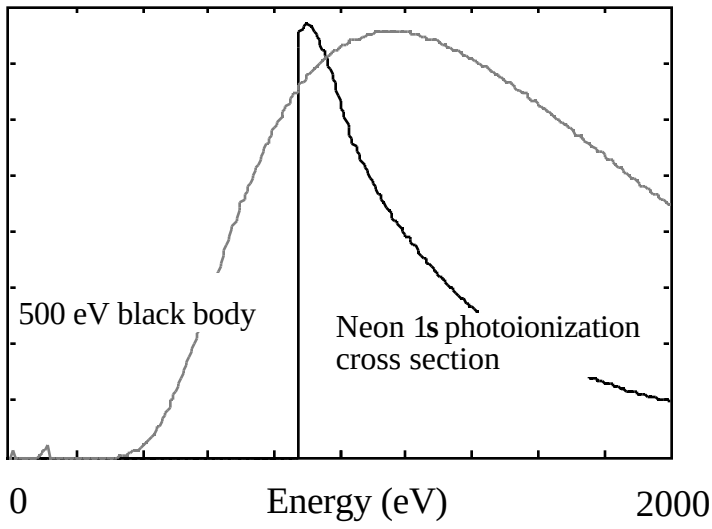

Figure 3.7: The neon inner-shell ionization cross section, compared with the x-ray flux (in photons per unit area) from a 500 eV blackbody radiator filtered by 3 μm beryllium.

Thus, the model predicts that substantial laser gain can be produced, provided a sufficiently bright x-ray source can be created. To experimentally demonstrate such a laser, one would need to obtain gain-lengths on order of $\mathbf{e}^{10}$, so that one will need a laser ~1 cm long. Since the population inversion lasts only 50 fsec (15 μm at the speed of light), one must move the excitation pulse synchronously with the light being amplified-- a traveling-wave excitation scheme. This can be done, as will be discussed. A more crucial question is whether the ultrashort pulse laser system required to implement this scheme is technologically feasible. One can obtain a rough estimate of the total energy requirements by extrapolating from Máiréad Murnane's experimental data on plasmas produced by femtosecond pulses. In her experiment, 160 fsec pulses with a cumulative energy flux on target of 300 J/cm^2 produced a peak plasma temperature of 230 eV, as measured by reflectivity and plasma spectroscopy experiments [211]. Using this data as a starting point, and extrapolating using the $T \quad F^{4/9}$ theoretical relation of temperature to laser flux [212](the temperature-pulse width relationship is very weak), one can estimate that the total laser flux

necessary to produce a 600 eV plasma would be ~3000 J/cm^2. This is an input laser intensity of about 10^{17} W/cm^2 which is considerably greater than the x-ray intensity in the energy region of interest; thus, the plasma need not be an extremely efficient x-ray converter. Considering a line focus plasma of 1 cm x 5μm dimensions, this translates into a laser requirement of about 1 Joule in 50 fsec. Although a laser of this capability does not yet exist, it is no longer beyond the state of the art. We are presently constructing a laser system capable of producing such pulses, as I will discuss in more detail later in the chapter.

Although these simulations show that a laser on the neon K-α transition may be practical, there are many possible problems that may prevent its successful demonstration. Other processes not considered in the model may have an effect on the population inversion. Ionization out of the upper or lower laser levels has been ignored; this is easily justified since the neon is only 3.5% ionized. The ionized upper and lower laser levels will have photon and electron ionization cross sections comparable to the neutral species, and thus will be only slightly ionized also. In the model, the neon $(2\mathbf{s})^{-1}$ and $(2\mathbf{p})^{-1}$ states are considered distinct, and there is no mechanism for mixing of the two states. Electron collisional mixing can be neglected since electron collisional excitation cross sections are a factor of a few smaller than electron ionization cross sections [42], which are not important.

Shake-up or shake-off processes during photoionization have been ignored in the simulation. About 15% of the time [218], inner-shell photoionization simultaneously excites or ionizes an outer-shell electron. However, this process will not have a detrimental effect except to reduce the effective $1\mathbf{s}$ ionization cross section by a small amount. Shake-up and shake-off processes during outer-shell ionization and electron collisional ionization have also been ignored. These processes would generally have the effect of populating the lower laser level more slowly, and thus would be beneficial.

Electron-ion recombination of the neon would be detrimental to the operation of the laser in that the Auger product states could recombine, and fill the lower laser level. General formulas for recombination rates yield, for three body recombination [219]:

$$R_{3b} = 8.75 \times 10^{-27} T_e^{-4.5} n_e^2 \quad , \qquad (3.7)$$

where $\mathbf{T_e}$ is the electron temperature in eV, $\mathbf{n_e}$ is the density in cm^{-3}, and $\mathbf{R_{3b}}$ is in sec^{-1}. For the conditions at the peak of the gain curve, this works out to be a recombination time of about 20 nsec, which is far too slow to be of consequence. Although this relation is only approximate, it tends to overestimate the rate [220], so that three body recombination is not likely to be a problem. For the radiative recombination rate, an estimate is [219]:

$$R_r = \frac{2.7 \times 10^{-13} Z^2 n_e}{\sqrt{T_e}} \quad . \qquad (3.8)$$

This relation estimates the radiative recombination lifetime to be about 200 nsec. Thus this process should also be negligible.

The radiative 2**p**-2**s** transition (at a wavelength of 46 nm) has a lifetime of 138 psec [221] and thus spontaneous emission on this transition is not important. However, examining the data of figure 3.6 reveals that there is a population inversion between these two levels(when taking into account degeneracies). This potentially could ASE quench the transition, equalizing the population in the $(2\mathbf{s})^{-1}$ and $(2\mathbf{p})^{-1}$ levels. This is the laser scheme proposed by Hagelstein [42] in his thesis. Depending on whether this transition is broadened by mechanisms other than Doppler broadening, the gain on this transition may be as high as 10^5 cm^{-1}. However, the absorption coefficient of solid H_2 at 46 nm is also about 10^5 cm^{-1}, so this laser oscillation will probably be suppressed. If the Hydrogen were not present strong laser operation at this wavelength would probably result, even at peak pump x-ray intensities several orders of magnitude below that necessary to exceed threshold on the K-α transition. However, even if this were the case, and the $(2\mathbf{s})^{-1}$ and $(2\mathbf{p})^{-1}$ levels were

clamped by ASE to their statistical values, it would have only a minimal effect on the K-α inversion. At the peak of the gain curve, the populations for the $(1\mathbf{s})^{-1}$, $(2\mathbf{s})^{-1}$, and $(2\mathbf{p})^{-1}$ levels are 3.9, 2.9, and 5.3 x 10^{17} cm^{-3}. If the $(2\mathbf{s})^{-1}$ and $(2\mathbf{p})^{-1}$ levels equalize, the population in the $(2\mathbf{p})^{-1}$ level will increase to 6.1 x 10^{17} cm^{-3}, and the net population inversion will decrease only 15%.

Another potential problem with this laser scheme would be transition linewidth broadening mechanisms which might reduce the gain cross section. Stark broadening of the $(2\mathbf{p})^{-1}$ level is the most prominent possibility. Quasi-static broadening of the level can easily be estimated, by considering the Stark splitting of the neon atom. At the peak of the gain curve, the electron density is 7.5 x 10^{19} cm^{-3}. Thus the mean separation between charged particles is $\sim \mathbf{n}^{-1/3}$, or ~ 2.3 nm, and the average neon atom will be subject to an electric field on order of $e/4\pi\varepsilon_o r^2 \approx 3 \times 10^8$ V/m. The Stark effect is a quadratic perturbation of the usual form [222]

$$\Delta E = \sum_j \frac{\left|\langle j|E \quad D|i\rangle\right|^2}{(E_j - E_i)} \quad , \tag{3.9}$$

summing over all transitions **j**. Since the dipole moment is just **D** = e**x**, and using the definitions of equations 1.11-1.14, one can write the Stark splitting as:

$$\Delta E = \sum_j \frac{E^2 \quad \frac{g_j}{3g_i} \frac{3\varepsilon_o \hbar c^3}{8\pi^2 \nu_{ij}^3} A_{ji}}{(E_j - E_i)} \quad , \tag{3.10}$$

summing over all allowed radiative transitions. Substituting for the average electric field, an estimate of the stark broadening is:

$$\Delta E = \frac{n^{4/3} \; e^2 \quad c^3}{256\pi^5 \varepsilon_o} \sum_j \frac{g_j \, A_{ji}}{g_i \, \nu_{ij}^4} \tag{3.11}$$

This expression is in MKS units. Considering only broadening due to the 2**p** -2**s** transition with a lifetime of 138 psec (the 2**p** -3**s** transitions are of almost the same transition energy but have longer lifetimes and thus are less important [221]), one can estimate the Stark splitting for the neon $(2\mathbf{p})^{-1}$ level to be ~ 2×10^{-7} eV. This is many orders of magnitude less than the natural linewidth of the transition, and thus quasi-static stark broadening is not likely to be a problem.

The other type of broadening is electron impact broadening. This broadening is due to dephasing of the atomic transition when a fast electron temporarily perturbs the atomic wavefunction. We can use the result of Sobel'man [223] equation 7.4.4-7.4.7, for electron impact broadening of non-hydrogenic levels, simplified:

$$\Delta\omega = 11.4\, C_4^{2/3}\, v^{1/3}\, n$$

$$\text{, where } C_4 = \frac{2\, e^2\, a_0^3\, f}{\hbar} \left(\frac{Ry}{E_j - E_i} \right)^2 . \qquad (3.12)$$

This expression is in cgs units (statcoulombs, etc.). **Ry** is the Rydberg energy, **f** is the transition oscillator strength (equation 1.36), and **v** is the mean electron velocity $\mathbf{v} = \sqrt{\frac{2E}{m}}$. For the $(2\mathbf{p})^{-1}$ level, considering only the same $(2\mathbf{p})^{-1}$ to $(2\mathbf{s})^{-1}$ transition, this broadening works out to be 3×10^{-4} eV-- larger than the quasi-static case, but still insignificant.

Refraction of the amplified beam out of the excited region can also be neglected. The index of refraction for x-rays was given by equation 1.43. For the conditions of the xenon laser, this works out to $\mathbf{n} = 1 - \delta$, with $\delta = 7 \times 10^{-8}$. Considering the case of the x-rays passing abruptly across the interface (**n**=1 outside the excited region), it is simple to calculate that

$$\varphi_0 = \sqrt{\varphi_i^2 + 2\delta} \ , \qquad (3.13)$$

where φ_i and φ_o are the grazing angles inside and outside the excited region. Given an angle typical of the aspect ratio of the excited region, 5 μm / 1 cm = 5 x 10^{-4} radians, the beam would only be refracted by about 1.2 x 10^{-4} radians as it passed from one region to the other. There is also a gain-induced index of refraction, related to equations 2.8-2.10. This index is maximum off the gain line-center, and of peak magnitude [100] $\delta = (\lambda/8\pi)\ \mathbf{G}$, where **G** is the gain at line center. For the neon laser case, $\delta = \pm 6 \times 10^{-8}$ -- of comparable magnitude to the plasma index, the sign of δ depending on whether the frequency is less than or greater than that of the gain maximum. However, the beam deflection due to these index effects is too small to be of importance. Gain guiding of the laser beam [100,101] would certainly dominate over these slight defocusing effects, to keep the amplified light within the high-gain region.

The last possible problem with this scheme is that it may simply not be possible to produce a sufficiently bright x-ray source. In the model, I have assumed that the plasma is emitting as a perfect blackbody radiator. This is of course not the case-- spectra from ultrashort plasmas have been observed to have much structure in the form of spectral lines, at least for light element targets [211]. It may be reasonable to expect that the plasma would approach blackbody, at least in the ~1 keV region where the neon photoionization cross section is high. Typical absorption depths for cold matter at ~1 keV are 50-100 nm [209]. The thickness of the x-ray emitting plasma heated by the incident laser pulse is on order of 10-100 nm, corresponding to the skin depth of the visible laser pulse and also allowing for heat conduction into the material [211]. Thus, if the continuum emission cross sections at high temperature are of similar magnitude to the absorption cross sections, one might expect an optical depth approaching unity, and thus a blackbody emitter. Of course, this is a rather simplistic assumption-- experimental data is necessary to have any degree of confidence in these estimates. Examining the x-ray brightness of these ultra-short pulse ultra-high intensity plasmas is the top priority of our on-going experimental work.

Computer simulations done on the LASNEX code for us by M. Rosen of the Lawrence Livermore National Laboratory do give predictions of the total x-ray intensity emanating from an ultrashort-pulse laser-produced plasma. The results of a computer simulation are shown in figure 3.8. The simulation assumed an energy flux of 10^4 Joules/cm^2 in 100 fsec, incident on a Molybdenum target. The peak radiated power is 3 x 10^{15} W/cm^2, approximately what is necessary to create a population inversion. However, for this simulation the primary x-ray emission is at 2.5 keV, which is somewhat higher in energy than can efficiently pump the neon 1**s** cross section. With a pump fluence of 10^4 Joules/cm^2, the total laser energy requirement for demonstrating the neon scheme would be ~ 10 Joules, which is still technologically feasible. Further optimization of the target material may be possible; however, since no experiments have been done under these high fluence conditions, the LASNEX results are not guaranteed to agree with reality. They do agree reasonably well in temperature prediction with experiments under the lower fluence ultra-short pulse conditions which have been experimentally examined [211].

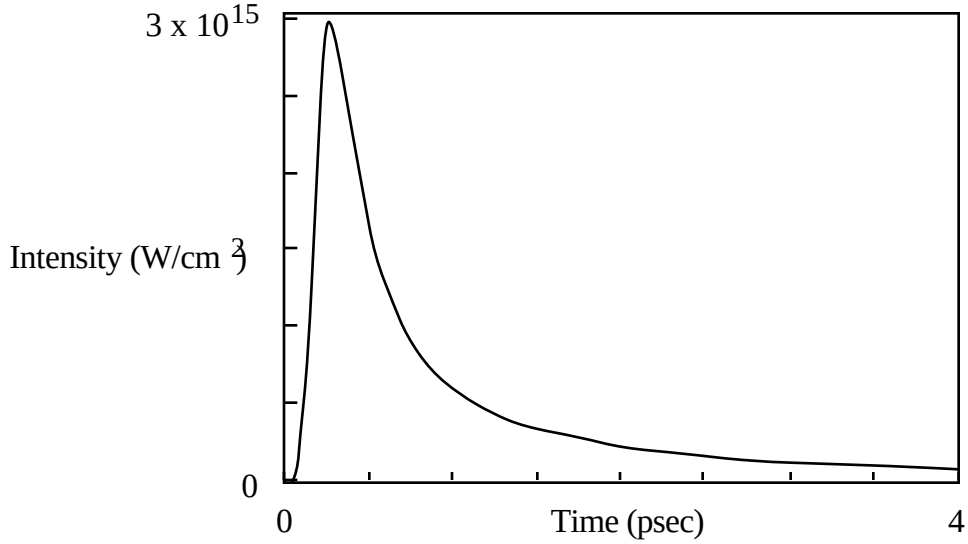

Figure 3.8: LASNEX prediction of total radiated power vs. time for a Mo target irradiated with 10^4 J/cm^2 of laser fluence in 100 fsec. Courtesy of M.D. Rosen of LLNL.

One possible way of reducing the laser energy requirements is to use a target consisting of an anti-reflection grating [224,225]. Plasmas produced by ultrashort laser pulses have a very high reflectivity (>75%) due to the high densities in which the laser light is absorbed [211]. An anti-reflection grating is analogous to an anti-reflection coating as used in ordinary optics (the coating creates a 1/2 wave delayed reflection which interferes with the surface reflection), except that instead of using a coating (which would turn to a plasma at high intensities), a structured surface (diffraction grating) is used. Since the structure of the surface will be retained for the duration of the fsec pulse, enhanced absorption of the incident high-intensity light is possible.

The variation in the pump laser energy required as a function of emissivity of the plasma is shown in figure 3.9. The necessary laser energy was estimated by adjusting the plasma temperature at each value of the emissivity until the gain per unit length predicted by the model was about 10 cm^{-1}. The laser flux was then calculated using the $T \quad F^{4/9}$ relation. The result is that the pump laser size goes up modestly for plasma emissivity of 0.1-1, and up very steeply for emissivity values below 0.1. The reason for this behavior is apparent if one considers the necessary temperature as a function of emissivity, as is also shown in figure 3.9. At an emissivity of 1, the peak plasma temperature is 600 eV. The peak of the blackbody curve, in terms of number of photons per unit area at a particular energy, occurs at $\mathbf{h}\nu = 1.59\ \mathbf{kT}$; thus, the 600 eV blackbody has a peak photon emission at 950 eV, which is matched well with the peak of the neon 1**s** ionization cross section (figure 3.7). However, as the emissivity is decreased, and the peak temperature therefore must increase to increase the x-ray flux, and the peak of the blackbody distribution is at higher energies than can efficiently pump the neon. In the limit where $\mathbf{kT} >> \mathbf{h}\nu_{pump}$, the photon intensity at $\mathbf{h}\nu_{pump}$ is only increasing linearly with temperature, while the total x-ray emission continues to increase as $\mathbf{T}^4$. Thus, an emissivity of 0.1 -1 for the plasma is necessary for the scheme to be practical.

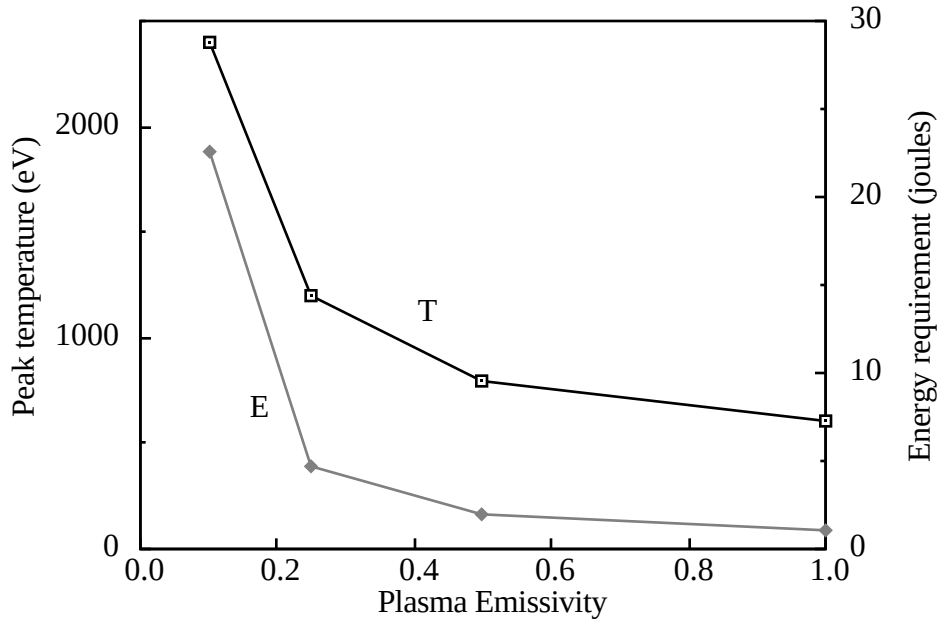

Figure 3.9: Graph of predicted peak plasma temperature, and pump laser energy requirement, as a function of blackbody emissivity of the plasma.

The situation may even be even worse than is implied in figure 3.9, because at higher temperatures the plasma will be more ionized, and the line radiation (bound-bound transitions) will tend to be at shorter wavelengths also. Thus, as **kT** gets >> $\mathbf{h}\nu_{pump}$, the emissivity at $\mathbf{h}\nu_{pump}$ will probably decrease. However, there are several factors which make the situation possibly more favorable. The first is that these high-density plasmas tend to be less ionized for a given temperature than a low-density plasma would be. This is a result of the Saha equation [226] for the ionization distribution in a plasma:

$$\frac{n_Z\, n_e}{n_{Z-1}} = 2\left(\frac{2\,\pi\, m\, k\, T_e}{h^2}\right)^{3/2} \frac{B_Z(T_e)}{B_{Z-1}(T_e)} \exp\left(-\frac{(IP)_{Z-1}}{k\, T_e}\right) = K(T) \qquad (3.14)$$

where the $\mathbf{B}_Z$'s are the partition functions of the atoms in the respective ion stages, and **IP** is the ionization potential of the **Z**-1 ion stage. This equation is the application of the Boltzmann distribution $n_i \quad \exp\left(-\frac{E_i}{k\,T}\right)$, taking into account the relative degeneracies of the

ionized atom and the free electron, compared with the non-ionized atom. Since the ionization process creates a free electron, one can approximately write that $n_Z n_e \quad n_{Z-1} \quad n_Z \quad \sqrt{n_{Z-1}}$, and thus as density is increased, the ionization stage of a plasma decreases. This result is a consequence of the fact that at higher densities the degeneracy of the free electron state decreases. The excited ionic levels will also be relatively more populated at higher densities, enhancing radiative emissions. Thus, high density plasmas should work well for pumping these K-α lasers.

The dependence of the laser energy requirements on the pulse width of the pump laser is shown in figure 3.10. This data was generated by varying the pulse width in the simulation, and scaling the pump energy requirement inversely with the peak gain predicted by the simulation, after optimizing the density of neon. One sees that the energy requirement varies roughly as the third power of the pulse width. Thus, very short pulses are imperative to make this laser scheme practical-- one would need 10^4-10^5 Joules of pump energy if the pulse width were ~1 psec. However, if one could generate 20 fsec pump pulses, the energy requirement might drop to as low as 0.1 Joules. Pulses this short should be technologically feasible. This steep pulse width dependence is due to the fact that the laser action occurs on the rising edge of the pulse, before electron impact ionization fills the lower laser level. Thus, the rise time, and not the total pulse width, of the pump pulse is the important parameter. The use of saturable absorbers to steepen the rising edge of the pump pulse would reduce the laser energy requirements. However, geometrical considerations limit the ultimate pulse width practical-- 20 fsec is only 6 μm at the speed of light, which is comparable to the width of the laser focus, and also comparable to the thickness of the beryllium filter. Thus divergence of the x-rays will result in some lengthening in the rise time of the x-ray pulse.

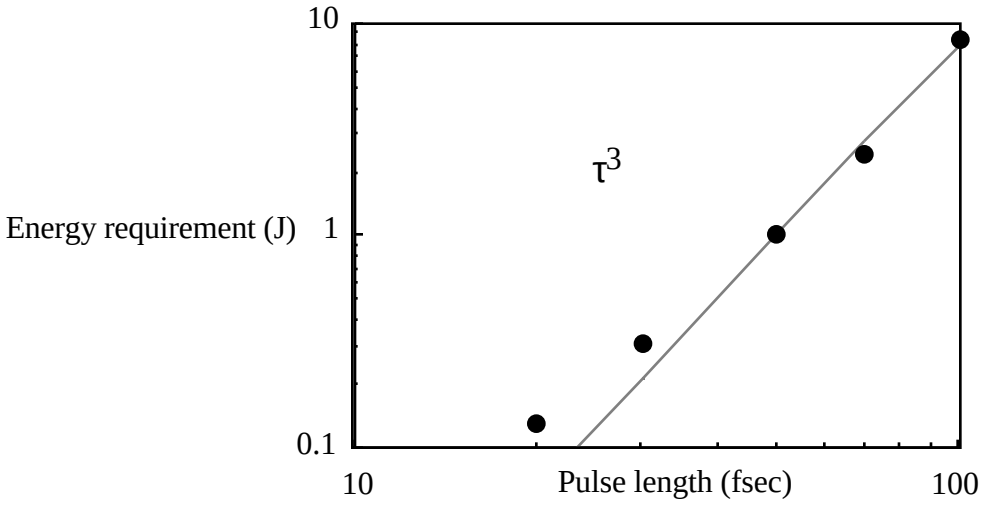

Figure 3.10: Neon K-α laser energy requirement as a function of pulse width of the pump laser.

Simulations were also done eliminating the solid density hydrogen, to evaluate the importance of electron cooling by the hydrogen. Elimination of the hydrogen reduces the peak gain by about 15% for 20 fsec pulses, and by 30% for 100 fsec pulses. The pulse length dependence reflects the fact that, at a cooling rate of 35 eV/fsec, the typical electron takes 20-30 fsec to cool completely, and thus hydrogen cooling is not so important for very short pump pulses lengths. Thus, although the hydrogen helps, it is not crucial to the demonstration of this scheme. However, the fact that freezing the gas confines it may be an important practical advantage-- 10^{20} cm^{-3} of neon is several atmospheres pressure, with an absorption coefficient at the laser wavelength of 2.4 cm^{-1}. Thus, the neon pressure must drop from several atmospheres to <<atmosphere in a few mm, or most of the x-ray laser energy will be uselessly absorbed in the gas. Freezing the neon in hydrogen is not likely to change the x-ray emission linewidth of the neon. The freezing points of both gases are very low -- 20 K for H_2, 28K for Ne or about ~10^{-3} eV << x-ray linewidth. Soft x-ray emission spectra of the same molecules in both the solid or gaseous state show no differences [208].

The output characteristics of such a neon K-α laser can be only crudely estimated since the gain dynamics in such a traveling-wave excitation scheme are complex. However, one would expect a nearly diffraction limited output beam. Far from the x-ray blackbody source, the gain on the transition will drop since the pump x-rays are diverging and the traveling-wave excitation is geometrically smeared. Thus, the aperture of the laser would correspond to approximately the pump laser focus width (~5-10 μm) in both transverse directions. Given a ~1 cm line focus geometry, the Fresnel number, which is defined [171] as $N = r^2/\lambda l$, is ≈2. The fresnel number is just the ratio of the geometric divergence angle defined by the excited region (= 5 μm / 1 cm), to the diffraction angle due to the defining aperture (= 1.46 nm / 5 μm). Thus, the output beam will have a divergence angle nearly as small as the diffraction limit. This is the ideal situation, since N<<1 would mean that much of the x-ray flux being amplified would diffract out of the gain region, and N>>1 would mean less than diffraction limited output beam characteristics. The pulse output energy would be on order of the energy stored in the upper laser level at the peak of the gain -- about 20 μJ. The time duration of the output pulse would be somewhere in the range of the duration of laser gain (50 fsec) to possibly as short as can be supported by the gain bandwidth (2.75 fsec).

My numeric simulations have shown that an x-ray laser on the K-α transition of neon may be feasible. The biggest uncertainty in implementing the scheme is whether plasmas created by laser pulses of <100 fsec duration, and total fluences of 10^3-10^4 Joules/cm^2 (> 10^{17} W/cm^2), will be sufficiently bright x-ray sources to create a population inversion. This question provides another motivation from studying the physics of ultrashort laser-produced plasmas.

3.3.3 K-α lasers in molecules

One way of potentially reducing the energy requirements for such a K-α laser would be to create an inversion on a longer-wavelength x-ray transition. As mentioned before, the

problem with doing this is that there are no lighter elements with longer K-α transition wavelengths, that exist stably in atomic form. If we use atoms in molecular form, the x-ray transition will be split into a number of subcomponents with a commensurately smaller gain cross section. However, there are a few molecules that do have x-ray emission that is split into only a small number (~10) subcomponents, and it is worth considering these cases. Figure 3.11 shows the x-ray emission spectra for the Carbon K-α line in CO_2 [227], and for the N_2 x-ray emission [228]. In the case, of CO_2, the emission is spread into a band about 1 eV wide, about an order of magnitude larger than the natural linewidth of 0.07 eV [227]. The individual lines are actually spaced about 0.12 eV apart, so that they only loosely overlap. The most intense sub-component consists of about 1/8 of the total emission. The CO_2 electronic structure is $1\sigma_g^2\ 1\sigma_u^2\ 2\sigma_g^2\ 3\sigma_g^2\ 2\sigma_u^2\ 4\sigma_g^2\ 3\sigma_u^2\ 1\pi_u^2\ 1\pi_g^2\ {}^1\Sigma_g$, and the x-ray emission is between the $2\sigma_g$ state (C1**s**) and the $3\sigma_u$ and $1\pi_u$ states, which both have some C2**p** character. Transitions to the $1\pi_g$ state are not allowed through symmetry-- the carbon atom is in the center of symmetry of the molecule, and thus the atomic dipole transition must be to a level of opposite symmetry to the original $2\sigma_g$ hole and the final state. The two allowed transitions overlap into the one band. Although CO_2 seems like it might be an attractive candidate to use for a K-α laser, its problem is that it contains oxygen atoms with a K- edge at 543 eV. Thus, x-rays above this energy will primarily ionize to the wrong state. The oxygen K-α emission in CO_2 is very broad, and thus is not suitable itself as a possible laser transition.

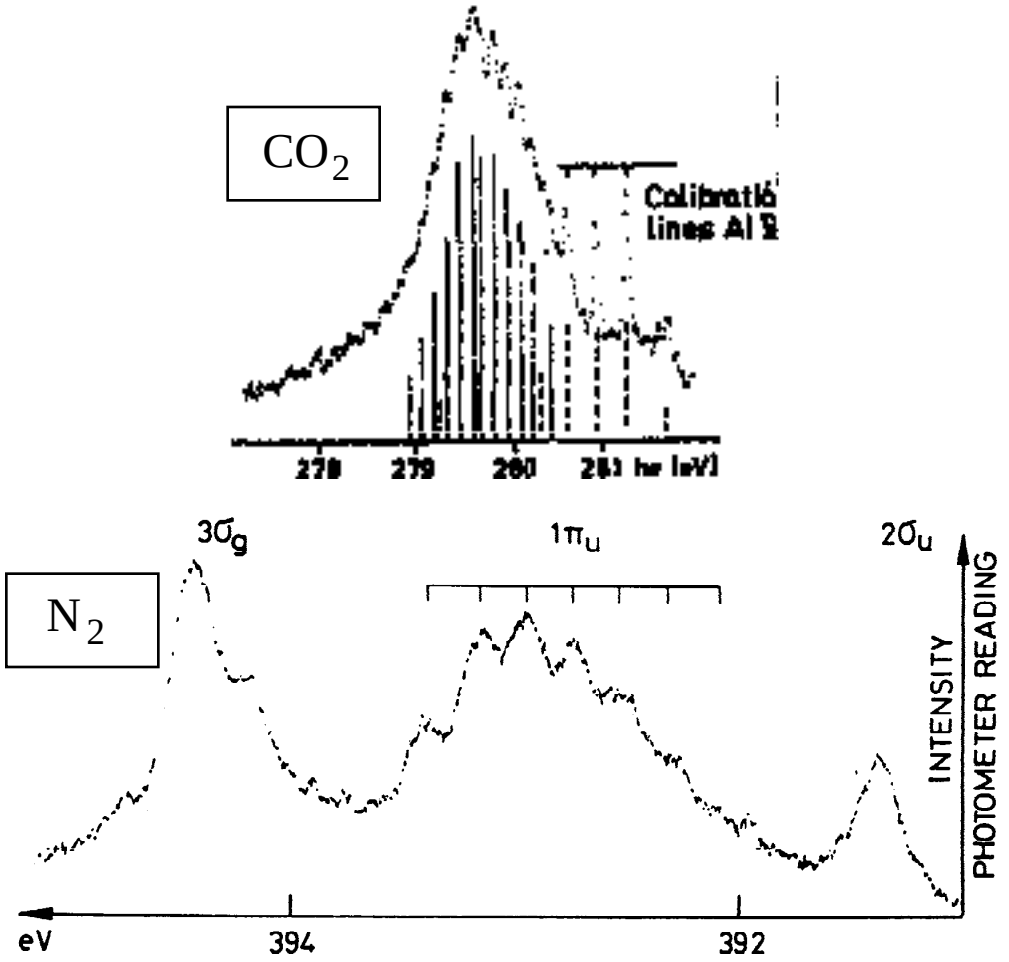

Figure 3.11: The ultrasoft x-ray emissions of CO_2 from Nordgren et al. [229], and of N_2 from Werme et al. [228].

Nitrogen looks like it has a substantially broader emission; however, this is primarily a result of low instrumental resolution. The electron configuration of nitrogen is $1\sigma_g^2\ 1\sigma_u^2\ 2\sigma_g^2\ 2\sigma_u^2\ 1\pi_u^4\ 3\sigma_g^2\ {}^1\Sigma_g$, and the three bands are to the $3\sigma_g$, $1\pi_u$, and $2\sigma_u$ levels. The vibrational spacing for N_2 is much larger than for CO_2, and the strongest x-ray component is about 20% of the total emission intensity [230,231].

Another possible K-α laser candidate is Methane, for which the x-ray emission spectrum has not been measured in high resolution. A low resolution spectrum of CH_4

shows an instrument-limited linewidth [232]. Methane has a highly symmetric tetragonal structure, with a configuration of $1\mathbf{a}_1^2\ 2\mathbf{a}_1^2\ 1\mathbf{t}_2^6$. The electrons from the hydrogen atoms fill the 2**p** shell of the carbon, creating a molecule with a closed-shell structure exactly analogous to the neon atom. Symmetry allows only one x-ray transition, from the $1\mathbf{a}_1$ to the $1\mathbf{t}_2$ level, analogous to the 1**s**-2**p** transition. One might then expect that methane would have a very narrow x-ray emission spectrum. The situation is not so simple, though. Although ground state methane has a very simple structure, the $(1\mathbf{t}_2)^{-1}$ state of methane is not stable, and the ionized molecule then distorts, with one of the hydrogen atoms moving further from the carbon [233]. This rearrangement of the atoms is a manifestation of the Jahn-Teller effect. Thus, the lower laser level is split, and this may result in a complex vibrational structure to the x-ray emission. The UV photoelectron spectrum, corresponding to the $2\mathbf{a}_1$ to $1\mathbf{t}_2$ transition is >2 eV wide due to this effect [234]. However, the low-resolution x-ray spectrum seems to rule out a linewidth this large. It is unclear to me whether this is a lifetime effect (can the molecule rearrange in the 6.2 fsec lifetime [235] of the methane core-hole level?), or a result of looking at photons rather than electrons, or some subtlety in the vibrational overlap integrals in the transitions. Perhaps this distortion would be an advantage in that the x-ray absorption of the lower laser level methane may spread in wavelength. The measurement of this spectral line is now being attempted in our laboratory.

The use of molecules rather than atoms has some beneficial side-effects which help to counter the broadened x-ray transitions. The degeneracies of the levels tend to be more favorable towards producing an inversion. For instance, in the free carbon atom (from table 3.1), photoionization-produced states with a total **g** = 18, of which 1/3 could decay to a lower level of **g** = 6. In methane, the electron configuration is neon-like, with $\mathbf{g}_{\text{upper}} = 2$ and $\mathbf{g}_{\text{lower}} = 6$. Given the fractional inversion is $\Delta N = N_{\text{upper}} - \frac{g_{\text{upper}}}{g_{\text{lower}}} N_{\text{lower}}$, the latter case is much more favorable, and thus in the methane case the theoretical maximum inversion lifetime (equations 3.1 and 3.2) is longer for the molecular case. This is a result of the

closed-shell structure, and since molecules tend to form closed shells, in general molecules have an advantage in relative degeneracies.

Other possible advantages are not so easily quantifiable. For instance, although the electron impact ionization cross sections for atoms and molecules are of similar magnitude, it is not clear whether electron impact will fill the same states that are filled by the x-ray transition, and thus constitute the lower laser level. There are many vibrational sub-levels, and it may well be that electron impact ionization tends to produce more highly vibrationally excited ions, or produces a much broader vibrational distribution of ions than does the electric dipole x-ray transition. Thus the lower laser level may not fill as quickly as in case of an atom. This is the same basic principle that is behind the VUV molecular hydrogen laser [17,18,20].

Another difference between atoms and molecules is that molecular Auger decay product states dissociate. Doubly ionized molecules are not stable-- the molecule can split into two repulsive single ionized fragments in a "coulomb explosion". This occurs on a femtosecond time scale, as is easy to see-- even if only a few eV of excess energy is converted to kinetic energy of the product atoms, they will be traveling at ~5-50 nm / psec, depending on the mass of the ejected atom. Thus, the atoms will move apart by a few atomic widths in 10-100 fsec. For N_2, the product is primarily N^+ atoms [159], while in an atom such as CH_4, one ends up with a wide variety of fragments(C, CH, CH_2, CH_3, H_2, etc. all in appreciable quantities [236]). The wide (5 eV) Auger linewidth for the CH_4 molecule is attributed to a coulomb explosion simultaneous with the Auger decay [237]. In the case of the K-α laser, the important question is whether any of these Auger product fragments resonantly absorb at the laser wavelength. In the case of the N_2 molecule, the atomic nitrogen K-α line (in N^+) is at 392.4 eV [199]. Referring to figure 3.11, this energy is a couple of eV removed from the brightest molecular emission, and thus absorption on this transition would have little effect on any population inversion. For the case of the more complex molecules, some of the

fragments will be molecular, and will have a broader absorption which may partially overlap with the intact molecular emission. However, especially with the case of initially highly symmetric molecules like methane, the product states will share none of the same symmetries, and will thus have a broader x-ray absorption. Thus it is likely that this absorption will not destroy the population inversion.

Radiative and Auger decay rates vary considerably depending on the molecular environment of an atom. For instance, the carbon K-ionized atom, the upper level lifetime is 9.4 fsec [227] in CO_2, but 6.2 fsec in CH_4 [235], while the calculated lifetime for atomic carbon is 10.3 fsec [201]. However, these variations are less that a factor of 2 (usually considerably less), and thus are not too important considering the other uncertainties in the problem.

The case of K-α lasers on molecular transitions is thus considerably more complex than in the case of atomic neon. With some simplifying assumptions, one can still do simulations that give insight into the practicality of such schemes. Primarily because of its similarity to the neon atom, I have chosen to do the simulation in the case of methane. Although its x-ray emission spectrum has not been measured, other important parameters are available in the literature. In these simulations, I have assumed that the peak x-ray emission is 33% of the total emission, resulting in a factor of 3 reduction in the gain cross section over the case of an atom. The photoionization cross sections are from Berkowitz [238], the electron impact ionization cross section is from Chatham et al. [239], the Auger lifetime from Apslund et al. [235], and the fluorescence yield (to determine the Radiative rate) from Langenberg and van Eck [240]. Electron ionization actually causes dissociation about 50% of the time; thus, 50% of the electron ionization was assumed to go into the lower laser level. Simulation results for a case using a plasma of 1000 eV peak temperature and a pump pulse rise time of 30 fsec are shown in figure 3.12. The peak gain in this case is 20 cm^{-1}. The outer-shell photoionization absorption of the neon-hydrogen mixture is much higher at the 277 eV carbon K-α transition energy, and thus the net gain of 20 cm^{-1} is only marginally above the

gain threshold, and is very dependent on the model parameters. However, the blackbody temperature needed is higher than in the case of neon, and the pulse rise time must be shorter, to get comparable gain with the neon case. Thus, it seems that it may be more difficult to invert these molecular systems, even though the transition wavelength is longer.

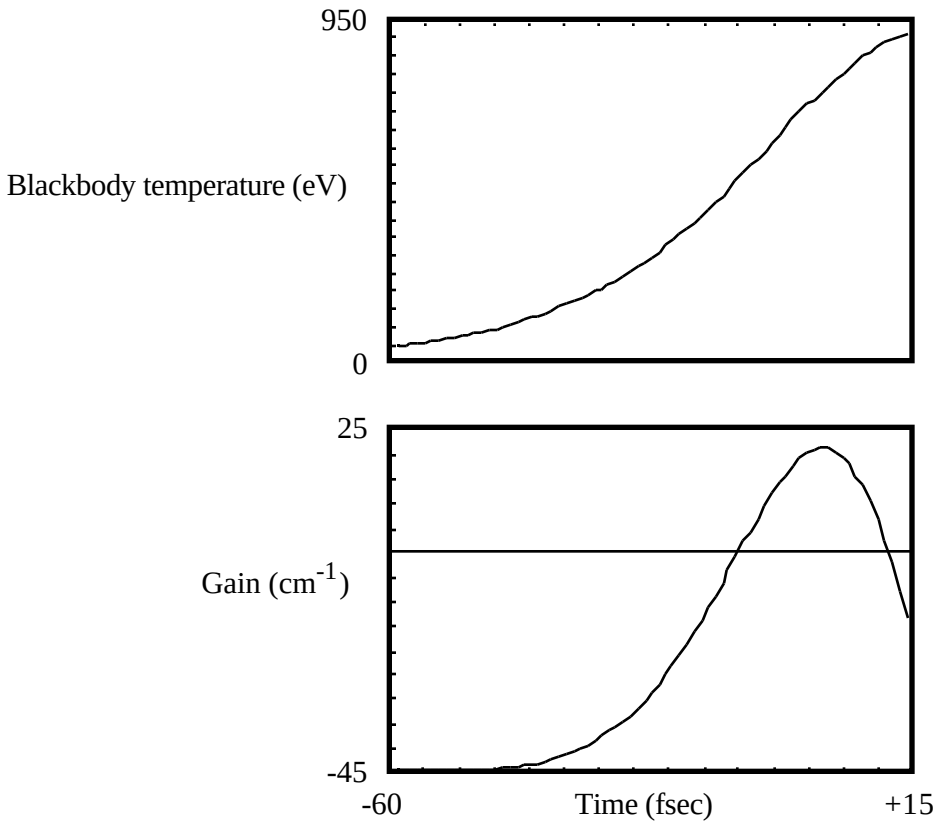

Figure 3.12: Simulation results for the K-α transition in CH_4, for the case of 3×10^{20} cm^{-3} of CH_4 in solid density hydrogen. The system is pumped by a blackbody radiator of 1 keV peak temperature, produced by a 30 fsec FWHM laser pulse.

This behavior is the result of a number of factors-- higher electron ionization cross sections, higher absorption at the laser wavelength, and molecular broadening of the x-ray emission. The result is that one needs a blackbody temperature for which the peak photon flux is at much higher energy than is useful for pumping the population inversion. As

discussed previously, this is an undesirable situation. At the peak of the gain curve, the blackbody temperature is 750 eV, and only ~3% of the total x-ray flux is in the energy region of 300-600 eV where the methane inner-shell cross section is high. However, if it is the case that ultrashort plasmas have a higher emissivity at low photons energies compared with the blackbody temperature, then the molecular species would be an attractive K-α laser candidate. Also, if the x-ray emission of methane is as narrow as for atomic carbon, then very high gain on the transition (~70 cm^{-1}) can be produced using the similar plasma conditions to the case of the neon laser. Higher gain would significantly reduce the pump laser energy requirements since a shorter illuminated length would be necessary. Also, one possibility that I have not yet examined in detail is whether the output of the neon K-α laser could be used as a pump source for inverting some of these molecular transitions, since the flux in the case of the x-ray laser output is not limited by any blackbody limitations. Thus, for a number of reasons it is worthwhile to further investigate the x-ray emission spectrum of methane.

3.3.4 X-ray lasers on L-shell transitions

Another possibility for creating a laser at more modest wavelengths would be to try inverting an L-shell transition. The obvious candidate for this is the $(2\mathbf{p})^{-1}$ to $(3\mathbf{s})^{-1}$ transition in atomic argon. The $(2\mathbf{p})^{-1}$ level is split into two levels, the $^2\mathbf{P}_{1/2}$ and $^2\mathbf{P}_{3/2}$ states, which are separated by about 2 eV; thus, there are two separate x-ray transitions, at 220.1 eV,. and 221.7 eV [216]. However, since the states will be statistically populated in the photoionization, the $^2\mathbf{P}_{3/2}$ state will get 2/3 the population, so that the line broadening in the Argon is much less than in molecules. The disadvantage of this transition is the low fluorescence yield-- about an order of magnitude less than in the case of methane [204]. Also, the degeneracies in the case of this transition are unfavorable-- for the upper level $\mathbf{g}$=6, while for the lower $\mathbf{g}$=2. The inversion filling time τ_F (equation 3.2) is only 70 fsec. However, this is not an unreasonable inversion time, and in the other cases investigated electron ionization

was the primary lower level population mechanism. In the case of Argon the 3**s** electron ionization cross section is quite small [215]. The $(2\mathbf{s})^{-1}$ to $(3\mathbf{p})^{-1}$ transition is of a transition energy above the absorption edge for the 2**p** electron, and thus is not a suitable laser transition candidate.

The a simulation was run for the $(2\mathbf{p})^{-1}$ to $(3\mathbf{s})^{-1}$ transition of argon, using atomic data from various sources [199,202,204,205,209,215,216]. Unfortunately, the simulation shows no reasonable set of physical conditions for which net gain is produced. The gain cross section is simply too low, due to the low fluorescence yield (equation 3.3). Thus, K-shell transitions seem the most likely candidates for such lasers. I have not examined M- or N-shell transitions, but I suspect these transitions would have similar disadvantages. One thing that I have not examined is whether any transitions metastable against Auger decay can be found for which the transition linewidth would be narrow, and thus the gain cross section would be high. This is the basis of some of the quasi-metastable short-wavelength laser schemes proposed by Harris et al. [71,108], and of the Auger cascade scheme of McGuire [65].

3.3.5 Conclusion

My simulations have shown that it may be possible to produce an x-ray laser by inverting K-α transitions in the light elements. The neon K-α transition at 1.46 nm (849 eV) is the most likely candidate for such a laser; however, transitions in molecular carbon or nitrogen containing species are also a possibility. Such a laser would have many potential uses. With the expected output energy of 10-100 μJ in 2.5-50 fsec, the peak x-ray output power could be as high as 1-10 GW, in a near diffraction limited output beam. If one could focus a reasonable fraction of this energy to a diffraction limited spot (a few nm diameter) using multilayer or grazing incidence x-ray optics, one could obtain power densities of $>10^{21}$ W/cm^2. Thus, a new field of physics-- x-ray non-linear optics-- may be born. With such a high-intensity focusable beam, the output from a neon K-α laser might

be capable of pumping K-α laser transitions in the molecular species. Given an x-ray laser beam of $>10^{11}$ photons, a time resolved x-ray hologram could be produced in ~ 10 fsec. Cross correlation experiments between x-ray and visible pulses, both of femtosecond duration, could be used to examine such phenomena as the "coulomb explosion" in x-ray excited molecules, on a time-resolved basis. There is much motivation for building such a K-α laser. In the next section I shall discuss the technology that may make such lasers a reality.

In the event that the physics of ultrashort laser-produced plasmas does not allow a sufficiently bright x-ray source, several more modest schemes are likely to work using similar ultrashort x-ray pump sources. The neon $(2\mathbf{p})^{-1}$ to $(2\mathbf{s})^{-1}$ transition at 46 nm [42] shows very large gain in my simulations. Additionally, the original Auger scheme proposed by McGuire [49] in Neon III (discussed in chapter 1) would also be expected to show substantial gain at 49 nm. The Duguay Sodium scheme [22] at 37 nm would be much more feasible using ultrafast excitation pulses, since one could create an inversion on a time scale short compared with electron collisional ionization times. Also, the lithium population transfer scheme at 21 nm [72] may be feasible using ultrashort x-ray pulses.

3.4 Ultra-high power ultrashort-pulse lasers

The realization of the neon K-α laser scheme requires the development of a new type of ultrashort-pulse laser system, capable of generating a pulse of 1-10 Joules in 50 fsec. This is about 3 order of magnitude more energy than any presently demonstrated laser system. This section will discuss the new technology that is now available to make such a laser system possible. I will also briefly discuss the possible experimental geometry of the neon K-α laser, and the implementation of the traveling-wave excitation necessary for the scheme. The purpose of this chapter is to construct a conceptual blueprint of a neon K-α laser, to show that it is not merely science fiction.

3.4.1 Titanium-doped sapphire

The principal breakthrough that allows the construction of ultrashort-pulse lasers with very high pulse energy is the recent development of a new solid-state laser material, Titanium-doped sapphire. This material was first examined in 1982 by Moulton [241], and has been extensively studied by researchers and commercial firms [242,243,244,245,246,247,248,249]. Recently the first commercial lasers based on Ti:sapphire have become available (from Spectra-physics, and from Candela laser). The desirable characteristic of Ti:Sapphire is its broad gain-bandwidth, which is shown in figure 3.13. There is appreciable gain in Ti:sapphire continuously in the range from 700 nm to >1000 nm. This is a considerably wider bandwidth than most laser dyes. For the amplification of short pulses, a wide gain bandwidth is necessary because very short pulses have a wide bandwidth. For a transform limited pulse, the FWHM bandwidth is related to the pulse width by the relation [250]:

$$\Delta\nu\,\Delta t = 0.3148\ , \qquad (3.15)$$

for short pulses of the form $I(t) = \mathrm{sech}^2(t)$, which is the most common ultrashort pulse shape. This is simply the result of the fourier transform, and is a consequence of the Heisenberg uncertainty relation. For Ti:sapphire, this means that there is sufficient bandwidth to amplify pulses as short as 10 fsec or less.

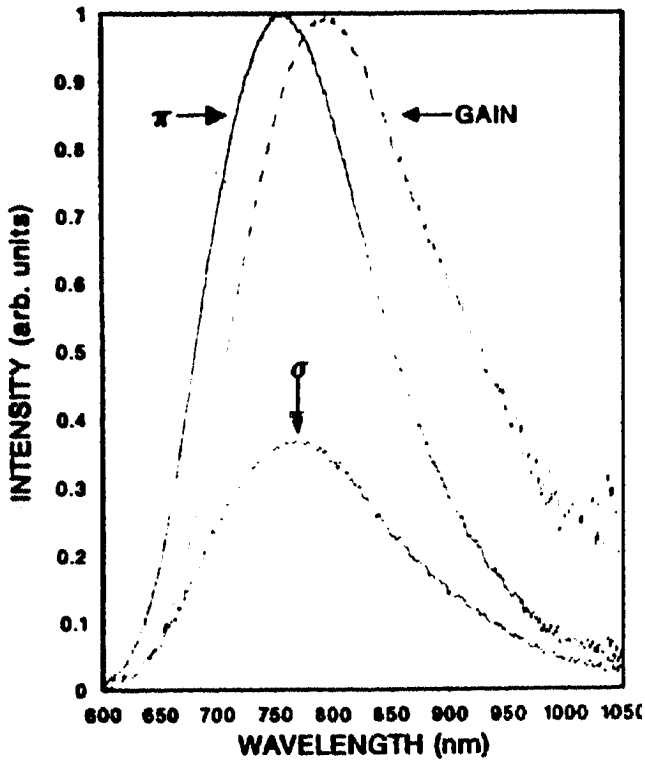

Figure 3.13: The spontaneous fluorescence spectra of both polarizations, and the gain, as a function of wavelength for Titanium-doped sapphire. From Moulton [246].

The advantage of this laser material over dyes, which also have sufficient bandwidth to amplify short pulses, is the gain cross section. Ti:sapphire has a peak gain cross section, at ~800 nm, of about 3 x 10^{-19} cm^2 [249]. This compares with gain cross sections in laser dyes on order of 10^{-16} cm^2. Since the gain in any amplifier is limited by ASE gain clamping to a value in the range of $\mathbf{e}^1$-$\mathbf{e}^{10}$, a lower gain cross section means that a higher density of atoms can be excited in the material , and therefore the stored energy per unit volume in Ti:sapphire can be 100-1000 times as much as in the case of dyes. Thus, there is the potential of extracting much higher beam energies from a Ti:sapphire laser amplifier than is possible from a dye amplifier.

The saturation fluence of an amplifier material is a measure of how much energy can be extracted from a laser amplifier. It is defined as

$$E_{sat} = \frac{h\nu}{\sigma_{gain}} \quad , \qquad (3.16)$$

which is just the energy per unit area stored in an amplifier of gain $\mathbf{e}^1$. For Ti:sapphire, this number is 0.8 Joules/cm^2. In general, the energy per unit area extractable from an amplifier is in the range of 1-5 **E**sat, given that the small signal gain of the amplifier can be greater than $\mathbf{e}^1$. Thus, a laser of 1-10 Joules in 100 fsec can be constructed with Ti:sapphire amplifiers using a beam diameter on the order of 1 cm, which is still a small-scale laser system.

The difficulty with using Ti:sapphire amplifiers is the high peak-power of the pulse being amplified. A pulse of ~1 J/cm^2 in 100 fsec has a peak power of 10^{13} W/cm^2, which is more than sufficient to damage the crystal. At intensities far below this, non-linear effects will cause undesirable self-focusing effects in the beam. This effect can be quantified using the definition of the non-linear "**B**" integral [251] :

$$B = \frac{2\pi}{\lambda} \int_{z=0}^{L} n_2 \, I \, dz \quad , \qquad (3.17)$$

where $\mathbf{n}_2$ is the non-linear index of refraction of the material and **I** is the intensity of the light. This number corresponds to the propagation phase delay for a light beam due to the non-linear index of refraction as it passes through the material. A value of $\mathbf{B}=2\pi$ would correspond to a non-linear delay of one wavelength. Since a beam being amplified usually has a non-uniform intensity profile in space and in time, different parts of the beam will experience different path delays, distorting the beam, if the **B** integral approaches one wave. Thus, it is desirable to keep $\mathbf{B}\leq 1$. The non-linear index for sapphire [251] is 2.5 x 10^{-16} cm^2/W. Given that the beam being amplified will pass through a few cm of sapphire at its

highest intensity, equation 3.17 implies that the peak intensity in the beam should be kept to $\leq 5 \times 10^{9}$ W/cm^2. This intensity is more than three orders of magnitude less than the saturation fluence of Ti:sapphire for 100 fsec pulses.

Fortunately, there is a solution to this problem. The **B** integral limit is an intensity limit, while the saturation flux is a total flux limit. Thus, if one can stretch the femtosecond pulse by a factor of a few thousand, amplify it, and then compress all the energy back into a short pulse, one can amplify the pulses to a very high energy. Fortunately, this is possible. The technique is called chirped-pulse amplification, and the basic concept is illustrated in figure 3.14. This technique has been developed theoretically by Martinez [252,253], and experimentally by Mourou [197,254,255,256].

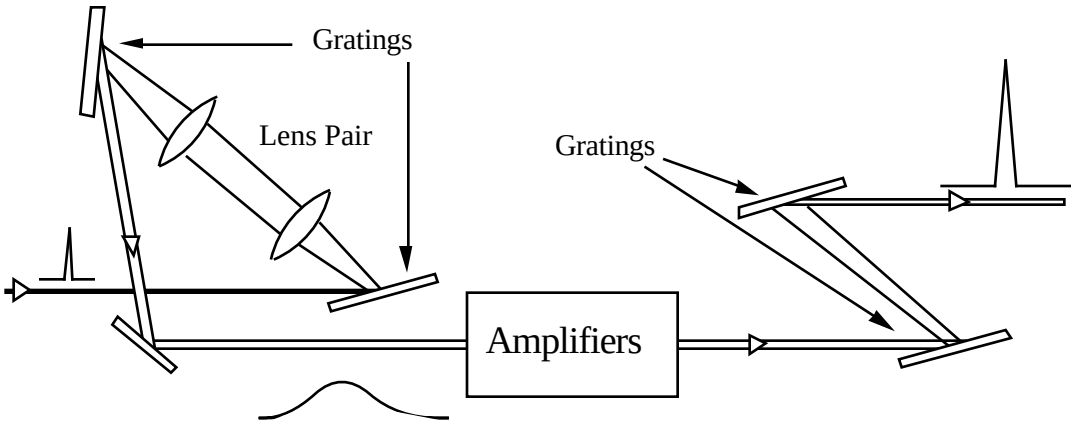

Figure 3.14: Chirped-pulse amplification of ultrashort pulses to very high peak power.

The idea of using diffraction gratings to stretch an optical pulse is based on the wide bandwidth of femtosecond pulses. The grating geometry was first proposed by Treacy in 1969 [257]. The concept is quite simple, as illustrated in figure 3.15. A short pulse with consequent wide bandwidth is dispersed by a diffraction grating. Another diffraction grating can then be used to recollimate the dispersed light, and it is easy to see that light of different

frequencies travels different path lengths. This results in a pulse that is longer in time than the original, and also has a frequency "chirp" on it-- in this configuration blue light travels a shorter path than red, and therefore the instantaneous frequency of the pulse varies linearly as a function of time. Although the output beam is also dispersed in space (the red light is on one side, the blue on the other), this can be easily eliminated by retro-reflecting the beam through the grating pair. A double pass configuration also gives twice the stretching.

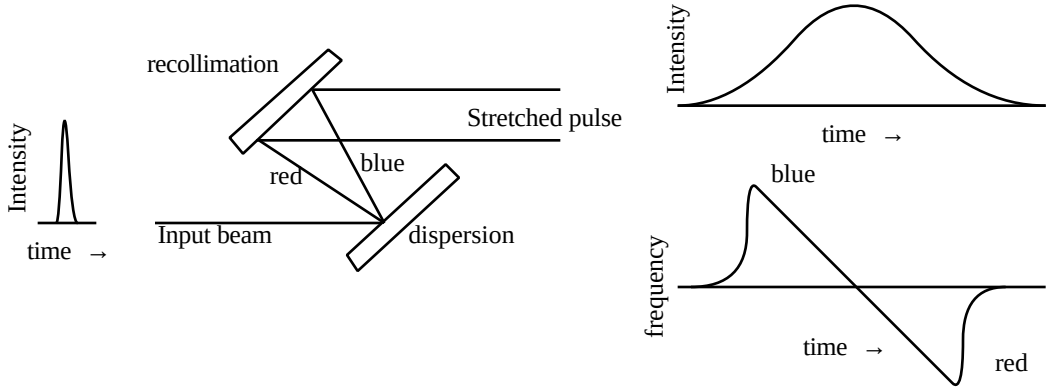

Figure 3.15: Optical pulse chirp using a grating pair.

Martinez [252,253] showed that the sign of the dispersion can be reversed by putting a lens pair between the two gratings. In this way, the blue light will travel a longer path length. Thus, a grating compressor as in figure 3.15, back-to-back with a grating pair-lens configuration, can convert a short pulse to a long pulse, and then back to a short pulse [252,254]. When the pulse is long, it can be amplified in Ti:sapphire, resulting in high peak-power pulses. This concept has been recently demonstrated using an Alexandrite laser medium [255]. Alexandrite is another broad bandwidth laser material similar to Ti:sapphire, except that it has a narrower bandwidth but a lower gain cross section than Ti:sapphire. Pulses of a few mJ in 300 fsec were produced in this manner.

A laser system based on this chirped pulse amplification technique is now under construction in this research group. I have done the preliminary design of the system, and graduate students Alan Sullivan and Harald Hamster are currently constructing it. The peak of the gain curve of Ti:sapphire is at about 800 nm, so that a source of <100 fsec optical pulses with a wavelength centered at 800 nm is necessary. Knox [258] has recently demonstrated a synchronously-pumped dye laser using the dye LDS-798 (Exciton Chemical Co.) and the saturable absorber HITC-I, which is capable of producing 80 fsec pulses centered at 807 nm. I have designed and Alan has constructed a copy of this laser, which is operating at similar pulse length to Knox's performance. The very stringent (<100 nm) cavity length stability requirements of this laser result in low amplitude stability for this laser. However, active cavity length stabilization, which has been demonstrated in similar synchronously-pumped laser systems [259], may be capable of stabilizing the system. Other problems that were encountered in operating the laser were (1) extra pulses circulating in the dye cavity, due to placement of the laser mirrors (the exact configuration that Knox used was the only successful configuration of several that we tried); (2) the wavelength bandpass of the cavity mirrors must be centered shorter than the laser wavelength, to keep the laser running at ~800 nm; and (3) oscillations in the dye jets, due to excessive pressure drop in the feed tubes to the sapphire dye jets. Recently, other methods of producing 800 nm femtosecond pulses, using traveling-wave ASE amplification [260], or the correct dye combinations in a more-stable colliding pulse mode-locked laser, or compression of picosecond 800 nm pulses to the femtosecond level, have been demonstrated.

The pulses from the synchronously-pumped laser have an energy of about 0.1 nJ, and thus must be amplified by a factor of ~10^{10} to reach the joule level. This is done by a series of Ti:sapphire amplifiers, pumped by a Quanta-Ray DCR-4 laser (Spectra-physics, Inc.), and by a Candela dye laser for the last stage. The spontaneous lifetime of Ti:sapphire is

about 3 μsec [249]; thus excitation pulses of a few microseconds or shorter are necessary to excite the Ti:sapphire. The Quanta-Ray has a pulse length of 10 nsec, while the dye laser has a pulse length of ~2 μsec. The peak of the pump-band absorption for Ti:sapphire is at about 490 nm, and is ~100 nm wide; the frequency-doubled 532 nm light of the Quanta-Ray, and the 490 nm light from the dye laser are both appropriate pump energy sources. Ti:sapphire can be pumped at intensities up to the level of a single-pass gain of ~$\mathbf{e}^5$ (=150) in a single pass; thus a total of <10 passes through the amplifier rods is necessary to get to ~1 Joule output. The initial stages will be pumped by a small amount (~10 mJ) of pump energy, focused to a small (~100-500 μm) spot to produce high gain-- hopefully the small pump beam, with the crystal at the focus of the beam, will avoid the beam non-uniformities that can result in locally high power densities which can cause crystal damage [245]. The final stages would be run at low amplification (~$\mathbf{e}^{2\text{-}3}$ ≈10) to avoid possible damage(occurring at a pump laser intensity of 10-20 J/cm^2 using a 10 nsec pulse [247]). Ti:sapphire amplifiers have a demonstrated conversion efficiency of ~30% from pump laser energy to amplified energy. Thus, a dye laser pulse of ~4 joules should be sufficient to amplify the pulses to ~1 joule. Even higher power (~100 J) dye lasers which run at low repetition rate are currently available, so that ultrashort pulse lasers of tens of joules should be possible in the near term.

Figure 3.16 shows a preliminary design of the laser system. The grating pulse stretcher used (designed by H. Hamster) will be a four-pass configuration with a grating separation of about 2 meters. On a single pass, one can stretch a pulse by a time comparable to the physical dimensions of the diffraction grating-- ~100 psec. Thus, four passes are required to stretch the pulse to the few hundred psec level desired. The compressor gratings are used in a double-pass configuration to minimize energy loss through the compressor (~20% loss per reflection).

There are a number of subtleties that must be taken into account in the laser system. Group velocity dispersion due to the pulse traveling through the Ti:sapphire amplifiers must be compensated for by the final set of compression gratings. This results in a slight mismatch between the grating expander and the compressor (resulting from higher-order terms in the dispersion function produced by the gratings), which places a limit of ~50 fsec on the attainable pulse length, unless more complex compensation is done. Pulses being amplified to energies of the saturation flux and above are subject to distortion, because the gain in the amplifier is being significantly depleted as the pulse passes through it. For very short pulses, this results in a broadening in time of the pulse. However, for chirped pulses, Harald Hamster has shown that the pulse broadening broadens the spectrum of the amplified pulse (since it is chirped), resulting in shorter pulses after compression. The last design consideration is that currently available diffraction gratings are the weak point in the system damage-wise-- the best can be used only at flux levels of <0.1 J/cm^2 without risk of damage. The output beam must therefore be expanded by a lens pair before passing through the grating compressor. However, sufficiently large gratings (Milton Roy Co.) are currently available to compress pulses of one or a few joules. In the future more robust gratings may become available.

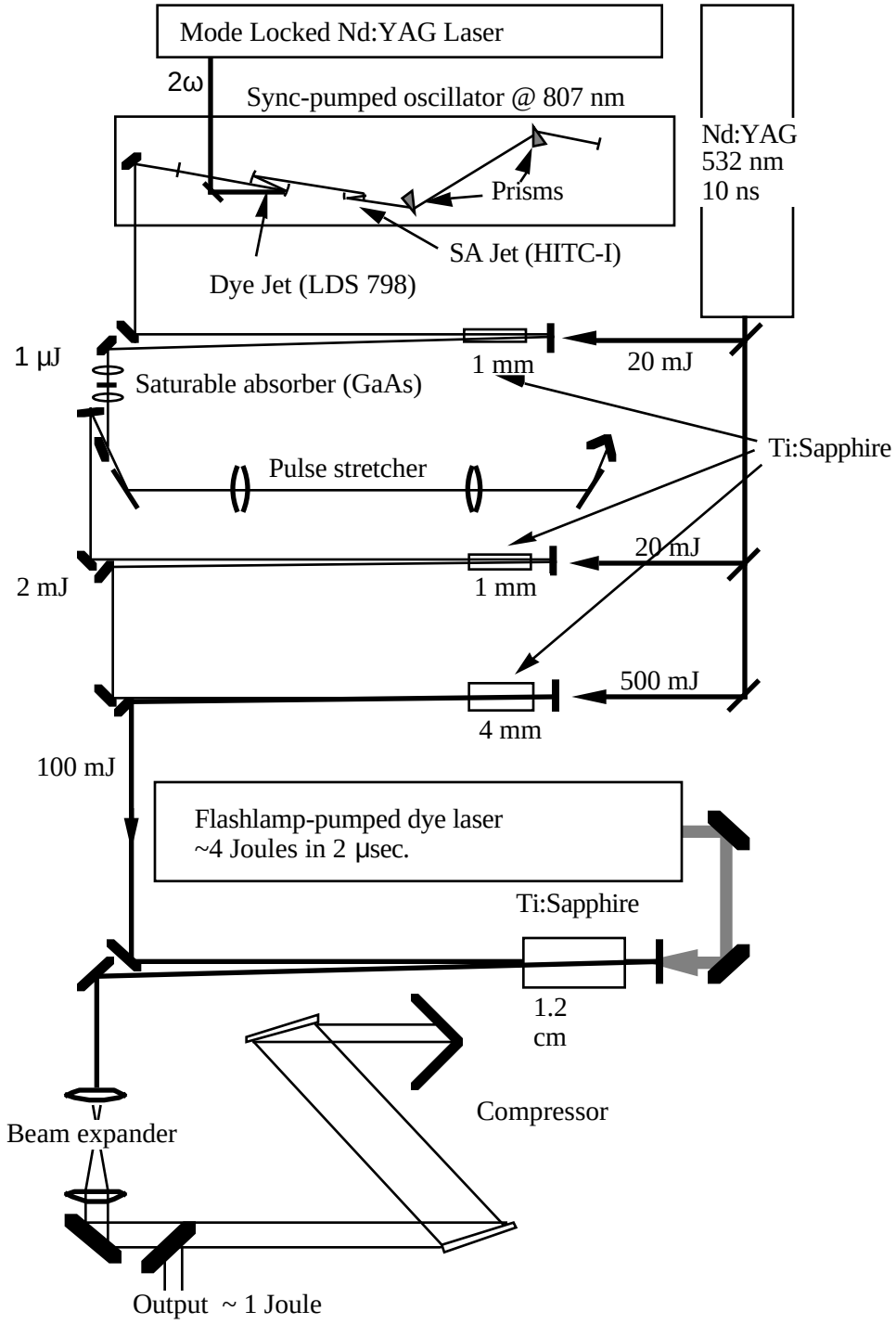

Figure 3.16: Preliminary design of titanium-doped sapphire laser system capable of producing >1 Joule in 50 fsec.

3.4.2 Traveling-wave excitation for x-ray lasers

The successful demonstration of the neon K-α laser would require the use of a traveling-wave excitation, so that the excitation pulse producing the gain moves synchronously with the x-ray pulse being amplified. This will allow the necessary gain-length of ~1 cm while the gain lifetime is only ~50 fsec. The basic scheme behind the traveling-wave setup is shown in figure 3.17. The concept is very similar to the pulse compressor of figure 3.15, in that a grating is used. However, in this case, the grating very directly produces a linear delay that varies spatially along the beam. This beam can then be line-focused in such a way that the excitation pulse travels along the target at the speed of light, if the two distances **d** in the figure are set equal. This requires proper selection of the groove spacing of the grating (to get the diffraction angle correct), and of the line focus length. A reflective focusing optic can be used to focus the beam; a paraboloidal reflector, used slightly off-axis so that the transverse and longitudinal directions focus at different distances, should be able to produce a very tight focus without chromatic dispersion. Novel line-focus configurations using spherical mirrors [261] may also be applicable.

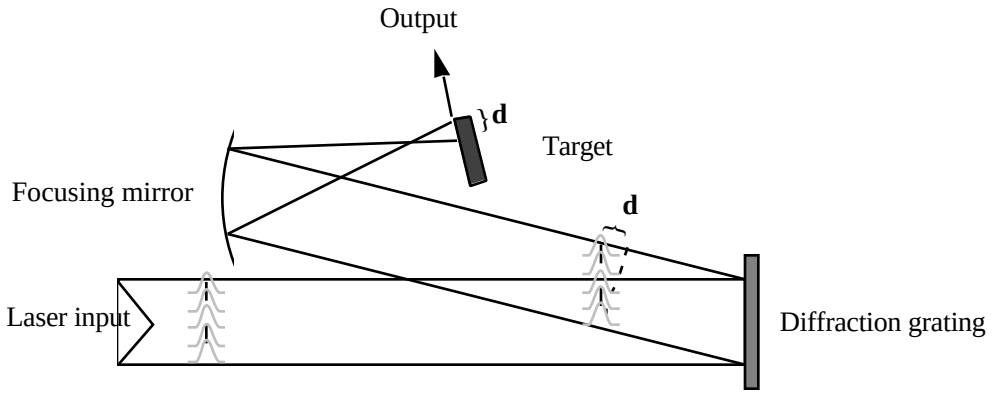

Figure 3.17: Traveling-wave excitation setup.

The idea of using a diffraction grating to provide a spatially varying delay originated in an autocorrelator design [262], and has also been used to provide traveling-wave amplification in laser dyes [263,264]. It is also the same as the traveling-wave geometry used by Barty et al. [108] to demonstrate the Cesium VUV laser discussed previously. The setup of figure 3.17 is somewhat complicated by the fact that the grating dispersion due to the bandwidth of the laser pulse will cause some smearing in the traveling-wave excitation. This occurs since different wavelength components travel different paths. However, this effect results in a linear chirp at the target (the red light arrives too late, the blue too early), which can be easily compensated for by adjusting the grating compressor so that the output beam has a slight negative (red-to-blue) chirp. One possibility that I have not examined is to combine the grating compressor with the traveling-wave setup. Probably one of the three gratings in the system could be eliminated, and two gratings with different groove spacings would be used in the compressor.

Another important attribute of the traveling-wave geometry of figure 3.17 is that the propagation speed of the excitation can be set to any speed $<\mathbf{c}$ or $>\mathbf{c}$. This is important in that the propagation speed of the light being amplified may be modified by the presence of laser gain, as described by equations 2.8-2.10. For the neon laser which is naturally broadened, this works out to $\beta = c\,\mathbf{G}\,\tau_{AUGER} \approx 10^{-3}$, so the propagation speed in this case is $0.999\mathbf{c}$, and this effect is of marginal importance. However, for other systems such as the Duguay sodium laser or the neon $(2\mathbf{s})^{-1}$ to $(2\mathbf{p})^{-1}$ transition at 46 nm, this factor may be important and should be accounted for in the traveling-wave excitation.

3.4.3 Neon K-α laser target geometry

A possible target geometry for the neon laser is shown in figure 3.18. A neon-hydrogen gas mixture can be frozen onto the backside of a thin multilayer target, using helium-cooled shroud to keep the mixture from melting [81,210]. The multilayer target could be supported by

a series of fork-like prongs so that dozens or hundreds of shots could be done on a single target by advancing it after each shot. The gas mixture would probably evaporate after every shot; however, with continuous gas flow the mixture could refreeze, and a repetition rate of ~1 min^{-1} is conceivable.

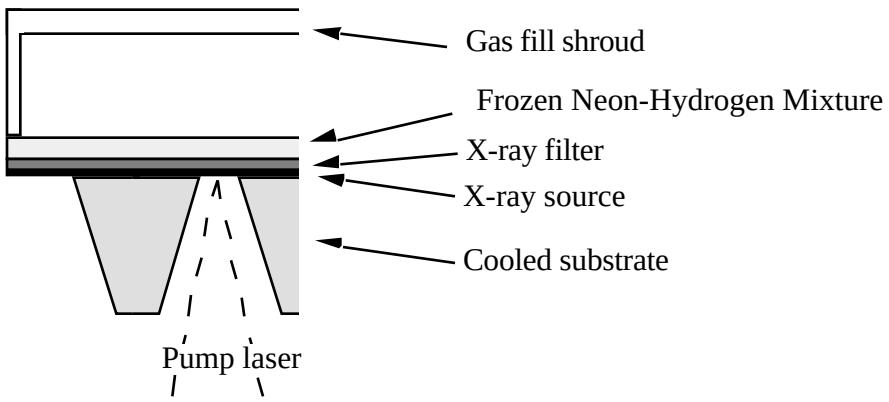

Figure 3.18: Possible neon K-α laser target geometry.

3.4.4 Conclusion

The technology for producing ultrashort pulses with energy of >1 Joule is now available. All that remains to be done is to put all the components together. Such a laser system would not only be useful for experiments relating to the neon K-α laser scheme, but also for a multitude of experiments in the physics of matter subject to very high (up to 10^{20} W/cm^2) power densities. Much of the physics relating to the K-α laser scheme is also of general interest. Techniques exist for implementing the traveling-wave excitation geometry necessary for the K-α laser scheme, and there are no other fundamental technological problems to be solved. However, nearly all of the technology I have discussed is state of the art, and thus is not trivial to implement.

Final Conclusion

In this thesis, I have discussed the past, present, and future prospects for photoionization-pumped short-wavelength lasers. The major experimental accomplishment was the first demonstration a VUV laser system based on photoionization pumping followed by Auger decay. These experiments unequivocally demonstrated a population inversion on two transitions, at 90.7 nm in krypton III, and at 108.9 nm in xenon III. Analyses of the experiments yield a good understanding of these laser systems, and illustrate the remarkable simplicity of the mechanisms involved in the laser. General considerations in the design of photoionization-pumped lasers are also discussed.

The major theoretical accomplishment was to develop a scheme for constructing an x-ray laser based on photoionization pumping by ultrashort plasmas. This scheme is based on one of the first x-ray laser proposals, and recently developed technology, along with a few novel innovations, make this scheme now a possibility. Numerical simulations of this x-ray laser, in neon II at 1.46 nm, demonstrate its feasibility. The technology necessary for its implementation is also discussed, and is shown to be feasible.

For number sequence only.

Appendix A: A Streak Camera with a MCP Photocathode

This appendix covers the characterization of the microchannel-plate streak camera [265] used in the gain demonstration experiments. Most of this characterization data was taken using a low-light level CCD imaging camera connected to an IBM PC AT, as opposed to the calibrated film used for data recording in the gain experiments. Although there is no direct cross-calibration between the film intensity and the CCD intensity scales, an approximate (photons / intensity) calibration can be inferred, as will be discussed. The streak camera and CCD camera have been used in varying incarnations in several other published experiments [198,266]. The persons involved with the construction and characterization of this instrument are G.D. Power at LLNL, and W.W. Craig and J. Schachter at UCB, as well as myself and Roger.

The camera is a modified commercial soft x-ray streak camera (Kentech Instruments Ltd.). This camera uses a microchannel plate (MCP) as a photocathode instead of a conventional thin film metal or CsI on plastic photocathode. The use of a microchannel plate as a streak camera photocathode was first demonstrated by Wang et al [267]. The MCP is rugged and permits gain in the front end of the system, allowing single photon sensitivity. Bare or CsI coated microchannel plates have good quantum efficiency for photons from the ultraviolet into the γ ray region of the spectrum. Transit time spread in the MCP limits the time resolution of the camera. However, we have demonstrated a time resolution of better than 200 psec. In this paper we also discuss the use of a CCD camera connected to a microcomputer for data acquisition. This system allows instant access to the acquired data, and has a dynamic range of over 3 orders of magnitude without adjusting camera operating parameters.

The x-ray streak camera was modified as shown in figure A.1. A variable 0-1 kV floating power supply is connected to the usual 15 kV photocathode power supply. In this

way a variable voltage can be supplied to the MCP without disturbing the 15 kV accelerating voltage. The MCP-grid spacing is about 4 mm. The MCP used in these tests was an uncoated 25 mm diameter plate (Galileo Electro-optics), with a 12 μm pore size and a 500 μm thickness.

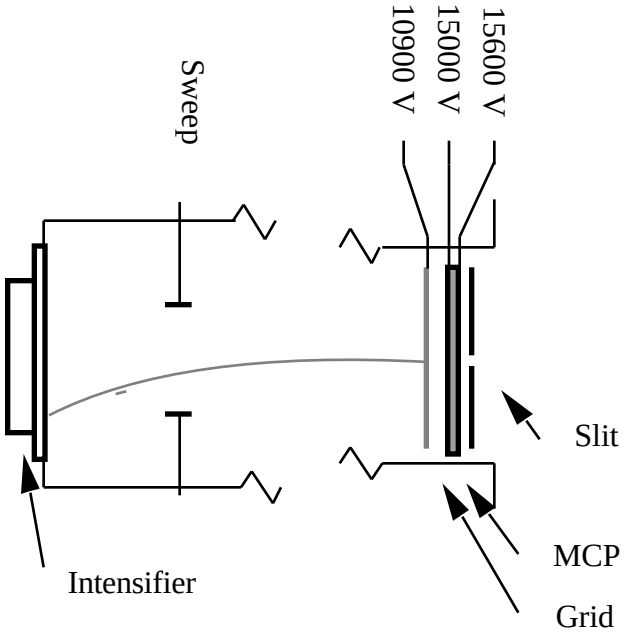

Figure A.1: Simplified diagram of the MCP photocathode streak camera.

An image intensifier (ITT F-4113) is used on the output of the streak camera; the intensifier was run at the maximum gain setting for all measurements presented here. Data is recorded with a high sensitivity thermoelectrically cooled CCD camera (Photometrics model CH 183), using a 56 mm wide field lens (JML Optical) to image the intensifier output onto a 384 x 576 pixel CCD array (Thomson CSF model TH7882CDA). The lens is about 15 cm from the intensifier and 5 cm from the CCD. The CCD pixel size is 23 μm, and considering the lens demagnification, the imaged field is 60 μm per pixel referenced to the intensifier plane. Through the Photometrics model CC 180A camera controller and a direct memory access interface, the image is transferred to an IBM PC AT computer and

displayed on an IBM professional graphics adapter. The intensity resolution of the camera is 14 bits with a noise level of about 1 count. A single image is approximately 400 kbytes of data and can be transferred into the computer in about 5 seconds, and displayed in another 15 seconds. The computer software (CCD-- Appendix B) does background subtraction, bad pixel elimination, and flat fielding if necessary. The image can then be examined by changing the false color scale of the image, and by taking lineouts in the time or space dimensions.

The apparatus used in taking the characterization data is shown in figure A.2. A Q-switched, mode locked Nd:YAG laser (Quantronix 416) outputs a burst of 100 psec long pulses, and an electro-optic cell is used to select one of these pulses. The pulse is double-passed through a Nd:YAG amplifier, and second and fourth harmonics are generated in KDP crystals. A maximum of 40 μJ at 266 nm is produced, which illuminates the streak camera slit. The entire system is timed using a Stanford Research Systems DG535 digital delay generator. The time duration of the 266 nm pulse was not measured but was assumed to be ~50 psec because of pulse shortening in the harmonic generation process.

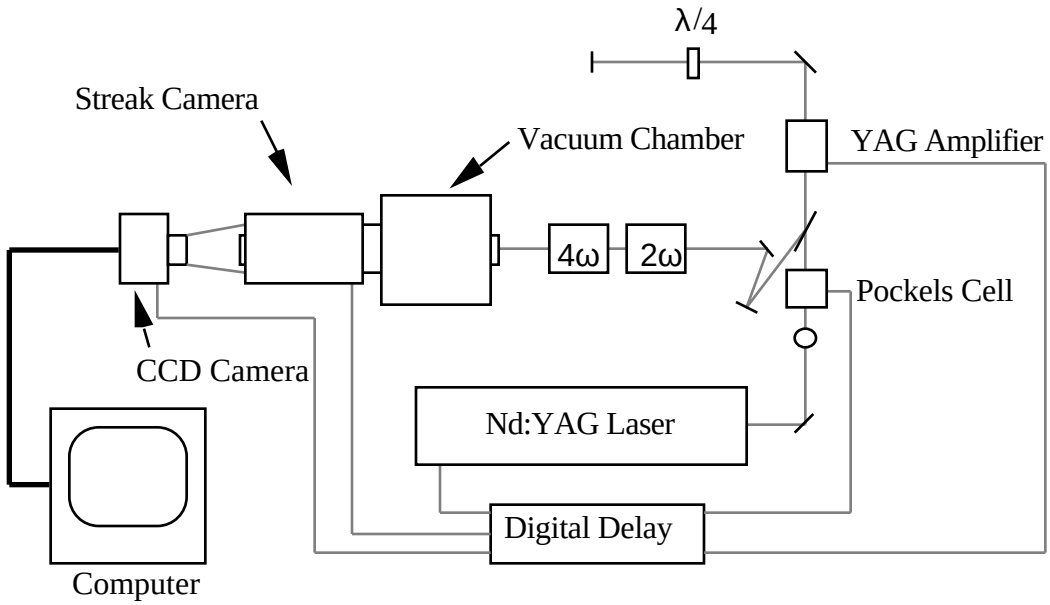

Figure A.2: Streak camera characterization setup.

The linearity of the streak camera was determined by comparing input laser energy, measured using a UV photodiode and various attenuators, with the peak intensity on the CCD image. The was done at two MCP voltage settings, as shown in figure A.3. As is seen, the instrument is linear until an output level of about 8000 out of a maximum CCD pixel intensity of 16384 counts. This saturation level is independent of the MCP voltage, indicating that saturation is occurring in the image intensifier or the CCD camera. Since the CCD camera saturates at nearly 16000 counts if the streak camera is triggered repetitively, the intensifier appears to be the limiting element.

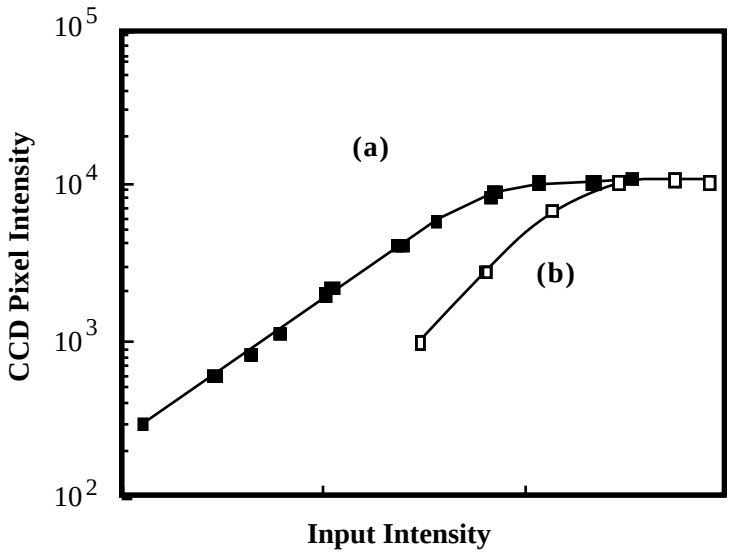

Figure A.3: Streak camera linearity at (a) 600 V, and (b) 488 V MCP potential for the streak camera-CCD system.

Pictures were taken using a defocused 266 nm beam at sufficiently low intensity that single photon traces were evident. At 600 volts on the MCP, single photons have an intensity of 2500 ± 1500 counts, spread over an area 7 pixels wide and 36 ± 8 pixels long (FWHM), at a sweep speed of 4.3 psec/pixel. This results in a peak pixel intensity of about 10 counts, well above the CCD noise level of 1 count. At slower sweep speeds or with better streak camera focusing, the peak pixel count for a single photon would be greater.

Data was then taken varying the MCP voltage. Figure A.4 is a plot of CCD intensity vs. voltage, in units of the single photon intensity as defined in the last paragraph. The FWHM time duration of the pulse as a function of MCP voltage was also examined. Assuming an input pulse width of 50 psec, the time resolution of the instrument vs. MCP voltage is plotted in figure A.5. At sufficiently high voltages, increasing transit time dispersion in the MCP accounts for the slow decrease in resolution with decreasing voltage. The behavior at low voltage can be explained by that fact that the MCP gain is unity at about 270 V, as

computed from figure A.4 and the manufacturer gain specification of the MCP at 900V. Thus below 270 V, electrons exit the MCP without multiplication.

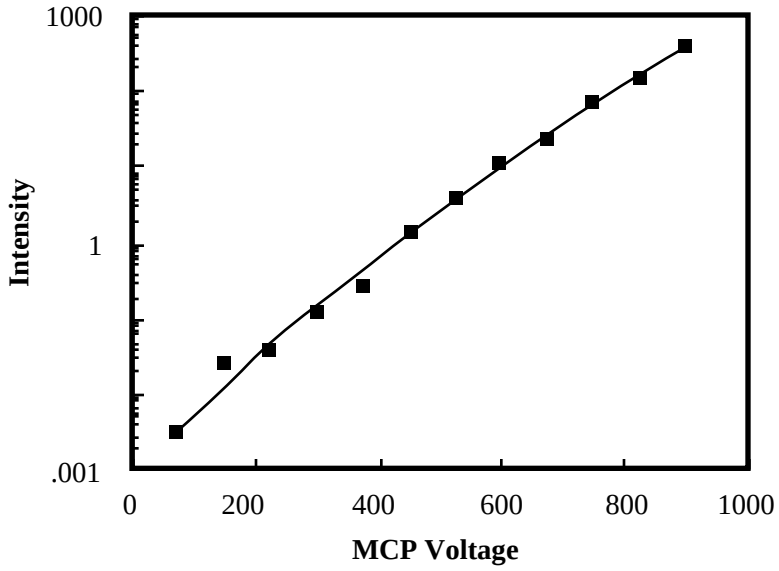

Figure A.4: Single photon level (in CCD pixel counts) vs. MCP voltage for the streak camera-CCD system.

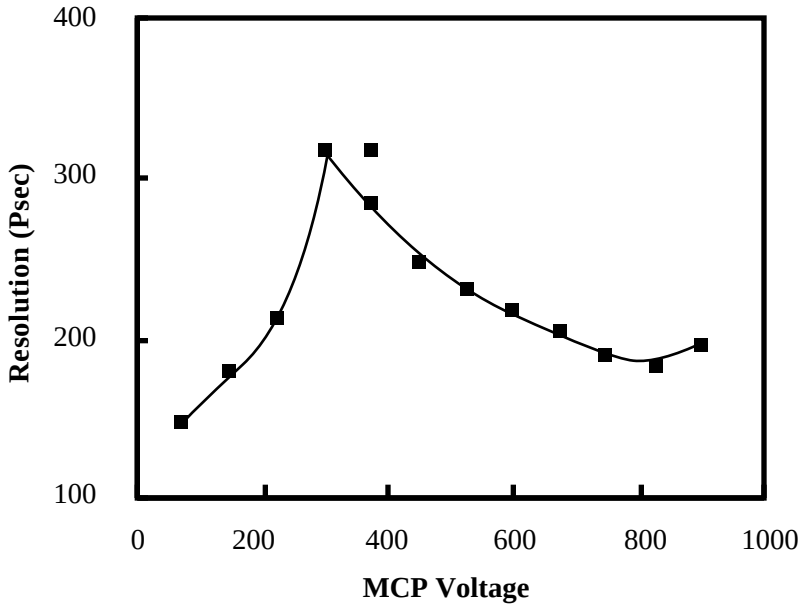

Figure A.5: Variation in streak camera time resolution with MCP voltage.

The time resolution of the streak camera is limited by the spatial and energy distributions of secondary electrons generated in the MCP. These secondary electrons have energies of up to a few hundred eV [268], with most having energy below 50 eV. This energy spread limits the time resolution to about 15 psec [269]. Therefore the major limiting factor is the time dispersion in electron emission. This dispersion has been estimated in computer models to be 200 psec [268], in agreement with our observation. Our observed single photon pulses are shorter in time duration than the actual time resolution of the camera. This is caused by the random path traversed by the initial photoelectron before multiplication, which has been measured to be 50 to 100 psec [173].

The camera was also used in a repetitively scanned mode. Using the CCD camera to integrate over 300 pulses, a FWHM of 230-270 psec was obtained at 600 Volts on the MCP. This compares with the 220 psec wide single shot trace. Thus the system can be repetitively scanned using the digital delay generator with little loss in time resolution. Using the digital delay also allows easy streak camera timing and accurate time scale calibration.

Figure A.6 shows the spatial response along the input slit at 600 V on the MCP, generated using a CW soft x-ray source (carbon K-α). The distance indicated is in terms of length at the image intensifier. Considering the streak camera magnification of 1.2, the slit response is flat along about 12 mm of the slit. More optimal focusing should increase the active area along the slit. The short period fluctuations in the response curve are approximately what is expected from photon statistics and are not necessarily characteristic of variations in streak camera response.

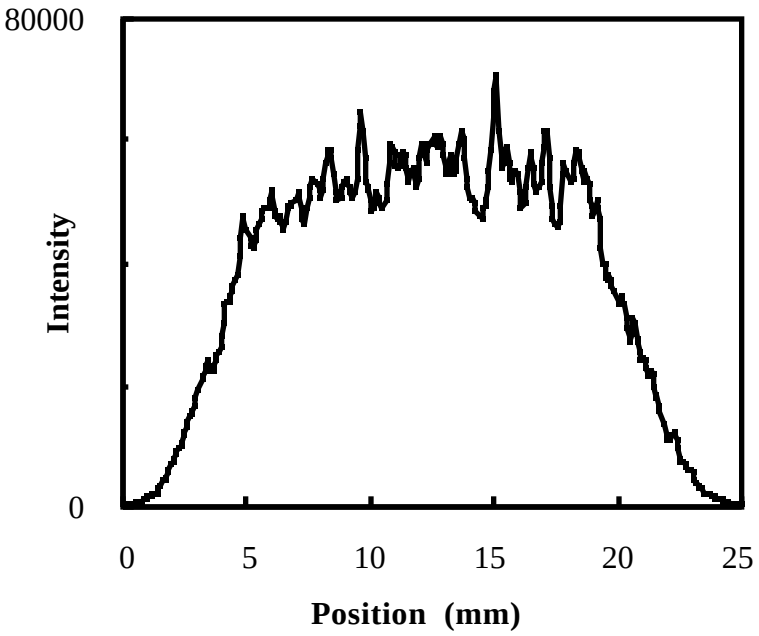

Figure A.6: CW Linearity of response along slit at 600 V MCP, performed using a Carbon K-α x-ray source. Intensity is integrated over 18 pixels.

An approximate cross calibration of the instrument when used with the calibrated film for the gain demonstration experiments is as follows. As evidenced in figure A.3, the saturation of the output due to the MCP intensifier is abrupt and repeatable. These saturated pulses have a profile in time which is flat-topped, as observed in the calibrationexperiments. The most intense data point from the gain experiment data of figure 2.5 also showed a similar flat-topped profile (as well as its peak intensity falling below the gain curve). This data point is saturated at a peak intensity of about 14,000, and thus this corresponds to a peak intensity of 10,500 counts on the CCD by figure A.3. A single photon is 2500 counts, with a count defined over a region of 1 pixel = $(60\ \mu m)^2$, for a conversion of (1 photon) / (9 counts-mm^2). Thus the approximate number of photons striking the photocathode in the case of a film trace is :

$$I_p * A * \frac{10{,}500}{14{,}000} * \frac{1\ \text{photon}}{9\ \text{counts-}\ mm^2} = \frac{I_p * A}{12}\ , \qquad \text{(A.1)}$$

where $\mathbf{I}_p$ is the peak intensity of the film trace and **A** is the FWHM area (in mm^2) of the film trace. This is only an estimate (probably good to within a factor of 2-3).

In conclusion, we have demonstrated the capabilities of a microchannel plate streak camera for doing time resolved studies in the VUV and soft x-ray region of the spectrum. Given that the single photoelectron level of the instrument is defined, and that the quantum efficiency of microchannel plates has been well characterized in other work [270], absolute flux calibration can be easily obtained with better than an order of magnitude accuracy and repeatability.

For number sequence only.

Appendix B: Software

A number of different software programs were written by me or by me in association with another person during the course of the thesis research. Any one who has an interest in obtaining any of the programs can contact me. This appendix contains basic operating instructions for the programs-- for the most part this is the first formal documentation for these programs. For detailed information on the codes themselves, refer to the comments in the source code. With the exception of the first data acquisition program (which is in Microsoft FORTRAN), all code is in Pascal. The data acquisition programs are for IBM PC's and are written in Borland Turbo Pascal, while the numerical simulations programs have all been transferred over to run on THINK Lightspeed Pascal v.2.0 on a Macintosh or MAC II.

B.1 Data acquisition programs

B.1.1 Monochromator control program SCAN

This program was written to take spectral scan data while controlling the Acton model 551 grazing incidence monochromator. Figure 2.31 is data taken using SCAN. The conversion of monochromator reading (in inches) to x-ray wavelength, or photon energy, is not linear; all data presentation must therefore linearize the data. The conversion relation is given in the monochromator manual. The monochromator is controlled using a Stanford Research Systems model SR245 computer interface, connected to the **COM1** RS232 serial port of the IBM PC. A small custom circuit was connected between the SR245 8-bit digital I/O port and the Acton model 786A monochromator stepper motor control unit, to control monochromator speed and direction of motion. A Hercules graphics card was used for the CRT display. The absolute position of the monochromator was kept track of by the computer using the **B2** input of the SR245 to count the motion strobe pulses from the

786A. Although the counter in the SR245 can only count modulo 65536, using timing in the computer, it is possible to successfully keep track of the carriage position in the software, with only an initial calibration input when SCAN is first run. Data is taken using the SR245 **#1** input to sample the MCP output through a Stanford Research Systems SR250 Boxcar integrator, using the SR265 **B1** input for the data strobe. The data rate must be accurately known for the software to properly keep track of the carriage position.

The operation of this program is relatively simple. The available commands are: (activated by the highlighted letter)

(**S**)can -- initiates a data acquisition scan. If this is the first scan after initializing the program, it will ask the current monochromator carriage position, the grooves/mm grating used, the limits for the current vacuum bellows in use, and the grating order. An answer of no change for the carriage position (<CR> only) will assume all other parameters are unchanged. After initializing the position, the scan command will ask for the starting and ending scan positions, and the scan speed. The positions can be entered either as inches, or as Angstroms (by appending an **a** to the end of the number), or as eV (by appending an **e**). The valid spectrometer speeds are 0.0004, 0.0008, 0.0016, 0.004, 0.008, 0.016, 0.04, 0.08, 0.16, 0.4, 0.8, 1.6, and 4 inches per minute. In the current interface hardware, either the 0.0008 and the 0.08, or the 0.008 and 0.8 speeds do do properly operate (this will be manifested by a grinding noise and improper tracking of carriage position). A title for the data is also asked for. After entering the parameters, the computer moves the carriage to the starting position, and waits for a manual input to start the scan.

(**P**)lot-- Plots the data. The endpoints can be given in inches, eV, or angstroms, as in the scan command. The full scale is in volts. If an **m** is appended to the full scale, a cursor will appear on the plot that can be used to mark the positions of spectral lines. To move the cursors, the **g**,**h**,**k**, and **l** keys move the cursor left fast, left slow, right slow, and right fast,

while the **j** key marks a position. The **prtsc**-**1** key sequence can then be used to print the spectrum.

(**R**)ead-- Reads a data file from disk.

(**W**)rite-- Writes a file to disk.

(**A**)verage-- Smooths the data points. Algorithm is to replace each data point with: $\mathbf{D}_{new}(\mathbf{n}) := {}^{1}/_{4}\mathbf{D}(\mathbf{n}\text{-}1) + {}^{1}/_{2}\mathbf{D}(\mathbf{n}) + {}^{1}/_{4}\mathbf{D}(\mathbf{n}+1)$. The program asks how many times to repeat this algorithm on the data. The title of the data can also be changed if desired.

(**B**)aseline-- Subtracts a constant voltage from the data, if the baseline of the data is not near zero.

(**D**)ivide-- Reduces the number of data points in the data set by the given factor. Generally, a good way of smoothing the data to show the spectral peaks is to divide it by the proper factor to give ~1000 data points, then to average 5 times.

(**M**)oveto-- Moves the monochromator carriage to the specified position, in inches, eV, or Å. Useful when looking at the intensity on a specific line, or when positioning the carriage to vent the monochromator.

(**C**)hange-- Changes the endpoint of the data, in case the program loses track of the carriage position. The command generally was not used, since the program keeps track of movement very well.

(**E**)xit-- Exits the program.

The program consists of 13 FORTRAN subroutine files, and one assembler routine, with a total of 700-1000 lines of code. It can be compiled and linked using the COMPILE.BAT file supplied.

B.1.2 Multichannel analyzer program MCA

Program MCA is a general purpose multichannel analyzer program, written especially to acquire and analyze time correlated photon counting data for the florescence spectroscopy experiments. It runs on an IBM PC, using a Hercules graphics card for display. Data acquisition is done using a Stanford Research Systems SR245 computer interface module. This module has a ±12 bit analog to digital converter, with a resolution of 0.0025 Volts, and a full scale of 10.240 V. For program MCA, only positive voltage input is used-- a voltage reading of less than zero is equivalent to zero volts. The SR245 is trigger by bit B1, and every time data is read in, the channel number corresponding to the voltage is incremented. For example a value of 3.420 Volts when a trigger arrives will correspond to channel (3.420)/(0.0025) = 1368, and this channel will be incremented by one. Data input from the SR245 is interrupt driven with a 10,000 element data buffer so that commands (such as rescaling the window) can be entered and processed without loss of data. The program source is all in one file, MCA.PAS, and consists of about 1,000 lines of code.

In the program, a data display window is always present, and commands are entered using single keystrokes. If needed, prompts for more data appear at the bottom of the screen. Any of the number keys pressed immediately before another command will cause the command to repeat the specified number of times (only for commands such as rescaling). There is also a cursor marking a specific channel (data of which is given above the data window). Commands are:

Left arrow-- Move cursor to the left one channel.

Home(just above left arrow)-- Move cursor to the left twenty channels.

Right arrow-- Move cursor to the right one channel.

Pgup(just above right arrow)-- Move cursor to the right twenty channels.

"-"-- Move to a specific channel (Prompted).

up arrow-- Decrease full scale number of counts (y axis) of the data window.

down arrow-- Increase full scale number of counts (y axis) of the data window.

end-- Increases the full scale range (x axis) of the data window.

PgDn-- Decreases the full scale range (x axis) of the data window.

"+"-- Changes the range (x axis) so that the current cursor position is centered in the window.

RUN (**F1**)-- Starts data acquisition.

STOP(**F2**)-- Stops data acquisition.

SAVE (**F3**)-- Saves data in a file. Data format is a record of type **dataset**, as specified in the source code.

Shift-F3-- Saves the data in ascii format to be imported into other programs.

Load (**F4**)-- Loads a data file of format **dataset**.

Olap (**F5**)-- Overlaps the data, to consolidate individual decay curves from Q-switched, mode-locked laser data, as in figure 2.34, to obtain a single aggregate curve such as figure 2.35. The procedure for doing this is: (1) Move the cursor to the beginning of the first interval that you wish summed. (2) Press the Olap (**F5**) key. (3) Move the cursor to the beginning of the last interval to be summed. (4) Hit **<CR>**. (5) Enter the total number of intervals to be consolidated. (6) Enter the units for the x axis, and the separation between individual intervals in these units. In this way, the timescale can be calibrated if the decay curves are at exact (10 nsec in this case) intervals.

Fit (**F6**)-- Fits the data to an exponential decay. Fits data to an exponential decay, yielding the lifetime, and the statistical error. Procedure is: (1) Move cursor to beginning of interval to be fit to. (2) Hit Fit (**F6**) key. (3) Move cursor to end of interval. (4) hit **<CR>**.

Shift-F6-- Fits to the data corrected for pileup, as described by equation 2.13. For the pile-up to work properly, the trigger input **B1** to the SR245 must be configured to be triggered every time a data shot is taken regardless of whether a photon was detected. The cutoff (see "**c**" command) must be set to a channel number somewhat greater than #0. The purpose of the cutoff is that triggers where no photon was detected tend to accumulate in the lowest few channels. Counts in any channel below the cutoff are assumed to be counts where no photon was detected.

Clear (**F7**)-- Clears the data file.

Sum (**F8**)-- Sums the total number of counts in the specified interval. Procedure is: (1) Move cursor to beginning of interval to be fit to. (2) Hit Sum (**F8**) key. (3) Move cursor to end of interval. (4) hit **<CR>**. **T** can be used to obtain the total number of counts in the data set.

Scal (**F9**)-- Sets the x axis scale of the data. Procedure is: (1) Move cursor to beginning of interval to be scaled to. (2) Hit Scal (**F9**) key. (3) Move cursor to end of interval. (4) hit **<CR>**. Then enter the units and the spacing in these units for this interval.

Titl (**F10**)-- Changes the title to the data set.

" " (space bar)-- Renormalizes the units so that the cursor is at the zero position.

"**a**"-- Averages the data set to smooth it. Uses the algorithm $\mathbf{D}_{new}(\mathbf{n}) := {}^1/_4\mathbf{D}(\mathbf{n}\text{-}1) + {}^1/_2\mathbf{D}(\mathbf{n}) + {}^1/_4\mathbf{D}(\mathbf{n}+1)$.

"**s**"-- Finds the center position and the standard deviation from this value for the peak within the desired interval, defined in the usual way.

"**c**"-- Sets the cutoff point for the pile-up correction (see **shift-F6**) to the current cursor position.

"**d**"-- Divides the data, binning data points to reduce the total resolution. Asks reduction factor by which the data is to be reduced.

"**p**"-- Superimposes an averaged (using the same algorithm as the "**a**" command) line onto the data, so the printed data is more visible. Does not alter the data. Asks how many times to average the line, and whether printing is desired.

"**X**" (capital letter only)-- Exits the program.

B.1.3 Streak camera imaging program CCD

Program CCD controls acquisition and simple processing of images on an IBM PC AT for a Photometrics Ltd. Model CH 183 CCD camera head, equipped with a model CC 180A controller using specially modified controller software. The CCD camera images the output of the streak camera using a fast (f1.2) lens. (JML Optical). The CC 180A controller is connected to the PC AT using a custom interface circuit, utilizing the DMA controller chip on the AT motherboard to do fast data transfer into the computer's memory. The image is then displayed on an IBM professional graphics adapter using a false color map. The program was written by me and by Jon Schachter, with some additions by Jing Zhu.

The CCD camera uses a format of 384 x 576 pixels, with an intensity resolution of 14 bits (16,384). After the CCD camera is triggered (using an external timing signal conditioned by a custom box), the data is transferred in 16 bit words (1 pixel / word with 2 unused bits) using the processor's high-speed DMA. This process takes ~5 sec. Display of

the data on the monitor takes an additional ~15 sec. Background subtraction is generally necessary for the image, to obtain the best signal to noise ratio. This process takes ~40 sec. The picture can also be flat-field adjusted to account for variations in quantum efficiency of the individual pixels. Also, rows or columns in the CCD imaging element which are defective due to a bad pixel can be replaced with the averaged value of the surrounding pixels.

The program source is in Borland Turbo Pascal version 3.0. An attempt to port it over to version 4.0 failed on the initial attempt. Some of the DMA transfer code seems to be sensitive to processor timing. The program is in two chained files, CCD.PAS and CCD2.PAS, and is about 2800 lines long. One image takes up 443 kilobytes of memory--the program and the one image barely fit in the maximum 640K memory.

The region of the image being analyzed is bracketed by two cursor lines in the **x** direction and two in the **y** direction. Motion of the cursors is controlled with the **left**,**right**,**up and down arrow** keys. In addition, the **ins** and **del** keys control whether the left and top cursor lines, or the right and bottom cursor lines, or both, move with the arrow keys. The current cursor mode is displayed on screen. It is important to note that the cursors bracket the region of interest; therefore the position of the cursor line is one pixel shifted from the pixel number displayed on the side of the graph. This is important to note if measuring distances using the cursors.

Other commands include:

"**D**"-- Take a picture. Asks the title of the picture, and the file name to be used (default in brackets), if the automatic save mode is on. In entry of the title, if the string typed in starts with "--", the text following will be substituted into the previous title to replace the portion of the previous title past the "--' sequence.

"**S**"-- Save an image onto disk. This takes ~45 sec.

"**L**"-- Loads an image.

"**?**"-- Help screen with available commands.

F1-- Rescale the false color intensity map. The False color map used to display the data is shown on the right-hand side of the screen. The **F1** key scales the map so that the colors corresponding to the extremes of the scale correspond to the least and most intense pixels within the region bounded by the four cursors.

Shift-F1 Rescales according to the least and most intense pixels in the entire picture.

F2-- Rescales as in the case of **F1**, but to a logarithmic intensity scale.

Shift-F2-- Analogous to **Shift-F1**.

"**0**"-"**9**"-- The number keys change the false color scheme used. "**0**"-"**5**" correspond to built-in professional graphics adapter (PGA) look-up tables, while "**6**"-"**9**" correspond to look-up table files on disk of name "LUT#.TBL". The PGA uses four bits intensity for each color red, green, and blue. The file format is apparent from examining an LUT file--the full scale resolution of the color table can be up to 251, with a few colors reserved for the program itself. I like the LUT9 table. LUT7 is a gray scale map.

F3-- Do a lineout in the x direction. Displays a two dimensional graph of the sum of the intensities of all the pixels between the two horizontal cursors. The graph is scaled according to the minimum and maximum total intensities in the region bracketed by the two vertical cursors. This command can be used to for instance look at the time history of a specific spectral line, if a spectrally dispersed image is incident on the streak camera slit.

Shift-F3-- As with **F3**, but scale the graph according to the minimum and maximum value along the entire length of the graph.

Control-F3-- As with **F3**, but the intensity scale is input from the keyboard using prompts.

F4-- Same as **F3,** but does lineout in the y direction.

Shift-F4-- Analogous to **Shift-F3** for the y direction.

Control-F4-- Analogous to **Control-F3** for the y direction.

" "(space bar)-- returns to the image view from the lineout view.

"<"-- Writes the data corresponding to the lineout into an ascii file, for further analysis or presentation. Will ask for file name. Use only while in lineout mode.

">"-- Transfers the data of the lineout into a temporary array buffer, for use with the following commands:

"*****"-- Multiplies the buffer array by the present lineout array. First do one lineout, use ">", then move the cursors and do another lineout. Then use the "*****" command. The product of the two arrays will then be graphed. The stored array can also be shifted by a specified number of pixels before being multiplied, in case of slight offsets.

"/"-- Divides the present lineout by the buffer array. The stored array can also be shifted by a specified number of pixels before being multiplied, in case of slight offsets. This command can be used, for instance, to look at the time history of a spectral line, normalized to the intensity of another line.

"**X**"-- Rescales the x axis. Procedure is: (1) Position the left and the right cursors to bracket the desired interval. (2) Press "**X**", (3) Enter the new label of the x axis, the position in these units for the left cursor, and the position for the right cursor.

"**Y**"-- Analogous to "**X**", but for the y axis.

F5-- Zero the left-hand cursor on the x axis scale, leaving the scaling, in for example, mm/pixel, unchanged. Useful for measuring distances.

Shift-F5-- Zero the right hand cursor analogous to **F5**.

F6-- Zero the top cursor on the y axis scale.

Shift-F6-- Zero the bottom cursor.

"**T**"-- Enter new title to picture.

"**Z**"or "**+**"-- Zooms the picture. The picture will zoom to the highest magnification that will still fit the cursor region. If the picture currently is zoomed in, returns to normal (full screen is full picture) size. **Note:** The current software will not do lineouts properly when the picture is zoomed.

"**P**"-- Parameters menu. Displays a screen to allow one to alter settings as follows:

> "**k**"-- Change name of background file to be subtracted from data. After a picture is taken, the program automatically subtracts this file from the new image. If the file name is preceded by a "**?**", the file will not be automatically subtracted before being displayed. The "**B**" command can then be used to subtract the background if the picture is to be saved. One can check if the background has already been subtracted in this mode by observing the file name displayed in the parameters screen.

"**b**"-- Changes the name of the bad pixels definition file to be used. The bad pixels file contains information on rows or columns of pixels in a particular CCD chip which are defective. The bad pixels file is in ascii, and specifies rows, columns, or blocks of pixels in a format self-apparent by examining the file.

"**f**"-- Changes the flat field file to be automatically used after taking a picture, or for the "**F**" command.

"**g**"-- Changes the gain level of the CCD camera. Not implemented as yet, so use a gain-level of 1.

"**o**"-- Changes the shutter time to be used for the CCD. A positive number sets the shutter to the specified number of milliseconds, or a negative number sets the shutter to the number of seconds. Enter numbers in milliseconds for <~1 sec.

"**s**"-- Changes the save mode for the CCD images. If **On**, the image is saved automatically after every image is acquired. If **Off**, it is not. If **Ask**, after displaying the image the program asks if you want it saved.

"**B**"-- Subtract the background from the current image. Uses the file name set in the parameters menu. Only use this command if you have entered the file name with a "**?**" prefix. Or, if you wish to subtract a background after taking a picture, enter a file name using "**k**" in the parameters menu, and then use "**B**".

"**F**"-- Flatfield the image. Uses the file name set in the parameters menu. If you wish to flatfield the picture after taking it, enter a file name using "**f**" in the parameters menu, and then use "**F**".

"**C**"-- Calculates the average pixel intensity for the image. This value is needed for the flat-field correction. If flat-field correction is desired, the procedure is as follows: (1) Set up the camera without a lens, illuminated uniformly by a lamp a reasonable distance away. (2) Take a picture. Adjust exposure or lamp brightness until a count of ~4000-8000 per pixel is obtained. (3) Use "**C**" command on the resulting image. (4) Save the file. (5) Enter the file name into the flat field file entry in the parameters menu. Flatfielding in general has been found to be of marginal value, so only use it if you have reason to believe it will improve things.

"**M**"-- Merges one flat field file into the presently displayed file, taking the average of the two pixel intensities for each pixel. Can be used to get a smoother flat field file. Not extensively tested.

"**E**"-- Finds the average pixel intensity in the region bounded by the cursors, and subtracts that value from the entire image.

"**V**"-- Gives the intensity values for the four pixels at the corners of the bounded region, as well as the total and average values within the cursors, and statistical deviations.

"**Q**"-- Quit the program.

B.2 Simulations programs

B.2.1 Time independent gain estimation programs GAIN4,5,6

Programs **GAIN4**, **GAIN5**, and **GAIN6** were used to calculate excited state densities in a gas excited by the x-rays from a laser-produced plasma. These programs do not simulate the dynamics of the gain as a function of time, but estimate the gain-length produced in a

particular geometry due to the cumulative flux emanating from the plasma. The general principles behind the programs are covered in more detail in sections 2.3.1 and 2.3.2.

The three programs **GAIN4**, **GAIN5**, and **GAIN6** share much code in common, but do simulations for different geometries. **GAIN4** simulates the geometry of a line-focus plasma illuminating a thin parylene-covered slit, as in the actual gain experiment. **GAIN5** simulates a line focus plasma without the slot, as in figure 2.17. **GAIN6** simulates a point focus plasma. The code consists of a large number of small units, so that units in common to all the codes can easily be used. I will discuss **GAIN4** in detail, and then discuss the changes for the other codes.

The parameters to be input into the **GAIN4** program are constants and variables defined in the unit **GAIN4VARS**. The program must therefore be recompiled with every new run. The constants are:

```
const
outfilename = 'output from gain';       {file name for the text output}
grph = 5;               {expansion factor for graphs}
                        {Graphs as a function of distance will print out for the full}
                        {distance range of nr*dr, and also only for distances}
                        {to nr*dr/grph, for an expanded scale close to the plasma}
pressure = 1.0;         {pressure of xenon in torr}
ncs = 2;                {number of cross sections for the gas used}
                        {for xenon, we have the 4d, and 5s,p combined cross sections}
ndists = 5;             {number of times to print info at specific distance}
                        {will print the photon distribution at distance specified in distance array}
                        {which is defined below in procedure initvars}
nr = 300;               {index for radius variables}
                        {densities will be calculated for nr different uniformly spaced distances}
dr = 0.05;              {corresponds to this many cm/step}
                        {spacing between distance points. calculation will run out to nr*dr}
ne = 600;               {index for energy variables}
                        {photon distribution, etc. will be calculated for ne different }
                        {uniformly spaced energies}
de = 0.5;               {corresponds to this many eV/step}
                        {spacing between energy grid points.  Calculation will run out to ne*de}
bbtemp = 30.0;          {blackbody temperature in eV}
lenergy = 55.0;         {laser energy in joules}
leff = 0.07;            {laser efficiency to X-rays}
plength = 8.00;         {length of plasma focus in cm}
```

```
clength = 9.00;          {length of channel illuminated by x-rays, in cm}
fnum = 30;               {f number of channel.}
                         { i.e. 9 cm long x 3 mm wide: fnum=30}
nl = 500;                {number of segments to break focus into}
                         {the line-focus plasma is split into this many small point focuses}
gain = 3.22e-13;         {gain cross section in cm^2 of transition}
ulbr = 0.0435;           {upper laser level branching ratio of Auger decay}
ulg = 1;                 {upper level degeneracy}
llbr = 0.0514;           {lower level branching ratio}
llg = 3;                 {lower level degeneracy}
filterfile = 'parylene.dat';     {parylene absorption data}
                         {contains absorption data for parylene}
fthick = 1.665e-5;       {thickness in gm/cm^2 of  the }
                         {parylene filter (density 1.11gm/cm^3)}
```

I have commented the variables sufficiently to be self-explanatory. In addition to the constants, there are a number of parameters defined in the procedure **initvars** in the same unit. This is done because Pascal does not allow array constants:

```
csfile[1] := 'xenon4d.ncs';          {name of first absorption cross section file}
                                     {this is the file the creates the inversion atoms}
csfile[2] := 'xenon5.ncs';           {name of second absorption cross section file}
auger[1] := true;                    {whether cross section #1 undergoes Auger decay}
auger[2] := false;
don_l[1] := true;                    {whether to do N*L products for this cross section}
don_l[2] := false;

                                     {following are distances at which to print out the photon distribution,
                                     in cm}
distance[1] := 0.2;
distance[2] := 0.5;
distance[3] := 1;
distance[4] := 2;
distance[5] := 3;
density := 3.30e16 * pressure;       {various factors to be set}
gfactor := gain * (ulbr / ulg - llbr / llg);
prnt := dskfile;                     {where to route the graphs to}
                                     {selection is either--}
                                     {print-- prints the graph on the printer}
                                     {scrap-- does nothing with graph}
                                     {clip-- puts it onto the clipboard}
                                     {dskfile-- puts it into a MacDrawII file}
                                     {if you put a "#" sign  somewhere the filename, }
                                     {it will no longer prompt for a name,}
                                     {but will automatically replace the "#" with}
                                     {sequential numbers for sequential graphs}
                                     {ask-- asks user what to do with the graph}
```

Usually, the program will be run using prnt := dskfile, and a "#" can be placed at the end of the file name to sequentially number the (large) number of graphs generated by the program. In addition to these variables, cross sections are read in by the program, the file names of which have been specified above. The format for the filter data file is of absorption in cm^2/gram as a function of photon energy in eV, in a double column format (**energy absorption**) , with no header. **filterfile = 'none'** removes the filter from the calculation. The cross section data for the xenon 4**d** and 5**s**,**p** data is of cross section in Mb (10^{-18} cm^2) as a function of energy, (**energy crosssection**), with the first line containing the ionization threshold of the shell corresponding to the cross section data.

The program consists of a variety of units which perform separate calculations. I will list them in the sequence called upon in the execution of the program:

header-- Prints out a header into the text file. Basically a repeat of the defined constants and variables.

bbody-- Calculates the blackbody distribution for a radiator of the specified temperature, and a total photon energy of **lenergy*leff**. The x-ray flux is in terms of number of photons in the specified energy bin, for the entire emissions from the plasma. The total number of energy bins is given by **ne**, and the energy spacing between bins is given by **de**. Outputs graph of the flux distribution.

filter-- Adds the x-ray filter attenuation to the blackbody x-ray flux. In the example above, this data will be read from the file **parylene.dat**. Outputs graph of the resulting absorption.

csection-- Reads in the cross section files for the different gas subshells. In the example above, they will be read from the files **xenon4d.ncs** and **xenon5.ncs**. Outputs graphs of the cross sections.

radial-- Calculates excited state densities for the various subshells, along with the electron densities, for the case of a point-focus plasma. Although this is not what we ultimately want, it is a useful intermediate step. Calculates both primary and secondary electron densities. Outputs a number of graphs.

densc-- Using the output of the last procedure, this procedure calculates the excited state densities for the case of a line focus, as specified by the total plasma length **plength**, broken up into **nl** segments for integration purposes. This procedure only calculates the excited state density at the point at the specified distance measured perpendicularly from the center of the line focus. Outputs various graphs.

ntimesl-- This procedure uses the results of **radial** to calculate the total N*L product along the length of the channel of length **clength**, which is illuminated by the line focus plasma. Does a numeric integration over the length of the channel, and the length of the plasma. Outputs a graph.

saturate-- Adds the effects of depletion of the xenon through photoionization, to the results of **densc** and **ntimesl**. This is done based on the excited state densities in the output of **densc**. Outputs graphs.

ntimeslt-- Calculates the N*L product for the transverse direction, at the center of the slot. For the case of the slot, this is assumed to be just the results of **densc**, multiplied by the width of the slot. Outputs graph.

ntimeslr-- Calculates the N*L product in the radial dimension, as specified by figure 2.17. Uses the results of densc, and also takes into account divergence according to equation 2.5. This number does not have meaning in the case of a parylene filter, since the parylene will isolate the channel from radially directed flux. Outputs graph.

elect-- Calculates the electron densities along the center of the line focus, analogously to what **densc** does with the excited state density data of **radial**. Outputs graphs.

aspect-- Calculates various aspect ratios for the plasma for the longitudinal/transverse N*L, etc.. Outputs various graphs.

gainplot-- Uses the **ntimesl** (processed by **saturate**), **ntimeslt**, and **ntimeslr** data to calculate gain-lengths in different directions for the plasma. This is just the N*L times the **gfactor** as defined in the above listing, taking into account the gain cross section and the Auger branching ratios. Outputs graphs.

stats-- Prints out numerically (into the text file) the results for all the distances in array **distance** as specified in the above listing.

newgain4-- The program that calls all the previous procedures in sequence.

graphdata and grdat4.p-- Procedures to do the numerical graphs.

Program **GAIN5** differs from **GAIN4** in a few subroutines:

header-- Slight variation appropriate for the new geometry. Do dot need the channel length parameters.

ntimesl-- For a plasma without a channel, the longitudinal gain-length will be identical to the transverse gain-length of a point focus plasma of the same total energy. Therefore the calculation is much simpler.

ntimeslt-- Does a numeric integration along the transverse direction using the data from **densc**. Somewhat more time consuming than in the case of the channel.

GAIN6 is different from **GAIN5** only in that the plasma length is set to zero, and a new header is used.

These programs are generally useful for calculating excited state densities resulting from plasma x-ray illumination, and each procedure is relatively simple, making the code readily modifiable. The complete GAIN4 program consists of 20 Pascal units and 2 libraries. Eighteen units are particular to the simulation, with a total of ~840 lines of code. A numerical graphing routines unit is also used.

B.2.2 Time dependent gain program MONTE CARLO

Program MONTE CARLO does a time dependent simulation of the gain dynamics of the xenon laser system. The program uses Monte Carlo techniques to estimate the effects of amplified spontaneous emission. The simulation considers the case of a rectangular slot, corresponding to the parylene covered slot of figures 2.2 and 2.23. The principles of operation of this program are discussed in section 2.3.3.

The since some of the operations of this program take considerable run-time even on a Macintosh II, the operations of the program are segmented. However, there are a number of parameters which are entered as constants, and the program must be recompiled for each different set of parameters:

```
const
totallength = 3000;     {total length of the slot in arbitrary units.}
                        {a larger number will increase run time of some}
                        {parts of the simulation. This should be the length}
                        {for the full slot– the simulation will run for}
                        {different fractions of the full length actually}
                        {illuminated}
width = 150;            {width of the slots in the same units. The aspect}
                        {ratio of the slot is just totallength/width}
                        {the units used should be such that width is a}
                        {reasonably large number to have good resolution}
                        {for the monte carlo simulation}
max = 3004;             {this is just sqrt(sqr(totallength) +sqr(width))}
                        {– the longest possible distance a photon could}
                        {travel in the medium}
outanglesq = 3600;      {square of the output angle of interest}
                        {this determines divergence angle of the output beam}
                        { it just corresponds to the inverse square of the half}
                        {angle of the output beam. For instance if the output}
                        {beam is all photons which exit with a half-angle}
```

```
                    {less than 1/60 radian, outanglesq = 3600}

ngains = 250;       {number of individual gain-lengths to evaluate}
                    {the ASE clamping values, and the fraction in output beam}
gainstep = 0.1;     {the increment between the intervals. The maximum total}
                    {gain-length evaluated for will be ngains*gainstep}

dowepmt = dskfile;  {what to do with the graphical output.}
                    {selection is either--}
                    {print-- prints the graph on the printer}
                    {scrap-- does nothing with graph}
                    {clip-- puts it onto the clipboard}
                    {dskfile-- puts it into a MacDrawII file}
                    {       if you put a "#" sign somewhere in the filename at}
                    {the prompt, it will no longer prompt for a name,}
                    {but will automatically replace the "#" with}
                    {sequential numbers}
                    {ask-- asks user what to do with the graph}
bin = 5;            {amount to bin photon distribution in graphs}
                    {one generally needs less resolution in the graph}
                    {than the totallength value.}

intgainstep = 1;    {is the step size for gains--}
                    {in contrast to gainstep, this controls the total}
                    {excitation intensities, measured in units of total}
                    {gain-length that would be created by an impulse}
                    {excitation (output of GAIN4).}
nintgains = 25;     {is the number of gain values to do time simulation for}
                    { for example, intgainstep = 1 and nintgains = 25 will}
                    {do the simulation for all excitation levels from GL=1}
                    {to GL=25}

nlengths = 4;       {the maximum number of fraction of illuminated total}
                    {lengths allowed by the simulation}
nltimesnint = 10;   {is =nintgains*nlengths}
upfac = 1.0;        {branching of Auger decay into upper laser level}
lowfac = 1.22;      {branching of Auger decay into lower laser level}
gupper = 1;         {degeneracy of upper laser level}
glower = 3;         {degeneracy of lower laser level}
pulsewidth = 0.6;   {pulsewidth in nsec of the laser excitation pulse, }
                    {in terms of the gaussian pulse width}
                    {relation is pulsewidth = 0.6 * FWHM of pulse, so}
                    {0.6 nsec is 1 nsec FWHM}
lifetime = 4.75;    {nsec upper level lifetime}
llifetime = 20.5;   {nsec lower level lifetime}
timestep = 0.025;   {nsec timestep for simulation}
ntimesteps = 200;   {total number of timesteps}
t0 = 1.5;           {Is the time of the peak of the laser pulse, in nsec.}
                    {for instance, timestep=0.025 and ntimesteps=200}
                    {means the simulation is run for a total of 5 nsec,}
                    {with t0=1.5, so that the peak of the laser pulse}
                    { is at 1.5nsec}
```

```
ninexptbl = 300;      {number of entries in the exponential gains}
                      { interpolation table}
                      {this table is meant to speed calculations}
                      {of ASE quenching taking into account doppler}
                      {width of the transition line}

expdg = 0.1;          {the interval between points for this table. Maximum}
                      {gain is ninexptbl*expdg. This table is stored in a disk}
                      {file to avoid recalculation}

fracerror = 0.1;      {this factor is for the fitting of the gain function to}
                      {the peak outputs of the time dependent simulations}
                      {this number is just the fractional error assumed in the}
                      {peak output for the gain fitting program}

nplotpoints = 200;    {number of plot points for the fitted gain curve}

nsteps = 10000;       {this is for the monte carlo simulation. Just is the number}
                      {of iterations to do before checking whether it is finished}
```

When executing the program, there is a choice of several procedures to run:

RUN-- Runs the actual Monte Carlo simulation of the geometry, to determine the distribution of photon trajectory distances. The program first asks you to select an old data file. This command at the end of each run stores its data in a set of files labeled **FILENAME #/##**, where each file is the file for the geometry of the slot with only the fraction #/## of the slot illuminated. For example **MONTERUN 1/4** would be the data for the geometry when 1/4 of the slot was illuminated. The monte carlo code can append its data onto an existing file so that one can accumulate long run times to get good statistics; for example the simulation can be run overnight for several nights. If you select a file from the displayed dialog box, it will assume read in all the files of form **FILENAME ?/##**. If you press the cancel button to the filename dialog box, the program will ask for a filename template (do not include the **#/##**, just the name), and also for the number of fractional lengths you would like the program to run for. It will then ask for a random number (for the pseudorandom sequence), and for the desired runtime in hours. The program will then run for the desired period of time, storing the result when it finishes. The data consists of arrays

such as figure 2.24 of the distribution of photon distances traveled in the excited region, as well as a similar array for the photons in the output beam.

PROC-- Processes the data from **RUN**, using the geometrical data to calculate a gain lifetime shortening factor as in figure 2.25, and also the fraction of photons in the output beam as in figure 2.27. It asks for both an input file, and an output file name. **PROC** must be run separately for each of the fractional illuminated lengths.

DISP-- Displays the results of the last two commands. Asks for the names of both a photon distribution file (from **RUN**), and a gain values file (from **PROC**). Graphs the results.

TDEP-- Does the time dependent simulation. Asks for the name for a text output file, and also a file in which to store summary data (peak output intensity, integrated output intensity, output FWHM, etc. as a function of total excitation intensity, and of illuminated channel length). Also asks the names of as many gain values files (**PROC** output) as desired to be run for (each of these file will be for one fractional illuminated length). The calculation follow after entering "cancel" to the filename dialog box. Does a time dependent simulation, plotting the output both as a function of illuminated length (for example figure 2.28), and as a function of excitation intensity.

GFIT-- Uses the summary output of **TDEP**, to fit the gain function (equation 2.3) to the simulation peak output intensity, in the same way the gain function is fit to experimental data. Also adds the resulting fit parameters to the same summary data file. Plots the simulation data with the best fit curve (as a function of illuminated distance), for each excitation intensity (for example figure 2.28).

SUM-- Prints out the summary data from **TDEP** and **GFIT**, in tabular form.

OTH-- Prints out graph of peak intensity vs. pulsewidth(for example the simulation data in figure 2.29). The data is taken from the summary data file, and selection of various subsets of the data for plotting is possible.

The program itself consists of 13 separate Pascal units and 2 libraries. Eleven of the units, consisting of a total of ~1350 lines of code, are particular to the **MONTE CARLO** code.

B.2.3 K-α x-ray laser simulation program XRAYLASER

Program XRAYLASER does a rate equation model of the population dynamics and gain as a function of time for an x-ray laser on atomic K-α transitions. The basic principles of operation are discussed in section 3.3.2. The basic energy level scheme for the rate equation model is shown in figure 3.3, with the exception that the $(2\mathbf{s})^{-1}$ level is also included in the model. No geometrical effects are taken into account in this model; the program computes the gain in the excited material in close proximity to a blackbody radiator, as in figure 3.4.

The simulation program itself has been appended to a text-editor program, to make it easy to edit values and re-run simulations. The simulation is activated by the "**Simulate**" menu item. When selected, all open text windows are closed, and the filename of the topmost window at the time of execution is used as the input file to the simulation (always tell the program to save changes before closing). The simulation is run, and then the original input file and also the text output file is opened in two separate editor windows. The program may or may not output graphs, depending on a setting in the input file. A sample input file follows:

```
Input file for X-ray laser simulation, Neon

Output file template            :output:output neon
{template for all the output files--}
{   "TEMPLATE text" -- text output file}
{   "TEMPLATE table" -- numerical output in tabular form}
{   "TEMPLATE grf"  -- graphical output; add a # sign to the}
```

```
{                              end of the filename when the graph save}
{                              dialog box shows up, to store the graphs}
{                              in sequentially numbered files.}
{                             The text file tells which file contains}
{                              which graph.}
{In this example the output will be put into a folder named "output"}


{The first line is title of simulation-- ignores this line}
{the program looks for prompt phrases, and uses as input what follows}
{thus the format of the input file is insensitive to extra <CR>'s etc, but}
{all the data must be there in the correct order, with the correctly spelled
{text..}

{lines that start with a left brace are comments which will be printed into}
{the text output. None must come before the output file template specification}
{or the program will not have the text file open}


Graphical output :          lin
{           what format to graph the data in:  "none"-- no graphs.
{                                              "lin"--  linear axes on graphs}
{                                              "logx"-- log x axis}
{                                              "logy"-- log y axis}
{                                              "loglog"-- log both axes}


Simulation:
Energy step =               5       eV
{                                              grid spacing for cross section graphs}
Maximum energy =            3000    eV
{                                              maximum energy for the graphs--}
{                                                    number of array elements =}
{                                                    (Maximum energy/Energy step)}
Time step =                 1.0     fsec
{                                              time step size for simulations}
Starting time =             -100    fsec
{                                              start time for simulations-- t=0 is}
{                                                    pump pulse peak}
Ending time =               20      fsec
{                                              end time for simulation}

Input impulse:
temperature function =      sech2
{                                              functional form for temperature rise as  fn of time--
{                                              "sech2"-- sech2 to the 4/9}
{                                                    power, as in equation 3.6}
{                                                    in this case, risetime is}
{                                                    the pulse FWHM (falltime}
{                                                    is ignored}}
{                                              "ramp"-- linear ramp of temp}
{                                                     risetime, falltime are ramp}
{                                                    times}
```

```
{                                                   "gaussian"-- gaussian, with}
{                                                           risetime, falltime the gaussian
{                                                           parameter exp(-(t/risetime)^2)}
risetime =              100     fsec
{                                                   as explained}
falltime =              300     fsec
{                                                   "   }
maximum temperature =   600     eV
{                                                   peak plasma temperature}
emissivity =            1
{                                                   emissivity of the plasma}

X-ray filters:
number of x-ray filters=    1
{                                                   number of x-ray filters between the x-ray}
{                                                   emitting and absorbing regions}

Beryllium               solid   3.0 um  thick
{                                                   filter specification-- density}
{                                                   is in cm^-3 or "solid"}
{                                                   name is used as a filename for  ionization cross section }
Electron cooling approximation=      accurate
{                                                   electron cooling approximation used in simulation}
{                                                   "fast"-- uses an average cooling rate in eV/fsec,}
{                                                           independent of energy and calculated from}
{                                                           the electron collisional cross sections}
{                                                   "accurate"-- uses a cooling rate as a function of}
{                                                           electron energy}
max energy for cool rate            800             eV
{                                                   used for the fast cooling approximation,}
{                                                   averages cooling rate from Ion. Pot. to this value}

Laser material=                     Neon
{                                                   material pumped by the x-rays}
{                                                   used as a template for the ionization cross section input}
Density=                            5e19    /cm3
{                                                   density}
upper level lifetime =              2.694   fsec
{                                                   Auger lifetime of the upper laser level}
radiative lifetime =        149.7   fsec
{                                                   Radiative lifetime of the upper laser level}
upper level degeneracy =            2
{                                                   degeneracy of upper laser level}
lower level degeneracy =            6
{                                                   degeneracy of lower laser level}
frac of auger into l.l. =           0       %
{                                                   Fraction of the Auger decay that goes into the}
{                                                   lower laser level, instead of the Auger product}
{                                                   level. Useful for molecular systems, where some}
{                                                   Auger product states might absorb at the laser}
{                                                   wavelength}
Auger electron energy =             794     eV
{                                                   Average Auger ejected electron energy}
```

```
Transition energy =             848.6   eV
{                                       energy of the laser radiative transition}
Transition FWHM=                natural eV
{                                       FWHM of the laser transition. in eV, or Natural}
{                                       calculates it from the upper level lifetime}
Gain reduction factor =         1
{                                       further reduce the gain cross section by this}
{                                       factor. I.E. "2" reduces cross section by 2}
Active X-ray band =             75      %
{                                       this factor defines an active band such that}
{                                       photons from the inner shell ion. pot. up to}
{                                       a particular energy account for say 75% of the}
{                                       population into the upper laser level, for a }
{                                       blackbody radiator of the peak temperature}
{                                       This number does not affect the simulation, but}
{                                       is used in output.}

Buffer material=                Hydrogen
{                                       the material used as the buffer that the laser}
{                                       material is dissolved into}
{                                       used as a template for the ionization cross section input}

Density                         solid
{                                       density of the buffer material-- "solid"}
{                                       give "solid" density, or density in cm^-3}

Buffer                          half depleted
{                                       how the buffer is depleted by electron ionization}
{                                       "not depleted"-- electron ionization does not}
{                                               deplete the buffer material}
{                                       "half depleted"-- electron ionization depletes}
{                                               at half the ionization rate-- useful}
{                                               for molecular gasses such as H2}
{                                       "depleted"-- electron ionization depletes}
{                                               at the ionization rate.}

Full output at
{these are the simulation times at which a full numeric output is printed into}
{the text file}
0               fsec
11              fsec
```

In Addition to this input file, a number of files containing absorption cross sections are read in. The format of the cross section files is as follows:

```
Neon upper level absorption cross section

density of solid =      3.60e22         /cm^3
ionization potential =  870.2           eV
x-ray edge energy =     none
```

energy (eV)	cross section (Mb)
871.070	.263
878.902	.285
896.306	.290
913.710	.288
957.220	.268
983.326	.250
1041.0	.2093
1253.6	.1328
1486.6	.86e-1
8047.8	.7e-3

The cross sections for photon and electron ionization, and for the x-ray filters, are all in the same format and units. The x-ray edge energy is used when the photoionization cross section is used to estimate the secondary electron distribution-- the secondary electron distribution is assumed to drop to zero at the inner shell x-ray transition energy. This is primarily useful if the buffer material (for which the photoionization cross section is the total of the inner-shell and outer-shell cross sections) has an jump in the cross section which would give an unrealistic secondary electron distribution. The cross section files used by the program are, given a laser material name **LASER**, a buffer material name **BUFFER**, and filter names **FILTER#** :

LASER upper-- Laser material upper level (1**s**) photoionization cross section.

LASER lower-- Laser material lower level (2**p**) photoionization cross section.

LASER other-- Laser material other level (2**s**) photoionization cross section.

LASER lelectron-- Laser material lower level (2**p**) electron ionization cross section.

LASER oelectron-- Laser material other level (2**s**) electron ionization cross section.

FILTER#-- Filter material photoabsorption cross section.

BUFFER-- Buffer material photoionization cross section.

BUFFER electron-- Buffer material electron ionization cross section.

The program consists of 25 Pascal units and 7 libraries, most of which are used by the text editor (Capps' Pedit from THINK, Inc.) . Five units are particular to the simulation, with a total of ~1425 lines of code. A numerical graphing routines unit is also used.

References

1. D. L. Matthews, *et al.*, "Demonstration of a Soft X-Ray Amplifier," Physical Review Letters **54** (2), p. 110 (1985).

2. S. Suckewer, C. H. Skinner, H. Milchberg, C. Keane and D. Voorhees, "Amplification of Stimulated Soft-X-Ray Emission in a Confined Plasma Column," Physical Review Letters **55** (17), p. 1753 (1985).

3. H. C. Kapteyn, R. W. Lee and R. W. Falcone, "Observation of a Short-Wavelength Laser Pumped by Auger Decay," Physical Review Letters **57** (23), p. 2939 (1986).

4. J. Weber, "Amplification of microwave radiation by substances not in thermal equilibrium," IRE Trans. Prof. Group on Electron Devices **3** p. 1 (1953).

5. J. P. Gordon, H. J. Zeigler and C. H. Townes, "The maser-- new type of microwave amplifier, frequency standard, and spectrometer," Physical Review **99** p. 1264 (1955).

6. N. G. Basov and A. M. Prokhorov, "Application for molecular beams to the radio spectroscopic study of the rotational spectrum of molecules," Journal of Experimental and Theoretical Physics of the USSR **27** p. 249 (1954).

7. A. L. Schawlow and C. H. Townes, "Infrared and optical masers," Physical Review **112** p. 1940 (1958).

8. T. H. Maiman, "Stimulated optical radiation in ruby," Nature **187** p. 493 (1960).

9. P. A. Franken, A. E. Hill, C. W. Peters and G. Weinreich, "Generation of optical harmonics," Physical Review Letters **7** p. 118 (1961).

10. W. B. Bridges, "Laser Oscillation in singly ionized argon in the visible spectrum," Applied Physics Letters **4** (7), p. 128 (1964).

11. D. L. Stockman, W. R. Mallory and K. F. Tittel, "Stimulated emission in aromatic organic compounds," Proceedings of the IEEE **52** p. 318 (1964).

12. P. P. Sorokin and J. R. Lankard, "Stimulated emission observed from an organic dye, chloroaluminum phtalocyanine," IBM Journal of Research and Development **10** p. 162 (1966).

13. S. K. Searles and G. A. Hart, "Stimulated emission at 281.8 nm from XeBr," Applied Physics Letters **27** (4), p. 243 (1975).

14. J. J. Ewing and C. A. Brau, "Laser action on the $^2\Sigma_{1/2} \rightarrow {}^2\Sigma_{1/2}$ bands of KrF and XeCl," Applied Physics Letters **27** (6), p. 350 (1975).

15. H. G. Heard, "Ultra-violet Gas Laser at Room Temperature," Nature **200** (4907), p. 667 (1963).

16. J. D. Shipman Jr., "Travelling wave excitation of high power gas lasers," Applied Physics Letters **10** (1), p. 3 (1967).

17. R. T. Hodgson, "Vacuum-ultraviolet laser action observed in the lyman bands of molecular hydrogen.," Physical Review Letters **25** (8), p. 494 (1970).

18. R. W. Waynant, J. D. Shipman Jr., R. C. Elton and A. W. Ali, "Vacuum ultraviolet emission from molecular hydrogen," Applied Physics Letters **17** (9), p. 383 (1970).

19. R. T. Hodgson and R. W. Dreyfus, "Vacuum-UV Laser Action Observed in H_2 Werner Bands: 1161-1240 Å," Physical Review Letters **28** (9), p. 536 (1972).

20. R. W. Waynant, "Observations of Gain by Stimulated Emission in the Werner Band of Molecular Hydrogen," Physical Review Letters **28** (9), p. 533 (1972).

21. R. H. Page, R. J. Larkin, A. H. Kung, Y. R. Shen and Y. T. Lee, "Frequency tripling into the 720-1025 Å region with pulsed free jets," Review of Scientific Instruments **58** (9), p. 1616 (1987).

22. M. A. Duguay and P. M. Rentzepis, "Some approaches to vacuum UV and x-ray lasers," Applied Physics Letters **10** (12), p. 350 (1967).

23. I. I. Sobelman, *Atomic Spectra and Radiative Transitions*, Volume 1, in Springer Series in Chemical Physics, J. P. Toennies, Eds. (Springer-Verlag, New York, 1979), p. 200.

24. A. Einstein, "On the Quantum Theory of Radiation," Physikalische Zeitschrift **18** p. 121 (1917).

25. A. P. Thorne, *Spectrophysics*, (Chapman and Hall, New York, 1988), p. 101.

26. G. R. Fowles, *Introduction to Modern Optics*, (Holt, Rinehart, and Winston, New York, 1975), p. 211.

27. L. I. Schiff, *Quantum Mechanics*, (McGraw-Hill, New York, 1968), p. 285.

28. A. Yariv, *Quantum Electronics*, (John Wiley & Sons, Inc., New York, 1975), p. 153.

29. A. Yariv, *Quantum Electronics*, (John Wiley & Sons, Inc., New York, 1975), p. 166.

30. A. P. Thorne, *Spectrophysics*, (Chapman and Hall, New York, 1988), p. 290.

31. H. A. Bethe and E. E. Salpeter, *Quantum Mechanics of One- and Two-Electron Atoms*, (Plenum, New York, 1977), p. 260.

32. I. I. Sobelman, *Atomic Spectra and Radiative Transitions*, Volume 1, in Springer Series in Chemical Physics, J. P. Toennies, Eds. (Springer-Verlag, New York, 1979), p. 26.

33. B. J. MacGowan, *et al.*, "Soft-x-ray amplification at 50.3 Å in nickellike ytterbium," Journal of the Optical Society of America B **5** (9), p. 1858 (1988).

34. W. M. Hughes, J. Shannon and R. Hunter, "126.1 nm molecular argon laser," Applied Physics Letters **24** (10), p. 488 (1974).

35. W. Sasaki, *et al.*, "Generation of Tunable Intense Coherent Radiation around 126 nm with an Argon Excimer Laser," in conference proceedings of *Short Wavelength Coherent Radiation: Generation and Applications*, D. T. Attwood, J. Bokor, Eds. (AIP, New York, 1986) #147, p. 391.

36. W. T. Silfvast and O. R. Wood II, "Photoionization lasers pumped by broadband soft-x-ray flux from laser-produced plasmas," Journal of the Optical Society of America B **4** (4), p. 609 (1987).

37. G. J. Pert, "A Survey of Current XUV Laser Experiments," Comments on Atomic and Molecular Physics **18** (6), p. 259 (1986).

38. I. I. Sobelman and A. V. Vinogradov, "On the problem of extreme UV and x-ray lasers," Advances in Atomic and Molecular Physics **20** p. 327 (1985).

39. F. V. Bunkin, V. I. Derzhiev and S. I. Yakovlenko, "Prospects for light amplification in the far ultraviolet (review)," Soviet Journal of Quantum Electronics **11** (8), p. 981 (1981).

40. A. Yariv, "Some feasibility considerations of x-ray laser action," Optics Communications **22** (1), p. 1 (1977).

41. C. K. Rhodes, "Review of Ultraviolet Laser Physics," IEEE Journal of Quantum Electronics **QE-10** (2), p. 153 (1974).

42. P. L. Hagelstein, "Physics of Short Wavelength Laser Design," Ph.D. thesis, Massachusetts Institute of Technology, 1981.

43. E. J. McGuire and M. A. Duguay, "Soft x-ray gain the in alkali earths," Applied Optics **16** (1), p. 83 (1977).

44. I. I. Sobelman, *Atomic Spectra and Radiative Transitions*, Volume 1, in Springer Series in Chemical Physics, J. P. Toennies, Eds. (Springer-Verlag, New York, 1979), p. 251.

45. Y. L. Stankevich, "The possibility of induced intensification of characteristic x radiation," Soviet Physics Doklady **15** (4), p. 356 (1970).

46. R. C. Elton, "Quasi-stationary population inversion on K-α transitions," Applied Optics **14** (9), p. 2243 (1975).

47. F. T. Arecchi, G. P. Banfi and A. M. Malvezzi, "Threshold evaluations for an x-ray laser," Optics Communications **10** (3), p. 214 (1974).

48. T. S. Axelrod, "Inner-shell photoionization-pumped x-ray lasers. Sulfur," Physical Review A **13** (1), p. 376 (1976).

49. E. J. McGuire, "Soft X-Ray Amplified Spontaneous Emission via the Auger Effect," Physical Review Letters **35** (13), p. 844 (1975).

50. H. Körber and W. Melhorn, "Das K-Auger-Spektrum von Neon," Zeitschrift für Physik **191** (16), p. 217 (1966).

51. H. Aksela, S. Aksela and H. Pulkkinen, "Auger-electron study of correlation effects in $5s^0 5p^6$ and $5s^1 5p^5$ configurations of xenon," Physical Review A **30** (2), p. 865 (1984).

52. L. O. Werme, T. Bergmark and K. Siegbahn, "The High Resolution $L_{2,3}MM$ and $M_{4,5}NN$ Auger Spectra from Krypton and $M_{4,5}NN$ and $N_{4,5}OO$ Auger Spectra from Xenon," Physica Scripta **6** p. 141 (1972).

53. H. Hertz, "VUV Emission of Xe III Levels Excited by Electron Impact via $N_{4,5}OO$ Auger Transitions," Zeitscrift für Physik A **274** p. 289 (1975).

54. E. H. S. Burhop, *The Auger Effect and Other Radiationless Transitions* (Cambridge University Press, Cambridge, 1952).

55. J. Bokor, R. R. Freeman and W. E. Cooke, "Autoionization-Pumped Laser," Physical Review Letters **48** (18), p. 1242 (1982).

56. W. T. Silfvast, J. J. Macklin and O. R. Wood II, "High-gain inner-shell photoionization laser in Cd vapor pumped by soft-x-ray radiation from a laser-produced plasma source," Optics Letters **8** (11), p. 551 (1983).

57. H. Lundberg, J.J.Macklin, W. T. Silfvast and O. R. Wood II, "High-gain soft-x-ray-pumped photoionization laser in zinc vapor," Applied physics letters **45** (4), p. 335 (1984).

58. R. A. Lacy, R. L. Byer, W. T. Silfvast, O. R. Wood II and S. Svanberg, "Optical gain at 185 nm in a laser ablated, inner-shell photoionization-pumped indium plasma," in conference proceedings of *Short Wavelength Coherent Radiation: Generation and Applications*, D. T. Attwood, J. Bokor, Eds. (American Institute of Physics, New York, 1986) #147, p. 96.

59. T. Mukoyama and K. Taniguchi, "Atomic excitation as the result of inner-shell vacancy production," Physical Review A **36** (2), p. 693 (1987).

60. W. T. Silfvast, O. R. Wood II and D. Y. Al-Salameh, "Direct photoionization pumping of high gain VUV, UV and visible inversions in helium, cadmium, and argon via two-electron (shakeup) and of sodium vie the output from the LLNL soft-x-ray laser," in conference proceedings of *Short Wavelength Coherent Radiation: Generation and Applications*, D. T. Attwood, J. Bokor, Eds. (American Institute of Physics, New York, 1986) #147, p. 134.

61. W. T. Silfvast, D. Y. Al-Salameh and O. R. Wood II, "Multielectron photoionization to the $3p^4 4p$ configuration of Ar^+ : Experiment and theory," Physical Review A **34** (6), p. 5164 (1986).

62. W. T. Silfvast, O. R. Wood II, J. J. Macklin and D. Y. Al-Salameh, in *Laser Spectroscopy VII* , T. W. Hänsch, Y. R. Shen, Eds. (Springer-Verlag, Berlin, 1985), p. 171.

63. S. E. Harris and R. G. Caro, "Shake-up as a mechanism for VUV lasers," Optics Letters **11** (1), p. 10 (1986).

64. D. J. Walker, C. P. J. Barty, G. Y. Yin, J. F. Young and S. E. Harris, "Observation of super Coster-Kronig-pumped gain in Zn III," Optics Letters **12** (11), p. 894 (1987).

65. E. J. McGuire, "Auger cascades in aluminum," Physical Review A **11** (6), p. 1889 (1975).

66. T. S. Axelrod, "Inner-shell photoionization-pumped x-ray lasers. Boron*," Physical Review A **15** (3), p. 1132 (1977).

67. P. D. Morley and J. Sugar, "Exploding-foil-photoionization x-ray laser," Physical Review A **38** (6), p. 3139 (1988).

68. V. A. Boiko, F. V. Bunkin, V. I. Derzhiev and S. I. Yakovlenko, "Possibilities of Amplification of Ultraviolet and Soft X-Ray Radiation on Multiply Charged Ion Transitions in a Recombining Plasma," IEEE Journal of Quantum Electronics **QE-20** (3), p. 206 (1984).

69. F. V. Bunkin, V. I. Derzhiev and S. I. Yakovlenko, "Specification for pumping x-ray laser with ionizing radiation," Soviet Journal of Quantum Electronics **11** (7), p. 971 (1981).

70. D. G. Goodwin and E. E. Fill, "Inversion and gain in hydrogenic ion levels induced by photoionization pumping," Journal of Applied Physics **64** (3), p. 1005 (1988).

71. S. E. Harris and J. F. Young, "Core-excited metastable levels: application to spectroscopy, to the generation of picosecond extreme-ultraviolet pulses, and to lasers," Journal of the Optical Society of America B **4** p. 4 (1987).

72. S. A. Mani, H. A. Hyman and J. D. Daugherty, "Lithium-ion soft x-ray laser," Journal of Applied physics **47** (7), p. 3099 (1976).

73. P. L. Csonka and B. Crasemann, "Feasibility of coherent x-ray production by x-ray pumping," Physical Review A **12** (2), p. 611 (1975).

74. P. L. Csonka, "Suggested method for coherent x-ray production by combined x-ray and low-energy photon pumping," Physical Review A **13** (1), p. 405 (1976).

75. B. Rozsnyai, H. Watanabe and P. L. Csonka, "Numerical simulation of a soft-x-ray Li laser pumped with synchrotron radiation," Physical Review A **32** (1), p. 357 (1985).

76. A. V. Vinogradov, I. I. Sobel'man and E. A. Yukov, "Possibility of constructing a far-ultraviolet laser utilizing transitions in multiply charged ions in an inhomogeneous plasma," Soviet Journal of Quantum Electronics **5** (1), p. 59 (1975).

77. B. A. Norton and N. J. Peacock, "Population inversion in laser-produced plasmas by pumping with opacity-broadened lines," Journal of Physics B **8** (6), p. 989 (1975).

78. F. L. Cochran, J. Davis and J. P. Apruzese, "X-ray lasing in a Na/Ne plasma environment," Journal of Applied Physics **57** (1), p. 27 (1985).

79. J. P. Apruzese, J. Davis and K. G. Whitney, "Plasma conditions required for attainment of maximum gain in resonantly photo-pumped aluminum XII and neon IX," Journal of Applied Physics **53** (6), p. 4020 (1982).

80. J. G. Lunney, *et al.*, "Ion-implanted target for soft x-ray laser investigations," Optics Communications **50** (6), p. 367 (1984).

81. R. H. Dixon, J. L. Ford, T. N. Lee and R. C. Elton, "Solid neon sources for plasmas and x-ray lasers," Review of Scientific Instruments **56** (3), p. 471 (1985).

82. J. G. Lunney, "Soft x-ray laser action using resonant photo-excitation of autoionizing states of lithium-like ions," Optics Communications **53** (4), p. 235 (1985).

83. V. A. Bhagavatula, "Experimental evidence for soft x-ray population inversion by resonant photoexcitation in multicomponent laser plasmas," Applied Physics Letters **33** (8), p. 726 (1978).

84. A. V. Vinogradov, B. N. Chichkov and E. A. Yukov, "Resonant photoexcitation as a pumping mechanism for far ultraviolet lasers," Soviet Journal of Quantum Electronics **14** (4), p. 444 (1984).

85. N. Qi and M. Krishnan, "Photopumping of a C III Ultraviolet Laser by Mn VI Line radiation," Physical Review Letters **59** (18), p. 2051 (1987).

86. P. Monier, C. Chenais-Popovics, J. P. Geindre and J. C. Gauthier, "Demonstration of quasiresonant x-ray photoexcitation in a laser-created plasma," Physical Review A **38** (5), p. 2508 (1988).

87. K. Boyer, H. Egger, T. S. Luk, H. Pummer and C. K. Rhodes, "Interaction of atomic and molecular systems with high-intensity ultraviolet radiation," Journal of the Optical Society of America B **1** (1), p. 3 (1984).

88. C. W. Clark, *et al*., "Possibilities for achieving x-ray lasing action by use of high-order multi-photon processes.," Journal of the Optical Society of America B **3** (3), p. 371 (1986).

89. J. N. Bardsley, "Excited-state stability and x-ray lasers," Optics Letters **11** (10), p. 612 (1986).

90. P. K. Cheo and H. G. Cooper, Journal of Applied Physics **36** p. 1862 (1965).

91. M. A. Duguay, "X-ray lasers: a status report," Laser focus **1973** (November), p. 41 (1973).

92. R. C. Elton, "Extension of 3p-3s Ion Lasers into the Vacuum Ultraviolet Region," Applied Optics **14** (1), p. 97 (1975).

93. A. N. Zherikhin, K. N. Koshelev and V. S. Letokhov, "Gain in the far vacuum ultraviolet region due to transitions in multiply charged ions," Soviet Journal of Quantum Electronics **6** (1), p. 82 (1976).

94. A. V. Vinogradov, I. I. Sobel'man and E. A. Yukov, "Population inversion of transitions in neon-like ions," Soviet Journal of Quantum Electronics **7** (1), p. 32 (1977).

95. L. A. Vaînshteîn, A. V. Vinogradov, U. I. Safronova and I. Y. Skobelev, "Stimulated emission in far ultraviolet due to transitions in multiply charged neon-like ions," Soviet Journal of Quantum Electronics **8** (2), p. 239 (1978).

96. A. V. Vinogradov and V. N. Shlyaptsev, "Gain in the 100-1000 Å range in a homogeneous stationary plasma," Soviet Journal of Quantum Electronics **13** (3), p. 303 (1983).

97. A. V. Vinogradov and V. N. Shlyaptsev, "Amplification of ultraviolet radiation in a laser plasma," Soviet Journal of Quantum Electronics **13** (11), p. 1511 (1983).

98. M. D. Rosen, *et al.*, "Exploding-Foil Technique for Achieving a Soft X-Ray Laser," Physical Review Letters **54** (2), p. 106 (1985).

99. W. K. H. Panofsky and M. Phillips, *Classical Electricity and Magnetism*, (Addison-Wesley, Reading, MA, 1978), p. 413.

100. E. E. Fill, "Gain guiding of x-ray laser beams," Optics Communications **67** (6), p. 441 (1988).

101. L. W. Casperson, "Gaussian Light Beams in Inhomogeneous Media," Applied Optics **12** (10), p. 2434 (1973).

102. T. N. Lee, E. A. McLean and R. C. Elton, "Soft X-Ray Lasing in Neonlike Germanium and Copper Plasmas," Physical Review Letters **59** (11), p. 1185 (1987).

103. D. Matthews, *et al.*, "X-ray laser research at the Lawrence Livermore National Laboratory Nova laser facility," Journal of the Optical Society of America B **4** (4), p. 575 (1987).

104. M. D. Rosen, *et al.*, "Dynamics of Collisional-Excitation X-Ray Lasers," Physical Review Letters **59** (20), p. 2283 (1987).

105. B. J. MacGowan, *et al.*, "Observation of soft x-ray amplification in neonlike molybdenum," Journal of Applied Physics **61** (12), p. 5243 (1987).

106. B. J. MacGowan, *et al.*, "Demonstration of Soft-X-Ray Amplification in Nickel-like Ions," Physical Review Letters **59** (19), p. 2157 (1987).

107. P. L. Hagelstein, "Short wavelength lasers: Something New, Something Old," in conference proceedings of *Proceedings of the AIP Conference on Short Wavelength Coherent Radiation*, R. W. Falcone, J. Kirz, Eds. (American Institute of Physics, New York, 1988) .

108. C. P. J. Barty, *et al.*, "12.8-eV Laser in Neutral Cesium," Physical Review Letters **61** (19), p. 2201 (1988).

109. R. G. Caro and J. C. Wang, "Population distributions in Li vapor excited by a photoionization electron source," Physical Review A **33** (4), p. 2563 (1986).

110. J. R. Willison, R. W. Falcone, J. C. Wang, J. F. Young and S. E. Harris, "Emission Spectra of Core Excited Even-Parity ^{2}P States of Neutral Lithium," Physical Review Letters **44** (17), p. 1125 (1980).

111. J. E. Rothenberg and S. E. Harris, "XUV Lasers by Quartet to Doublet Energy Transfer in Alkali Atoms," IEEE Journal of Quantum Electronics **QE-17** (3), p. 418 (1981).

112. J. C. Bellum, W. W. Chow, K. Drühl and M. O. Scully, "Analysis of VUV and soft x-ray lasing based on charge-exchange mechanisms," in conference proceedings of *Laser*

Techniques for Extreme Ultraviolet Spectroscopy, T. J. McIlrath, R. R. Freeman, Eds. (American Institute of Physics, New York, 1982) #90, p. 184.

113. V. O. Papanyan, A. E. Martirosyan and F. K. Tittel, "Collisionally Excited XUV Lasers," IEEE Journal of Quantum Electronics **QE-19** (12), p. 1835 (1983).

114. A. R. Turner-Smith, J. M. Green and C. E. Webb, "Charge transfer into excited states in thermal energy collisions," Journal of Physics B **6** (1), p. 114 (1973).

115. H. Milchberg, C. H. Skinner, S. Suckewer and D. Voorhees, "Measurement of population inversions and gain in carbon fiber plasmas," Applied Physics Letters **47** (11), p. 1151 (1985).

116. S. Suckewer and H. Fishman, "Conditions for soft x-ray lasing action in a confined plasma column," Journal of Applied Physics **51** (4), p. 1922 (1980).

117. C. Chenais-Popovics, *et al*., "Laser Amplification at 18.2 nm in Recombining Plasma from a Laser-Irradiated Carbon Fiber," Physical Review Letters **59** (19), p. 2161 (1987).

118. D. Kim, *et al.*, "Soft-x-ray amplification in lithiumlike Al XI (154Å) and Si XII (129Å)," Journal of the Optical Society of America B **6** (1), p. 115 (1989).

119. L. I. Gudzenko and L. A. Shelepin, "Radiation Enhancement in a recombining plasma," Soviet Physics Doklady **10** (2), p. 147 (1965).

120. W. L. Bohn, "Possible population inversions for VUV and soft x-ray transitions in hydrogenlike ions," Applied Physics Letters **24** (1), p. 15 (1974).

121. L. I. Gudzenko, S. I. Yakovlenko and V. V. Yevstigneyev, "Application of the principle of a plasma-laser to amplification in the x-ray region," Physics Letters **48A** (6), p. 419 (1974).

122. V. V. Zhukov, V. S. Kucherov, E. L. Latush and M. F. Sém, "Recombination lasers utilizing vapors of chemical elements. II. Laser action due to transitions in metal ions," Soviet Journal of Quantum Electronics **7** (6), p. 708 (1977).

123. W. T. Silfvast, L. H. Szeto and O. R. Wood II, "Recombination lasers in Nd and CO_2 laser-produced cadmium plasmas," Optics Letters **4** (9), p. 271 (1979).

124. W. T. Silfvast and O. R. Wood II, "Recombination laser transitions in expanding plasmas of Cu, Zn, Ag, Cd, In, Sn, Pb, and Bi," Optics Letters **7** (1), p. 34 (1982).

125. W. T. Silfvast and O. R. Wood II, "Recombination lasers in the vacuumultraviolet,"in conference proceedings of *Laser Techniques for Extreme Ultraviolet Spectroscopy*, T. J. McIlrath, R. R. Freeman, Eds. (American Institute of Physics, New York, 1982) #90, p. 128.

126. M. H. Key, C. L. S. Lewis and M. J. Lamb, "Transient population inversion at 18.2 nm in a laser produced CVI plasma," Optics Communications **28** (3), p. 331 (1979).

127. F. E. Irons and N. J. Peacock, "Experimental evidence for population inversion in C^{5+} in an expanding laser-produced plasma," Journal of Physics B **7** (9), p. 1109 (1974).

128. K. Muroo, Y. Tanaka and H. Kuroda, "Amplification and Gain Measurement of XUV Radiation (42.4 Å, 45Å and 46Å) in He-like Al Laser Plasma," (1988).

129. E. E. Fill, "Gain on Free-Bound Transitions by Stimulated Radiative Recombination," Physical Review Letters **56** (16), p. 1687 (1986).

130. A. V. Andreev, S. A. Akhmanov and V. L. Kuznetsov, "Possibility of stimulated emission by channeled particles," Soviet Technical Physics Letters **7** (6), p. 292 (1982).

131. V. V. Beloshitskiî and M. A. Kumakhov, "Quantum theory of spontaneous and induced radiation of channeled electrons and positrons," Soviet Physics JETP **47** (4), p. 652 (1978).

132. M. A. Kumakhov, "On the theory of electromagnetic radiation of charged particles in a crystal," Physics Letters **57** (1), p. 17 (1976).

133. M. Strauss, "Buildup of x-ray laser gain by fluctuations in channeled relativistic beam systems," Physical Review A **38** (3), p. 1358 (1988).

134. M. J. Alguard, R. L. Swent and R. H. Pantell, "Observation of Radiation from Channeled Positrons," Physical Review Letters **42** (17), p. 1148 (1979).

135. L. D. Miller, "Tunable x-ray laser from high energy accelerator," Optics Communications **30** (1), p. 87 (1979).

136. B. A. Norton and E. R. Wooding, "Proposed method for obtaining population inversion for vacuum-ultraviolet and x-ray transitions," Physical Review A **11** (5), p. 1689 (1975).

137. K. J. Kim and C. Pellegrini, "High-Gain Free Electron Lasers as Generators of Short Wavelength Coherent Radiation," in conference proceedings of *Short Wavelength Coherent Radiation: Generation and Applications*, D. T. Attwood, J. Bokor, Eds. (American Institute of Physics, New York, 1986) #147, p. 1.

138. J. E. La Sala, J. M. J. Madey and D. A. G. Deacon, "Options and issues for XUV free electron laser oscillators," in conference proceedings of *Short Wavelength Coherent Radiation: Generation and Applications*, D. T. Attwood, J. Bokor, Eds. (American Institute of Physics, New York, 1986) #147, p. 1.

139. A. Gover, A. Friedman and A. Luccio, "Three dimensional modelling and numerical analysis of super-radiant harmonic emission in an FEL (optical klystron)," Nuclear Instruments and Methods in Physics Research A **A259** p. 163 (1987).

140. D. J. Bamford and D. A. G. Deacon, "Measurement of the Coherent Harmonic Emission from a Free-Electron Laser Oscillator," Physical Review Letters **62** (10), p. 1106 (1989).

141. H. C. Kapteyn and R. W. Falcone, "Auger-pumped short-wavelength lasers in xenon and krypton," Physical Review A **37** (6), p. 2033 (1988).

142. M. Agentoft, T. Andersen, J. E. Hansen, W. Persson and S. Pettersson, "A study of the $ns^0\ np^6\ ^1S$ States in the Rare Gas Ions," Physica Scripta **29** p. 57 (1983).

143. S. Southworth, *et al.*, "Electron-spectroscopy study of inner-shell photoexcitation and ionization of Xe," Physical Review A **28** p. 261 (1983).

144. H. Aksela, S. Aksela and H. Pulkkinen, "Correlation effects in $4s^04p^6$ and $4s^14p^5$ configurations of krypton studied by the M-NN Auger decay," Physical Review A **30** (5), p. 2456 (1984).

145. E. J. McGuire, "Auger spectrum of the noble gases. II. Krypton*," Physical Review A **11** (1), p. 17 (1975).

146. W. Persson, *et al.*, "Spectrum of Doubly Ionized Xenon (Xe III)," Physica Scripta **38** p. 347 (1988).

147. R. Stern and F. Paresce, "Mass Absorption Coefficients of Parylene N at Soft X-Ray and Vacuum-ultraviolet Wavelengths," Journal of the Optical Society of America **65** p. 1515 (1975).

148. J. H. Scofield, personal communication, (1986).

149. G. J. Linford, E. R. Peressini, W. R. Sooy and M. L. Spaeth, "Very Long Lasers," Applied Optics **31** (2), p. 379 (1974).

150. G. Y. Yin, *et al.*, "Low Energy Pumping of a 108.9 nm Xe Auger Laser," Optics Letters **12** (5), p. 331 (1987).

151. R. C. Weast, M. J. Astle and W. H. Beyer, *CRC Handbook of Chemistry and Physics*, (CRC Press, Boca Raton, FL, 1986), p. B-301.

152. M. F. H. Schuurmans, Q. H. F. Vheren and D. Polder, "Superfluorescence," Advances in Atomic and Molecular Physics **17** p. 167 (1981).

153. M. H. Sher, personal communication, (1989).

154. D. M. Roessler and W. C. Walker, "Optical Constants of Magnesium Oxide and Lithium Fluoride in the Far Ultraviolet," Journal of the Optical Society of America **57** p. 835 (1967).

155. T. B. Lucatordo, T. J. McIlrath and J. R. Roberts, Journal of the Optical Society of America **18** p. 2505 (1979).

156. R. C. Weast, M. J. Astle and W. H. Beyer, *CRC Handbook of Chemistry and Physics*, (CRC Press, Boca Raton, FL, 1986), p. B-243.

157. R. G. Caro, J. C. Wang, J. F. Young and S. E. Harris, "Population distributions in Li vapor excited by a photoionization electron source," Physical Review A **30** (3), p. 1407 (1984).

158. F. Reif, *Fundamentals of statistical and thermal physics*, in McGraw-Hill series in fundamentals of physics, E. U. Condon, Eds. (McGraw-Hill, New York, 1965), p. 387.

159. J. Berkowitz, *Photoabsorption, Photoionization, and Photoelectron Spectroscopy*, (Academic Press, New York, 1979), p. 216.

160. H. Tawara and T. Kato, "Total and partial ionization cross sections of atoms and ions by electron impact," Atomic Data and Nuclear Data Tables **36** (1), p. 167 (1987).

161. W. T. Silfvast and O. R. Wood II, "Simple efficient traveling-wave excitation of short-wavelength lasers using a conical pumping geometry," Optics Letters **14** (1), p. 18 (1989).

162. M. H. Sher, J. J. Macklin, J. F. Young and S. E. Harris, "Saturation of the Xe III 109-nm laser using traveling-wave laser-produced-plasma excitation," Optics Letters **12** (11), p. 891 (1987).

163. C. Martin and S. Bowyer, "Quantum efficiency of opaque CsI photocathodes with channel electron multiplier arrays in the extreme and far ultraviolet," Applied Optics **21** (23), p. 4206 (1982).

164. L. Casperson and A. Yariv, "Pulse Propagation in a High-Gain Medium," Physical Review Letters **26** (6), p. 293 (1971).

165. L. Casperson and A. Yariv, "Longitudinal modes in a high-gain laser," Applied Physics Letters **17** (6), p. 259 (1970).

166. N. Skribanowitz, I. P. Herman, J. C. MacGillivray and M. S. Feld, "Observation of Dicke Superradiance in Optically Pumped HF Gas," Physical Review Letters **30** (8), p. 309 (1973).

167. R. H. Dicke, "Coherence in Spontaneous Radiation Processes," Physical Review **93** (1), p. 99 (1954).

168. J. C. MacGillivray and M. S. Feld, "Theory of superradiance in an extended, optically thick medium," Physical Review A **14** (3), p. 1169 (1976).

169. R. Friedberg and S. R. Hartmann, "Superradiant damping and absorption," Physics Letters **37A** (4), p. 285 (1971).

170. R. Friedberg and S. R. Hartmann, "Superradiant lifetime: Its definitions and relation to absorption length.," Physical Review A **13** (1), p. 495 (1976).

171. G. R. Fowles, *Introduction to Modern Optics*, (Holt, Rinehart, and Winston, New York, 1975), p. 279.

172. H. Kume, K. Koyama, K. Nakatsugawa, S. Suzuki and D. Fatlowitz, "Ultrafast microchannel plate photomultipliers," Applied Optics **27** (6), p. 1170 (1988).

173. T. Murao, I. Yamazaki and K. Yoshihara, "Applicability of a microchannel plate photomultiplier to the time-correlated photon counting technique," Applied Optics **21** (13), p. 2297 (1982).

174. J. Girard and M. Bolore, "Heavy Ion Timing with Channel-Plates," Nuclear Instruments and Methods **140** p. 279 (1977).

175. B. Leskovar, "Recent advances in high-speed photon detectors," Laser Focus **20** (2), p. 73 (1984).

176. M. M. Murnane and R. W. Falcone, "Short pulse laser interactions with solids," in conference proceedings of *SPIE,* (Society of Photo-Optical Instrumentation Engineers, Bellingham, WA, 1988) #913, p. 5.

177. P. R. Bevington, *Data Reduction and Error Analysis for the Physical Sciences*, (McGraw-Hill, New York, 1969), p. 184.

178. A. Striganov and N. Sventitskii, *Tables of Spectral Lines of Neutral and Ionized Atoms* (IFI/Plenum, New York, 1968).

179. C. E. Moore, *Atomic Energy Levels* (U.S. Government Printing Office, Washington D.C., 1971).

180. D. V. O'Conner and D. Phillips, *Time-Correlated Single Photon Counting*,(Academic Press, London, 1984), p. 164.

181. P. B. Coates, "Pile-up corrections in the measurement of lifetimes," Journal of Physics E **5** p. 148 (1972).

182. C. C. Davis and T. A. King, "Correction methods for photon pile-up in lifetime determination by single-photon counting," Journal of Physics A **3** p. 101 (1970).

183. C. Holzapfel, "On statistics of time-to-amplitude convertor systems in photon counting devices," Review of Scientific Instruments **45** (7), p. 894 (1974).

184. T. Möller and G. Zimmerer, "Time Resolved Spectroscopy with Synchrotron Radiation in the Vacuum Ultraviolet," Physica Scripta **T17** p. 177 (1987).

185. R. A. Rosenberg, M. G. White, E. D. Poliakoff, G. Thornton and D. A. Shirley, "Lifetime of the Xe II $5s5p^6\ ^2S_{1/2}$ state," Journal of Physics B **11** (23), p. L719 (1978).

186. J. A. R. Samson, "The Measurement of the Photoionization Cross Sections of the Atomic Gases," in *Advances in Atomic and Molecular Physics* , D. R. Bates, I. Estermann, Eds. (Academic Press, New York, 1966), p. 177.

187. "FTD 2003 specifications," Galilleo Electro-optics 1986.

188. S. E. Harris, personal communication, (1985).

189. M. H. Chen, personal communication, (1985).

190. W. T. Silfvast, J. M. Green and O. R. Wood II, "Population Inversions and the Measurement of Gain in Laser-Produced Plasmas," Physical Review Letters **35** (7), p. 435 (1975).

191. A. E. Siegman, "Unstable Optical Resonators," Applied Optics **13** (2), p. 353 (1974).

192. L. O. Werme, T. Bergmark and K. Siegbahn, "The $L_{2,3}MM$ Auger spectrum of Argon," Physica Scripta **8** p. 149 (1973).

193. E. J. McGuire, "Auger spectrum of the noble gases. II. Argon*," Physical Review A **11** (6), p. 1880 (1975).

194. R. D. Hudson and L. J. Kieffer, "Compilation of ultraviolet photoabsorption cross sections for atoms between 5 and 3500 Å," NASA #SP-3064, 1971.

195. J. Berkowitz, *Photoabsorption, Photoionization, and Photoelectron Spectroscopy*, (Academic Press, New York, 1979), p. 183.

196. M. M. Murnane and R. W. Falcone, "High-power femtosecond dye-laser system," Journal of the Optical Society of America B **5** (8), p. 1573 (1988).

197. P. Maine, D. Strickland, P. Bado, M. Pessot and G. Mourou, "Generation of Ultrahigh Peak Power Pulses by Chirped Pulse Amplification," IEEE Journal of Quantum Electronics **24** (2), p. 398 (1988).

198. M. M. Murnane, H. C. Kapteyn and R. W. Falcone, "High-Density Plasmas Produced by Ultrafast Laser Pulses," Physical Review Letters **62** (2), p. 155 (1989).

199. J. Kirz, *et al.*, *X-ray Data Booklet* (Lawrence Berkeley Laboratory, Berkeley, CA, 1985).

200. L. L. House, "Theoretical wavelengths for K-α type x-ray lines in the spectra of ionized atoms (carbon to copper)," Astrophysical Journal Supplement **18** (155), p. 21 (1969).

201. E. J. McGuire, "K-Shell Auger Transition Rates and Fluorescence Yields for Elements Be-Ar," Physical Review **185** (1), p. 1 (1969).

202. M. O. Krause and J. H. Oliver, "Natural Widths of Atomic K and L Levels, Kα X-Ray Lines and Several KLL Auger Lines," Journal of Physical and Chemical Reference Data **8** (2), p. 329 (1979).

203. R. J. Maurer and R. L. Watson, "Dirac-Fock energies for multiple k- plus l-shell vacancy states of ions with Z=9 to 18," Atomic Data and Nuclear Data Tables **34** (2), p. 185 (1986).

204. M. O. Krause, "Atomic Radiative and Radiationless Yields for K and L Shells," Journal of Physical and Chemical Reference Data **8** (2), p. 307 (1979).

205. J. J. Yeh and I. Lindau, "Atomic subshell photoionization cross sections and asymmetry parameters: $1 \leq Z \leq 103$," Atomic Data and Nuclear Data Tables **32** (1), p. 1 (1986).

206. D. J. Fabian, *Soft X-ray Band Spectra* (Academic Press, London, 1968).

207. J. Kieser, "On the Electronic Structure of Graphite," Zeitscrift für Physik B **26** (1), p. 1 (1977).

208. J. Nordgren and C. Nordling, "Ultrasoft X-Ray Emission from Atoms and Molecules," Comments on Atomic and Molecular Physics **13** (5), p. 229 (1983).

209. B. L. Henke, P. Lee, T. J. Tanaka, R. L. Shimabukuro and B. K. Fujikawa, "Low energy x-ray interaction coefficients: photoabsorption, scattering, and reflection," Atomic Data and Nuclear Data Tables **27** (1), p. 1 (1982).

210. D. L. Musinski, T. M. Henderson, R. J. Simms, T. R. Pattinson and R. B. Jacobs, "Technological aspects of cryogenic laser-fusion targets," Journal of Applied Physics **51** (3), p. 1394 (1980).

211. M. Murnane, "Sub-Picosecond Laser-Produced Plasmas," Ph.D. thesis, University of California at Berkeley, 1989.

212. A. Caruso and R. Gratton, "Interaction of short laser pulses with solid materials," Plasma Physics **11** p. 839 (1969).

213. L. Spitzer, *Physics of fully ionized gases*, in Interscience tracts on physics and astronomy, R. E. Marshak, Eds. (Interscience Publishers, Inc., New York, 1956), p. 78.

214. J. Berkowitz, *Photoabsorption, Photoionization, and Photoelectron Spectroscopy* (Academic Press, New York, 1979).

215. W. Lotz, "An Empirical Formula for the Electron-Impact Ionization Cross-Section," Zeitschrift für Physik **206** p. 205 (1967).

216. J. A. Beardon, "X-Ray Wavelengths," Reviews of Modern Physics **39** (1), p. 78 (1967).

217. C. P. Bhalla, N. O. Folland and M. A. Hein, "Theoretical K-Shell Auger Rates, Transition Energies, and Fluorescence Yields for Multiply Ionized Neon," Physical Review A **8** (2), p. 649 (1973).

218. J. Berkowitz, *Photoabsorption, Photoionization, and Photoelectron Spectroscopy*, (Academic Press, New York, 1979), p. 173.

219. D. L. Book, *NRL Plasma Formulary* (Naval Research Laboratory, Washington, DC, 1983).

220. Y. B. Zel'dovich and Y. P. Raizer, *Physics of Shock Waves and High-Temperature Hydrodynamic Phenomena*, Volume 1, W. B. Hayes, R. F. Probstein, Eds. (Academic Press, New York, 1966), p. 408.

221. D. J. G. Irwin, A. E. Livingston and J. A. Kernahan, "Radiative Mean-Life Measurements in Neon below 1000Å," Canadian Journal of Physics **51** p. 1948 (1973).

222. A. P. Thorne, *Spectrophysics*, (Chapman and Hall, New York, 1988), p. 51.

223. I. I. Sobelman, L. A. Vainshtein and E. A. Yukov, *Excitation of Atoms and Broadening of Spectral Lines*, Volume 7, in Springer Series in Chemical Physics, J. P. Toennies, Eds. (Springer-Verlag, New York, 1981), p. 289.

224. T. K. Gaylord, E. N. Glytsis and M. G. Moharam, "Zero-reflectivity homogeneous layers and high spatial-frequency surface-relief gratings on lossy materials," Applied Optics **26** (15), p. 3123 (1987).

225. N. F. Hartman and T. K. Gaylord, "Antireflection gold surface-relief gratings: experimental characteristics," Applied Optics **27** (17), p. 3738 (1988).

226. J. Cooper, "Plasma Spectroscopy," Reports on Progress in Physics **29** (1), p. 35 (1966).

227. J. Nordgren, *et al.*, "Determination of the natural lifetime width of the C 1s state in CO_2," Journal of Physics B **15** p. L153 (1982).

228. L. O. Werme, B. Grennberg, J. Nordgren, C. Nordling and K. Siegbahn, "Observation of Vibrational Fine Structure in X-Ray Emission Lines," Physical Review Letters **30** (12), p. 523 (1973).

229. J. Nordgren, *et al.*, "Core state vibrational excitations and symmetry breaking in the CK and OK emission spectra of CO_2," Journal of Chemical Physics **76** (8), p. 3928 (1982).

230. H. Ågren, R. Arneberg, J. Müller and R. Manne, "X-ray emission of the nitrogen molecule following photon or electron impact. A theoretical study using configuration-interaction wavefunctions.," Chemical Physics **83** p. 53 (1984).

231. H. Ågren, L. Selander, J. Nordgren, C. Nordling and K. Siegbahn, "X-ray spectra and core hole energy curves of some diatomic molecules," Chemical Physics **37** p. 161 (1979).

232. R. C. C. Perera and B. L. Henke, "Low energy x-ray emission spectra and molecular orbital analysis of CH_4, CCl_4, and $CHCl_3$," Journal of Chemical Physics **70** (12), p. 5398 (1979).

233. K. Takeshita, "A theoretical analysis of the Jahn-Teller effect in the photoelectron spectrum of methane," Journal of Chemical Physics **86** (1), p. 329 (1986).

234. J. W. Rabalais, T. Bergmark, L. O. Werme, L. Karlsson and K. Siegbahn, "The Jahn-Teller Effect in the Electron Spectrum of Methane," Physica Scripta **3** (1), p. 13 (1971).

235. L. Apslund, *et al.*, "Vibrational structure and lifetime broadening in core-ionised methane," Journal of Physics B **18** p. 1569 (1985).

236. J. Berkowitz, *Photoabsorption, Photoionization, and Photoelectron Spectroscopy*, (Academic Press, New York, 1979), p. 283.

237. R. Spohr, *et al.*, "Electron Spectroscopic Investigation of Auger Processes in Bromine Substituted Methanes and Some Hydrocarbons," Physica Scripta **2** (1), p. 31 (1970).

238. J. Berkowitz, *Photoabsorption, Photoionization, and Photoelectron Spectroscopy*, (Academic Press, New York, 1979), p. 273.

239. H. Chatham, D. Hils, R. Robertson and A. Gallagher, "Total and partial electron collisional ionization cross sections for CH_4, C_2H_6,SiH_4, and Si_2H_6," Journal of Chemical Physics **81** (4), p. 1770 (1984).

240. A. Langenberg and J. van Eck, "Carbon, nitrogen, neon and argon K-shell ionization by proton and helium-ion impact: x-ray emission cross sections and fluorescence yields," Journal of Physics B **9** (14), p. 2421 (1976).

241. P. F. Moulton, "Solid State Research Report," MIT Lincoln Laboratory 1982.

242. P. Albers, E. Stark and G. Huber, "Continuous-wave laser operation and quantum efficiency of titanium-doped sapphire," Journal of the Optical Society of America B **3** (1), p. 134 (1986).

243. M. Birnbaum and A. J. Pertica, "Laser material characteristics of Ti:Al_2O_3," Journal of the Optical Society of America B **4** (9), p. 1434 (1987).

244. P. Lacovara, L. Esterowitz and R. Allen, "Flash-lamp-pumped Ti:Al_2O_3 laser using fluorescent conversion," Optics Letters **10** (6), p. 273 (1985).

245. D. D. Lowenthal, C. Muller, K. Kangas and D. Ford, "Tunable, Efficient, Ti:Sapphire Amplifiers for Four-Wave Mixing Experiments," in conference proceedings of *Topical*

Meeting on Tunable Solid State Lasers, (Optical Society of America, Washington, DC, 1987) , p. 51.

246. P. F. Moulton, "Spectroscopic and laser characteristics of Ti:Al_2O_3," Journal of the Optical Society of America B **3** (1), p. 125 (1986).

247. P. F. Moulton, "Titanium-Doped Sapphire Laser Research and Design Study," NASA Contractor Report #4093, 1987.

248. P. A. Schulz, K. F. Wall and R. L. Aggarwal, "Simple model for amplified spontaneous emission in a Ti:Al_2O_3 amplifier," Optics Letters **13** (12), p. 1081 (1988).

249. K. F. Wall, R. A. Aggarwal, R. E. Fahey and A. J. Strauss, "Small-Signal Gain Measurements in a Ti:Al_2O_3 Amplifier," IEEE Journal of Quantum Electronics **24** (6), p. 1016 (1988).

250. K. L. Sala, G. A. Kenney-Wallace and G. E. Hall, "CW Autocorrelation Measurements of Picosecond Laser Pulses," IEEE Journal of Quantum Electronics **QE-16** (9), p. 990 (1980).

251. M. J. Weber, D. Milam and W. L. Smith, "Nonlinear refractive Index of Glasses and Crystals," Optical Engineering **17** (5), p. 463 (1978).

252. O. E. Martinez, "3000 Times Grating Compressor with Positive Group Velocity Dispersion: Application to Fiber Compensation in 1.3-1.6 μm Region," IEEE Journal of Quantum Electronics **QE-23** (1), p. 59 (1987).

253. O. E. Martinez, "Design of High-Power Ultrashort Pulse Amplifiers by Expansion and Recompression," IEEE Journal of Quantum Electronics **QE-23** (8), p. 1385 (1987).

254. M. Pessot, P. Maine and G. Mourou, "1000 times expansion/compression of optical pulses for chirped pulse amplification," Optics Communications **62** (6), p. 419 (1987).

255. M. Pessot, J. Squier, P. Bado, G. Mourou and D. J. Harter, "Chirped Pulse Amplification of 300 fs Pulses in an Alexandrite Regenerative Amplifier," IEEE Journal of Quantum Electronics **25** (1), p. 61 (1988).

256. P. Maine and G. Mourou, "Amplification of 1-nsec pulses in Nd:Glass followed by compression to 1 psec," Optics Letters **13** (6), p. 467 (1988).

257. E. B. Treacy, "Optical Pulse Compression With Diffraction Gratings," IEEE Journal of Quantum Electronics **QE-5** (9), p. 454 (1969).

258. W. H. Knox, "Generation and kilohertz-rate amplification of femtosecond optical pulses around 800 nm," Journal of the Optical Society of America B **4** (11), p. 1771 (1987).

259. M. D. Dawson, D. Maxson, T. F. Boggess and A. L. Smirl, "Cavity-length detuning effects and stabilization of a synchronously pumped femtosecond linear dye laser," Optics Letter **13** (2), p. 126 (1988).

260. J. Hebling and J. Kuhl, "Generation of femtosecond pulses by traveling-wave amplified spontaneous emission," Optics Letters **14** (5), p. 278 (1989).

261. I. N. Ross, *et al.*, "Design and performance of a new line focus geometry for x-ray laser experiments," Applied Optics **26** (9), p. 1584 (1987).

262. R. Wyatt and E. E. Marinero, "Versatile Single-Shot Background-Free Pulse Duration Measurement Technique, for Pulses of Subnanosecond to Picosecond Duration," Applied Physics **25** p. 297 (1981).

263. Z. Bor, S. Szatmári and A. Müller, "Picosecond Pulse Shortening by Travelling Wave Amplified Spontaneous Emission," Applied Physics B **32** p. 101 (1983).

264. L. Wenchong, N. Changlong, H. Zuozhu, C. Jian and W. Wanlun, "Investigation of ultrashort traveling-wave amplified spontaneous emission," Chinese Physics- Lasers **14** (7), p. 469 (1987).

265. H. C. Kapteyn, W. W. Craig, G. D. Power, J. Schachter and R. W. Falcone, "A soft x-ray streak camera using a microchannel plate photocathode," in conference proceedings of *SPIE*, (Society of Photo-Optical Instrumentation Engineers, Bellingham, WA, 1987) #832, p. 376.

266. A. Zigler, J. H. Underwood, J. Zhu and R. W. Falcone, "Rapid lattice expansion and increased x-ray reflectivity of a multilayer structure due to pulsed laser heating," Applied Physics Letters **51** (23), p. 1873 (1987).

267. C. L. Wang, *et al.*, "Microchannel plate streak camera," Review of Scientific Instruments **56** (5), p. 835 (1985).

268. A. J. Guest, "A computer model of channel multiplier plate performance," Acta Electronica **14** (1), p. 79 (1971).

269. G. L. Stradling, J. K. Studebaker, C. Cavailler, J. Launspach and J. Planes, "Characterization results from several commercial soft x-ray streak cameras," in conference proceedings of *SPIE*, (Society of Photo-Optical Instrumentation Engineers, Bellingham, WA, 1986) #693.

270. O. H. W. Siegmund and R. F. Malina, "Detection of EUV and soft x-rays with microchannel plates: a review," American Chemical Society Symposium Series **236** p. 253 (1983).